**Charles University**

**The Second Faculty of Medicine**

Doctoral study programme: Imaging Methods in Medicine

**Yeva Prysiazhniuk**

# Optimizing Arterial Spin Labeling MRI for the diagnosis and monitoring of brain diseases

Optimalizace Arterial Spin Labeling MRI pro diagnostiku a monitoring onemocnění mozku

Dissertation Thesis

Supervisor: doc. MUDr. Martin Kynčl

Advisors: prof. MUDr. Jakub Otáhal, PhD., Mgr. Jan Petr, Ph.D.

Prague, 2025

**Declaration**

I declare hereby that I made this dissertation thesis by myself and that I mentioned and cited properly all the sources and literature. At the same time, I declare that this thesis was not used to obtain another or the same title.

I agree with permanent deposition of an electronic version of my thesis in the system database of interuniversity project Thesis.cz for a permanent control of similarities of theses.

In Prague on……

Yeva Prysiazhniuk

…….

**Acknowledgement**

First and foremost, I owe my deepest gratitude to my supervisors. Dr. Jan Petr, thank you for introducing me to the world of perfusion MRI with such thoughtful and kind guidance – it truly changed the course of my life and steered me from the comfort of corporate IT into the endlessly intriguing chaos of academia. Prof. Jakub Otáhal, your unwavering support for my wildest research ideas and your gift for providing both freedom and wisdom have made this work possible – without your mentorship, this thesis would still be just a theory. Dr. Martin Kynčl, thank you for grounding my research in clinical reality; your insights, trust, and commitment to involving me in clinical practice gave true meaning to my work – without you, my writing would risk becoming the whim of a graphomaniac. To all my supervisors, thank you for your open-minded, supportive guidance, and for your steady wisdom during both scientific and personal storms.

I am grateful to my colleagues at the Second Faculty of Medicine and University Hospital Motol – Zuzana Holubová, David Kala, Lukáš Michal, Bruno Jurášek, and Šárka Danačíková – for creating a motivating environment and reminding me that even an engineer can feel at home in the clinic. Special thanks to our MRI technicians, Veronika Borovcová and Jan Brhel, for their patience and spirit of experimentation, always ready to push clinical protocols just a little further.

My work would not have been possible without the support of the vibrant international community that welcomed me, encouraged me to grow, and helped bring new ideas to Prague. The GliMR initiative was indispensable in my early PhD years, providing a platform for both inspiration and practical learning. Thanks to GliMR STSM, I was fortunate to spend an internship in Oslo, immersed in world-class MRI research at Oslo University Hospital. I am especially grateful to Wibeke Nordhøy for supporting this adventure and affording me ample opportunity to develop the fine arts of stress management and independence, and, just as importantly, for becoming a friend along the way.

A special thank you to Rui Armindo Duarte: I'm still not sure how I merited your unflagging support, but your encouragement, introductions, and invitations to the international stage have been a gift. Moss Zhao, thank you for believing in our shared research dreams and for stimulating discussions on ASL, life, literature, and the joy of travel. Your visit to Prague was a true highlight, and I look forward to many more collaborations (Rui, this goes for you as well). Sasha Alexander and Elizabeth Tong, thank you for championing our research ideas

and helping them grow; I am convinced our drive to improve pediatric neuroimaging will lead to important progress.

I am grateful to Vera Keil for involving me in many research adventures and for trusting me in ongoing projects – your clinical wisdom and deliciously sharp humor have been both grounding and motivating. To Aynur Azizova, my research partner extraordinaire, thank you for your drive, intelligence, and determination; our teamwork has set a standard I hope to match in all future collaborations. I look forward to many more projects together – with Vera and Aynur – built not only on scientific curiosity, but on the human values that make collaboration truly worthwhile.

Finally, I express my deepest admiration and gratitude to my family – my lifelong role models in kindness, stoicism, optimism, strength, and humanity. Not a day passes without gratitude for your love, which has allowed me to grow as a scientist and a person. Even in the hardest times, your example is a reminder that people like you are the reason the future is possible.

## Abstract

Perfusion imaging is a medical diagnostic method that indicates the passage of blood through organs and tissues; this method is currently gaining more and more applications in clinical diagnostics and research. Perfusion imaging can detect decreased blood supply (ischemia), restricted blood flow due to the changes in the blood vessels, physiological changes and abnormalities; it is also closely correlated with the metabolism in the tissue and electrical activity in brain. Perfusion is the important parameter in research and diagnostics of age-related changes in the brain, neurodegenerative diseases, neurovascular diseases, multiple sclerosis, brain tumors, traumatic brain injury, psychiatric disorders, etc. The goal of the thesis is to analyze the clinical applicability and relevance of currently available perfusion MRI techniques in various clinical conditions. In the course of this work, a special emphasis will be put on Arterial spin labelling MRI (ASL MRI), as on the perfusion imaging technique that does not require the administration of any exogenous contrasting agent, thus being safer and easier in the implementation. Nevertheless, it is still not common in routine clinical practice, thus the other goal of the project is to prepare a framework for the implementation and introduction of the method into clinical practice. ASL MRI will also be compared with other perfusion imaging method called DSC (Dynamic Susceptibility Contrast) MRI, which is based on the signal changes generated by a contrasting agent.

## Abbreviations

AD – Alzheimer's Disease

ADC – Apparent Diffusion Coefficient

AI – Artificial Intelligence

ANTs – Advanced Normalization Tools

ASL – Arterial Spin Labeling

ATT – Arterial Transit Time

BBB – Blood-Brain Barrier

BOLD – Blood Oxygen Level Dependent

CBV – Cerebral Blood Volume

CBF – Cerebral Blood Flow

CNS – Central Nervous System

CSF – Cerebrospinal Fluid

CVR – Cerebrovascular Reactivity

DCE – Dynamic Contrast-Enhanced (MRI)

DSC – Dynamic Susceptibility Contrast (MRI)

DTI – Diffusion Tensor Imaging

EPI – Echo Planar Imaging

FLAIR – Fluid-Attenuated Inversion Recovery

FOV – Field of View

GM – Gray Matter

IDH – Isocitrate Dehydrogenase

IV – Intravenous

MAP – Mean Arterial Pressure

MNI – Montreal Neurological Institute

MRI – Magnetic Resonance Imaging

NVC – Neurovascular Coupling

NVU – Neurovascular Unit

OEF – Oxygen Extraction Fraction

PC – Phase Contrast

PET – Positron Emission Tomography

PLD – Post-Labeling Delay

pCASL – Pseudocontinuous Arterial Spin Labeling

ROI – Region of Interest

SNR – Signal-to-Noise Ratio

TE – Echo Time

TI – Inversion Time

TIV – Total Intracranial Volume

TR – Repetition Time

TSC – Tuberous Sclerosis Complex

T1/T2 – Longitudinal/Transverse Relaxation Time

VOI – Volume of Interest

WM – White Matter

WHO – World Health Organization

**Table of Contents**

# 1. Introduction

## 1.1 Importance of Cerebral Perfusion Imaging

The brain – our most enigmatic organ – depends on a remarkable life-sustaining process: cerebral perfusion. This intricate choreography of blood delivery through the brain's vast capillary network is not merely important – it is absolutely essential for neural survival, structural integrity, and metabolic function. The constant electrical activity of neuronal signaling, synaptic transmission, and maintaining ion gradients requires tremendous energy resources. Yet neurons live precariously, possessing minimal energy reserves and relying almost exclusively on aerobic metabolism, making them uniquely vulnerable to even momentary disruptions in blood flow that can trigger devastating cellular cascade failures and permanent damage. Beyond its critical role in delivering life-giving oxygen and glucose, cerebral blood flow (CBF) orchestrates another vital function: the efficient removal of potentially toxic metabolic waste products. The discovery of the glymphatic system – an elegant brain-wide perivascular network – has transformed our understanding of how the brain cleanses itself from large molecules. This sophisticated system harnesses the power of perfusion to drive the convective exchange of cerebrospinal fluid (CSF) and interstitial solutes (Iliff *et al.*, 2012). The implications are profound: compromised perfusion may sabotage these essential clearance pathways, potentially accelerating the accumulation of devastating neurotoxic proteins like amyloid-β that lie at the heart of Alzheimer's disease and other neurodegenerative disorders.

Cerebral perfusion is not evenly distributed across the brain, but is precisely regulated to match changing metabolic demands through the critical process of neurovascular coupling(Claassen *et al.*, 2021). This precise regulation ensures that highly active brain regions, such as the prefrontal cortex responsible for executive function or areas controlling language, receive blood flow matching their high metabolic needs. Disruption of this delicate relationship between neural activity and blood flow, whether due to vascular injury, inflammation, or metabolic dysfunction, can impair cognitive function and contribute to progressive neurodegeneration.

In the clinical realm, deviations in cerebral perfusion serve as both revealing windows into neurological disease and as driving forces behind brain pathology across an array of disorders. Following arterial occlusion in acute ischemic stroke, a central region of

irreversibly damaged tissue known as the ischemic core rapidly develops, surrounded by a penumbra of hypoperfused but potentially salvageable brain tissue. At this point, a critical race against time begins: while rapid medical intervention to restore blood flow is essential, the survival of the penumbra also depends on the effectiveness of collateral circulation in sustaining tissue viability until reperfusion can be achieved. Perfusion imaging techniques have significantly enhanced stroke management by delineating these distinct territories, informing evidence-based reperfusion therapy decisions with greater precision (Campbell *et al.*, 2015a). Compelling evidence shows perfusion abnormalities extend well beyond acute conditions into chronic neurodegenerative disorders. In Alzheimer's disease, early blood flow reductions in temporoparietal regions can appear before visible brain shrinkage and track alongside cognitive deterioration (Iturria-Medina *et al.*, 2016). Cerebral small vessel disease (CSVD), a major driver of vascular cognitive decline, features persistent hypoperfusion coupled with white matter injury and breakdown of the blood-brain barrier (BBB) (Wardlaw, Smith and Dichgans, 2019). Patients with difficult-to-treat focal epilepsy show distinctive perfusion patterns – both increased and decreased blood flow – that prove valuable for pinpointing seizure origins and planning surgical interventions (Sierra-Marcos *et al.*, 2016; Lam *et al.*, 2020). In progressive conditions like moyamoya disease, characterized by narrowing of brain arteries, profound regional perfusion deficits correlate directly with ischemic damage and guide critical revascularization decisions (Zhao *et al.*, 2023). These diverse examples reveal cerebral perfusion imaging as not just a functional measurement but a vital indicator of disease mechanisms and outcomes across neurological conditions.

Perfusion imaging's clinical utility extends even further, offering unique advantages in the evaluation and management of brain tumors. It plays a transformative role at every stage – diagnosis, treatment planning, and ongoing monitoring. Unlike conventional imaging, perfusion metrics reveal critical insights into tumor blood supply, new vessel formation, and tumor infiltration into surrounding healthy tissue – all key indicators of tumor grade and aggressiveness. Pre-treatment perfusion MRI can distinguish high-grade from low-grade gliomas by identifying molecular marker patterns characteristic of aggressive tumors through the detection of elevated intratumoral CBF (Prysiazhniuk *et al.*, 2024). After treatment, perfusion imaging becomes essential for the challenging task of separating true tumor growth from treatment-related changes that mimic progression, especially in glioblastoma where standard imaging often proves inconclusive (Moltoni *et al.*, 2024). In

pediatric populations, where biopsy availability is often limited, perfusion imaging offers a valuable non-invasive window into tumor biology and response to therapy (Iacoban *et al.*, 2024). The integration of perfusion-based markers into standard neuro-oncology practice represents a fundamental shift from purely structural evaluation to dynamic functional characterization of tumors, while also significantly improving agreement among neuroradiologists in their clinical interpretations of glioma imaging (Yamin *et al.*, 2024).

Cerebral perfusion can be assessed using both non-MRI and MRI-based techniques. Computed tomography (CT) is commonly employed in emergency medicine due to its rapid image acquisition, broad availability, and relatively low operational costs. However, it involves exposure to ionizing radiation, the use of iodinated contrast agents, and offers limited soft-tissue resolution. Positron emission tomography (PET) with $^{15}$O-water is regarded as the gold standard for quantitative perfusion imaging, thanks to its high validation and ability to directly measure perfusion using a water tracer. Nevertheless, its clinical application is restricted by limited availability, the requirement for on-site cyclotrons, high operational costs, and exposure to ionizing radiation. In contrast, MRI-based perfusion imaging offers a radiation-free, anatomically detailed, and increasingly accessible alternative. Dynamic susceptibility contrast (DSC) and dynamic contrast-enhanced (DCE) imaging utilize intravenous administration of exogenous contrast agents and are thus invasive, while arterial spin labeling (ASL) offers a completely non-invasive alternative by using magnetically labeled arterial blood water as an endogenous tracer. Ongoing methodological advances and multicenter standardization efforts are supporting the wider clinical adoption of perfusion MRI in neurology, offering robust and patient-friendly tools to monitor cerebral hemodynamics.

While the diversity of MRI-based perfusion methods provides clinicians and researchers with a powerful toolkit for probing brain health, each technique carries distinct limitations that affect its utility in specific patient populations and clinical scenarios. The growing demand for repeatable, accurate, and non-invasive assessment of cerebral perfusion across the lifespan and disease spectrum highlights the need for refined methodologies that can overcome these constraints (Leidhin *et al.*, 2021). Among available techniques, ASL stands out for its potential to fulfill this role – particularly in contexts where contrast agents are contraindicated, longitudinal monitoring is required, or quantitative perfusion measurement is essential. Its non-invasive nature also positions ASL as a promising tool for preventative medicine, enabling large-scale monitoring of at-risk populations without manifested

pathology. The following section explores the persistent clinical and technical gaps in current perfusion imaging and outlines the emerging role of ASL in addressing these unmet needs.

### 1.2 Unmet Clinical Needs and Role for ASL

Despite the clinical relevance of cerebral perfusion in a wide range of neuropathologies, there remains a critical need for imaging methods that are both non-invasive and quantitatively robust. Although DSC and DCE MRI are relatively well-established perfusion imaging techniques, their dependence on gadolinium-based contrast agents (GBCAs) entails risks including nephrogenic systemic fibrosis (NSF), gadolinium deposition in the brain (particularly with repeated administration), and patient discomfort (Vergauwen *et al.*, 2018a; Wamelink *et al.*, 2023; Coimbra *et al.*, 2024). These limitations are particularly concerning in pediatric patients, individuals with renal impairment, or populations requiring serial imaging (Ouyang and Bao, 2025a). Additionally, contrast-based methods often yield semi-quantitative or relative perfusion metrics, susceptible to inter-individual variability (Keil *et al.*, 2017a). This limits their reliability for longitudinal studies and multi-center trials. Even in established clinical settings such as glioma assessment or stroke triage, the lack of fully quantitative, reproducible perfusion parameters can hinder objective treatment decisions and personalized care (Nasel *et al.*, 2019; Henriksen, del Mar Álvarez-Torres, *et al.*, 2022). Furthermore, perfusion imaging in patients with disrupted BBB or susceptibility artifacts – particularly near the skull base, resected areas, or inferior temporal lobes – demands techniques that are both precise and robust to these physiological and technical challenges (Lee *et al.*, 2003; Moyaert *et al.*, 2023).

To address these challenges, there is a growing emphasis on the development and clinical translation of non-invasive, contrast-free imaging methods capable of delivering accurate, reproducible measurements of CBF. Among these, ASL MRI has emerged as a promising technique with substantial clinical potential, enabling direct quantification of perfusion without the need for exogenous tracers. ASL utilizes magnetically labeled arterial blood water as an endogenous tracer, thereby eliminating risks associated with contrast agents and making it ideal for vulnerable populations. Its inherent safety profile makes ASL particularly suitable for use in pediatric imaging, longitudinal disease monitoring, and in patients with renal insufficiency.

Technical advances have further bolstered the feasibility of ASL in clinical settings. Developments such as pseudocontinuous labeling (PCASL), 3D single shot readouts, background suppression, and multi-delay Hadamard-encoded readouts have led to improved signal-to-noise ratios, spatial coverage, reproducibility, and time-efficiency (Alsop *et al.*, 2015a; Woods *et al.*, 2024). Multi-delay ASL protocols address transit time artifacts, enhancing accuracy in patients with altered hemodynamics, most relevant to cerebrovascular disease. The widespread availability of 3T MRI scanners, now standard in most clinical and research institutions, has further facilitated ASL adoption, as higher field strengths improve SNR and prolong longitudinal relaxation of blood while maintaining patient safety. Importantly, quantitative CBF maps derived from ASL are comparable across imaging centers when harmonized protocols are used, making the technique attractive for multi-site trials and longitudinal cohort studies. For example, the RADAR trial demonstrated that site-specific differences in ASL implementation (e.g., scanner hardware, readout modules) could be corrected during data analysis, enabling robust cross-center CBF comparisons (Jarutyte *et al.*, 2025).

There is growing clinical and research interest in advancing arterial spin labeling (ASL) MRI, with new approaches emerging to address specific diagnostic needs – from neurovascular coupling studies to BBB integrity assessment (Hernandez-Garcia *et al.*, 2022a). Recent developments like multi-echo ASL (ME-ASL), diffusion-weighted ASL (DW-ASL), and velocity-selective ASL (VS-ASL) are further pushing the boundaries of perfusion imaging without contrast agents. ME-ASL quantifies BBB water exchange rates (e.g., time of exchange, $T_{ex)}$ by leveraging multi-echo readouts to separate intravascular and extravascular signal compartments, enabling detection of subtle BBB dysfunction in aging and neurodegenerative diseases (Mahroo *et al.*, 2021a). DW-ASL follows a different approach by using diffusion gradients to distinguish between capillary-restricted and tissue-exchanged water, providing a 'pseudo-permeability' metric for conditions like stroke and Alzheimer's disease (Wells *et al.*, 2017). VS-ASL labels blood based on velocity rather than spatial location, reducing sensitivity to arterial transit time artifacts – critical for moyamoya or collateral flow evaluation (Qin *et al.*, 2022a). Meanwhile, hybrid techniques such as ASL/BOLD further enhance utility by simultaneously capturing perfusion and oxygenation dynamics, ideal for functional neuroimaging and neurovascular coupling studies (Cohen, Nencka and Wang, 2018).

Despite these significant technical advances in ASL methodology, several challenges remain particularly relevant for clinical pediatric imaging, where unique physiological and practical considerations demand further optimization. Given the particular vulnerability of pediatric patients, the need for safe, non-invasive cerebral perfusion imaging is especially pronounced in this population, making ASL particularly appealing for clinical use. In pediatric neuroimaging, patient compliance and motion artifacts pose significant challenges. These challenges are exacerbated by the distress caused by intravenous catheter placement and gadolinium administration, both of which negatively impact image quality and diagnostic accuracy (Tyc *et al.*, 1995). Here, the non-invasive nature of ASL offers clear advantages for pediatric populations. However, a major barrier to clinical integration is the lack of standardized reference values for CBF and arterial transit time (ATT) across different developmental stages. Several studies have documented non-linear CBF trajectories throughout childhood and adolescence, reflecting dynamic changes in cerebral metabolism and vascular structure, yet no unified framework exists for age-appropriate interpretation (Satterthwaite *et al.*, 2014a; M. Y. Zhao *et al.*, 2024). In neonates, where the clinical implications of perfusion alterations are profound – such as in hypoxic-ischemic injury or congenital heart disease – the need for robust and feasible perfusion markers is critical. Nonetheless, the inherently slow flow in the neonatal cerebrovasculature and potential motion sensitivity complicate the application of ASL (Tortora, Severino and Rossi, 2020). While feasibility remains to be conclusively demonstrated, ASL holds strong potential to become a cornerstone in pediatric brain perfusion imaging.

A second area where ASL's role remains under active investigation is its comparability with the better-established DSC and DCE. While not formally recommended by the RANO criteria, DSC is widely used in clinical practice as the standard method for perfusion imaging evaluation in adult neuro-oncology, particularly for assessing brain tumor perfusion and treatment response. However, concerns about GBCA have spurred growing interest in developing contrast-free alternatives based on the application of AI or novel approaches to conventional MRI (Azizova *et al.*, 2025a). While ASL has proven valuable for preoperative tumor characterization and longitudinal monitoring, several factors complicate definitive assessment of its clinical utility relative to DSC: (1) the paucity of same-population comparative studies, (2) evolving diagnostic criteria in the WHO CNS tumor classification system, and (3) substantial technical variability in both ASL and DSC implementations across institutions. In epilepsy, both ASL and DSC have been explored for interictal and

periictal perfusion mapping, but neither has achieved widespread clinical consensus (Bansal *et al.*, 2017; Kim *et al.*, 2021). Notably, the contrast mechanism may play a critical role in such contexts: ASL measures water flux and thus may be more sensitive to permeability changes or glymphatic alterations (Marchi *et al.*, 2012), whereas DSC relies on intravascular GBCA dynamics. Furthermore, emerging ASL-derived markers such as $T_{ex}$ are beginning to parallel parameters traditionally obtained from DCE imaging, such as $K^{trans}$, though they reflect different underlying mechanisms – membrane permeability to water in ASL versus leakage across tight junctions in DCE. To ensure clinical adoption, rigorous head-to-head validation of these methods across patient populations, scanner platforms, and disease states remains imperative.

In summary, while challenges exist in perfusion imaging across age groups, neurological conditions, and healthcare settings, significant progress continues to drive the field forward. **Quantitative, non-invasive measurement of CBF is increasingly essential for modern clinical practice, especially in vulnerable populations such as children, where safety, speed, and patient comfort address urgent clinical unmet needs.** ASL has emerged as a leading solution to many of these challenges, offering a repeatable, completely non-invasive method of assessing cerebral hemodynamics with expanding capabilities. Importantly, the implementation of consensus guidelines and standardization frameworks for ASL has already established a solid foundation for clinical adoption. Major research hospitals worldwide are actively validating ASL protocols, integrating this technology into clinical workflows, and demonstrating its utility across diverse patient populations. As the field advances, our improving understanding of cerebrovascular physiology, blood-brain barrier dynamics, and developmental vascular changes continues to refine perfusion imaging applications, with ASL positioned at the forefront of clinical translation and routine implementation.

Having examined the clinical applications and technological evolution of perfusion imaging, we now turn our attention to the underlying physiological foundations that govern these measurements. A comprehensive understanding of cerebral perfusion imaging requires careful consideration of the anatomical architecture and regulatory mechanisms that maintain brain blood flow. The following section explores the intricate physiology of cerebral vasculature and dynamic mechanisms that collectively ensure precise regulation of perfusion. This theoretical framework provides essential context for interpreting perfusion

imaging findings and guides the refinement of quantitative models that more accurately reflect true cerebrovascular physiology.

### 1.3 Physiology of Cerebral Vasculature and Perfusion Regulation

Cerebral blood flow (CBF) represents the volume of blood reaching brain tissue per unit time and is essential for maintaining neuronal function by ensuring continuous delivery of oxygen and nutrients and removal of metabolic byproducts. Although the brain constitutes only approximately 2% of total body weight, it accounts for about 20% of the body's energy consumption and receives around 14% of cardiac output, underscoring its status as the most metabolically demanding organ (Kety and Schmidt, 1948). An extensive and precisely regulated vascular network enables the brain to meet its exceptional metabolic. This complex vascular architecture, encompassing large arteries, arterioles, capillaries, venous drainage systems, and blood-brain barrier (BBB), plays a fundamental role in maintaining cerebral homeostasis. Regulation of cerebral perfusion is achieved through a set of tightly controlled physiological mechanisms collectively referred to as cerebral autoregulation, which maintains relatively stable CBF despite systemic arterial blood pressure (ABP) fluctuations of up to ±50% from baseline.

In this section, we review the anatomical and physiological features of the cerebral vasculature that support effective perfusion, with particular emphasis on the mechanisms governing CBF regulation.

#### 1.3.1 Overview of Cerebral Circulation

The cerebral vasculature forms a highly complex, structurally heterogeneous, and intricately interconnected network of blood vessels that ensures the delivery of oxygenated blood to brain tissue and the removal of metabolic waste. Cerebral circulation is broadly divided into an arterial system that supplies blood to the brain and a venous system that facilitates its drainage. Two primary arterial systems contribute to cerebral perfusion: the anterior circulation, derived from the internal carotid arteries (ICAs), and the posterior circulation, originating from the vertebral arteries (Moore, Dalley and Agur, 2014). While the ICAs are often regarded as the primary conduits for cerebral blood supply (Shyam Prabhakaran, 2015), the contribution of the vertebral arteries should not be underestimated, particularly given their essential role in perfusing the brainstem. The vertebral arteries merge to form the basilar artery (BA), which then joins the anterior circulation to complete the Circle of Willis.

This arterial ring – situated approximately within the interpeduncular fossa and encircling the optic chiasm – plays a critical role in maintaining cerebral perfusion by providing collateral pathways for blood flow (as schematically visualized in Fig. 1).

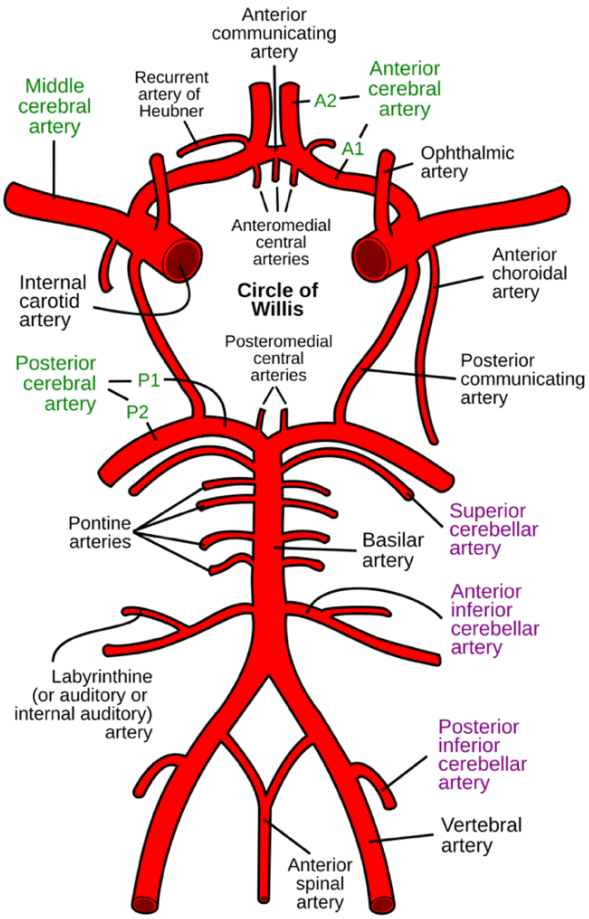


**Figure 1.** Labeled illustration of the major cerebral and brainstem arteries, viewed from the inferior aspect.

Following its intracranial course, the ICA bifurcates into the middle cerebral artery (MCA) and the anterior cerebral artery (ACA). The MCAs primarily supply the motor and sensory cortices associated with the upper limbs and face. They also perfuse Broca's area in the dominant frontal lobe and Wernicke's area in the dominant temporal lobe, both of which are critical for language processing (Gray, Standring and Anhand, 2021). In contrast, the ACAs supply the medial portions of the frontal and parietal lobes, including regions involved in motor and sensory function of the lower limbs (Fig. 2).

On the posterior side, the posterior cerebral arteries (PCAs) originate from the terminal bifurcation of the BA and are anatomically incorporated into the Circle of Willis through

their connection to the internal carotid system via the posterior communicating arteries (PCoAs). The PCAs are primarily responsible for perfusing the occipital lobes, the inferior temporal lobes, most of the midbrain and thalamus, and parts of the posterior limb of the internal capsule (Gray, Standring and Anhand, 2021). While the brainstem and cerebellum receive their blood supply largely from branches of the vertebrobasilar system – including the BA – they are not predominantly supplied by the PCAs (Fig. 3).

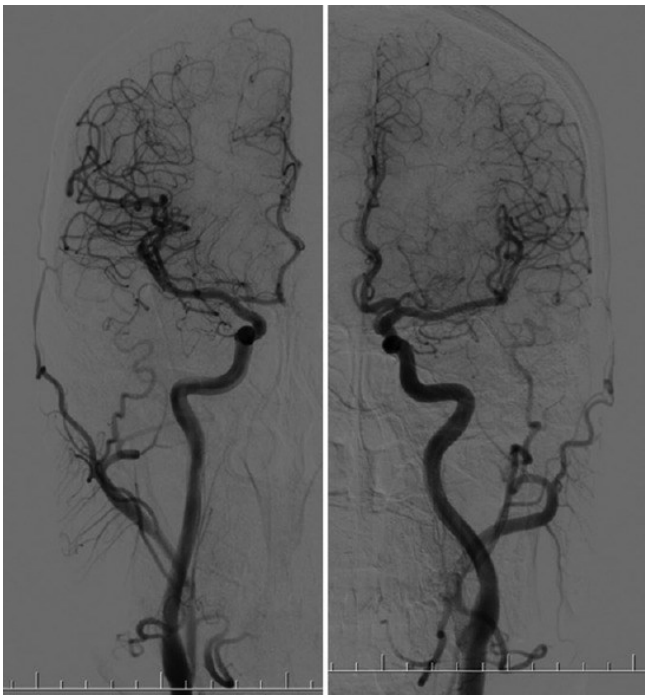

**Figure 2.** Anteroposterior angiographic view of the anterior cerebral circulation, showing the left and right internal carotid arteries. *Adapted from* (Chandra *et al.*, 2017)*, licensed under CC BY-NC-SA 3.0.*

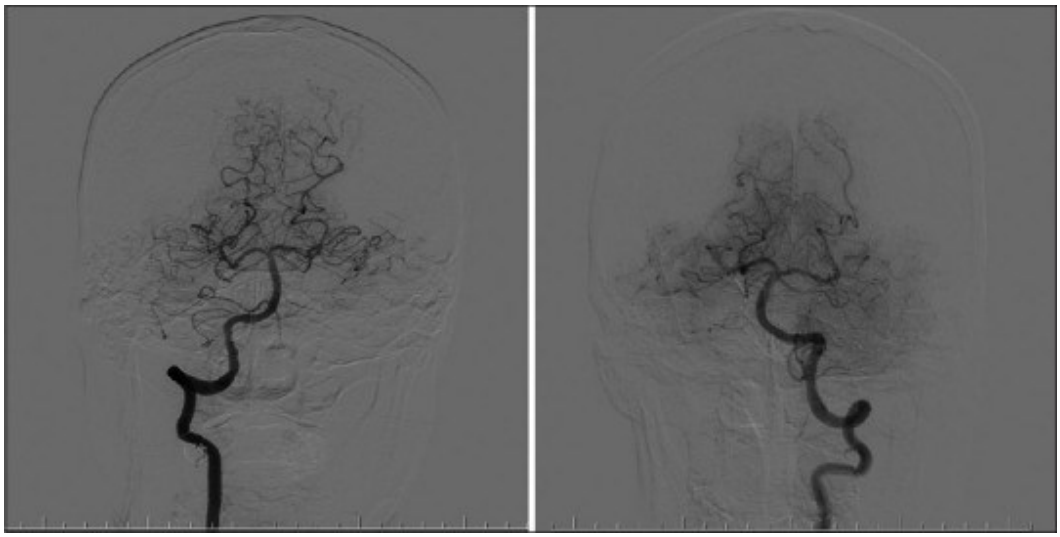

**Figure 3.** Angiographic view of the posterior circulation, depicting the left and right vertebral arteries and the basilar artery. *Adapted from* (Chandra *et al.*, 2017)*, licensed under CC BY-NC-SA 3.0.*

The Circle of Willis exhibits significant structural diversity even among healthy individuals (Krabbe-Hartkamp *et al.*, 1998). Anatomical variations likely have genetic origins, developing during early embryonic stages and continuing throughout life (Crompton, 1962). Deviations from the circle's normal structure may influence both the emergence and intensity of cerebrovascular disorders, including aneurysms, infarcts, and other vascular abnormalities (Menshawi, Mohr and Gutierrez, 2015). The circle's condition plays a crucial role in determining CBF adequacy during procedures such as cerebral aneurysm operations and internal carotid artery ligation.

This anatomical organization of the cerebral vasculature underpins the concept of vascular territories – distinct regions of the brain perfused by specific arterial branches (Tatu *et al.*, 1998). The cerebral vasculature is organized into distinct arterial territories primarily supplied by the ACA, MCA, and PCA (Fig. 4). Identifying which vascular territory is affected during a stroke aids in localizing the occlusion, understanding the patient's clinical symptoms, and formulating an appropriate treatment plan (Hasan *et al.*, 2018; Schneider *et al.*, 2023). The regions where vascular territories converge are known as watershed zones or border zones. These zones are particularly vulnerable to ischemia during episodes of systemic hypoperfusion, as they are located at the distal reaches of multiple arterial supplies. Ischemic events in these areas, termed watershed infarcts, can lead to unique clinical syndromes depending on the specific regions affected (Dogariu *et al.*, 2023). Recent studies have also demonstrated that chronic active lesions in multiple sclerosis tend to be concentrated in watershed regions (Toubasi *et al.*, 2024). This localization may be attributed to hypoxia triggering inflammation in tissues by causing vascular leakage, which initiates the inflammatory cycle. Understanding vascular territories is essential for interpreting neuroimaging findings, particularly in cerebrovascular pathology, where infarct location often corresponds to the affected arterial supply.

In parallel with arterial supply, a sophisticated venous system ensures the drainage of deoxygenated blood and metabolic waste products from the brain. The cerebral venous system, responsible for returning blood from the brain to the systemic circulation, is functionally and structurally distinct from the arterial system. Unlike arteries, cerebral veins

and dural venous sinuses lack valves, permitting bidirectional flow and rendering them particularly vulnerable to fluctuations in intracranial or thoracic pressure. The greater blood volumes and higher distensibility of these vessels confer upon the venous system a critical role in regulating cerebral blood volume (Payne, 2016). Venous drainage is conventionally classified into superficial and deep systems. The superficial veins drain the cerebral cortex and subcortical white matter, ultimately emptying into the superior sagittal and transverse sinuses. The deep venous system comprises the internal cerebral veins, basal veins of Rosenthal, and the great vein of Galen, which collectively drain into the straight sinus before joining the confluence of sinuses. Notably, the venous drainage system interfaces with cerebrospinal fluid circulation through arachnoid granulations and has been implicated in the function of the glymphatic pathway (Louveau *et al.*, 2017). Disruptions in venous drainage – whether through thrombosis, elevated central venous pressure, or impaired glymphatic clearance – may precipitate venous congestion, increased intracranial pressure, or inflammatory pathologies.

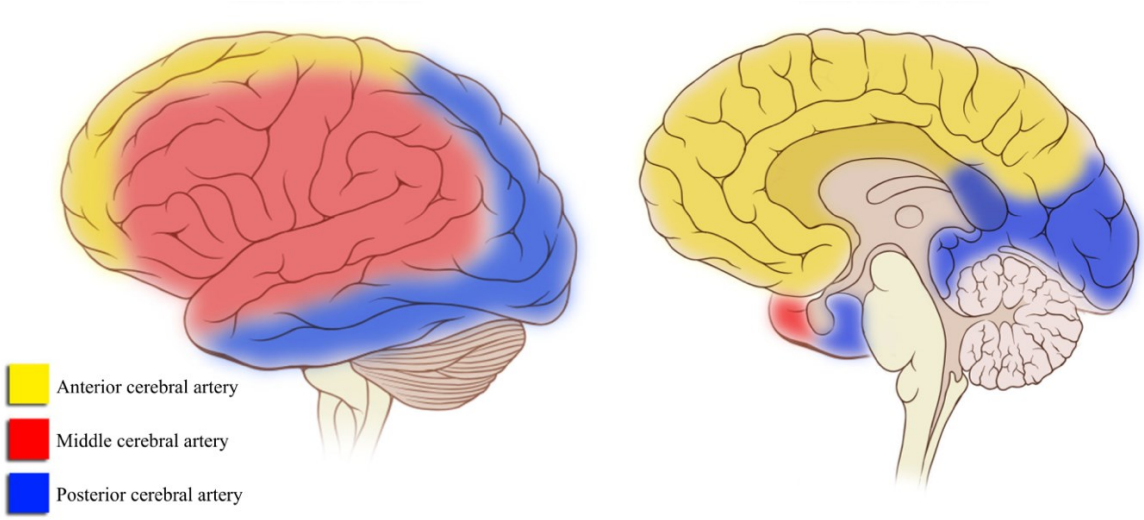


**Figure 4.** Vascular territories of the brain as supplied by the ACA, MCA, and PCA, depicted on lateral (left) and medial (right) brain surfaces. Adapted from Patrick J. Lynch, licensed under CC BY-SA 3.0. Source: Wikimedia Commons.

Global cerebral blood flow demonstrates significant regional heterogeneity, characterized by distinctive perfusion patterns across different brain compartments. Gray matter (GM) typically exhibits substantially higher blood flow rates compared to white matter (WM), with regional perfusion ranging approximately 2-3 times higher in GM (50-70 mL/100g/min) versus WM (15-30 mL/100g/min) (Bammer, 2016). Anterior and posterior cerebral

circulations also demonstrate nuanced flow characteristics, with the anterior circulation supplying approximately 70-75% of total cerebral blood flow, predominantly supporting metabolically active cortical and subcortical structures. The posterior circulation, while accounting for a smaller volumetric proportion, plays a critical role in perfusing brainstem, cerebellum, and occipital regions essential for vital autonomic functions and sensory processing.

While large vessels define the major routes of CBF, it is the brain's microvascular architecture that ensures the precise delivery of oxygen and nutrients at the tissue level. The organization and regulation of this microcirculation are critical for maintaining neuronal health and function, particularly in the context of cerebral perfusion. The following section explores the structural and functional properties of the cerebral microvasculature, highlighting its role in supporting both normal brain activity and responses to pathology.

### 1.3.2 Microvascular Architecture

The cerebral microvasculature comprises a dense and highly specialized network of arterioles, capillaries, and venules that collectively govern the fine-scale distribution and drainage of blood within brain tissue. Beyond passive conduits, these vessels actively regulate local perfusion in response to metabolic demands, playing a central role in maintaining homeostasis and supporting neurovascular coupling.

#### Arterioles: Structure and Regulatory Function

Arterioles serve as critical regulators within the cerebral arterial tree, situated immediately upstream of capillary bed (Rhodin, 2014). Together with terminal arteries, they contribute approximately 80% of total vascular resistance, primarily due to their ability to dynamically adjust luminal diameter through changes in smooth muscle tone (Martinez-Lemus, 2012). Distinguished by walls composed mainly of smooth muscle cell layers, arterioles are essential for regulating vascular resistance and regional cerebral blood flow. Although changes in arteriolar tone can influence perfusion pressure within a given vascular bed, arterioles do not directly control systemic blood pressure; rather, systemic pressure responses are a downstream consequence of cumulative resistance changes across the vascular network. This thin muscular structure typically contains 1-2 smooth muscle cell layers depending on their diameter and location within the cerebral vasculature. Structurally, the arteriolar wall comprises three layers – intima, media, and adventitia – containing both

cellular and extracellular components. Rather than functioning as discrete layers, these components form a highly interconnected architecture, with extensive cross-talk between cellular and extracellular elements (Touyz *et al.*, 2018). These intercellular and matrix interactions are vital for the integrated function of the vascular wall, particularly in modulating vascular tone, mechanotransduction, and neurovascular coupling.

The intimal layer of resistance arteries and arterioles is formed primarily by endothelial cells, acting not only as a barrier between blood and tissue but also as active regulators of vascular tone and permeability (Martinez-Lemus, 2012). Their capacity to sense and transduce mechanical forces – such as shear stress and intraluminal pressure – is tightly linked to their cytoskeletal organization, which undergoes dynamic remodeling in response to hemodynamic stimuli (Chien, 2007). Endothelial cell architecture varies regionally and along the vascular tree, reflecting functional heterogeneity (Aird, 2007). For example, stress fibers and microtubule organization are prominent in feed arterioles but diminish in smaller branches, correlating with changes in flow patterns and vessel size.

Structurally, endothelial cells synthesize and release vasoactive mediators that influence smooth muscle cell contraction, thereby fine-tuning vessel diameter. Inflammatory or toxic insults can alter their cytoskeletal integrity and junctional complexes, leading to increased permeability – particularly in venular segments. These observations underscore the critical role of endothelial structure-function relationships in maintaining vascular homeostasis.

The medial layer of arterioles consists primarily of vascular smooth muscle cells (VSMCs), typically arranged in one to two layers and embedded in a basement membrane along with extracellular matrix (ECM) components such as collagen and elastin (Davis and Hill, 1999). An internal elastic lamina (IEL), a fenestrated elastin sheet, separates the smooth muscle layer from the endothelium, facilitating signaling between layers and undergoing remodeling in response to hemodynamic forces. (Comper, 1996). VSMCs function as key mechanosensors, detecting changes in luminal pressure and stretch through integrin-mediated interactions and dense bodies at cell surfaces. These cells can modulate vessel diameter and structure by reorganizing cytoskeletal elements and releasing ECM-modifying enzymes such as transglutaminases and metalloproteinases, contributing to inward or outward remodeling in both physiological adaptation and pathological states (Martinez-Lemus, Hill and Meininger, 2009).

The adventitia forms the outermost layer of arterioles and is composed of fibroblasts, loosely organized ECM (primarily collagen), elastic fibres, and autonomic nerve endings (Tuma, Durán and Ley, 2008). Although traditionally viewed as a passive support structure, it plays an active role in vascular homeostasis and remodeling. Adventitial fibroblasts can sense injury and stress, releasing cytokines, growth factors (e.g., TGF-β, endothelin-1), and reactive oxygen species that influence smooth muscle phenotype and matrix turnover (Martinez-Lemus, 2012). Under chronic stress or inflammation, these fibroblasts may transdifferentiate into myofibroblasts, gaining contractile features and contributing to neointima formation and fibrosis (Forte *et al.*, 2010). The presence of mesenchymal progenitor-like cells within the adventitia further underscores its potential role in vascular repair and remodeling.

Changes in arteriolar wall structure – particularly in the media and adventitia – are central to the pathogenesis of several cerebrovascular diseases. In moyamoya disease, for instance, narrowing of large arteries is hypothesized to be accompanied by medial thinning, intimal thickening, and abnormal remodeling of internal elastic laminae (KURODA *et al.*, 2015). Related pathological alterations occur in cerebral small vessel disease, hypertensive vasculopathy, and CADASIL, where arteriolar remodeling leads to impaired autoregulation, reduced perfusion, and increased vulnerability to ischemia and hemorrhage (André, 2010; Wardlaw, Smith and Dichgans, 2013). These findings highlight the importance of microvascular wall integrity in maintaining cerebral perfusion and preventing disease.

**Capillaries and venules**

Capillaries, forming the interface between arterioles and venules, consist solely of endothelial cells supported by a basement membrane and occasional pericytes. Their lack of smooth muscle facilitates efficient molecular exchange, while pericytes contribute to local flow regulation, BBB maintenance, and vascular stability. In the brain, these pericytes are the first vascular elements to respond to neuronal activity by dilating, making them critical initiators of neurovascular coupling and the functional imaging signals that arise from it (Hall *et al.*, 2014). However, pericytes are particularly vulnerable to ischemia and die rapidly under hypoperfusion conditions, which can compromise capillary integrity and exacerbate brain injury.

Venules, structurally continuous with capillaries, gradually acquire pericytes and a thin layer of smooth muscle as they increase in diameter. They are central to immune surveillance and inflammation, mediating leukocyte trafficking and becoming highly permeable in pathological states such as vasogenic edema. Importantly, venous vessels, not arterioles, are the primary modulators of BOLD MRI signals (Lee *et al.*, 2001). This is because venous blood contains paramagnetic deoxyhemoglobin, which induces local magnetic field inhomogeneities and dephases NMR signals due to its susceptibility contrast with surrounding tissue. As a result, functional MRI predominantly reflects changes in venous blood volume and oxygenation, and this venous-weighted signal is often used to estimate relative CBF.

**Regional variations in Cerebral Microvascular Architecture**

The cerebral microvasculature exhibits remarkable spatial complexity, characterized by distinct architectural and functional variations across different brain regions. Vessel density serves as a fundamental metric of microvascular organization, with gray matter (GM) demonstrating a remarkably dense capillary network that significantly exceeds the vessel density observed in white matter (WM) (MacGregor Sharp *et al.*, 2020). This architectural disparity reflects the distinct metabolic requirements of neuronal populations. GM capillaries form an intricate, highly interconnected lattice that facilitate rapid nutritional and metabolic support, while WM microvascular networks exhibit a more longitudinally aligned configuration, predominantly oriented parallel to axonal tracts (Viessmann *et al.*, 2022).

Beyond the GM/WM distinction, regional variations in vascular density are also evident across the cerebral cortex, reflecting the diverse functional specializations of different brain areas. Rather than a simple anterior–posterior gradient, recent analyses reveal that vascular density varies in a region-specific manner. It was demonstrated that arterial and venous densities are highest in the frontal, lateral, and visual cortices – areas associated with high metabolic activity and robust synaptic connectivity (Bernier, Cunnane and Whittingstall, 2018). These differences likely correspond to localized neurovascular demands, with both anterior and posterior regions encompassing zones of dense microvascular supply. Such spatial heterogeneity in vascular architecture underscores the importance of considering both microstructural and functional context in studies of cerebral perfusion and metabolism.

The transition from the discussion of capillaries and venules naturally leads to BBB, which represents a critical functional interface between the brain's vasculature and its parenchyma. While capillaries and post-capillary venules are the primary sites of exchange and immune signaling, the BBB is essential for maintaining cerebral homeostasis by tightly regulating the movement of molecules, ions, and cells between blood and brain tissue.

### 1.3.3 The Neurovascular Unit and Blood-Brain Barrier

The blood-brain barrier (BBB) represents a sophisticated molecular and cellular interface critical for maintaining central nervous system (CNS) homeostasis. Fundamentally, the BBB comprises a complex arrangement of endothelial cells, basement membrane, pericytes, and astrocytic end-feet, collectively forming the neurovascular unit (NVU). Beyond serving as a physical and metabolic barrier, the NVU plays a central role in dynamically regulating cerebral perfusion in response to neuronal activity (Fig. 5). Rather than operating through a classical feedback mechanism based on energy deficit detection, neurovascular coupling is primarily a feedforward process: neuronal activation and synaptic signaling rapidly initiate a cascade of events - mediated by neurons, astrocytes, and vascular cells - that lead to local vasodilation and increased regional cerebral blood flow. This regulation ensures the timely delivery of oxygen and glucose to active brain regions, tightly matching perfusion to metabolic demand in both space and time.

#### Structural Components and Functions

The NVU integrates multiple cellular components with distinct yet interdependent functional roles: vascular elements (endothelial cells, pericytes, VSMCs), glial cells (astrocytes, microglia), neurons, and extracellular matrix constituents. Intercellular signaling mechanisms and communication pathways facilitate neurovascular coupling, enabling the translation of neuronal activity into localized hemodynamic responses (Abbott, Rönnbäck and Hansson, 2006; Wu *et al.*, 2023).

Endothelial cells constitute the primary structural element of the BBB, characterized by specialized junctional complexes that severely restrict paracellular molecular transport. The endothelial cells of the BBB are tightly sealed by complex junctional proteins – tight junctions (e.g., claudins, occludin) and adherens junctions (e.g., VE-cadherin) – which form a restrictive paracellular barrier. These junctions, combined with low rates of vesicular

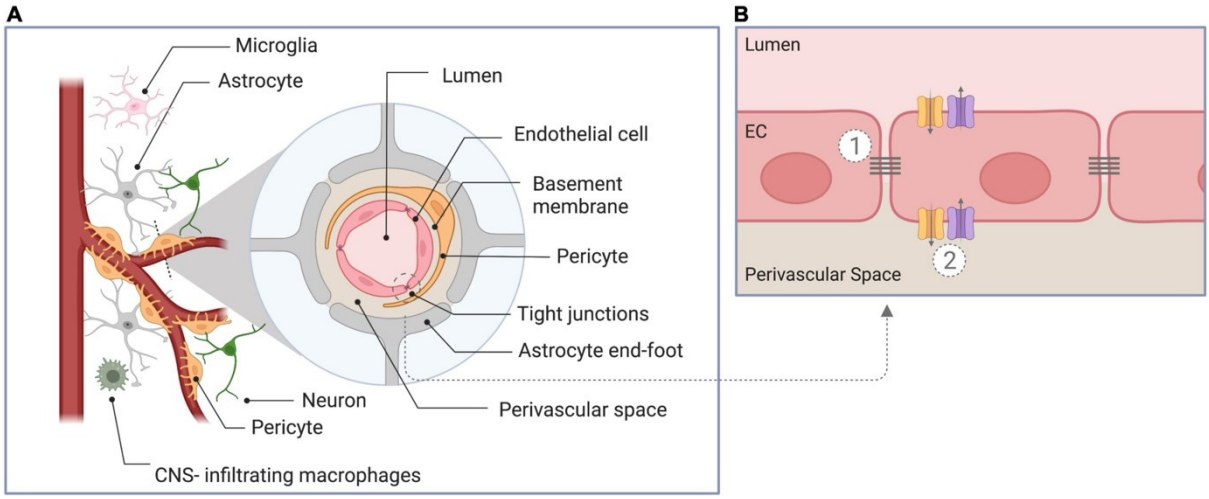


**Figure 5.** Structural components of the blood–brain barrier and neurovascular unit. (A) Schematic cross-section of the NVU, illustrating the close anatomical and functional interplay between endothelial cells, pericytes, astrocytic endfeet, the basement membrane, neurons, and immune cells. (B) Key features of the brain endothelial cells tha t form the BBB: (1) Tight junctions between adjacent endothelial cells and lack of fenestrations, which together restrict paracellular diffusion, and (2) the presence of selective transport systems that mediate tightly regulated transcellular trafficking of substances. *Adapted from (Moyaert et al., 2023), licensed under CC BY 4.0.*

glucose, amino acids, and certain lipophilic agents to cross via dedicated transporter systems (Daneman and Prat, 2015; Zhao *et al.*, 2015a). This selectivity is critical for maintaining ionic gradients, neurotransmitter balance, and protection from systemic toxins or pathogens.

Pericytes, strategically positioned within the basement membrane, contribute critical regulatory functions, including endothelial proliferation control, barrier maintenance, and microvascular stabilization. Astrocytic interactions represent another pivotal mechanism in BBB functional modulation. Through complex paracrine signaling pathways, astrocytes modulate endothelial properties while simultaneously managing ionic homeostasis and neurotransmitter recycling. The precise wrapping of astrocytic end-feet around cerebral blood vessels provides an additional structural and functional regulatory layer (Zlokovic, 2008; Hall *et al.*, 2014).

Microglia, the CNS's resident immune surveillance cells, maintain intimate associations with NVU structures and play a critical role in responding to pathological challenges. Under conditions of injury or inflammation, microglial activation can dynamically modulate BBB

permeability, initiating and amplifying neuroinflammatory cascades. Meanwhile, neurons contribute to this complex system through vasoactive signaling that modulates vascular tone across the NVU, ensuring precise localized hemodynamic adaptations (Zlokovic, 2008).

### 1.3.4 Hemodynamic Parameters: Cerebral Blood Flow, Volume, and Metabolism

The brain's complex microvascular network, together with the specialized components of the NVU, forms the anatomical basis for cerebral perfusion and metabolic regulation. This framework provides essential context for understanding critical hemodynamic parameters – cerebral blood flow (CBF), cerebral blood volume (CBV), and cerebral metabolic rate of oxygen consumption ($CMRO_2$). These physiological metrics serve as primary indicators of brain perfusion and energy requirements, underpinning both functional neuroimaging applications and clinical interpretation.

#### Cerebral Blood Flow

CBF represents the volume of blood delivered to a given mass of brain tissue per unit time, typically measured in milliliters per 100 grams of tissue per minute (mL/100g/min). This parameter is critical for sustaining brain function, as it ensures the continuous delivery of oxygen and glucose while facilitating the removal of metabolic byproducts such as carbon dioxide and lactate (Willie *et al.*, 2014). In the healthy adult brain, global CBF averages approximately 50 mL/100g/min, though substantial regional variations exist depending on metabolic demand and functional specialization (Bammer, 2016).

The brain exhibits pronounced heterogeneity in blood flow due to differences in neuronal activity and energy requirements. Gray matter, which contains densely packed neuronal cell bodies, synapses, and glial cells, typically receives 60-80 mL/100g/min, reflecting its high metabolic demand. In contrast, white matter, primarily composed of myelinated axons with lower metabolic activity, receives significantly less perfusion (20-25 mL/100g/min). Furthermore, highly active regions such as the visual cortex and primary motor areas can exhibit transient increases in CBF during task performance, underscoring the dynamic relationship between neural activity and perfusion.

## Cerebral Blood Volume

CBV quantifies the total volume of blood within the cerebral vasculature at a given moment, typically expressed in milliliters of blood per 100 grams of brain tissue (mL/100g). Despite constituting only 4-5% of total intracranial volume (LEENDERS *et al.*, 1990), CBV serves as a critical parameter in neuroimaging, providing insights into vascular dynamics and hemodynamic coupling in both resting-state and task-based studies.

The distribution of blood volume across cerebral vascular compartments is non-uniform and reflects the structural and functional organization of the brain's microvasculature. In healthy tissue, CBV is distributed approximately as:

- 20-30% arterial (high-pressure, low-volume conduits),
- 40% capillary (the primary site of oxygen/glucose exchange)
- 30-40% venous (low-pressure, high-capacity drainage) (Piechnik, Chiarelli and Jezzard, 2008; Hua *et al.*, 2019)

This distribution ensures efficient oxygen extraction and metabolic waste removal while maintaining hemodynamic stability. The capillary compartment, despite its small individual vessel diameter, dominates CBV due to its immense collective surface area (~20 $m^2$ in the human brain) (Zlokovic, 2005). Alterations in this distribution can occur in various pathological states, including ischemia, where compensatory vasodilation may increase CBV despite reduced CBF (Powers *et al.*, 1985).

CBV is intrinsically linked to CBF through the Grubb relationship ($CBV = CBF^{\alpha}$, where $\alpha \approx 0.38$ under normoxic conditions) (GRUBB *et al.*, 1974). This power-law model describes how changes in flow elicit subproportional changes in blood volume, reflecting vascular compliance and the balance between arterial inflow and venous outflow.

## Cerebral Metabolic Rate of Oxygen Consumption

$CMRO_2$ denotes the rate at which oxygen is consumed by the brain and is a direct measure of cerebral oxidative metabolism, usually measured in milliliters of $O_2$ per 100 grams of brain tissue per minute (mL $O_2$/100g/min). Global $CMRO_2$ averages approximately 3.5 mL $O_2$/100g/min in adults, though like CBF, this varies regionally according to functional specialization (Raichle and Gusnard, 2002). $CMRO_2$ is tightly linked to neuronal activity and energy demand, with approximately 60-80% of energy expenditure supporting synaptic

transmission and action potential propagation (Harris, Jolivet and Attwell, 2012). The remaining energy supports cellular housekeeping functions, protein synthesis, and membrane potential maintenance. Disturbances in $CMRO_2$ are observed in various pathophysiological conditions including hypoxia, ischemia, and neurodegenerative diseases.

Experimental study by Lin et al. (Lin *et al.*, 2010) has established the quantitative relationship between neural activity and $CMRO_2$ increases during functional activation, demonstrating that oxygen metabolism typically increases by 15-30% compared to the much larger CBF increases (50-70%). This mismatch reflects the brain's apparent "luxury perfusion" during neural activation (Le *et al.*, 2023).

These three parameters are interconnected through the Fick principle, a fundamental concept in cardiovascular physiology first described by Adolf Fick in 1870. The principle states that the rate of oxygen consumption ($CMRO_2$) is equal to the product of blood flow (CBF) and the arteriovenous oxygen difference (A-V $O_2$). Mathematically expressed:

$$CMRO_2 = CBF \times (C_aO_2 - C_vO_2),$$

where $C_aO_2$ and $C_vO_2$ are the arterial and venous oxygen contents, respectively, typically measured in mL $O_2$/100 mL blood. This arteriovenous difference represents the amount of oxygen extracted from the blood during its passage through the cerebral circulation. Under normal physiological conditions, arterial blood contains approximately 20 mL $O_2$/100 mL blood, while cerebral venous blood contains about 13 mL $O_2$/100 mL blood, yielding an extraction fraction of roughly 35-40% (Ibaraki *et al.*, 2008). At rest, the brain maintains relatively constant extraction fractions, meaning that metabolic fluctuations are primarily accommodated through flow adjustments rather than increased extraction (Ito *et al.*, 2023).

Rearrangement of the Fick equation allows for determination of oxygen extraction fraction (OEF):

$$OEF = (C_aO_2 - C_vO_2)/C_aO_2 = CMRO_2/(CBF \times C_aO_2).$$

This relationship illustrates that for a given arterial oxygen content, the OEF is determined by the ratio of metabolism to blood flow. Thus, conditions of metabolic-flow mismatch—whether due to pathologically elevated metabolism, reduced perfusion, or both—will manifest as alterations in OEF (Liu and Li, 2016).

Alterations in CBF, CBV, or $CMRO_2$ may occur independently or in tandem in response to physiological demands or pathological insults. Therefore, understanding the baseline properties and interdependence of these parameters is critical for interpreting changes in brain perfusion and metabolism, especially in the context of clinical imaging and cerebral pathophysiology.

### 1.4 Mechanisms of Blood Flow Regulations

The brain has evolved intricate regulatory mechanisms to ensure the precise delivery of oxygen and nutrients while efficiently removing metabolic byproducts. These processes are critical for maintaining homeostasis, particularly given the brain's high metabolic demand and limited energy reserves. Building upon the foundational principles of hemodynamic parameters discussed earlier, this section examines the systems that actively modulate cerebral perfusion: neurovascular coupling, cerebrovascular reactivity, and cerebral autoregulation.

Neurovascular coupling (NVC) ensures that regional blood flow is dynamically matched to neuronal activity, facilitating the rapid delivery of energy substrates to active brain areas. This spatially and temporally precise mechanism, which is primarily mediated by the NVU, underpins functional hyperemia and is essential for normal cognitive function. In contrast, cerebrovascular reactivity (CVR) reflects the capacity of cerebral vessels to dilate or constrict in response to vasoactive stimuli, such as changes in the partial pressure of arterial carbon dioxide ($PaCO_2$). CVR serves as a critical indicator of vascular reserve and endothelial health, often assessed clinically to evaluate cerebrovascular dysfunction. Meanwhile, cerebral autoregulation (CA) maintains stable CBF across fluctuations in systemic blood pressure through myogenic, metabolic, and neurogenic mechanisms, thereby protecting the brain from hypoperfusion or hyperperfusion injury.

Though functionally distinct, these systems operate synergistically to adapt cerebral perfusion to both immediate metabolic needs and systemic physiological challenges. Their integrated function is especially vital during development, aging, and pathophysiological states, where dysregulation can contribute to neurological impairment. A comprehensive understanding of these mechanisms provides the necessary framework for interpreting alterations in brain perfusion and metabolism, as explored in the preceding section, and offers insights into the vascular contributions to neurological disease.

### 1.4.1 Neurovascular coupling – the link between neuronal activity and vascular response

NVC describes the dynamic adjustment of local CBF to match the metabolic demands of active neurons. This precise regulation is essential to preserve synaptic function and prevent energy deficits, as the brain lacks significant energy reserves and requires immediate delivery of oxygen and glucose to active regions. Furthermore, the coupled flow increase facilitates clearance of metabolic byproducts (e.g., lactate, $CO_2$, amyloid-β, and tau) and helps regulate brain temperature (Iadecola, 2017).

**Neuronal Initiation**

Neurons serve as the primary initiators of the NVC cascade which is mediated by coordinated interactions within NVU. Glutamatergic synaptic activity, which dominates excitatory signaling in the cortex, activates postsynaptic AMPA and NMDA receptors, leading to calcium influx and activation of $Ca^{2+}$-dependent enzymes. Two key enzymatic pathways are engaged:

- Neuronal nitric oxide synthase (nNOS), which produces nitric oxide (NO), a potent vasodilator that diffuses to VSMCs and activates soluble guanylyl cyclase (sGC), increasing cGMP and reducing intracellular $Ca^{2+}$ (Yang *et al.*, 2025).
- Cyclooxygenase-2 (COX-2), expressed predominantly in pyramidal neurons, catalyzes the formation of prostanoids, including prostaglandin $E_2$ ($PGE_2$). $PGE_2$ binds to EP2/EP4 receptors on VSMCs, triggering cAMP-mediated relaxation (Lecrux *et al.*, 2011).

Inhibitory interneurons also modulate the vascular response. GABAergic interneurons expressing vasoactive intestinal peptide (VIP) or neuropeptide Y (NPY) can induce biphasic hemodynamic responses - vasodilation via VIP and vasoconstriction via NPY. Somatostatin-positive interneurons contribute to NVC through NO release, while parvalbumin-positive interneurons exert indirect effects by suppressing pyramidal cell activity (Stackhouse and Mishra, 2021). Additionally, subcortical neuromodulatory systems – such as cholinergic projections from the basal forebrain and noradrenergic inputs from the locus coeruleus – fine-tune CBF. Although they do not initiate focal hyperemia, these pathways modulate baseline tone and enhance NVC efficiency by altering vascular reactivity and astrocytic signaling (Yang *et al.*, 2025).

### Astrocytes in Signal Transmission

Astrocytes bridge synaptic activity and vascular responses through $Ca^{2+}$-dependent mechanisms. Glutamate spillover activates metabotropic glutamate receptor 5 (mGluR5), triggering IP3-mediated $Ca^{2+}$ release from internal stores (Tesler, Linne and Destexhe, 2023). These $Ca^{2+}$ transients stimulate:

- **Vasoactive agent synthesis**, such as $PGE_2$ via COX-1 and EETs via cytochrome P450 enzymes, which act on VSMCs to promote dilation (Huneau, Benali and Chabriat, 2015).
- **Potassium efflux** through BK channels in astrocytic endfeet, leading to elevated extracellular $K^+$ and hyperpolarization of VSMCs via inward-rectifying $K^+$ (KIR) channels (Cauli and Hamel, 2010).

There is ongoing debate regarding the timing and causality of astrocytic $Ca^{2+}$ responses. While some studies report delayed $Ca^{2+}$ elevations (~2-4 s post-stimulus) (Tesler, Linne and Destexhe, 2023), others describe rapid, capillary-associated $Ca^{2+}$ transients preceding arteriolar dilation (Stackhouse and Mishra, 2021), suggesting regional variability in astrocyte-mediated NVC.

### Signal Propagation and Amplification with Endothelial Cells

Endothelial cells amplify and propagate vasomotor signals initiated by neurons and glia. Capillary endothelial cells sense extracellular $K^+$ increases via KIR channels, generating membrane hyperpolarization that spreads electrotonically through gap junctions to upstream arterioles. This process coordinates vessel dilation over larger distances. Shear stress from elevated blood flow also activates endothelial nitric oxide synthase (eNOS), producing NO to sustain vasodilation. Genetic deletion of endothelial KIR channels reduces CBF responses by approximately 50%, highlighting their key role in integrating local and conducted vascular signals (Yang *et al.*, 2025).

### Vascular Effectors

Contractile elements of the vasculature, such as arteriolar smooth muscle cells (SMCs) and capillary pericytes, execute changes in vessel diameter. SMCs integrate signals from NO, prostaglandins, and hyperpolarizing currents to modulate tone and contribute to the

myogenic response. Pericytes exhibit diverse, context-dependent behaviors. Some respond rapidly to neurotransmitters like glutamate and noradrenaline, while others regulate capillary flow via slower, $Ca^{2+}$-dependent pathways (Stackhouse and Mishra, 2021). Although the extent of their contractile role remains under investigation, pericyte loss is associated with impaired NVC and reduced tissue oxygenation.

**Spatial Coordination**

Effective NVC requires spatially coordinated responses across the vascular tree. Capillaries, positioned close to neurons and astrocytes, detect local metabolic changes (e.g., $K^+$, lactate) and initiate retrograde signals that propagate to arterioles via endothelial pathways. This ensures that CBF increases are localized to active regions and prevents vascular "steal" phenomena. This hierarchical integration enables perfusion matching with submillimeter spatial resolution. However, at the microvascular level, increases in CBF can extend beyond the boundaries of the activated region. For example, in the auditory, visual, and cerebellar cortices, the vascular response extends beyond the area of neuronal activation, in contrast to the olfactory bulb, where vascular and neuronal activity show a close spatial match (Chaigneau *et al.*, 2003; O'Herron *et al.*, 2016; Iadecola, 2017).

In conclusion, NVC is a multicellular dialogue involving neurons, astrocytes, endothelia, SMCs, and pericytes. Its spatiotemporal precision relies on the following components (Fig. 6):

1. Feedforward signaling (glutamate, $CA^{2+}$, vasoactive agents).
2. Feedback loops (shear stress, eNOS).
3. Conducted responses ($K^+$, endothelial hyperpolarization).

Nevertheless, the traditional view of NVC as a mechanism primarily driven by the brain's metabolic demand has been increasingly challenged by recent advances in neuroscience. In a contemporary perspective article, Drew (Drew, 2022) argues that baseline CBF is often sufficient to meet the brain's oxygen requirements, even during periods of heightened neural activity. This observation suggests that the classical explanation may not fully capture the functional complexity of NVC.

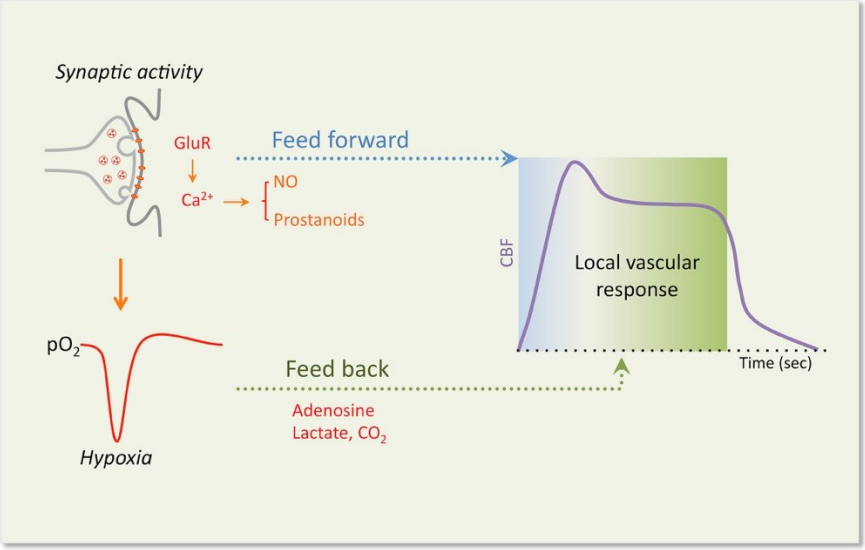


**Figure 6.** Proposed feedforward and feedback mechanisms mediating neurovascular coupling during synaptic activity. *Adapted from (Iadecola, 2017), licensed under CC BY (license agreement 6032971173819).*

An alternative role of NVC that has gained attention is its involvement in waste clearance via the glymphatic system, a topic also actively explored in the context of glymphatic imaging. Functional hyperemia – defined as the increase in CBF following neural activation – may facilitate the movement of cerebrospinal fluid (CSF), thereby enhancing the clearance of metabolic waste products from the brain (Holstein-Rønsbo *et al.*, 2023). This dual function positions NVC as a key player in both nutrient delivery and waste removal, contributing to the broader maintenance of cerebral homeostasis.

Beyond these roles, several additional physiological functions of NVC have been proposed, including:

- Supporting neuromodulator synthesis**:** Some neuromodulators require oxygen for their production, and NVC may contribute to regulating their synthesis through modulation of local oxygen supply.
- Regulating brain temperature**:** Increases in blood flow may help dissipate heat generated by neural activity, thus contributing to thermal homeostasis.
- Acting as a signaling mechanism**:** Hemodynamic changes may serve as modulatory signals that influence neuronal excitability and network dynamics.
- Maintaining vascular integrity**:** NVC may also contribute to the structural stabilization and functional optimization of the cerebral vasculature.

This broadened conceptualization of NVC holds important implications, particularly in the context of neurodegenerative diseases, where both vascular dysfunction and impaired glymphatic clearance frequently coexist. Recognizing the multifaceted roles of NVC offers a more comprehensive framework for understanding its contribution to brain health and pathology and underscores the importance of further research into its regulatory mechanisms.

### 1.4.2 Cerebrovascular Reactivity

CVR is a fundamental mechanism by which the brain regulates blood flow in response to changes in arterial blood gases, particularly $CO_2$. In contrast to NVC, which is closely linked to localized neuronal activity, CVR reflects the capacity of cerebral blood vessels to dilate or constrict globally or regionally in response to fluctuations in $PaCO_2$. This reactivity is commonly assessed in clinical settings using vasodilatory agents such as acetazolamide. The CVR response plays a crucial role in maintaining cerebral homeostasis, especially under conditions of altered respiratory function, increased metabolic demand, or vascular pathology.

Under normal physiological conditions, $PaCO_2$ ranges between 35 and 45 mmHg. Within this range, even small deviations can lead to significant changes in CBF. For each 1 mmHg increase in $PaCO_2$, CBF rises by approximately 2.5-5%, and conversely, hypocapnia results in vasoconstriction and decreased CBF (Sforza *et al.*, 2022). Small arterioles exhibit high sensitivity to the vasodilatory effects of elevated arterial $pCO_2$, following a sigmoidal response curve: CBF increases linearly within the physiological $pCO_2$ range (40–60 mmHg) but deviates from linearity outside these limits. This sensitivity highlights the role of CVR as a "chemical buffer" system that protects the brain from hyper- or hypoperfusion due to respiratory or metabolic imbalances.

The underlying mechanism of CVR is rooted in the physicochemical effect of $CO_2$ on brain tissue pH. Upon diffusing freely across the BBB, $CO_2$ undergoes hydration in cerebral tissue to form carbonic acid ($H_2CO_3$), a reaction catalyzed by carbonic anhydrase. Subsequent dissociation yields bicarbonate ($HCO_3^-$) and hydrogen ions ($H^+$), generating extracellular acidosis (Iadecola, 2017):

$$CO_2 + H_2O \rightleftharpoons^{(\text{carbonicanhydrase})} H_2CO_3 \rightleftharpoons HCO_3^- + H^+$$

This drop in pH initiates vasodilation through two principal signaling pathways.

First, the nitric oxide (NO) pathway is activated by both decreased extracellular pH and increased shear stress, which together stimulate eNOS activity. While the core mechanisms of NO-mediated vasodilation – via cGMP-dependent calcium reduction – are shared with NVC, their recruitment during hypercapnia reflects a broader systemic regulatory response. Experimental studies using eNOS-deficient murine models have shown attenuated vasodilatory responses to $CO_2$, which can be partially restored with exogenous NO donors, underscoring the pathway's importance in CVR (Faraci and Heistad, 1998; Attwell *et al.*, 2010).

Similarly, acidosis modulates vascular tone through the activation of ATP-sensitive (KATP) and calcium-activated (KCa) potassium channels. These channels facilitate membrane hyperpolarization of VSMCs, which in turn suppresses voltage-gated calcium influx and promotes vasodilation. Although potassium channel signaling also participates in NVC, its role in CVR becomes particularly prominent during sustained or systemic acidosis, highlighting its capacity to buffer against fluctuations in arterial gas composition. (Faraci and Heistad, 1998).

Prostaglandins – lipid molecules derived from cell membranes – are also key players in $CO_2$-mediated blood vessel dilation. When $CO_2$ levels rise, astrocytes and endothelial cells increase production of a $PGE_2$ via the enzyme COX-1. $PGE_2$ then binds to receptors on blood vessel walls, triggering relaxation and widening of the vessels. This process depends on antioxidant levels (e.g., glutathione), which may explain why conditions like Alzheimer's or chronic inflammation impair CVR (Brian, 1998).

The cerebrovascular system employs distinct vasodilatory mechanisms depending on the severity of hypercapnia (elevated $CO_2$), reflecting a hierarchical response to maintain perfusion while minimizing metabolic stress. This hierarchical organization reflects the brain's need to balance perfusion efficiency with metabolic stability.

**Moderate Hypercapnia ($PaCO_2 \approx 40–60$ mmHg)**

Within this physiological range, vasodilation is primarily mediated by NO, prostaglandins, and potassium channel activity. These pathways act in concert to decrease vascular tone via intracellular calcium modulation and membrane hyperpolarization. Their coordinated

activation maintains CBF homeostasis in response to subtle changes in $CO_2$ and pH, without engaging high-energy compensatory systems. The effectiveness of these mechanisms depends not only on the vascular architecture but also on the integrity of redox-sensitive enzymes and astrocytic signaling. In particular, the prostaglandin pathway's reliance on glutathione highlights the vulnerability of CVR to oxidative stress and may partially explain its impairment in neurodegenerative and cerebrovascular disease states.

**Severe Hypercapnia ($PaCO_2$ >60 mmHg)**

When $PaCO_2$ levels rise above 60 mmHg, additional signaling pathways are recruited to augment the vasodilatory response. Chief among these are acid-sensing ion channels (ASICs), particularly ASIC1a, which become activated in response to extracellular acidosis when brain pH drops below ~6.9 (Xiong *et al.*, 2008). Upon activation, ASICs facilitate the influx of $Na^+$ and $Ca^{2+}$, leading to membrane depolarization and enhanced vasodilation. Although ASICs are not major contributors to CVR under moderate conditions, they gain prominence in severe hypercapnic or ischemic environments where pH regulation becomes compromised. Their activation has been shown to amplify the effects of canonical pathways such as NO and $PGE_2$ signaling, particularly in pathological contexts where perfusion is threatened.

Spatially, CVR is not confined to a single vascular compartment. While smaller arterioles and capillaries demonstrate the most pronounced diameter changes relative to baseline (Hall *et al.*, 2014), hypercapnic vasodilation occurs globally across the cerebrovascular tree, encompassing pial arteries, penetrating arterioles, and parenchymal microvessels. This systemic response distinguishes CVR from the spatially restricted, synapse-specific mechanisms of NVC(Attwell *et al.*, 2010). Nevertheless, overlap exists: both processes share vasoactive mediators (e.g., NO and PGE2) and target VSMCs and pericytes.

### 1.4.3 Cerebral Autoregulation

CA represents the brain's intrinsic capacity to maintain stable CBF across fluctuations in systemic arterial pressure. The classical concept of CA has been largely shaped by the seminal work of Lassen published in 1959 (Lassen, 1959), which presented a CBF versus mean arterial pressure (MAP) curve derived from data across 11 subject groups, including individuals subjected to vasoactive agents and those with pathological systemic hypertension. This work introduced the notion of a broad autoregulatory plateau, wherein

CBF remains relatively stable across MAP values ranging from approximately 60 to 150 mmHg. Lassen's findings have profoundly influenced neuroscience education and clinical practice, forming the foundation of standard physiological teaching and current clinical guidelines.

However, accumulating evidence in recent years is challenging this traditional concept. Both pharmacological and non-pharmacological studies indicate that CBF may be more pressure-passive than previously believed (Brassard *et al.*, 2021). In contrast to the wide autoregulatory plateau described by Lassen, more recent data suggest that CBF stability is maintained only within a relatively narrow MAP range – approximately 5-10 mmHg – following a sigmoidal rather than plateaued curve. There is also a growing recognition of an asymmetric autoregulatory response: the cerebral vasculature appears to respond more robustly to increases in MAP than to decreases (Numan *et al.*, 2014). Individual variability in the lower and upper limits of autoregulation, as well as in the slope and extent of the plateau region, further complicates the traditional model (Gropper, Miller and Cohen, 2020). Finally, one of the foundational assumptions underpinning the theory of CA – the Monro-Kellie doctrine – is being confronted with the novel discoveries. This doctrine posits that the total intracranial volume, composed of brain tissue, blood, and cerebrospinal fluid (CSF), remains constant; thus, any increase in one component must be compensated by a decrease in another, typically through the displacement of blood or CSF, while brain tissue volume is assumed to be static. However, recent findings from studies on ischemic and hemorrhagic stroke suggest that the brain parenchyma may exhibit a degree of compliance, calling into question the assumption of its rigidity under pathological conditions (Kalisvaart *et al.*, 2020). Additionally, there is evidence that the skull may undergo expansion in response to elevated intracranial pressure (Benson *et al.*, 2023).

These emerging findings highlight the need for a revised model of CA and the development of updated clinical guidelines that reflect current evidence and move beyond outdated assumptions. There is increasing momentum toward integrating this updated understanding into clinical protocols, particularly in contexts such as traumatic brain injury, cardiac surgery, and the management of anesthesia (Manquat *et al.*, 2023; Tsigaras *et al.*, 2023).

A fundamental distinction must be made between static and dynamic CA when considering measurement approaches, each characterizing the relationship between MAP and CBF over different temporal scales (van der Scheer *et al.*, 2018). Static CA typically involves

evaluating the steady-state changes in CBF in response to sustained alterations in MAP. For instance, this can be assessed by analyzing mean CBF responses to MAP changes induced by orthostatic stress over a period of approximately two minutes. In contrast, dynamic CA focuses on the brain's ability to buffer transient, spontaneous fluctuations in MAP, often assessed through transfer function analysis (TFA) applied to concurrent recordings of MAP and cerebral blood flow velocity (CBFV), typically via transcranial Doppler ultrasonography. It is important to emphasize that static and dynamic CA do not represent distinct physiological mechanisms but rather complementary methodological approaches to probing cerebrovascular autoregulation across different time domains.

The limited investigation of CA stems partly from the challenges inherent in its quantification, as no gold standard exists for comprehensively assessing this complex physiological mechanism (Brassard *et al.*, 2023). Methods vary widely – from static protocols measuring changes in CBF in response to induced blood pressure shifts, to dynamic techniques analyzing spontaneous fluctuations – each carrying distinct assumptions and limitations. The inability to isolate CA from other overlapping physiological processes such as NVC, metabolic demand, and CVR also adds interpretive ambiguity. Moreover, technical constraints such as the indirect nature of many surrogate markers limit the accuracy and spatial resolution of assessments. The translation of these metrics into meaningful clinical thresholds remains an unresolved issue, impeding their practical implementation.

Despite these challenges in measurement, the fundamental physiological basis of CA is well characterized and involves multiple overlapping control pathways. This critical homeostatic function is mediated through three integrated mechanisms: pressure-dependent myogenic responses in VSMCs; metabolic regulation driven by local tissue oxygenation and substrate availability; and neurogenic modulation via autonomic innervation of cerebral vessels (Payne, 2016).

**Myogenic Response**

A central component of CA is the myogenic mechanism, which is driven by the inherent contractile responses of VSMCs within cerebral resistance vessels, including both pial and parenchymal arterioles. These cells sense mechanical stretch through mechanotransduction pathways involving stretch-activated ion channels, such as transient receptor potential (TRP) and Piezo channels (Retailleau *et al.*, 2015). Activation of these channels leads to calcium influx and subsequent actin-myosin contraction, allowing vessels to constrict in response to

rising intraluminal pressure. Vasoconstriction is typically observed at MAP values above 150 mmHg, whereas vasodilation predominates below 60 mmHg (Tzeng and Ainslie, 2014). These thresholds, however, are not static and can shift in pathological conditions such as hypertension and with aging. Disruption of the myogenic response is clinically significant; for example, in traumatic brain injury (TBI) or stroke, impaired autoregulatory tone renders CBF more directly dependent on systemic pressure, increasing vulnerability to secondary insults (Kranawetter *et al.*, 2024). Experimental studies have demonstrated that genetic ablation of VSMC ion channels abolishes pressure-induced vasoconstriction, and clinical evidence links impaired myogenic responses to poorer outcomes, particularly in cases of subarachnoid hemorrhage.

**Metabolic Pathway**

Complementing the pressure-sensitive myogenic response is the metabolic, also often refered to as endothelial mechanism of CA, which aligns CBF with local metabolic demands. This regulation is highly sensitive to changes in arterial blood gases and tissue pH. Hypercapnia and acidosis elicit vasodilation through the activation of eNOS and the production of vasodilatory prostaglandins, similarly to mechanisms of CVR (Claassen *et al.*, 2021). Hypoxia, in turn, activates ATP-sensitive potassium channels, promoting vascular relaxation. In states of energy deficit, ATP depletion elevates extracellular adenosine levels, which bind to A2A receptors on vascular cells to induce further vasodilation(Wang *et al.*, 2022). Failure of this metabolic coupling has been implicated in various clinical conditions; for instance, in sepsis-associated delirium, systemic inflammation appears to blunt $CO_2$ reactivity, undermining this autoregulatory pathway.

**Neurogenic Mechanism**

The neurogenic mechanism also contributes to CA, modulating vascular tone through autonomic innervation. Sympathetic nerves originating from the superior cervical ganglion can induce vasoconstriction of large cerebral arteries during acute hypertensive episodes, thereby shielding downstream microvessels from damaging pressure surges (Sriram *et al.*, 2012). Conversely, parasympathetic input, mediated via structures such as the sphenopalatine ganglion, may promote vasodilation, counteracting excessive vasoconstriction during periods of stress (Wang *et al.*, 2022). Although experimental denervation often preserves basic autoregulatory function, the integrity of neurogenic input

remains important in pathological states. For example, autonomic dysfunction in diabetes mellitus may accelerate cerebrovascular injury by impairing fine-tuned vascular responses.

**Differentiating CA, NVC, and CVR**

Although CA shares some signaling overlap with other regulatory processes, it is mechanistically and functionally distinct from both NVC and CVR. The primary distinction between CA and NVC lies in their initiating stimuli and objectives. CA is a homeostatic response to changes in systemic arterial pressure, engaging myogenic, metabolic, and neurogenic pathways to maintain consistent CBF. In contrast, NVC is a feedforward and feedback mechanism driven by neuronal activity, where active synapses induce localized vasodilation to meet increased metabolic demands. NVC operates rapidly – within milliseconds to seconds – through neurotransmitter release, astrocytic calcium signaling, and the production of vasoactive mediators like NO and prostaglandins. Although both CA and CVR involve vascular responses, they are not equivalent. CA continuously adjusts CBF in real-time to maintain metabolic homeostasis in response to systemic pressure changes. CVR, on the other hand, is often assessed under controlled conditions to evaluate the vasodilatory reserve and does not necessarily reflect the brain's ability to maintain flow during blood pressure fluctuations, which is the hallmark of true autoregulation.

In summary, CA, NVC, and CVR all contribute to the regulation of cerebral perfusion but operate through distinct physiological triggers, temporal dynamics, and functional goals. CA ensures global perfusion stability during systemic pressure changes; NVC supports local perfusion in response to neural activity; and CVR assesses the cerebral vasculature’s responsiveness to specific vasoactive stimuli. Disruptions in any of these mechanisms can lead to cerebrovascular pathology, underscoring the importance of distinguishing their roles in both research and clinical contexts.

### 1.4.4 Developmental Aspects in Vascular Regulation

The principal mechanisms of hemodynamic regulation in the brain undergo significant changes across the human lifespan, particularly during periods of rapid maturation in early life and gradual functional decline with aging. These changes reflect the dynamic interplay between brain maturation, cerebral vasculature growth, and changing metabolic demands, all of which evolve with age. In this section, we will review the key factors that influence hemodynamic regulation during early brain development and in the aging brain, with a focus

on the underlying physiological mechanisms and their functional implications for cerebral perfusion and neurovascular health.

The neonatal brain exhibits profound immaturity in both the NVU and NVC, reflecting the parallel but asynchronous development of neuronal networks and vascular supply systems. Unlike the stereotyped hemodynamic responses, increased CBF and oxygenation, seen in mature brains, preterm infants demonstrate variable NVC strategies, including positive, negative, or mixed responses to similar neural activations (Nourhashemi *et al.*, 2019). This variability is attributed to the parallel but asynchronous maturation of neuronal and vascular networks, which rely on shared guidance cues during development (Stackhouse and Mishra, 2021). For instance, spontaneous cortical bursts in preterm neonates elicit divergent hemodynamic reactions – ranging from increased oxyhemoglobin (HbO) and CBF to paradoxical decreases in oxygenation – highlighting the immaturity of the NVU and its regulatory mechanisms (Hendrikx *et al.*, 2019). Notably, NVC maturation progresses with gestational age, transitioning from unstable, bidirectional responses to more consistent hyperemic patterns as vascular and astrocytic networks integrate with neuronal activity. This developmental trajectory underscores the delicate balance between metabolic demand and vascular supply in the immature brain, where energy accessibility and waste clearance are tightly coupled but less efficient than in adults.

In healthy adults, NVC is characterized by a robust, feed-forward mechanism that ensures rapid oversupply of blood flow to active brain regions, preemptively meeting metabolic demands. This process is mediated by well-coordinated signaling within the NVU, which together optimize regional CBF within seconds of neural activation. In contrast, children exhibit intermediate NVC profiles as their NVU components mature. For example, fMRI studies reveal that BOLD signals in infants are often negative (reflecting a transient mismatch between metabolism and blood flow), gradually shifting to adult-like hyperemia as astrocytic endfeet envelop vasculature and synaptic pruning refines neural circuits (Kozberg and Hillman, 2016; Iadecola, 2017; Stackhouse and Mishra, 2021). By adolescence, NVC stabilizes, with vascular responses becoming more predictable and spatially localized, mirroring the structural and functional refinement of the NVU. This developmental continuum highlights the critical role of NVC maturation in supporting the brain's evolving metabolic and computational needs, from the plasticity-driven demands of early life to the efficiency-focused homeostasis of adulthood.

With advancing age, the BBB becomes increasingly permeable, a phenomenon attributed to tight junction degradation, pericyte loss, and mitochondrial dysfunction within endothelial cells (Sweeney, Sagare and Zlokovic, 2018). These changes permit the extravasation of plasma proteins such as fibrinogen and immunoglobulins into the parenchyma, where they provoke microglial activation and promote a pro-inflammatory environment. This neuroinflammatory state, in turn, exacerbates vascular dysfunction through multiple pathways, impairing critical NVC mechanisms and contributing to a vicious cycle of cerebral hypoperfusion, glial stress, and eventual neuronal injury (Knox *et al.*, 2022; Smith *et al.*, 2023).

Importantly, disruptions in the NVU or BBB integrity can significantly impair CBF. With age or under pathological conditions such as ischemia or neurodegeneration, increased BBB permeability allows leakage of plasma proteins and infiltration of immune cells, triggering neuroinflammatory responses (Zenaro, Piacentino and Constantin, 2017). Activated microglia and astrocytes release reactive oxygen species and pro-inflammatory cytokines (e.g., IL-1β, TNF-α) that not only exacerbate BBB damage but also impair vasodilatory capacity. These changes in vascular function and structure are not merely consequences of disease but may actively contribute to disease onset and progression. For example, early BBB breakdown and impaired CBF regulation have been implicated in Alzheimer's disease, vascular dementia, and stroke, suggesting a causative link between NVU dysfunction and neurodegeneration (Sweeney, Sagare and Zlokovic, 2018; Chen *et al.*, 2023; Moyaert *et al.*, 2023). Moreover, recent studies suggest that diminished vascular health in aging not only compromises nutrient delivery but also impairs the clearance of metabolic byproducts, thereby contributing to functional decline, aligning with the growing understanding of NVU role in brain function (Mangia *et al.*, 2025).

CVR also undergoes significant changes across the lifespan, reflecting the dynamic evolution of cerebral hemodynamics. In children and adolescents, CVR follows a biphasic trajectory, increasing with age until the mid-teens before declining. A study assessing CVR in healthy subjects aged 9–30 years found that reactivity in both gray and white matter peaks at approximately 14.7 years, after which it begins to decrease (Leung *et al.*, 2016). This pattern suggests that cerebrovascular reserve capacity strengthens during childhood, likely due to maturation of vascular tone regulation and increasing metabolic demands, before transitioning to an age-related decline in early adulthood. Sex differences may further modulate developmental CVR trajectories, though findings remain under investigation.

Some evidence suggests that hormonal influences during puberty could contribute to variations in vascular responsiveness between males and females (Leung *et al.*, 2016; Chen, Di and Biswal, 2024).

In adulthood, CVR decline becomes more pronounced, particularly in middle age. Longitudinal studies reveal that the rate of CVR reduction is not uniform across brain regions; the temporal lobe shows the fastest decline, followed by parietal and frontal regions (Peng *et al.*, 2018). This spatial heterogeneity suggests that vascular aging may differentially affect neurocognitive networks. Notably, middle-aged individuals (approximately 40–60 years) exhibit the most rapid deterioration in CVR, which then stabilizes somewhat in later life.

In parallel, developmental changes in CA follow a similarly dynamic trajectory, influenced by both vascular and neural maturation processes across early life stages. In neonates, particularly preterm infants, CA is underdeveloped due to immature vascular structures and incomplete vasomotor reactivity. The cerebral vasculature in preterm neonates lacks fully developed muscularis layers in arteries and arterioles, which only mature after approximately 25 weeks of gestation in humans (Rhee *et al.*, 2018). Functional autoregulation progressively improves between 23 and 33 weeks of gestation, with vasoreactive mechanisms becoming more robust during the third trimester. Term neonates exhibit functional autoregulation, but their CBF remains highly sensitive to hemodynamic changes. Unlike adults, neonatal CBF is influenced by cardiac cycle dynamics, particularly in hypotensive preterm infants, where diastolic blood pressure often fails to sustain adequate perfusion. The autoregulatory plateau is narrower in neonates, increasing their susceptibility to hypoperfusion or hyperperfusion injuries (Howlett *et al.*, 2013).

As the brain matures, CA undergoes significant refinement. In healthy adolescents, dynamic CA stabilizes, with improved buffering of blood pressure fluctuations compared to neonates. Studies using transcranial Doppler and MRI indicate that dynamic CA efficiency increases with age, correlating with cerebral vascular maturation and enhanced neurovascular coupling (Wagner *et al.*, 2012; Hamner and Tan, 2014; Immink *et al.*, 2019). Regional differences in dynamic CA have been observed, with posterior circulation exhibiting stronger autoregulatory responses than anterior circulation, possibly due to variations in vascular resistance and metabolic demand (Nakagawa *et al.*, 2009). Similarly to CVR, sex differences

in CA emerge during adolescence, though these variations are not significantly influenced by menstrual cycle phases in young women (Favre and Serrador, 2019).

In aging populations, CA undergoes gradual decline, though compensatory mechanisms often preserve baseline CBF. Elderly individuals exhibit reduced cerebrovascular $CO_2$ reactivity and slower dCA responses, likely due to arterial stiffening, endothelial dysfunction, and diminished baroreflex sensitivity (Vavilala *et al.*, 2002; Weijs *et al.*, 2024). Despite lower resting CBF, healthy older adults maintain autoregulatory capacity within normotensive ranges, though the autoregulatory plateau may shift upward, requiring higher perfusion pressures to sustain adequate flow (Immink *et al.*, 2019). Hypercapnic vasoreactivity remains intact in aging, but the vasodilatory reserve diminishes, increasing susceptibility to ischemic insults during hypotension. Notably, while static CA is preserved, dynamic CA deteriorates, contributing to cognitive vulnerability in elderly populations.

Disruption of these finely tuned vascular control mechanisms plays a critical role in the pathophysiology of numerous brain disorders, where altered perfusion is increasingly recognized as both a consequence and a potential driver of disease processes.

### 1.5 Alterations of CBF and NVU in Brain Diseases

Building on the foundational principles of CBF regulation, increasing evidence highlights that disturbances in cerebral perfusion and dysfunction of the NVU are not merely secondary consequences of brain pathology, but may act as early and active contributors to disease onset and progression. Abnormalities in CA, NVC, and CVR have been implicated across a wide spectrum of neurological conditions, including neurodegenerative disorders, cerebrovascular disease, brain tumors, epilepsy, and psychiatric disorders. Importantly, these alterations often precede structural changes or overt clinical symptoms, positioning perfusion imaging as a potentially powerful tool for early detection and monitoring. The disruptions in NVU can lead to impaired BBB integrity, metabolic imbalance, and neuroinflammation, further exacerbating disease processes. This section outlines the growing understanding of how cerebral perfusion abnormalities and NVU dysfunction contribute to brain pathology and how these shared mechanisms may unify diverse neurological conditions under a common vascular framework.

### 1.5.1 Cerebral Perfusion Abnormality as a Driver and Marker of Disease

As previously discussed, the delivery of oxygen and nutrients to healthy brain tissue is critically dependent on adequate CBF. Abnormalities in CBF – manifesting as either hypo- or hyperperfusion – can indicate pathological states arising from dysfunctions in the cerebrovascular system, NVU, or the neural tissue itself. While delineating the precise sequence of events in disease pathogenesis remains challenging or practically impossible, it is evident that CBF plays a pivotal role in maintaining brain health.

#### Neurodegeneration

Traditionally, alterations in CBF were viewed as downstream consequences of neurological disease. However, recent advances have prompted a conceptual shift, suggesting that changes in CBF may not only reflect but also contribute to the initiation and progression of neurological disorders. This shift is particularly evident in research on neurodegenerative diseases such as Alzheimer's disease (AD), where CBF has emerged as a promising non-invasive biomarker. Reduced perfusion has been documented even in cognitively unimpaired individuals with amyloid-β pathology, underscoring the potential of CBF alterations as an early indicator of disease (Falcon *et al.*, 2024). Furthermore, CBF reductions have been correlated with increased amyloid-β accumulation, tau pathology, and markers of synaptic and axonal dysfunction (Ahmadi *et al.*, 2023; Falcon *et al.*, 2024) , highlighting the potential causative role of vascular dysregulation in the pathogenesis of AD.

The search for early diagnostic and prognostic biomarkers in neurodegenerative diseases is of growing importance, given their rising global prevalence and the parallel development of novel therapeutic agents (Steinmetz *et al.*, 2024). CBF has long been proposed as a diagnostic tool in early AD (Prohovnik *et al.*, 1988; Binnewijzend *et al.*, 2016; Swinford *et al.*, 2023) , and its relevance continues to grow in light of accumulating evidence linking vascular dysfunction to disease onset. In fact, current models of AD pathophysiology increasingly emphasize the role of early vascular dysregulation as a key upstream event that precipitates downstream pathology, including CBF abnormalities (Iturria-Medina *et al.*, 2016) (Figure 7). Hypoperfusion may contribute to BBB disruption by failing to meet the brain's metabolic demands and may also impair the clearance of amyloid-β and tau proteins via disturbances in glymphatic flow and perivascular drainage mechanisms (Simons, Levin and Dichgans, 2023).

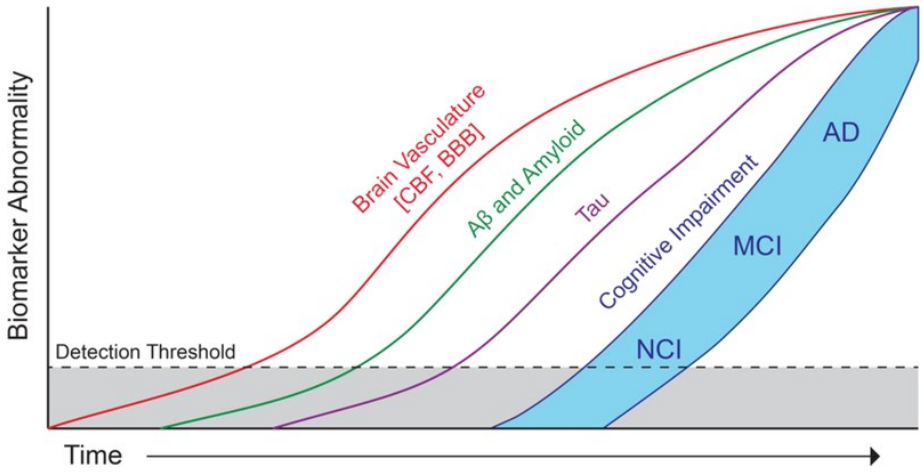


**Figure 7.** Proposed model of AD where vascular disruptions participate in initial stages from no cognitive impairment (NCI) to mild cognitive impairment (MCI) to clinically manifested AD . *Adapted from (Sweeney et al., 2018), licensed under CC-BY.*

Chronic cerebral hypoperfusion is increasingly recognized as a pivotal factor in the pathogenesis of vascular cognitive impairment (VCI), a spectrum of cognitive disorders resulting from cerebrovascular pathology. Hypoperfusion initiates a cascade of deleterious processes, including oxidative stress, neuroinflammation, and BBB dysfunction, which collectively contribute to neuronal damage and brain atrophy (He *et al.*, 2023). Recent studies have demonstrated that impaired CBF is significantly associated with accelerated cognitive decline in individuals with VCI. For instance, van Dinther et al. (van Dinther *et al.*, 2024) found that lower baseline global CBF predicted greater cognitive deterioration over a two-year period, particularly affecting attention, psychomotor speed, and memory domains. This association is reinforced by findings from a large population-based cohort, where hypoperfusion was significantly correlated with a higher risk of developing dementia over a seven-year follow-up period from the initial scan (Wolters *et al.*, 2017). Together, these studies support the view that impaired CBF is not merely a marker but a driving mechanism in cognitive decline.

As imbalanced cerebral perfusion is increasingly recognized as a contributing factor to the development and progression of neurodegenerative disorders, considerable attention has been directed toward identifying effective interventions aimed at restoring cerebral circulation. Among the potential interventions, physical activity stands out as an accessible and cost-effective approach that has been demonstrated to improve CBF in older adults (Ainslie *et al.*, 2008; Sanders *et al.*, 2023; Norling and Lipsitz, 2024). Notably, aerobic exercise has proven effective in enhancing both CBF and cognitive performance in healthy

older individuals, as evidenced by findings from randomized controlled trials (Tomoto *et al.*, 2023). Furthermore, research indicates that regular aerobic exercise not only improves CBF but also promotes the redistribution of blood flow to regions particularly vulnerable to AD pathology, thereby contributing to cognitive improvements in patients with MCI (Thomas *et al.*, 2020).

However, it is important to acknowledge that some studies have reported no significant improvements in CBF following exercise interventions, particularly in patients with VCI and AD (van der Kleij *et al.*, 2018; van Hout *et al.*, 2025). It should be noted, however, that studies failing to demonstrate significant effects generally implemented shorter intervention periods (with hypotheses predicated on observing significant changes within 14 weeks), whereas those reporting positive outcomes were conducted over longer durations. This discrepancy underscores the gradual nature of modifying cerebral hemodynamics and suggests that longer intervention periods may be necessary to elicit measurable improvements.

**Cerebral Small Vessel Disease**

Both AD and VCI are increasingly recognized to share a common underlying pathology in cerebral small vessel disease (CSVD) – a heterogeneous group of disorders affecting primarily small arteries and microvessels in the brain (Kim, Hong and Jeon, 2020). CSVD is characterized by chronic microvascular alterations, including vessel wall thickening, perivascular space enlargement, reduced vascular density, and increased tortuosity, which contribute to impaired cerebral perfusion and tissue integrity. These structural changes are thought to arise from a complex interplay of chronic hypoperfusion, BBB dysfunction, inflammation, venous collagenosis, and impaired oligodendrocyte precursor cell function.

Radiologically, CSVD manifests as white matter hyperintensities (WMHs) on T2/FLAIR scans, cerebral microbleeds, lacunes, and microinfarcts – features detectable on MRI scans and closely associated with cognitive impairment. Of these, WMHs are the most prominent and widely studied markers, and their development has been repeatedly linked to chronic reductions in CBF. In cross-sectional studies, regions with established WMHs consistently show lower CBF compared to normal-appearing white matter (NAWM) (Promjunyakul *et al.*, 2018; Thammasart *et al.*, 2025). Furthermore, longitudinal analyses reveal that the perilesional zones—termed the “CBF penumbra”—are at higher risk of WMH expansion,

indicating that focal hypoperfusion likely precedes lesion growth (Promjunyakul *et al.*, 2015).

The directionality of this association, however, has remained a subject of debate. Some evidence now supports the notion that CBF reductions may represent a primary event in CSVD pathogenesis, contributing to downstream structural changes. For instance, hypoperfusion has been proposed to promote WMH development via chronic ischemia, neuroinflammation, and impaired waste clearance pathways (Sasannia *et al.*, 2025). A recent study demonstrated that WMHs exhibiting growth over a two-year period had significantly lower baseline relative CBF than those that remained stable, with juxtaventricular and periventricular regions particularly vulnerable (Thammasart *et al.*, 2025).

**Stroke**

Another perspective is offered when considering CBF in the context of stroke – a cerebrovascular pathology that both arises from and exacerbates CBF abnormalities, and one that further underscores the centrality of perfusion as both a driver and marker of disease. The temporal evolution of CBF following ischemic stroke is characterized by distinct pathophysiological phases that not only inform prognosis but also guide therapeutic strategies. In the hyperacute phase (minutes to hours), there is a precipitous decline in CBF within the infarct core and surrounding penumbra, creating a narrow therapeutic window during which prompt restoration of blood flow can salvage at-risk tissue (Nogueira *et al.*, 2021; Premilovac and Sutherland, 2022). This acute loss of perfusion initiates a cascade of metabolic dysfunction, ion imbalance, and excitotoxicity that culminates in irreversible cell death if not rapidly reversed.

The acute phase (first 48 hours) is marked by heterogeneous patterns of CA and presents the optimal window for reperfusion therapies, such as thrombolysis or mechanical thrombectomy, which aim to restore CBF and limit infarct expansion (Demeestere *et al.*, 2020). Accurate assessment of CBF using advanced imaging is thus crucial for identifying patients with a substantial penumbra – severely hypoperfused yet viable tissue encircling the infarct core – who are most likely to benefit from reperfusion (Schaller and Graf, 2004; Campbell *et al.*, 2015b). Beyond patient selection, CBF mapping also improves occlusion localization, differentiates stroke from stroke mimics, and informs individual management strategies (Becks *et al.*, 2019).

As the brain transitions to the subacute phase (2–7 days), impaired autoregulation and reduced CBF often persist, although collateral flow and endogenous repair mechanisms may support partial perfusion recovery. The chronic phase (weeks to months) is associated with variable degrees of CBF restoration, largely determined by stroke subtype and the extent of vascular remodeling. While atherothrombotic infarcts may demonstrate gradual increases in regional CBF due to collateral vessel formation, lacunar strokes frequently result in sustained hypoperfusion and persistent tissue injury (Toyoda, Minematsu and Yamaguchi, 1994)

The restoration of CBF is not without complexity; phenomena such as luxury hyperperfusion, characterized by excessive blood flow to previously ischemic regions, and the "steal" phenomenon, where dysregulated autoregulation diverts CBF from vulnerable territories, highlight the delicate balance required to optimize reperfusion without incurring additional harm (Kirchoff-Torres and Bakradze, 2018; Bellomo *et al.*, 2025). Recent research has also illuminated the role of environmental enrichment as a non-pharmacological approach to enhance post-stroke recovery. Xie et al. (Xie *et al.*, 2020) demonstrated that environmental enrichment increases resting CBF in unaffected brain tissue, improves global cerebral circulation, and reduces infarct volume, supporting the concept that CBF augmentation, even outside the acute intervention window, can have neuroprotective and reparative effects.

Importantly, the consequences of CBF restoration extend beyond hemodynamics to influence secondary injury cascades. Improved perfusion can help stabilize the BBB, reduce leukocyte infiltration, and modulate the neuroinflammatory response—all factors known to shape both acute outcomes and long-term recovery (Jin *et al.*, 2013; Xie *et al.*, 2020). There is growing recognition that the immune response to stroke, including the polarization of microglia and macrophages, is tightly linked to changes in regional CBF and reperfusion dynamics, with optimal recovery requiring a coordinated vascular and immune repair process (Xiong, Liu and Yang, 2016).

**Migraine**

While cerebral hypoperfusion has been extensively studied in the context of cognitive decline and neurodegeneration, chronic cerebral hyperperfusion also plays a significant role in various neurological disorders. Elevated CBF can also act both as a marker of underlying pathology and, in certain conditions, as a driver of disease progression.

In migraine, particularly with aura, studies have demonstrated alterations in CBF, with increased perfusion in specific brain regions during attacks (Olesen, 2024; Schramm *et al.*, 2024; Wu *et al.*, 2024). These perfusion changes are thought to be associated with cortical spreading depression (CSD), a wave of neuronal and glial depolarization followed by suppression of brain activity, which may underlie the aura phenomenon and contribute to migraine pathophysiology. In migraine with aura, studies have revealed a pattern of initial hypoperfusion corresponding to the aura phase, followed by hyperperfusion during the headache phase. This sequence supports the hypothesis that CSD initiates the aura and subsequent vascular changes contribute to the headache. For instance, patients with migraine with aura exhibited significant CBF alterations in the occipital cortex during attacks, aligning with the visual symptoms commonly reported during aura (T. Fu *et al.*, 2022).

Moreover, research indicates that even during interictal periods (between attacks), migraine patients may exhibit persistent CBF abnormalities. These findings suggest that migraine is associated with ongoing neurovascular dysregulation, not limited to the ictal phase. For instance, altered CBF was obserbed in the thalamus and somatosensory cortex of migraine patients without aura during interictal periods, indicating sustained changes in brain perfusion (Park *et al.*, 2022). Understanding these dynamics between CBF alterations and migraine pathophysiolog can inform the development of targeted therapies aimed at normalizing CBF and mitigating migraine symptoms.

The recognition of cerebral hypoperfusion as an early and potentially causative factor in brain diseases underscores the necessity to delve deeper into the underlying mechanisms that compromise CBF. Among these, the integrity and functionality of the NVU emerge as critical determinants. Disruptions within the NVU may not only suffer from or precipitate hypoperfusion but also contribute to a cascade of pathological. Thus, understanding NVU dysfunction offers valuable insights into the pathophysiology of brain fuction.

### 1.5.2. NVU Dysfunction and Barrier Breakdown

Dysfunction of the NVU represents a critical nexus in the pathophysiology of a wide spectrum of central nervous system disorders. Disruptions within the NVU can manifest in various forms, including compromised BBB integrity, impaired NVC, and pathological vascular remodeling, each contributing to distinct clinical syndromes. These disturbances not only underlie neurodegenerative processes, but are also implicated in acute cerebrovascular events, inflammatory and infectious diseases, neoplastic conditions, and a

range of other neurological pathologies. Understanding the diverse mechanisms and clinical manifestations of NVU dysfunction is therefore essential for appreciating its role in both common and rare disorders affecting the brain.

#### 1.5.2.1 BBB Leakage

The BBB is a critical structure that maintains CNS homeostasis by regulating the passage of substances between the bloodstream and neural tissue. Disruption of the BBB can lead to increased permeability, allowing the uncontrolled passage of immune cells, plasma proteins, and other blood-derived components into the brain parenchyma (Zhao *et al.*, 2015b). Such breaches can result from various interrelated mechanisms, including inflammatory responses, oxidative stress, hypoxia, and mechanical injury.

**Inflammatory Responses**

Pro-inflammatory cytokines such as TNF-α and interleukins induce the production of matrix metalloproteinases (MMPs), which degrade tight junction proteins and compromise the structural integrity of the BBB (Candelario-Jalil *et al.*, 2007). This breakdown not only permits the infiltration of peripheral immune cells but also amplifies neuroinflammation within the CNS. Systemic inflammation, whether acute or chronic, further disrupts BBB function by altering the signaling environment at the brain endothelium and modulating tight junction protein expression (Varatharaj and Galea, 2017). Recent evidence from individuals with long COVID has demonstrated that persistent systemic inflammation can drive sustained BBB disruption, as reflected by altered biomarkers and ongoing neuroinflammatory activity, which are closely linked to cognitive impairment (Greene *et al.*, 2024).

**Oxidative Stress**

Reactive oxygen species (ROS) generated during pathological conditions can damage endothelial cells and tight junctions, leading to increased permeability (Lochhead, Ronaldson and Davis, 2024). Oxidative stress is recognized as a central mediator of BBB disruption in both acute and chronic neurological disorders. Excessive ROS, produced through cellular metabolic pathways or in response to injury and inflammation, can oxidize lipids, proteins, and nucleic acids within the endothelial cells, thereby compromising cell integrity and tight junction assembly (Kim, Jung and Kim, 2024). A key mechanism involves the activation of MMPs under oxidative conditions, similar to inflammatory processes.

NADPH oxidase is a principal enzymatic source of ROS in the CNS, and its activation has been particularly implicated in BBB breakdown following traumatic brain injury (TBI), where increased permeability and edema can result (Cash and Theus, 2020).

Furthermore, mitochondrial dysfunction in brain microvascular endothelial cells is a major contributor to oxidative stress at the BBB. Disruption of mitochondrial homeostasis enhances ROS production, which triggers a cascade of signaling events that culminate in barrier dysfunction and increased paracellular flux (Wang *et al.*, 2023). Recent studies also indicate that ischemic stroke is characterized by a surge in oxidative stress, and clinical trials targeting antioxidant pathways have shown promise in limiting BBB disruption during the acute phase (Lochhead, Ronaldson and Davis, 2024)

**Hypoxia**

Reduced oxygen availability, or hypoxia, has profound effects on BBB integrity by altering the expression, localization, and function of tight junction proteins (Halder and Milner, 2020). Hypoxic conditions lead to the stabilization of hypoxia-inducible factors (HIFs), which can trigger the downregulation of key tight junction proteins such as claudin-5, occludin, and zonula occludens-1, thereby increasing BBB permeability (Engelhardt, Patkar and Ogunshola, 2014). This barrier weakening is compounded by the hypoxia-induced upregulation of vascular endothelial growth factor (VEGF), a potent mediator of vascular permeability, which further enhances paracellular leakage across the endothelium. The cellular response to hypoxia is not uniform; instead, it is highly cell-specific, with brain endothelial cells, astrocytes, and pericytes each displaying distinct patterns of gene and protein regulation in response to oxygen deprivation. Hypoxia can also compromise other central nervous system barriers, including the blood-cerebrospinal fluid (CSF) and CSF-brain barriers, affecting the broader homeostatic environment of the brain (Dunn and Isaacs, 2021).

Experimental and clinical studies further demonstrate that hypoxic-ischemic events, such as those occurring in perinatal brain injury or stroke, result in ultrastructural alterations to the BBB, including endothelial swelling, disruption of the basal lamina, and detachment of astrocytic end-feet (Kaur and Ling, 2008). These morphological changes, together with molecular disruption of tight junctions, contribute to increased barrier permeability and subsequent brain edema.

**Mechanical Injury**

Mechanical insults, such as those caused by rapid acceleration, deceleration, compression, or other traumatic forces, can physically disrupt the BBB. These forces may directly damage endothelial cells, disrupt tight junctions, and disturb the architecture of the NVU, resulting in both immediate and progressive increases in BBB permeability. Mechanical disruption not only alters barrier integrity but can also trigger the release of endothelial-derived microvesicles, which propagate inflammatory and coagulative cascades within the cerebral vasculature and contribute to ongoing vascular dysfunction (Andrews *et al.*, 2016). In addition to the primary physical effects, secondary biochemical events such as oxidative stress and MMP activation frequently follow mechanical insult, further degrading tight junction proteins and the extracellular matrix and amplifying BBB breakdown. Experimental evidence demonstrates that even mild mechanical insults can induce ultrastructural changes in endothelial junctions and increase paracellular leakage (Johnson *et al.*, 2018). A clinically relevant example of this mechanism is TBI, where direct mechanical forces not only cause immediate BBB disruption but also initiate inflammatory cascades and oxidative stress, contributing to both acute and delayed increases in permeability (Cash and Theus, 2020).

A comprehensive understanding of the mechanisms underlying BBB disruption is essential for advancing diagnostic approaches and unraveling the pathogenesis of various neurological disorders. The multifactorial nature of BBB breakdown is closely intertwined with disturbances in CBF, which can both contribute to and result from impaired barrier function. Recognizing these interconnections enhances our ability to interpret clinical and imaging biomarkers indicative of BBB integrity and CBF dynamics across a range of central nervous system pathologies.

**Clinical Manifestation**

In TBI, BBB disruption is not merely a passive consequence of mechanical insult but actively shapes the evolving pathophysiology. Initial mechanical forces, including those from impact or acceleration-deceleration, directly damage cerebral endothelium, rapidly increasing BBB permeability. This breach facilitates the uncontrolled entry of plasma proteins, leukocytes, and inflammatory mediators into the parenchyma, which amplifies neuroinflammation and perpetuates secondary tissue injury (Andrews *et al.*, 2016; Johnson *et al.*, 2018). Notably, spreading depolarizations – waves of neuronal and glial depolarization – emerge after TBI and further compromise BBB integrity, while also altering local cerebral

blood flow regulation (van Hameren *et al.*, 2024). The interaction of BBB breakdown with microvascular dysfunction, impaired CBF autoregulation, and neuroimmune signaling creates a feedback loop that sustains edema, exacerbates metabolic mismatch, and promotes long-term neurodegeneration. Thus, BBB disruption in TBI is best understood as a dynamic participant in a multifactorial network of injury mechanisms.

Acute ischemic stroke provides a prototypical example of the reciprocal relationship between BBB dysfunction and cerebral blood flow impairment. Ischemia-induced hypoperfusion rapidly initiates endothelial activation, oxidative stress, and tight junction breakdown, setting the stage for increased BBB permeability (Mathias *et al.*, 2024). This loss of barrier function permits extravasation of immune cells and blood-borne molecules, fueling a cascade of inflammation and cytotoxic edema. The resulting tissue environment disrupts local CBF regulation, further aggravating hypoxia and perpetuating barrier breakdown (Gao *et al.*, 2023). Emerging evidence highlights that the timing and severity of BBB opening are tightly linked to the risk of hemorrhagic transformation and delayed neuronal death, and that bidirectional crosstalk between BBB and CBF regulation is crucial in determining both acute and chronic outcomes (Krueger *et al.*, 2013). This interplay reinforces the notion that BBB disruption is not merely a marker of tissue injury but an active contributor to the evolving neurovascular pathology of stroke.

In multiple sclerosis (MS), BBB dysfunction is a critical event that underpins both acute lesion formation and chronic disease progression. The disruption of endothelial tight junctions and upregulation of adhesion molecules enable autoreactive lymphocytes and monocytes to traverse the barrier and initiate immune-mediated demyelination and axonal injury(Ortiz *et al.*, 2014; Zierfuss, Larochelle and Prat, 2024). However, the relationship is not unidirectional: local neuroinflammation and CBF disturbances resulting from perivascular immune infiltration feed back to exacerbate BBB impairment and alter microvascular hemodynamics. Moreover, BBB permeability fluctuates dynamically during relapses and remission, reflecting the ongoing interaction between immune activity, neurovascular function, and the local CNS microenvironment (Kermode *et al.*, 1990). This multifaceted interplay positions BBB disruption as both a gateway for pathogenic immune entry and a modulator of the broader NVU dysfunction in MS.

#### 1.5.2.2 Disrupted NVC

Disruption of NVC arises from a complex interplay of cellular, molecular, and vascular factors, each compromising the ability of cerebral vessels to respond to dynamic neuronal activity. Astrocytic dysfunction remains a central mechanism; astrocytes, through impaired calcium signaling or altered production of vasoactive messengers (such as prostaglandins, NO, and epoxyeicosatrienoic acids), lose their capacity to appropriately regulate vessel diameter in response to synaptic activity (Mishra *et al.*, 2016; Tarantini *et al.*, 2017; Meyer-Baese, Jaeger and Keilholz, 2025). Endothelial dysfunction, resulting from reduced NO synthase activity, oxidative stress, and pro-inflammatory signaling, further impairs the vasodilatory capacity of cerebral arterioles.

Emerging evidence highlights the role of pericyte loss and dysfunction in NVC breakdown. Pericytes, which ensheath the capillaries, are vital for microvascular tone regulation; their degeneration, as observed in neurodegeneration and chronic vascular disease, results in impaired capillary responses and NVC at the microcirculatory level (Sweeney, Ayyadurai and Zlokovic, 2016; Kisler *et al.*, 2017). Microvascular rarefaction and basement membrane thickening, common in hypertension and diabetes, disrupt the architecture required for coordinated vascular responses (Fletcher *et al.*, 2023).

Inflammatory mechanisms and oxidative stress also play pivotal roles. Chronic or acute neuroinflammation elevates cytokine levels and induces oxidative damage, directly impairing endothelial and glial function, and altering the bioavailability of vasoactive mediators (Lecrux and Hamel, 2011; Iadecola, 2017). Mitochondrial dysfunction within neurons and glia is another emerging contributor; energy failure reduces the neuronal output of vasodilatory signals and exacerbates local hypoxia, further perpetuating NVC disruption (Stobart and Anderson, 2013).

Finally, disruption of ion channel function, including ATP-sensitive potassium (KATP) channels and inward rectifying potassium (Kir) channels, can blunt neurovascular responses by interfering with the hyperpolarization of vascular smooth muscle and endothelium, thereby reducing activity-induced increases in local blood flow (Isaacs *et al.*, 2024).

Taken together, these mechanisms – astrocyte and endothelial dysfunction, pericyte loss, microvascular remodeling, inflammation, oxidative and metabolic stress, and altered ion channel signaling – intertwine to create an environment in which the cerebral vasculature

becomes increasingly unresponsive to neuronal demands. The multifaceted disruption of NVC underpins a broad spectrum of neurological disorders. The downstream consequences of these mechanisms manifest in diverse clinical contexts, ranging from the paroxysmal hyperexcitability of epilepsy to the diffuse and progressive deficits seen in traumatic brain injuries and neurodegenerative diseases. In the following subsection, the clinical implications and disease-specific patterns of NVC failure will be explored, highlighting how these mechanistic disruptions translate into observable pathophysiological phenomena.

**Clinical Manifestation**

NVC disruptions are increasingly recognized as a hallmark of both acute and chronic epilepsy, profoundly influencing cerebral hemodynamics during interictal and ictal states. In epilepsy, synchronous neuronal discharges can result in either excessive or paradoxically blunted local vascular responses, reflecting impaired communication between neurons, glia, and cerebral vasculature (Schwartz, 2007; Voges *et al.*, 2012). Experimental and clinical studies demonstrate that seizure activity may evoke an initial hyperemic response, but this can be followed by a period of hypoperfusion or vascular "exhaustion," indicating a failure of the vasculature to sustain prolonged metabolic demand (Song *et al.*, 2016; Yin *et al.*, 2022). Over time, recurrent seizures may remodel the NVU and diminish the efficacy of astrocyte-mediated and endothelial-mediated vasodilatory signaling, leading to progressive NVC dysfunction (Wan *et al.*, 2025). Chronic epilepsy is associated with persistent abnormalities in NVC, including delayed and spatially disorganized vascular responses to neural activity, which may underlie the increased risk of neuronal injury and cognitive impairment seen in these patients (Wan *et al.*, 2025). Thus, epilepsy exemplifies a dynamic and often maladaptive remodeling of neurovascular function, with both immediate and long-term consequences for brain health.

Following TBI, disruption of NVC emerges as a critical factor in both acute pathophysiology and long-term functional deficits. The immediate impact of TBI can damage the NVU through mechanical shear, leading to loss of endothelial and astrocytic integrity, disruption of pericyte function, and breakdown of signaling pathways that normally mediate rapid vascular responses to neuronal activation (Jang *et al.*, 2017; van Hameren *et al.*, 2024). In severe brain trauma, cortical spreading depolarizations frequently induce "inverse NVC," wherein increased neuronal activity is paradoxically met by reductions in local blood flow, compounding metabolic stress and risking secondary neuronal injury (Hinzman *et al.*, 2014).

Mitochondrial dysfunction within neurovascular cells further impairs the production of vasoactive signals and amplifies oxidative stress, disrupting the fine-tuned relationship between metabolic demand and CBF. Long-term survivors of TBI often exhibit persistent impairments in NVC, which are correlated with cognitive decline and executive dysfunction (Magyar-Sumegi *et al.*, 2025). This chronic disruption is thought to arise from maladaptive vascular remodeling, persistent inflammation, and deficits in cellular energy metabolism, underscoring the lasting impact of TBI on neurovascular function (Wing *et al.*, 2017).

Impairment of NVC is a prominent and early feature in several neurodegenerative disorders, most notably AD, but also in other forms of dementia and age-related cognitive decline. In these conditions, astrocytic and endothelial dysfunction, pericyte degeneration, and microvascular rarefaction converge to blunt the hemodynamic response to neuronal activation (Tarantini *et al.*, 2017; Zhu *et al.*, 2022). Chronic neuroinflammation and vascular oxidative stress further disrupt the molecular cascades responsible for NVC, with amyloid-β and tau pathology directly impeding both astrocytic calcium signaling and NO production (van der Heide *et al.*, 2022) (Zhu et al., 2022; van der Heide et al., 2022). As a result, brain regions affected by neurodegenerative processes demonstrate diminished or delayed increases in blood flow in response to cognitive or sensory stimulation, which may accelerate neuronal injury through chronic hypoperfusion and impaired waste clearance (de Montgolfier et al., 2020). This vicious cycle of NVC dysfunction, microvascular pathology, and neurodegeneration is increasingly seen as a core mechanism underlying progressive cognitive impairment, and highlights the NVU as a promising therapeutic target for these disorders.

#### 1.5.2.3 Vascular Remodeling and Abnormal Permeability

Vascular remodeling in the brain refers to the structural and functional changes that cerebral blood vessels undergo in response to physiological demands or pathological stimuli. While healthy remodeling supports neurovascular plasticity and adapts the vasculature to metabolic needs, pathological remodeling is maladaptive and underlies several neurological diseases. This maladaptive process leads to vessel wall thickening, luminal narrowing, aberrant angiogenesis, and ultimately, impaired cerebral blood flow and NVU dysfunction (Wardlaw, Smith and Dichgans, 2013).

A key driver of pathological vascular remodeling is chronic disruption of endothelial tight junctions. Inflammatory cytokines, such as TNF-α, upregulate matrix metalloproteinases (notably MMP-2 and MMP-9), which degrade tight junction proteins (e.g., claudins, occludins) and extracellular matrix components (Rempe, Hartz and Bauer, 2016; Yang and Torbey, 2020). This degradation compromises endothelial barrier function, resulting in increased permeability and infiltration of plasma proteins and immune cells into the brain parenchyma. Such BBB breakdown fuels neuroinflammation and disrupts the fine regulation of CBF, with consequences for NVC mechanisms. In parallel, MMP-mediated matrix degradation facilitates pathological angiogenesis and vessel wall remodeling, contributing to vessel wall thickening and narrowing.

Oxidative stress further amplifies vascular remodeling. Excess ROS, whether generated during inflammation, hypoxia, or metabolic dysfunction, damages endothelial cells and tight junctions, exacerbating vascular leakage and BBB disruption (Higashi, 2022). Oxidative signaling also promotes VSMC proliferation and migration, which thickens vessel walls and reduces lumen diameter, impeding blood flow (Carvalho and Moreira, 2018). This impairment of endothelial function – a cornerstone of the NVU – directly undermines NVC by reducing the vasculature's ability to respond to neuronal cues.

Hypoxia is another potent stimulus for pathological vascular remodeling. By upregulating VEGF, hypoxic conditions drive angiogenesis but also increase vascular permeability by inducing endothelial fenestrations and destabilizing tight junctions. The resulting immature, leaky vessels further perpetuate BBB dysfunction, create local edema, and disrupt the balance between neuronal activity and blood flow regulation (Fischer *et al.*, 2002).

Understanding the overlapping molecular and cellular mechanisms underlying vascular remodeling, abnormal permeability, and impaired neurovascular coupling is essential for appreciating their roles across a range of cerebrovascular and neurological diseases. These interconnected processes manifest in diverse pathological contexts, with unique patterns and consequences depending on the underlying disorder. In the following subsection, we will examine how vascular remodeling and abnormal permeability contribute to disease pathogenesis in brain tumors, moyamoya disease, and chronic hypertension. Exploring these specific examples will highlight the spectrum of vascular alterations within the brain and underscore the relevance of NVU dysfunction to both focal and diffuse cerebrovascular pathology.

**Clinical Manifestation**

Vascular remodeling and abnormal permeability are defining features of malignant brain tumors such as glioblastoma. The vasculature within these tumors is highly abnormal, characterized by excessive, disorganized, and leaky vessels formed through dysregulated angiogenesis driven by tumor hypoxia and pro-angiogenic factors like VEGF (Rieger and Welter, 2015). As a result, the BBB is significantly compromised, leading to increased extravasation of plasma proteins, growth factors, and immune cells, which in turn promote a pro-tumorigenic and immunosuppressive microenvironment (Ahir, Engelhard and Lakka, 2020). The chaotic tumor vasculature impedes efficient delivery of oxygen and therapeutic agents, thereby fostering hypoxic niches that further stimulate pathological angiogenesis and tumor progression (Farnsworth *et al.*, 2014). Furthermore, tumor-associated immune cells, such as macrophages, secrete additional pro-angiogenic and remodeling factors, amplifying vascular abnormalities and creating a vicious cycle of vascular and tumor evolution. Clinically, these vascular changes are associated with peritumoral edema, increased risk of hemorrhage, and resistance to conventional therapies due to poor drug penetration, underscoring the central role of abnormal vascular remodeling and permeability in brain tumor pathophysiology.

Moyamoya disease exemplifies a unique pattern of vascular remodeling, manifesting as progressive stenosis of the terminal internal carotid arteries and their proximal branches, accompanied by the compensatory development of fragile collateral networks known as "moyamoya vessels" (Fox *et al.*, 2021). Histopathological studies reveal concentric intimal thickening, medial thinning, and disruption of the internal elastic lamina in affected arteries, resulting in increased vascular fragility and a propensity for both ischemic and hemorrhagic strokes (Kuroda *et al.*, 2015). The collateral vessels that form in response to progressive stenosis are structurally immature and display high permeability, lacking robust smooth muscle and exhibiting poorly formed tight junctions, making them susceptible to rupture and microbleeds (Uchino *et al.*, 2025). Imaging and pathological evidence indicate that these abnormalities are associated with breakdown of the BBB, persistent low-grade inflammation, and ongoing vascular remodeling within the circle of Willis and its branches (Mikami *et al.*, 2015). Clinically, these vascular changes manifest as recurrent transient ischemic attacks, progressive cognitive decline, and intracranial hemorrhage, with the risk and severity shaped by the balance between arterial occlusion, collateral vessel development, and the stability of the newly formed vasculature.

After ischemic stroke, vascular remodeling and changes in permeability are central to both tissue recovery and secondary injury. In the aftermath of acute ischemia, hypoxia-driven upregulation of VEGF and related angiogenic factors induces robust, though disorganized, angiogenesis in the peri-infarct region (Fang, Wang and Miao, 2023). The newly formed vessels are often immature, with incomplete tight junctions and basement membrane degradation, resulting in increased BBB permeability and a heightened risk of vasogenic edema and secondary neuronal injury (Yang and Torbey, 2020). Concomitantly, inflammatory cells such as neutrophils and macrophages infiltrate the ischemic tissue and release proteases and cytokines, further exacerbating vascular leakage and impairing vascular stabilization. Over time, the persistence of these processes determines whether vascular remodeling will support neurovascular recovery or lead to chronic microvascular dysfunction, impaired revascularization, and ongoing tissue damage (Brown *et al.*, 2007; Liu *et al.*, 2014). Clinically, these changes contribute not only to acute complications such as brain swelling and hemorrhagic transformation but also to long-term outcomes including cognitive impairment and stroke recurrence.

### 1.5.3 Maladaptive Vascular Responses

Building upon the mechanisms discussed in Section 1.5.2, it is evident that disruptions in the NVU – particularly in NVC, BBB integrity, and vascular structure – have profound effects on cerebrovascular regulation, specifically CVR and CA. These impairments are interconnected processes contributing to the pathophysiology of various neurological disorders. NVC ensures that neuronal activity is met with appropriate changes in CBF. However, pathological conditions can impair NVC by inducing endothelial dysfunction and reducing NO availability, leading to diminished vasodilatory responses (Presa *et al.*, 2020). This impairment in NVC directly affects CVR, as the vessels become less responsive to metabolic demands and vasoactive stimuli. BBB integrity is crucial for maintaining the homeostatic environment of the brain. Inflammatory processes and oxidative stress can compromise the BBB, allowing neurotoxic substances to enter the brain parenchyma, exacerbating neuronal injury and disrupting CBF regulation (Sweeney, Sagare and Zlokovic, 2018; Carrera-González, Cantón-Habas and Rich-Ruiz, 2022). The resulting endothelial dysfunction impairs CA by reducing the vessels' ability to constrict or dilate in response to blood pressure changes, leading to either hypoperfusion or hyperperfusion states. Other pathological conditions may induce structural changes in cerebral vessels, such as increased wall thickness and reduced lumen diameter, a process known as vascular remodeling (Faraco

and Iadecola, 2013). These changes increase vascular resistance and decrease compliance, impairing both CVR and CA. The stiffened vessels cannot adequately adjust to fluctuations in blood pressure or metabolic demands, leading to cerebral hypoperfusion and increased susceptibility to ischemic events.

Vascular pathology has emerged as a unifying principle across a broad spectrum of neurological disorders, highlighting the fundamental role of cerebrovascular health in the preservation of neural function. Disruptions in NVC, BBB integrity, and vascular remodeling do not occur in isolation; rather, they represent interdependent processes that collectively shape the trajectory of cerebral pathology. These interconnected alterations manifest clinically and radiologically as characteristic changes in regional CBF, which increasingly serve as surrogate markers for both diagnosis and disease monitoring. The interplay between structural and functional disruptions of the cerebral vasculature is mirrored in hemodynamic parameters measurable by advanced imaging. Notably, regional and global perfusion alterations are not only sensitive to acute hemodynamic compromise, as seen in stroke, but are also capable of capturing the more insidious, subtle shifts associated with chronic neurodegeneration and small vessel disease (Christen *et al.*, 2014; Bernetti *et al.*, 2025). Thus, evaluation of cerebral perfusion has transcended the realm of research and is now firmly embedded within standard clinical protocols, reflecting its diagnostic and prognostic value.

In summary, the centrality of vascular pathology across neurological disorders underscores the value of hemodynamic assessment in both clinical and research settings. The intricate correlation between perfusion parameters, structural changes, and functional impairment situates cerebral perfusion evaluation as a cornerstone in the modern investigation of brain disease. In the following section, the discussion will focus on those specific disease entities that are of principal interest to this thesis, with particular attention to their distinct pathological manifestations as reflected in deviations of CBF.

### 1.6 Specific Disease Contexts: Altered Perfusion

Having established the structural and functional foundations of cerebral vasculature and perfusion regulation, as well as the overarching mechanisms of systemic pathogenesis, this section will turn to the theoretical background of CBF disruption in CNS diseases that are central to this doctoral thesis. The discussion will begin with an examination of hemodynamic markers in both adult and pediatric brain tumors, exploring the underlying

pathological mechanisms driving perfusion abnormalities and their diagnostic significance. The section will then address the unique challenges presented by perfusion changes in the developing pediatric brain, including neonatal populations, and assess the diagnostic relevance of hemodynamic parameters in these particularly vulnerable cohorts. Finally, attention will be given to hemodynamic alterations associated with epilepsy, concluding with a discussion of the clinical utility of CBF assessment in this context.

### 1.6.1 Brain Tumors

Brain tumors represent a persistent and complex challenge for global healthcare systems as well as for affected patients and their families. In 2020, tumors of the brain and CNS accounted for approximately 1.6% of all cancer cases and 2.6% of cancer-related deaths worldwide, with notably higher incidence rates reported in high-income regions (Ferlay *et al.*, 2024). Between 1990 and 2021, the global age-standardized incidence rate (ASIR) for brain and CNS malignancies increased from 3.75 to 4.28 per 100,000 population, a trend largely attributable to demographic changes such as population growth and aging, particularly in regions with a high sociodemographic index (SDI) (Zhou *et al.*, 2025). Despite this rise in incidence, the age-standardized mortality rate (ASMR) has remained relatively stable over the same period, reflecting advancements in both diagnostic modalities and therapeutic interventions. Within the pediatric population, brain tumors constitute the second most common malignancy after leukemia, accounting for an estimated 15–20% of all childhood cancers. Data from the European Cancer Inequalities Registry indicate that, in 2022, CNS tumors represented 15% of all new cancer diagnoses and 39% of cancer-related deaths among children aged 0 to 14 years within the European Union (Munoz *et al.*, 2023). The clinical and societal burden of brain tumors extends beyond mortality statistics, as these neoplasms impose significant psychological and financial hardship (Bradley *et al.*, 2007; Newton *et al.*, 2025). Furthermore, the long-term quality of survival among children who overcome brain tumors often remains poor due to the unique vulnerability of the developing brain to both the disease and its treatment (Pancaldi *et al.*, 2023).

Medical imaging remains a cornerstone in the clinical management of brain tumors, with recent advancements acquiring even greater importance as the field shifts toward molecular subtyping and personalized approaches (Vagvala *et al.*, 2022). While tissue biopsy continues to serve as the gold standard for prognostication and guiding follow-up decisions, neurosurgical procedures can be suboptimal in certain cases due to the significant risks of

neurological injury. This is particularly relevant in pediatric populations, where neoplasms are more frequently located in eloquent brain areas, raising concerns regarding long-term cognitive outcomes (Luglietto *et al.*, 2025). In this context, the development and clinical validation of advanced imaging biomarkers have become increasingly crucial – not only for diagnosis but also for the expanding domains of targeted therapy and precision medicine (Chiu and Yen, 2023).

Perfusion imaging has emerged as a pivotal tool in the evaluation of brain tumors, owing to its ability to assess tumor vascularity and hemodynamics. Angiogenesis, primarily driven by VEGF, plays a crucial role in tumor growth and aggressiveness. CBF has thus emerged as a marker that correlates with tumor grade and vascular proliferation (Lacerda and Law, 2009). Evaluating both intratumoral and peritumoral CBF is crucial, as alterations in these parameters can inform treatment strategies. Advancements in MRI techniques have enabled the seamless incorporation of perfusion imaging into routine clinical protocols for brain tumor assessment. Reflecting its strong diagnostic and prognostic value, there is increasing consensus that perfusion imaging should be regarded as an essential part of standard brain tumor imaging protocols (Hu *et al.*, 2025).

In the subsequent sections, we will delve into the specific characteristics of perfusion imaging in adult and pediatric brain tumors, acknowledging the differences in pathogenesis, treatment approaches, and histopathological markers. We will explore the significance of regional intra- and peritumoral perfusion patterns and their potential relationship with histopathological profiles. Furthermore, we will discuss the clinical implications of hemodynamic parameters in patient management.

#### 1.6.1.1 Adult Brain Tumors

The classification of brain tumors is primarily based on the World Health Organization (WHO) Classification of Tumors of the Central Nervous System, which is revised every 5 years to incorporate advances in neuropathology (WHO Classification of Tumous Editorial Board, 2021). The most recent edition emphasizes the pivotal role of molecular markers, which have become essential for accurate tumor classification and clinical decision-making (Louis *et al.*, 2021). Among malignant primary brain tumors, gliomas – neoplasms arising from the glial cells of the brain and spinal cord – constitute approximately 75% of cases (Sharifian *et al.*, 2024), as well as they are the most common adult primary brain tumors

(van den Bent *et al.*, 2023). Gliomas continue to represent a major clinical challenge due to their infiltrative growth, resistance to therapy, and high rates of recurrence.

Gliomas are classified into five subgroups based on molecular criteria: glioblastoma, astrocytoma, oligodendroglioma, pediatric-type gliomas, and other gliomas (Figure 8). Among adults, glioblastomas account for approximately 50% of cases, astrocytomas for 27%, and oligodendrogliomas for 12%, with the remaining 11% comprising diffuse gliomas not otherwise specified and gliomas with rare or mixed histological features (Ghosh *et al.*, 2025). The isocitrate dehydrogenase (*IDH*) mutation status is the primary molecular marker used in glioma classification. Glioblastomas are defined as *IDH1/2*-wildtype gliomas and commonly exhibit additional molecular alterations, including *TERT* promoter mutations, *EGFR* amplification, and/or concurrent gain of chromosome 7 with loss of chromosome 10 (7+/10-). Astrocytomas are characterized by mutations in *IDH1* or *IDH2* without codeletion of chromosomal arms 1p and 19q, while oligodendrogliomas are identified by the presence of both *IDH1/2* mutations and 1p/19q codeletion. In cases where 1p/19q status cannot be established in an *IDH*-mutant glioma, detection of *ATRX* or *TP53* mutations supports a diagnosis of astrocytoma rather than oligodendroglioma.

Glioblastomas have the poorest prognosis among gliomas, with a median overall survival of 12–15 months and a 5-year survival rate below 10%. Standard treatment consists of maximal safe surgical resection followed by radiotherapy and concomitant temozolomide chemotherapy; however, recurrence rates remain high, necessitating close follow-up (Stupp *et al.*, 2005). Astrocytomas generally have a more favorable prognosis, which varies by grade: for example, WHO grade 2 astrocytomas have a median survival of approximately 10 years. Management options for grade 2 astrocytomas include observation, surgical resection, and radiotherapy, while higher-grade astrocytomas (grades 3 and 4) typically require a combination of surgical resection, radiotherapy, and chemotherapy. Within this subgroup, *ATRX* status may be diagnostically relevant, as *ATRX*-deficient glioma cells show increased sensitivity to DNA-damaging therapies such as ionizing radiation and certain chemotherapeutic agents (Y. Zhao *et al.*, 2024). Oligodendrogliomas are defined by the co-deletion of chromosome arms 1p and 19q, a molecular feature linked to a favorable response to treatment and prolonged survival, often exceeding 10–15 years (Alnahhas, 2024). Standard therapy for oligodendroglioma includes surgical resection followed by radiotherapy and chemotherapy, typically with the PCV regimen (procarbazine, lomustine, and vincristine), regardless of tumor grade.

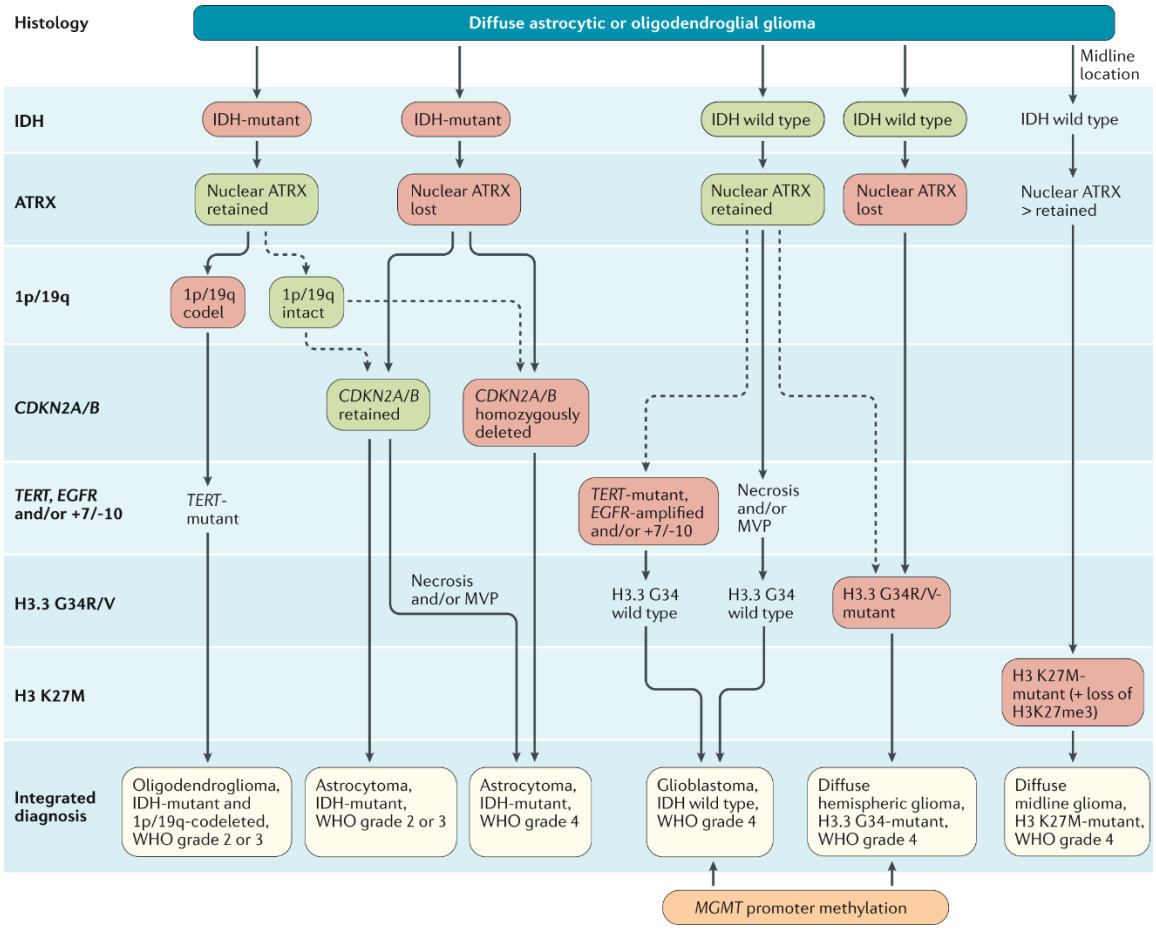


**Figure 8.** Diagnostic algorithm for adult glioma subtyping based on molecular markers according to WHO 2021. *Adapted from (Weller et al., 2021), licensed under CC-BY-4.0.*

### Correlation between Radiological and Molecular Markers

*IDH*-wildtype tumors are frequently characterized by intratumoral contrast enhancement on MRI, reflecting their aggressive behavior and disruption of the blood-brain barrier – histopathologically linked to pronounced microvascular proliferation and necrosis. While this imaging feature is commonly seen in glioblastomas (Roux *et al.*, 2024), a subset of *IDH*-wildtype tumors can lack contrast enhancement and is associated with improved overall survival and distinct histopathological characteristics (Foltyn-Dumitru *et al.*, 2025). Another hallmark of glioblastoma is reduced diffusivity on diffusion-weighted MRI, corresponding to high tumor cellularity and dense packing of malignant cells (Azizova *et al.*, 2025a) (Figure 9). Additionally, ill-defined tumor borders are a notable feature of *IDH*-wildtype gliomas, reflecting their infiltrative growth pattern and diffuse infiltration into surrounding brain parenchyma (Kibe *et al.*, 2023).

Histopathologically, loss of *ATRX* expression is associated with alternative lengthening of telomeres (ALT), a telomerase-independent telomere maintenance mechanism frequently observed in astrocytomas. This mechanism promotes genomic instability and increased tumor heterogeneity, which may manifest radiologically as ill-defined tumor margins and heterogeneous signal intensities on T2-weighted and T2-FLAIR MRI sequences, reflecting the infiltrative growth pattern characteristic of these tumors (Meng *et al.*, 2022) (Figure 10).

A particularly important and highly specific radiological feature for distinguishing *IDH*-mutant, 1p/19q non-codeleted astrocytomas is the T2-FLAIR mismatch sign. This imaging feature is primarily attributable to distinctive histopathological characteristics, most notably the presence of microcystic changes and low tumor cellularity (Ozono *et al.*, 2024). The microcystic components, filled with fluid, contribute to the tumor's homogeneous hyperintensity on T2-weighted images, while on FLAIR sequences—where the signal from free fluid is suppressed—these regions appear relatively hypointense except for a hyperintense peripheral rim. It is important to note, however, that although the T2-FLAIR mismatch sign demonstrates high specificity for *IDH*-mutant, 1p/19q non-codeleted astrocytomas, its sensitivity is limited, meaning that a substantial proportion of such tumors may not exhibit this feature (Deguchi *et al.*, 2020).

Currently, *CDKN2A/B* homozygous deletion is not associated with any characteristic MRI features and thus cannot be reliably predicted by conventional imaging (Lasocki *et al.*, 2023). Consequently, the diagnosis of astrocytomas may remain indeterminate in the absence of the T2-FLAIR mismatch sign and overt heterogeneity on T2-weighted images, highlighting the ongoing need for integrated advanced radiological and molecular assessment.

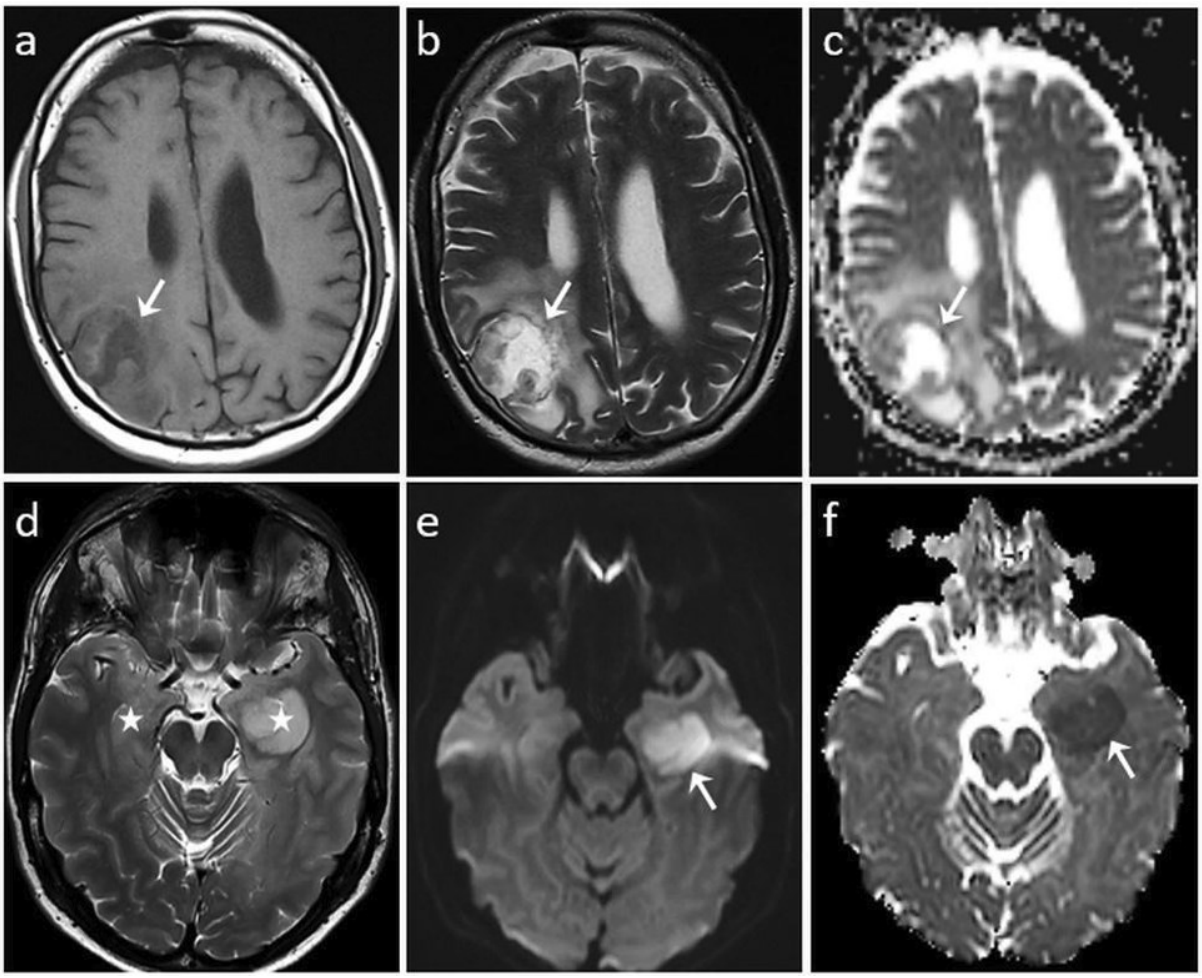


**Figure 9.** Illustrative cases: assessment of necrosis and diffusion in glioblastoma. Necrosis (a, b, c; glioblastoma, *IDH*-wildtype): axial MRI scans reveal a lesion in the right parietal region, exhibiting classic radiological features of central necrosis. The area appears hypointense on T1-weighted imaging (a) and hyperintense on T2-weighted imaging (b), with the ADC map demonstrating a fluid-like hyperintense signal (c). The necrotic core is surrounded by thick, irregular margins, as indicated by the white arrows. Restricted diffusion (d, e, f; glioblastoma, IDH-wildtype): in a separate example, axial MR images show bilateral, infiltrative lesions involving the mesial temporal and hippocampal regions, both of which are hyperintense on T2-weighted imaging (d, white stars). On the left, there is evidence of restricted diffusion, demonstrated by increased signal intensity on TRACE/DWI (e, white arrow) and a corresponding decrease in ADC signal (f, white arrow). *Adapted from (Azizova et al., 2025b), licensed under CC-BY-4.0.*

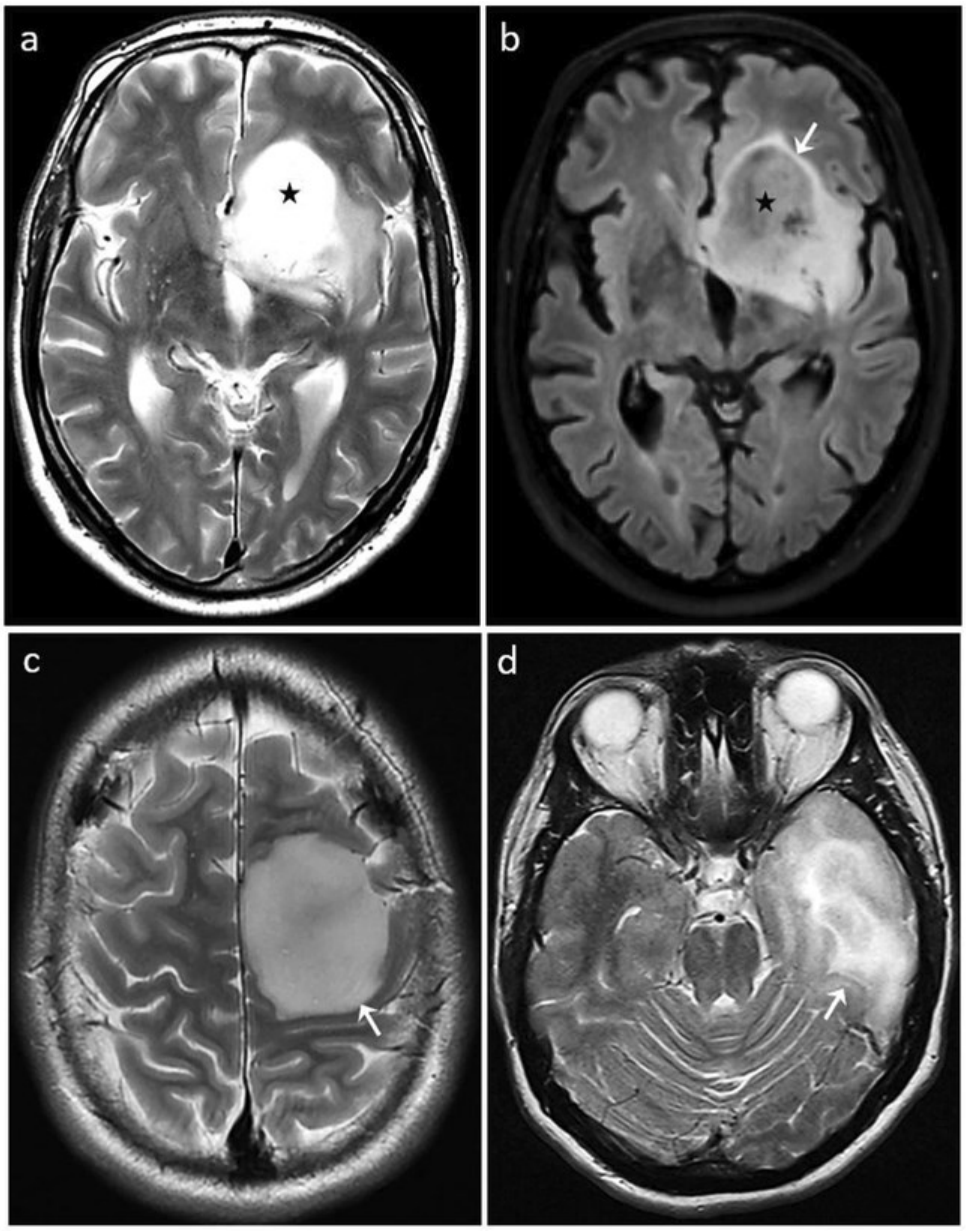


**Figure 10.** Representative cases: assessment of the T2-FLAIR mismatch sign, tumor margins, and T2 signal uniformity. T2-FLAIR mismatch sign (a, b; low-grade astrocytoma, *IDH*-mutant): Axial T2-weighted image shows a homogeneous hyperintense lesion in the left fronto-insular region (a, black star), while the FLAIR sequence reveals marked signal suppression except for a peripheral hyperintense rim (b, white arrow), consistent with the T2-FLAIR mismatch sign. Well-defined margins and T2 homogeneity (c; low-grade astrocytoma, *IDH*-mutant): Axial T2-weighted image displays a left frontal lesion with uniform hyperintensity and sharply defined borders (white arrow). Ill-defined margins and T2 heterogeneity (d; high-grade astrocytoma, IDH-mutant): Axial T2-weighted image demonstrates a left temporal lesion with heterogeneous signal and poorly defined margins (white arrow). *Adapted from (Azizova et al., 2025b), licensed under CC-BY-4.0.*

Oligodendrogliomas exhibit several characteristic MRI features that are closely linked to their underlying molecular profile. Notably, the presence of calcifications, indistinct tumor margins, and preferential involvement of the frontal lobes are features more commonly associated with *IDH*-mutant, 1p/19q-codeleted tumors (Lasocki *et al.*, 2018) (Figure 11). Calcifications, in particular, are frequently observed and are believed to result from dystrophic mineralization occurring within areas of tumor necrosis or degeneration (Zhu *et al.*, 2024). This phenomenon is more pronounced in the slow-growing, indolent course that typically characterizes 1p/19q-codeleted oligodendrogliomas. The predominance of frontal lobe involvement may be related to the origin of these neoplasms from oligodendrocyte precursor cells, which are found in greater density within the frontal white matter. While *TERT* promoter mutation serves as an important prognostic marker, conferring a favorable prognosis in the context of oligodendrogliomas, there are currently no established radiological features that can reliably differentiate *TERT*-mutant from *TERT*-wildtype tumors within this subgroup. Although recent studies have explored radiomics-based approaches to predict *TERT* mutation status, no definitive imaging markers have been validated to date (Tang *et al.*, 2024).

Despite substantial progress in elucidating correlations between MRI features and molecular markers in adult gliomas, a significant proportion of tumors still lack distinctive radiological hallmarks on conventional imaging, thereby complicating non-invasive differentiation of specific subtypes (Hu *et al.*, 2023). Consequently, surgical resection or biopsy remains necessary in many cases to achieve definitive diagnosis and accurate molecular classification. Although artificial intelligence and radiomics-based approaches have shown promise in predicting molecular alterations and patient prognosis from MRI data, their integration into routine clinical practice remains limited by the need for extensive, multi-center validation and standardization (Cheong *et al.*, 2024).

**Monitoring Treatment Response**

MRI remains the cornerstone for monitoring treatment response and disease progression in adult patients with gliomas. Conventional MRI sequences are routinely employed to evaluate changes in tumor size, morphology, and enhancement patterns. However, these conventional techniques often fall short in distinguishing true tumor progression from pseudoprogression. True progression (TP) denotes actual tumor growth or recurrence, whereas

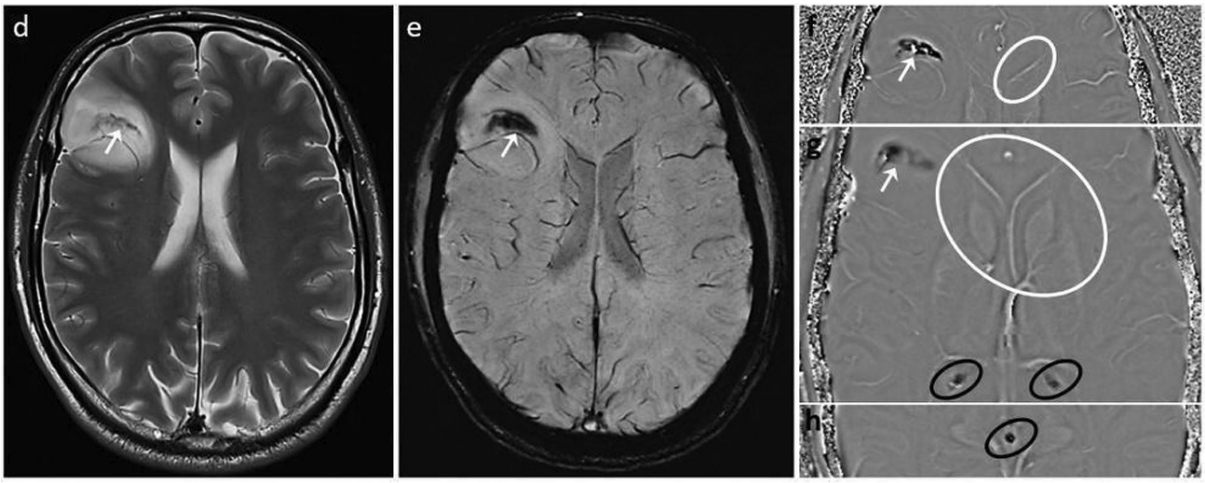


**Figure 11.** Calcification in low-grade oligodendroglioma (d–h; *IDH*-mutant, 1p/19q-codeleted): axial MR images demonstrate a heterogeneous, hyperintense lesion in the right frontal lobe (d, white arrow), with internal calcification evident by blooming artifact on SWI (e, white arrow). The corresponding area is hypointense on filtered phase images (f, g; white arrows), matching the signal of the calcified choroid plexus (g, dark circles) and pineal gland (h, dark circle), in contrast to the internal cerebral veins (f, g, white circles). These findings support calcification rather than hemorrhage, with internal veins serving as a reference for hemorrhagic signal and the choroid plexus/pineal gland for calcification. *Adapted from (Azizova et al., 2025b), licensed under CC-BY-4.0.*

pseudoprogression (PsP) refers to transient imaging changes that mimic tumor progression but are attributable to treatment-related effects such as inflammation, edema, or necrosis. PsP is particularly prevalent within the first three months following concurrent chemoradiotherapy, occurring in up to 30% of glioblastoma patients (Le Fèvre *et al.*, 2021). The inability to reliably differentiate TP from PsP using conventional MRI can lead to misinterpretation of treatment efficacy and inappropriate alterations in therapeutic strategies. On conventional MRI, both TP and PsP can present with new or increased contrast enhancement, mass effect, and peritumoral edema, rendering differentiation challenging. Nonetheless, certain imaging features may provide clues; for instance, subependymal enhancement has been associated with TP, demonstrating a specificity of 93.3% but a sensitivity of only 38.1% (Taylor *et al.*, 2022).

**Perfusion MRI in Glioma Assessment**

The limitations associated with pre-treatment differential diagnosis and treatment monitoring in glioma patients have intensified interest in advanced MRI techniques that offer

a more comprehensive parametric assessment of tumor characteristics. Among these, perfusion parameters such as CBF have garnered particular attention due to their ability to reflect the underlying vascularity and metabolic activity of gliomas (Henriksen, Del Mar Álvarez-Torres, *et al.*, 2022). Elevated CBF values have been associated with higher tumor grade and increased aggressiveness, offering biological insights beyond what is attainable through standard structural imaging alone (Alsaedi *et al.*, 2019). Incorporating CBF and other perfusion-derived metrics into glioma evaluation has been shown to enhance grading accuracy, support molecular subclassification, and improve clinicians' confidence in assessing brain tumors, ultimately benefiting both prognostic evaluation and treatment planning (Yamin *et al.*, 2024). Another investigation suggested the use of perfusion markers to triage brain tumor patients for additional imaging with PET, optimizing resource allocation, minimizing radiation risk, and significantly improving the overall accuracy of the workflow (Kadali *et al.*, 2025). Hemodynamic parameters have been found useful in

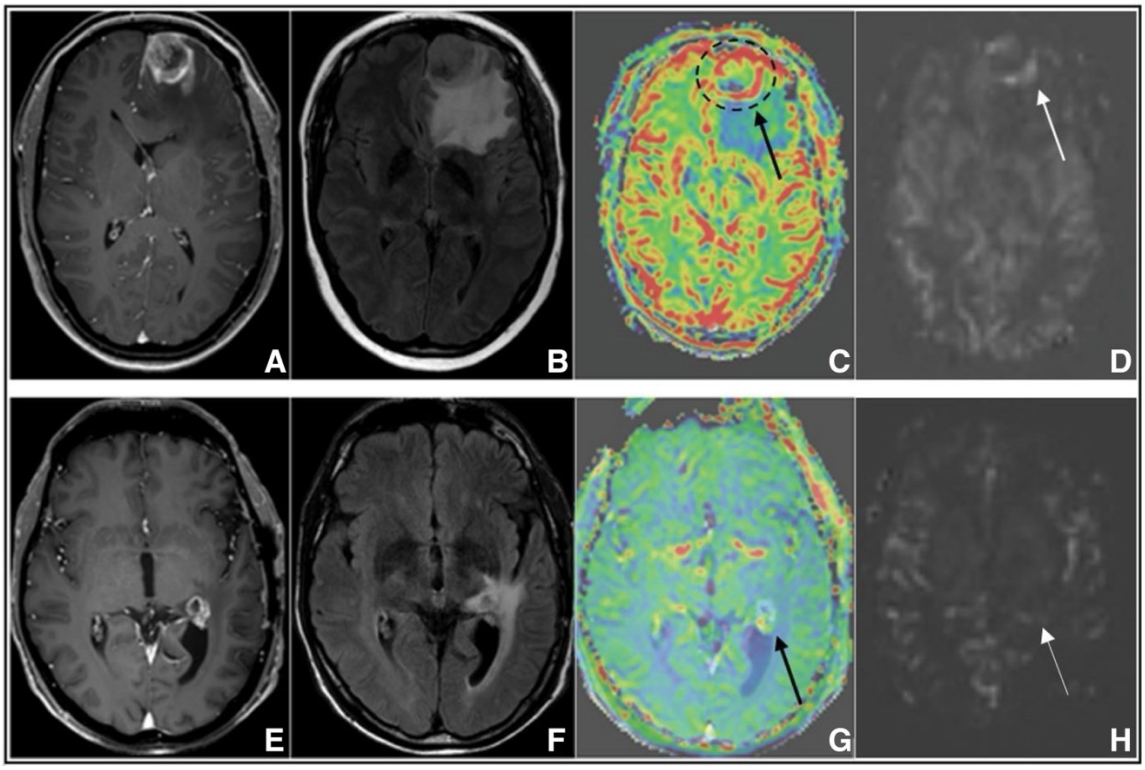


**Figure 12.** Representative post-contrast T1-weighted images (A, E), T2 FLAIR sequences (B, F), dynamic susceptibility contrast-derived relative CBV (DSC-rCBV) maps (C, G), and arterial spin labeling CBF (ASL-CBF) maps (D, H) are shown for two patients: one with confirmed TP (top row, A–D) and one with confirmed PsP (bottom row, E–H). *Adapted from (van Dorth et al., 2025), licensed under CC-BY-4.0.*

distinguishing TP from PsP, as elevated CBF values are indicative of TP, whereas lower values suggest PsP (Lavrova *et al.*, 2022; van Dorth *et al.*, 2025) (Figure 12). The integration of perfusion imaging parameters with conventional MRI enhances the accuracy of glioma monitoring, facilitating timely and appropriate therapeutic interventions.

While the integration of advanced MRI techniques – particularly perfusion imaging – has markedly improved the precision of glioma assessment in adults, the clinical reality remains that no single imaging modality or protocol can fully resolve the diagnostic complexities inherent to brain tumors. In daily practice, critical treatment decisions often hinge on subtle imaging findings, with clinicians increasingly reliant on quantitative markers such as CBF to supplement the anatomical detail provided by conventional MRI. This multiparametric approach not only supports individualized therapy but also helps minimize the risk of both overtreatment and undertreatment. The ongoing evolution of neuroimaging underscores an important paradigm shift: the transition from purely structural to functionally and physiologically informed tumor characterization.

The urgency for robust imaging biomarkers is even more pronounced in pediatric neuro-oncology, where tumor biology is exceptionally heterogeneous and the stakes of misclassification are particularly high. Pediatric brain tumors encompass a diverse range of pathologies that differ significantly from their adult counterparts in terms of genetics, growth patterns, and treatment responses. Moreover, children are more vulnerable to the long-term sequelae of both disease and therapy, making precise and timely monitoring essential for optimizing outcomes and preserving neurodevelopmental trajectories.

#### 1.6.1.2 Pediatric Brain Tumors

Pediatric brain tumors are the most prevalent solid tumors in children and adolescents and represent the leading cause of cancer-related mortality in individuals aged 0–19 years. For children aged 0–14 years, the average annual incidence rate is approximately 4.3 per 100,000 person-years, with the highest rates observed in the 0–4-year age group. In adolescents aged 15–19 years, the incidence rates tend to be slightly lower, though specific data for this age group are less consistently reported across studies (Abuhamed *et al.*, 2022). Globally, the burden of pediatric CNS tumors reflects significant regional differences in incidence, access to care, and survival outcomes. According to the study by , childhood cancers—including brain tumors—account for more than 11 million disability-adjusted life-years (DALYs)

worldwide each year, underscoring both the direct impact of malignancy and the long-term effects of treatment and survivorship (Bhakta *et al.*, 2019).

The 2021 WHO Classification of Tumors of the CNS introduced significant changes (Figure 13) , emphasizing molecular diagnostics to enhance tumor classification and prognostication.

Key categories relevant to pediatric brain tumors now include:

- Pediatric-type diffuse low-grade gliomas (pLGG): These generally indolent tumors are characterized by specific genetic alterations, notably *MYB* or *MYBL1* rearrangements and *MAPK* pathway mutations.
- Pediatric-type diffuse high-grade gliomas (pHGG): This aggressive group, associated with poor prognosis, includes entities such as diffuse midline glioma, *H3 K27*-altered, and diffuse hemispheric glioma, *H3 G34*-mutant.
- Circumscribed astrocytic gliomas: These well-demarcated tumors, such as pilocytic astrocytoma, often have favorable outcomes and distinctive molecular features.
- Glioneuronal and neuronal tumors: A heterogeneous category encompassing tumors such as ganglioglioma and dysembryoplastic neuroepithelial tumor (DNET), frequently associated with epilepsy and characteristic molecular alterations.
- Embryonal tumors: Highly malignant neoplasms, including medulloblastoma and atypical teratoid/rhabdoid tumor (AT/RT), predominantly affect younger children and often feature recurrent genetic drivers.

Gliomas are the most common histological type, comprising approximately 51.2% of tumors in children aged 0–14 years (Ostrom *et al.*, 2022). Pilocytic astrocytoma is the most prevalent glioma subtype, accounting for 18.3% of all tumors in this age group. Embryonal tumors, including medulloblastoma and atypical teratoid/rhabdoid tumor (AT/RT), represent 12.3% of pediatric brain tumors. In adolescents aged 15–19 years, pituitary tumors are the most common, constituting 33.1% of all tumors.

It is important to note that pediatric brain tumors frequently arise from disturbances in normal developmental processes, resulting in a far greater diversity of tumor types compared to those seen in adults (Abedalthagafi *et al.*, 2021). The tumor microenvironment in pediatric cases also differs markedly from that of adults, influencing both tumor biology and response

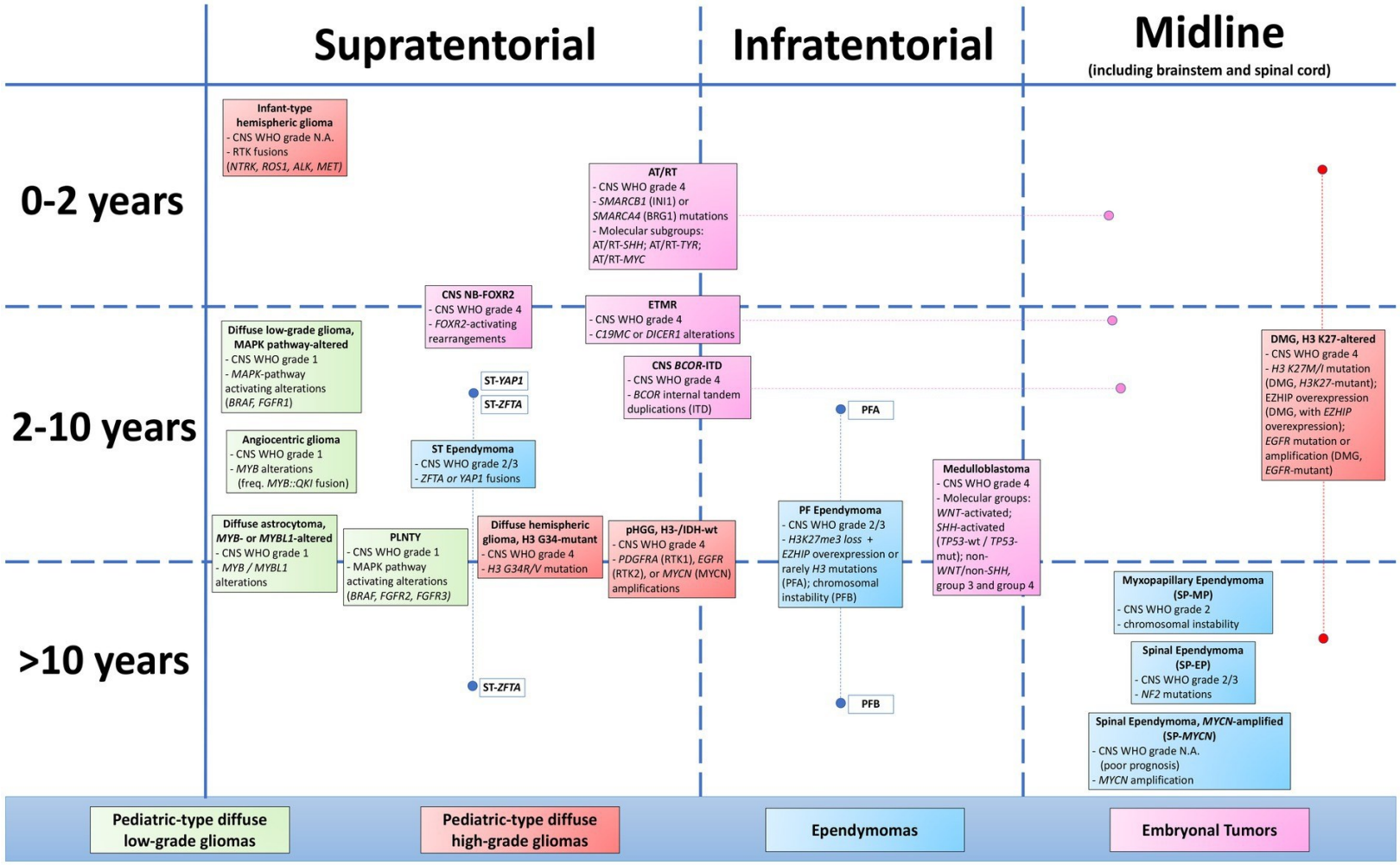


**Figure 13.** Overview of pediatric CNS tumor types, organized by typical age at presentation (left column) and anatomic site (top row). The diagram includes CNS WHO grading and highlights key molecular markers for each tumor entity, grouped as diffuse low-grade gliomas, diffuse high-grade gliomas, ependymomas, and embryonal tumors. *Adapted from (d'Amati et al., 2024), licensed under CC-BY.*

to treatment. For example, pediatric tumors often exhibit a less immunosuppressive microenvironment, which may impact the effectiveness of immunotherapies. The pronounced heterogeneity among pediatric tumor subgroups, the increased sensitivity of some subtypes to therapy, and the heightened risks associated with surgical interventions and potential brain injury in the developing brain all underscore the crucial role of MRI in enabling non-invasive differential diagnosis.

**Correlation between Radiological and Molecular Markers**

Same as in the adult brain tumors, MRI plays a critical role in non-invasive assessment by delineating tumor location, extent, and internal architecture, which can guide differential diagnosis and subsequent management. Distinct MRI features aid in distinguishing between tumor subtypes (AlRayahi *et al.*, 2023):

- Pediatric-type diffuse low-grade gliomas (LGGs): These tumors typically appear as T2-hyperintense, non-enhancing or minimally enhancing lesions with little to no peritumoral edema or mass effect, most commonly involving cortical or subcortical regions. The tumor margins are usually ill-defined, reflecting their infiltrative growth pattern.
- Pediatric-type diffuse high-grade gliomas (HGGs): These lesions generally appear as poorly marginated, T2/FLAIR-hyperintense masses with heterogeneous and often ring-like enhancement, marked peritumoral edema, and regions of necrosis or hemorrhage. Diffusion-weighted imaging frequently demonstrates areas of restricted diffusion.
- Pilocytic astrocytoma: Characteristically seen as well-circumscribed, often cystic lesions with an enhancing mural nodule, predominantly located in the cerebellum, optic pathway, or brainstem. These tumors typically show minimal edema and mass effect relative to their size (Figure 14).
- Glioneuronal tumors (e.g., ganglioglioma, DNET): May display cortical or subcortical involvement with mixed solid and cystic components, variable contrast enhancement, and frequent calcifications. The “bubbly” or multicystic appearance on T2-weighted images, together with minimal edema, is characteristic (Figure 15).
- Embryonal tumors (e.g., medulloblastoma, ATRT): Usually manifest as midline, hypercellular masses with restricted diffusion and heterogeneous enhancement,

reflecting high cellularity and rapid proliferative rate. These tumors often invade the fourth ventricle and demonstrate leptomeningeal dissemination at diagnosis.

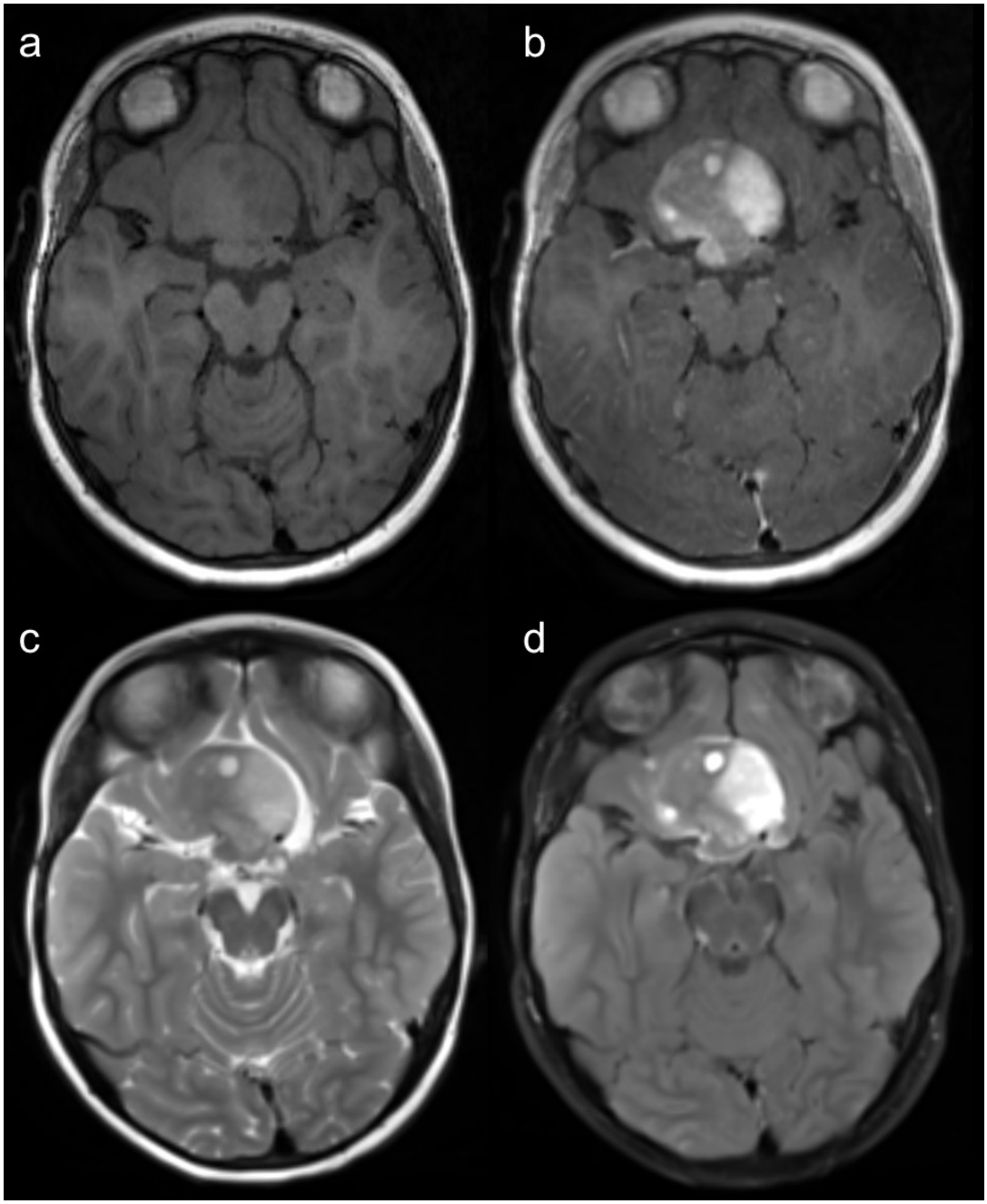


**Figure 14.** Pre- and post-contrast T1-weighted (a, b), T2-weighted (c), and T2-FLAIR (d) MRI scans of a 6-year-old patient with pilocytic astrocytoma harboring the *KIAA1549::BRAF* fusion gene. The images demonstrate heterogeneous contrast enhancement and mixed cystic and solid components. Data acquired at University Hospital Motol.

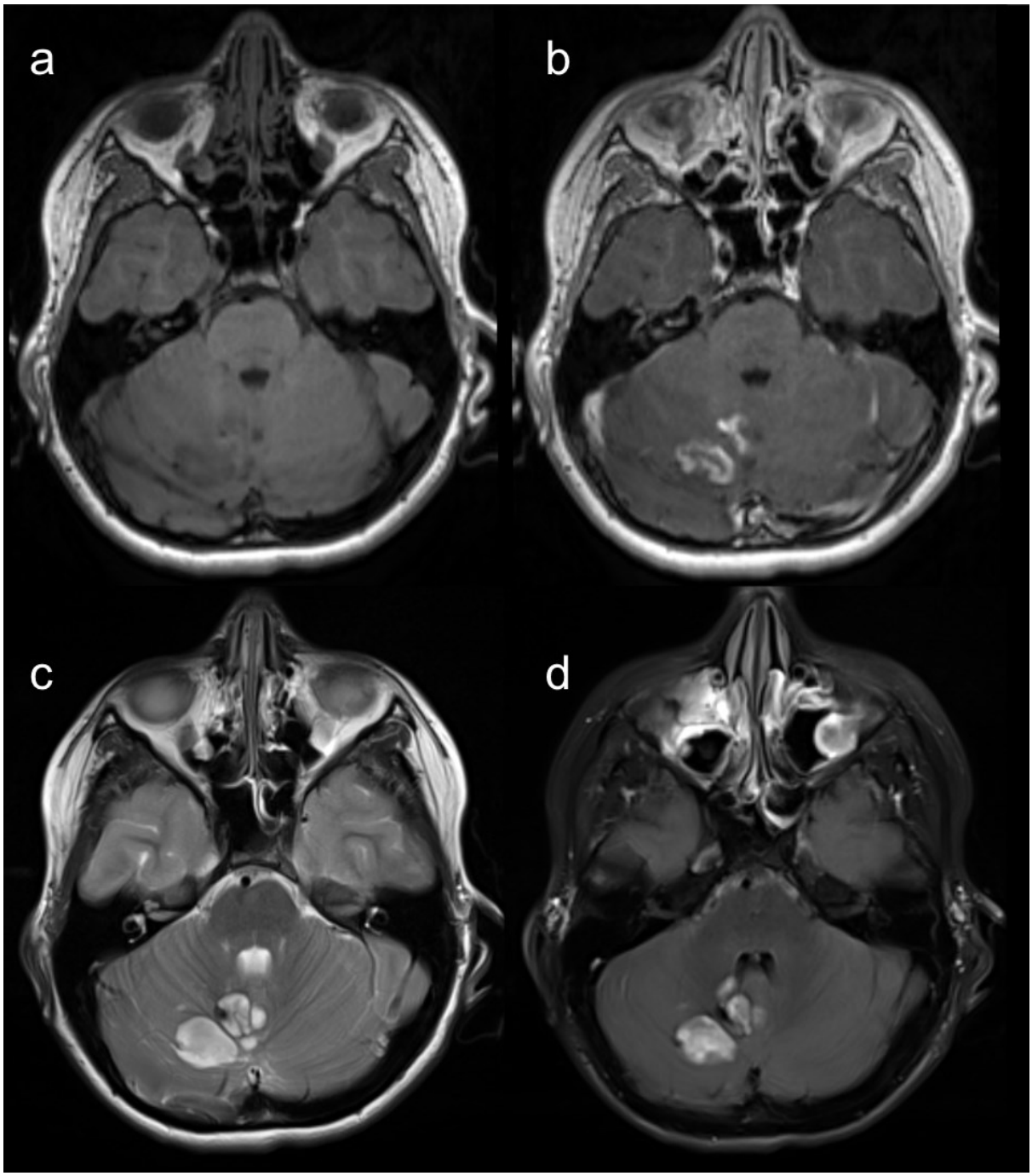


**Figure 15.** Pre- and post-contrast T1-weighted (a, b), T2-weighted (c), and T2-FLAIR (d) MRI scans of a 12-year-old patient with rosette-forming glioneuronal tumor in the cerebellum. The images demonstrate cystic components and heterogenous contrast enhancement. Data acquired at University Hospital Motol.

Standard MRI protocols are indispensable for detecting and anatomically characterizing pediatric brain tumors. However, they often fall short in accurately differentiating tumor types and grades due to overlapping imaging features among various neoplasms. This limitation can impede precise diagnosis and tailored treatment planning, which are crucial

for improving patient outcomes (Limaye and Ahmad, 2024). Similar to adult brain tumors, advanced imaging techniques have emerged as valuable tools to overcome these challenges by providing functional insights into tumor physiology. Among these, the assessment of CBF has shown significant promise. Quantitative measurements of CBF can aid in distinguishing between low-grade and high-grade tumors, as higher-grade neoplasms typically exhibit increased perfusion due to elevated angiogenic activity (Grist *et al.*, 2021). Studies have demonstrated that incorporating CBF measurements into the diagnostic workflow enhances the accuracy of tumor grading. For instance, research indicates that high-grade pediatric brain tumors display significantly higher CBF values compared to low-grade tumors, facilitating more accurate preoperative assessments and treatment strategies (Dangouloff-Ros *et al.*, 2016).

Nevertheless, given the heterogeneity of pediatric brain tumor entities and the importance of diverse diagnostic markers, standardization and clinical validation remain significant challenges. Further studies are needed to validate advanced non-invasive MRI sequences and protocols, particularly in evaluating the added value of markers such as CBF. Importantly, findings derived from adult patient populations cannot be directly extrapolated to pediatric cohorts due to fundamental biological and developmental differences. Thus, the integration of these advanced imaging techniques into routine clinical practice is overdue and necessitates rigorous, pediatric-specific research.

### 1.6.2 Brain Development

Metabolic demands in the developing brain fluctuate significantly during early life, yet the associated hemodynamic changes and their relationship to neurodevelopment remain incompletely characterized in infants and children. Maintaining adequate CBF is crucial for ensuring the delivery of oxygen and nutrients while facilitating the removal of metabolic waste, underscoring its fundamental role in brain physiology (Vernooij *et al.*, 2008).

In early infancy, CBF is relatively low, largely due to limited cardiac output, smaller brain volume, and lower neural activity (Younkin *et al.*, 1988). As the brain grows and the neurovascular architecture matures, CBF rises progressively. This increase closely parallels key neurodevelopmental processes, such as synaptogenesis, myelination, and the expansion of cognitive functions (Carsin-Vu *et al.*, 2018; Paniukov *et al.*, 2020). Notably, during the preschool years, CBF peaks at levels that exceed those observed in adults, coinciding with rapid cognitive and behavioral development. This phase is followed by a gradual decline in

CBF through later childhood and adolescence, reflecting synaptic pruning and the stabilization of neural networks (Satterthwaite *et al.*, 2014b).

The spatial distribution of CBF also undergoes profound changes across childhood. Early in development, higher CBF is observed in primary sensory and motor cortices—areas that mature first and underpin basic sensory and motor functions (Ouyang *et al.*, 2024). The evolution of regional CBF is intimately linked to the maturation of the NVU and the increasing vascular density within the developing brain (Sydnor *et al.*, 2021). This regional evolution of CBF is intimately tied to the maturation of the NVU and rising vascular density. During early development, the NVU undergoes substantial morphological and functional changes, enhancing NVC and ensuring that metabolically active regions receive sufficient perfusion to support synaptic activity and cognitive growth (Bell *et al.*, 2020).

Sex differences further modulate brain development and CBF trajectories throughout childhood and adolescence. Multiple studies have shown that females exhibit higher global and regional CBF than males, particularly during adolescence (Satterthwaite *et al.*, 2014b). These differences are attributed to variations in brain maturation rates, the influence of sex hormones, such as estrogen's impact on neurovascular regulation, and divergent gray matter development between sexes (Gur and Gur, 2016). For example, the onset of puberty triggers a more pronounced increase in CBF in females, a trend that can persist into adulthood and influence both brain structure and function (Satterthwaite et al., 2014).

Despite the central importance of CBF in pediatric neurodevelopment, the field still lacks standardized protocols for quantifying and comparing cerebral perfusion in children. One notable confounding factor is the variable time required for blood to arrive at regions of interest, also known as arterial transit time, which is often not accounted for and remains understudied in pediatric populations (Carsin-Vu *et al.*, 2018). This variability complicates the establishment of normative CBF values and impedes accurate interpretation in both clinical and research settings. Advancing our understanding of age- and sex-specific CBF patterns, while considering factors such as blood arrival time, NVU maturation, and vascular density, is essential for improving the diagnosis and management of cerebrovascular and neurodevelopmental disorders in children.

### 1.6.3 Brain Injury in Preterm Neonates

Preterm birth, defined as delivery before 37 completed weeks of gestation, is the leading cause of neonatal mortality and morbidity worldwide (Ohuma *et al.*, 2023). Survivors of preterm birth frequently experience long-term neurodevelopmental impairments, including cognitive and motor deficits. A key physiological hallmark for these impairments is the reduced cerebral blood flow (CBF), which has been strongly correlated with severe brain injuries such as intraventricular hemorrhage (IVH) and periventricular leukomalacia (PVL) (Fukuda *et al.*, 2008; Hak *et al.*, 2022; Langley, Blake and Coe, 2022), as well as the long-term risks of neurodevelopmental impairments (Davis *et al.*, 2014; Sarda, Sarri and Siffel, 2021). Notably, preterm neonates demonstrate distinct CBF patterns compared to their full-term counterparts (Bouyssi-Kobar *et al.*, 2018), particularly during the first postnatal weeks. This highlights the need for robust, non-invasive techniques capable of accurately monitoring cerebral perfusion during early neonatal care.

Impaired CBF in preterm neonates contributes to the brain's heightened vulnerability to hypoxic-ischemic events, inflammation, and fluctuations in cerebral oxygen delivery, all of which can exacerbate injury to the developing white and gray matter (Benavides *et al.*, 2019; Nourhashemi *et al.*, 2019). Reduced and dysregulated CBF is associated not only with acute injuries such as IVH and PVL, but also with disruptions in cortical and subcortical growth that may underlie subsequent cognitive, motor, and behavioral deficits observed later in childhood (Bouyssi-Kobar *et al.*, 2018). Moreover, the relationship between impaired perfusion and adverse neurodevelopmental outcomes in preterm infants may be influenced by sex, although recent evidence suggests that the connection is not straightforward, with studies yielding inconsistent results regarding whether preterm boys are at greater risk for white matter injury and poorer long-term outcomes (Christians *et al.*, 2023).

Given these associations, there is a clinical need for the development and standardization of protocols for cerebral perfusion assessment in preterm neonates. Current approaches lack harmonization in terms of quantification and interpretation of CBF measurements, leading to variability in reported values and limiting their clinical utility (Leon *et al.*, 2022a). There remains limited understanding of the typical quality and clinical utility of perfusion imaging acquired in preterm infants, particularly when performed without sedation. The added value of perfusion assessment beyond conventional structural imaging has yet to be clearly established. Furthermore, the impact of key confounding factors, including sex, arterial

transit time (which is often prolonged in preterm neonates with impaired cerebral autoregulation), and imaging artifacts such as motion, requires careful consideration in the development of standardized protocols. A comprehensive evaluation of these factors is essential to ensure reliable, reproducible, and clinically meaningful perfusion measurements in this vulnerable population. It is essential that protocols account for sex-specific differences in brain development and CBF patterns to avoid systematic biases in both research and clinical care. The clinical implementation of CBF assessment must also prioritize feasibility in real-world neonatal care settings, ensuring that techniques are safe, reproducible, and suitable for the fragile preterm population.

### 1.6.4 Epilepsy

Epilepsy is a neurological disorder characterized by recurrent, unprovoked seizures resulting from abnormal, excessive, or synchronous neuronal activity in the brain. These aberrant electrical discharges are associated with complex alterations in cerebral physiology, among which disruptions in CBF are particularly significant. In epilepsy, NVC is also frequently disrupted, leading to both acute and chronic changes in regional and global cerebral perfusion.

During the ictal phase, there is a marked increase in metabolic demand due to heightened neuronal firing. This is typically associated with a corresponding increase in regional CBF, a process known as functional hyperemia, intended to meet the increased energy requirements (Leal-Campanario *et al.*, 2017). However, this hyperemic response can be exaggerated, dysregulated, or even insufficient in some circumstances, depending on the brain region, seizure type, and underlying pathology (Becker, 2018). Studies have demonstrated focal hyperperfusion in epileptogenic zones during seizures, followed by postictal hypoperfusion (Dupont *et al.*, 2009; Li *et al.*, 2025). For example, Dupont et al. (Dupont *et al.*, 2009) characterized highly dynamic and spatially heterogeneous perfusion patterns in temporal lobe epilepsy, while Krishnan et al. (Krishnan *et al.*, 2021) directly correlated ictal perfusion changes with intracranial electrophysiology, revealing a close temporal association between abnormal neuronal firing and blood flow alterations.

The postictal period is often characterized by a significant reduction in CBF, which may persist for several minutes to hours. This hypoperfusion is hypothesized to contribute to the transient neurological deficits and cognitive dysfunction observed in the aftermath of seizures, a phenomenon known as the postictal state (Pottkämper *et al.*, 2020). The

mechanisms underlying postictal hypoperfusion may include vasoconstriction, NVC, metabolic exhaustion, and the release of vasoactive substances such as adenosine and. Recent evidence has also implicated seizure-induced neutrophil adhesion in cerebral microvessels as a factor in prolonged postictal hypoperfusion (Lim *et al.*, 2023).

Over time, repeated seizures can induce chronic alterations in CBF, including both hypo- and hyperperfusion in various brain regions. Chronic hypoperfusion may contribute to progressive neuronal injury, gliosis, and the formation of epileptogenic networks. Impaired NVC and CVR may predispose individuals with epilepsy to comorbidities such as cognitive impairment (Xu *et al.*, 2023). Additionally, BBB dysfunction is increasingly recognized as a consequence of both ictal and interictal activity in epilepsy, with evidence of chronic BBB leakage in people with epilepsy, particularly during the interictal period (Jt *et al.*, 2024).

Recent neuroimaging studies have highlighted significant alterations in NVC even in patients with MRI-negative (non-lesional) focal epilepsy. Xu et al. (Xu *et al.*, 2023) demonstrated abnormal NVC in patients without structural lesions, suggesting that functional network disturbances can exist independently of visible anatomical changes. Similarly, Li et al. (Li *et al.*, 2025) used fMRI to show that patients with non-lesional epilepsy exhibit altered neurovascular responses during task performance, supporting the hypothesis that neurovascular dysfunction is a core feature of epilepsy regardless of etiology. Wan et al. (Wan *et al.*, 2025) further differentiated between early-onset and late-onset epilepsy of unknown etiology, reporting distinct NVC patterns in these subgroups, thereby underlining the heterogeneity of cerebral hemodynamics in epilepsy. These findings are reinforced by Krishnan et al., who demonstrated that blood perfusion changes during seizures are tightly linked to intracranial electrical activity, and by Dupont et al., who identified dynamic, regionally specific perfusion shifts during and between seizures. The clinical implications of chronic neurovascular disruption in epilepsy are substantial. Besides contributing to neuronal injury and epileptogenicity, persistent hypoperfusion and repeated episodes of vascular dysfunction are implicated in cognitive deficits and may increase susceptibility to other neurological comorbidities. The interrelationship between BBB breakdown and neurovascular dysfunction further complicates the pathophysiology, as chronic BBB impairment has been shown to promote neuroinflammation and exacerbate network instability.

The pronounced variability in NVC abnormalities and perfusion changes across patients with epilepsy, driven by factors such as seizure type, etiology, onset age, and even the absence of identifiable structural lesions, highlights a pressing need for the development of novel, individualized biomarkers (Kynčl *et al.*, 2023). Advances in neuroimaging and computational modeling have paved the way for precision MRI biomarkers that can capture patient-specific patterns of neurovascular dysfunction and epileptogenicity (R *et al.*, 2025). Markers of regional cerebral perfusion are of particular significance in clinical neuroimaging of epilepsy, given the established associations between CBF, NVC, and BBB integrity. Perfusion-based biomarkers are especially valuable in identifying epileptogenic zones in MR-negative epilepsy, as subtle alterations in regional CBF, driven by ongoing epileptogenic activity, can both reflect and perpetuate BBB disruption, ultimately resulting in chronic perfusion abnormalities.

The diverse manifestations of cerebral perfusion disruptions in brain disorders underscore the importance of regional perfusion-related markers in clinical diagnostics. Distinct pathologies and clinical applications impose varying requirements with respect to acquisition speed, technological accessibility, and considerations of safety and toxicity. The following section will review the principal imaging methods used to obtain perfusion-weighted scans, with particular emphasis on their clinical utility and integration into routine practice.

### 1.7 Imaging Modalities for Cerebral Perfusion

Quantitative assessment of cerebral perfusion has become a cornerstone of modern neuroimaging, providing critical insights into the hemodynamic status of brain tissue in both health and disease. A variety of imaging modalities are available to measure CBF, blood volume, and related parameters, each offering unique advantages and limitations. Computed tomography (CT) perfusion imaging enables rapid evaluation of cerebral hemodynamics and is widely accessible in acute clinical settings, particularly for the assessment of stroke. Ultrasound-based techniques, including transcranial Doppler and contrast-enhanced ultrasound, offer real-time, bedside monitoring of cerebral perfusion with minimal invasiveness. MRI provides a comprehensive and versatile platform for perfusion measurement, leveraging techniques such as phase-contrast (PC) imaging, dynamic susceptibility contrast (DSC), dynamic contrast-enhanced (DCE), and arterial spin labeling (ASL) to quantify CBF, CBV, and CVR. In the following section, the principles,

methodologies, and clinical applications of these imaging approaches will be discussed in detail, with attention to their respective strengths, limitations, and roles in contemporary neuroimaging practice.

### 1.7.1 CT Perfusion

Perfusion CT is an imaging technique that enables quantitative assessment of tissue hemodynamics, such as CBF, CBV, mean transit time (MTT, the average time blood takes to traverse a given brain region), and time-to-peak (TTP, the time from contrast arrival to its maximum concentration), by tracking the temporal distribution of iodinated contrast agents through brain parenchyma during dynamic scanning (García-Figueiras *et al.*, 2013). The underlying principle involves the rapid acquisition of sequential CT images at a fixed anatomical level during and after intravenous administration of a bolus of iodinated contrast medium. Time-attenuation curves generated from the passage of contrast through the cerebral vasculature can then be analyzed using mathematical models to derive perfusion parameters that reflect the vascular status of the tissue.

Perfusion CT has gained widespread clinical application, particularly in the acute setting of ischemic stroke, where it can help distinguish between irreversibly infarcted core tissue and potentially salvageable penumbra (Mayer *et al.*, 2000; Konstas, Wintermark and Lev, 2011). By identifying regions with critically reduced CBF and prolonged MTT, perfusion CT guides acute therapeutic decisions, such as thrombolysis or endovascular thrombectomy, and serves as a prognostic tool for patient outcome after recanalization (Campbell *et al.*, 2011). Beyond stroke, perfusion CT has found utility in oncologic imaging, where it aids in tumor characterization, assessment of angiogenesis, and evaluation of treatment response by quantifying tumor perfusion and vascular permeability (García-Figueiras *et al.*, 2013). The technique has also been explored for evaluating other cerebral pathologies, including trauma and infection, where perfusion abnormalities may provide additional diagnostic information. For example, in TBI, perfusion CT enables early identification of cerebral perfusion abnormalities, such as regions of hypoperfusion or ischemia, that may not be visible in conventional imaging. Early perfusion deficits detected by CT have been shown to correlate with clinical outcomes, providing valuable prognostic information for patient management (Wintermark *et al.*, 2004).

Despite its clinical value, perfusion CT is subject to several important limitations. One major challenge is spatial and temporal resolution: the temporal resolution may be insufficient to capture rapid hemodynamic changes, and the limited brain coverage of conventional CT scanners may result in incomplete assessment of the affected territory (Konstas, Wintermark and Lev, 2011). Radiation exposure is another significant concern, as perfusion CT protocols often involve repeated scans over the same anatomical region, resulting in higher cumulative radiation doses compared to standard CT imaging. Efforts to minimize radiation include optimization of scanning protocols, dose reduction algorithms, and selective coverage of regions of interest. The use of iodinated contrast agents introduces additional risks, particularly in patients with pre-existing renal impairment, thyroid dysfunction, or a history of contrast allergy (Andreucci *et al.*, 2015; Owens, Anton and Attia, 2023). Contrast-induced nephropathy remains a notable adverse effect, and strategies such as pre-procedural hydration and the use of low- or iso-osmolar agents are employed to mitigate this risk. Furthermore, while generally well tolerated, contrast agents may provoke hypersensitivity reactions and, in rare cases, severe anaphylactoid events. These safety considerations underscore the importance of careful patient selection and risk assessment prior to the use of perfusion CT.

In summary, perfusion CT is a valuable tool in the quantitative evaluation of cerebral hemodynamics, with established roles in the diagnosis and management of acute stroke, oncologic disease, and as a rapid decision-making aid in emergency medicine. However, its application is tempered by technical constraints, including limitations in spatial and temporal resolution that can hinder comprehensive assessment of brain perfusion, as well as concerns regarding radiation exposure and the potential toxicity of contrast media. These challenges necessitate judicious use and ongoing refinement of imaging protocols to maximize clinical benefit while minimizing risks.

### 1.7.2 Ultrasound Perfusion

Ultrasound perfusion imaging encompasses a range of techniques that enable real-time, non-invasive assessment of cerebral hemodynamics by tracking blood flow and microvascular perfusion within the brain (Cosgrove and Lassau, 2010). Among these, contrast-enhanced ultrasound utilizes intravenously administered microbubble contrast agents, capitalizing on their unique acoustic properties to dynamically visualize and quantify perfusion parameters such as blood flow velocity and volume across different brain regions. Additionally, Doppler

ultrasound, particularly transcranial Doppler (TCD), measures blood flow velocities in major cerebral arteries, providing valuable surrogate markers for cerebral perfusion, autoregulation, and vascular reactivity (Whitaker *et al.*, 2024). Both approaches are increasingly applied in clinical and research settings to assess global and regional cerebral hemodynamics.

Clinically, ultrasound perfusion imaging is particularly valuable in emergency and critical care settings owing to its portability, rapid acquisition, and absence of ionizing radiation (Eyding *et al.*, 2020). In acute stroke, TCD and contrast-enhanced ultrasound can be used to assess cerebral blood flow velocities, detect arterial occlusions, and monitor recanalization or reperfusion after intervention (Wiesmann and Seidel, 2000). Parameters of interest include mean flow velocity, pulsatility index, and time-to-peak enhancement, which provide insight into vessel patency, collateral flow, and cerebral autoregulation. Rapid, bedside assessment enables prompt identification of patients at risk of further ischemic injury, facilitates monitoring during and after thrombolytic therapy, and can guide decision-making regarding further interventions

For brain tumors, ultrasound perfusion imaging, particularly using microbubble contrast agents, enables the assessment of tumor vascularity, perfusion heterogeneity, and treatment response (Tang *et al.*, 2023). Quantitative parameters such as blood flow, blood volume, and time-to-peak can help distinguish between high- and low-grade tumors, monitor for recurrence, and evaluate the efficacy of antiangiogenic or other targeted therapies. The ability to perform repeated, non-invasive assessments at the bedside or intraoperatively provides valuable information for tailoring individualized treatment regimens and optimizing patient outcomes.

In neonatology care, ultrasound perfusion imaging plays a central role as a safe and practical modality for evaluating cerebral hemodynamics in preterm and term infants (Baranger *et al.*, 2021). The open fontanelles provide an excellent acoustic window, allowing for detailed assessment of cerebral blood flow, perfusion patterns, and detection of abnormalities such as hypoxic-ischemic injury or intraventricular hemorrhage. Parameters such as regional cerebral blood flow, mean flow velocity, and perfusion indices inform early diagnosis, prognosis, and guide neuroprotective strategies when other imaging modalities may be less accessible or feasible.

However, the broader clinical application of ultrasound perfusion imaging remains limited by several factors. Technical challenges include lower spatial and temporal resolution compared to CT and MRI, significant operator dependence, and the restricted acoustic window in adult patients, which can hinder comprehensive assessment of deeper or posterior brain regions (Eyding *et al.*, 2020). Quantitative perfusion and velocity measurements can be affected by patient-specific anatomical factors and the properties of the skull, introducing variability in interpretation. Despite these challenges, continued technological advancements and the integration of both contrast-enhanced and Doppler-based techniques are expanding the role of ultrasound in cerebral perfusion imaging.

### 1.7.3 $^{15}$O-water PET

$^{15}$O-water PET is recognized as the gold standard for the quantitative measurement of CBF and OEF due to its unmatched physiological validity and accuracy (Pantel *et al.*, 2024). The principle of the technique relies on the intravenous administration of [$^{15}$O]$H_2O$, a radioisotopically labeled water molecule in which oxygen is replaced by the positron-emitting radioisotope $^{15}$O (half-life ~2 minutes). After injection, [$^{15}$O]$H_2O$ rapidly diffuses across the capillary endothelium and equilibrates with tissue water, reflecting CBF with high fidelity (Ibaraki *et al.*, 2008). The decay of $^{15}$O produces positrons, which subsequently annihilate with electrons in the tissue, emitting pairs of 511 keV photons in opposite directions. The PET scanner detects these coincident photons, enabling the dynamic mapping of tracer distribution and kinetics across the brain with a temporal resolution that, while higher than many other PET tracers, remains limited compared to some MR-based techniques; achieving adequate signal often requires relatively long or noisy frame durations.

Dynamic acquisition protocols are paired with compartmental modeling of tracer kinetics to derive absolute, quantitative measurements of CBF at the voxel level (Slart *et al.*, 2024). This approach allows for the generation of regional perfusion maps, as well as global CBF estimates, and, when combined with other $^{15}$O-labeled tracers (such as [$^{15}$O]$O_2$), enables the assessment of additional physiological parameters such as $CMRO_2$ and OEF. These capabilities have established $^{15}$O-water PET as the reference standard for cerebral perfusion imaging and validation of emerging imaging modalities.

Clinical applications of $^{15}$O-water PET are broad and impactful. In the setting of cerebrovascular disease, $^{15}$O-water PET is used for quantification of regional and global CBF

in patients with acute and chronic ischemic stroke, transient ischemic attack, and carotid artery disease, though not in an acute setting (Slart *et al.*, 2024). By delineating perfusion deficits and identifying tissue at risk of infarction, PET findings guide therapeutic decisions such as revascularization and can predict patient outcomes. In neuro-oncology, $^{15}$O-water PET provides maps of tumor perfusion, which are useful for tumor grading, therapy planning, and the assessment of antiangiogenic treatment response (Johnson *et al.*, 2020). Its ability to distinguish viable tumor from necrosis or post-treatment changes can significantly impact patient management.

$^{15}$O-water PET also plays a promising role in the evaluation of neurodegenerative diseases (such as Alzheimer's disease and other dementias), where regional perfusion changes may serve as early biomarkers of disease and help differentiate between pathologies (Anderson *et al.*, 2007). Furthermore, in epilepsy, PET-based perfusion mapping supports the localization of epileptogenic foci during pre-surgical evaluation, improving the likelihood of successful intervention (von Oertzen *et al.*, 2023). The precision and quantification of $^{15}$O-water PET make it invaluable in both clinical research and for validating new MRI or CT perfusion techniques (Slart *et al.*, 2024).

Despite these strengths, $^{15}$O-water PET is limited by substantial practical constraints. The extremely short half-life of $^{15}$O requires an on-site cyclotron for tracer production, resulting in high operational costs and restricted accessibility to specialized centers with the necessary infrastructure (Alavi *et al.*, 2021). The technique also exposes patients to ionizing radiation, which must be carefully weighed, especially in pediatric or vulnerable populations. Crucially, absolute quantification of cerebral blood flow with [$^{15}$O]-water PET requires calibration using repeated arterial blood sampling – a logistically complex, labor-intensive, and often uncomfortable procedure for patients and clinical staff alike. This is a major barrier to routine use, and as a result, many studies forego arterial sampling and instead report only relative perfusion measures. Additionally, dynamic imaging protocols and quantitative data analysis are complex and resource-intensive, further limiting widespread adoption in routine clinical practice. Nevertheless, $^{15}$O-water PET remains the gold standard for absolute perfusion quantification and continues to play a pivotal role in advanced neuroimaging and clinical research.

### 1.7.4 MRI Perfusion Techniques: PC, DSC, and DCE

MRI offers a diverse array of techniques for assessing cerebral perfusion, including phase-contrast MRI, dynamic contrast-enhanced (DCE) MRI, dynamic susceptibility contrast (DSC) MRI, and arterial spin labeling (ASL). Compared to CT and ultrasound, MRI provides significantly superior soft-tissue resolution, making it particularly well-suited for neuroimaging applications. In addition, MRI-based approaches do not involve ionizing radiation and include both contrast-agent-based and non-invasive methods for quantifying CBF and other perfusion-related parameters. However, widespread use of MRI in perfusion imaging is limited by factors such as higher costs, reduced accessibility, and longer acquisition times than CT.

#### 1.7.3.1 Phase-Contrast Imaging

Phase-contrast (PC) MRI is a non-invasive technique that exploits the phase shifts induced by moving spins in a magnetic field to directly measure the velocity and direction of blood and CSF flow (Wymer *et al.*, 2020). By applying velocity-encoding gradients, PC MRI enables quantitative assessment of flow dynamics within major cerebral arteries and veins, as well as CSF spaces, providing high spatial and temporal resolution data without the need for exogenous contrast agents. The principal parameters derived from PC MRI include volumetric CBF, peak and mean flow velocities, and pulsatility indices; in the context of CSF imaging, parameters such as flow amplitude and net flow are routinely quantified.

In the clinical environment, PC MRI is used to evaluate global and regional (per vascular territory) CBF in various populations, including healthy adults, neonates, and infants (Varela *et al.*, 2012). In neonates and infants, PC-MRI provides a non-invasive and reproducible method to quantify whole-brain CBF, a critical marker for brain development and injury in this vulnerable population, where exposure to ionizing radiation or contrast agents must be minimized (Liu *et al.*, 2019). The high reliability and direct quantification offered by PC-MRI make it a reference standard for neonatal and pediatric perfusion studies, as well as for research on normal cerebral maturation and neurodevelopmental disorders.

In adults, PC MRI is applied to the assessment of cerebrovascular diseases such as carotid artery stenosis, occlusive disease, and arteriovenous malformations, where it provides direct measurements of flow in major arteries and veins, supporting the diagnosis and evaluation of disease severity (Wymer *et al.*, 2020). For example, in patients with carotid stenosis, PC-

MRI can non-invasively quantify reduced flow through the internal carotid arteries and evaluate compensatory changes in collateral vessels. This information is valuable for clinical decision-making regarding revascularization procedures or medical management. Furthermore, PC-MRI has been shown to correlate well with $^{15}$O-water PET measurements of CBF, highlighting its accuracy and potential as a safer, more accessible alternative for global flow quantification (Vestergaard *et al.*, 2017).

Despite these strengths, phase-contrast MRI has several notable limitations. The technique can be sensitive to artifacts caused by patient motion, arrhythmias, or improper velocity encoding, which may compromise measurement accuracy. Importantly, PC MRI provides quantitative flow measurements in large cerebral arteries and veins, enabling accurate estimation of global or territory-specific blood flow, but it cannot generate high-resolution, tissue-specific perfusion maps of regional CBF within the brain parenchyma. As a result, PC MRI may not capture regional perfusion heterogeneity with the same sensitivity as other techniques. Acquisition and post-processing can also be time-consuming, and the need for careful sequence optimization and user expertise may limit widespread adoption in routine clinical practice (Peng *et al.*, 2015). Nevertheless, PC MRI remains a robust and reproducible method for quantifying blood and CSF flow, offering important advantages for research and selected clinical applications where direct, non-invasive measurement of vascular flow is required.

#### 1.7.3.2 Dynamic susceptibility contrast and dynamic contrast-enhanced

DSC and DCE MRI are widely used perfusion techniques that utilize the passage of gadolinium-based contrast agents through the cerebral vasculature to extract quantitative and semi-quantitative metrics of tissue hemodynamics. Each technique is optimized for the assessment of distinct aspects of tissue perfusion and vascular permeability, and both are increasingly central in neuro-oncologic and neurovascular imaging.

DSC is based on monitoring the signal decrease during the first pass of a paramagnetic contrast bolus, using either gradient-echo (GE) or spin-echo (SE) echo-planar imaging sequences to capture dynamic signal changes as the contrast agent traverses the microvasculature (Schmainda *et al.*, 2019). GE-DSC is primarily sensitive to both macrovascular and microvascular contributions, allowing robust assessment of total CBV and CBF in most clinical contexts. In contrast, SE-DSC is more selectively sensitive to

microvascular (capillary-level) perfusion, as the spin-echo pulse refocuses dephasing due to larger vessels, thus offering improved specificity for microvascular blood volume and flow, which may be particularly advantageous in tumor imaging or studies of the BBB permeability.

The core of DSC quantification is the analysis of the signal intensity-time curve, which is converted to a concentration-time curve based on the relationship between T2* (GE-DSC) or T2 (SE-DSC) signal loss and the concentration of the contrast agent (Figure 16). This relationship is expressed as follows:

$$\Delta R_2(t) = -\frac{1}{TE}\ln\left(\frac{S(t)}{S_0}\right),$$

Where $\Delta R^2(t)$ is the change in the effective transverse relaxation rate at time $t$, $TE$ is the echo time, $S(t)$ is the signal intensity at time $t$, and $S_0$ is the pre-contrast signal intensity.

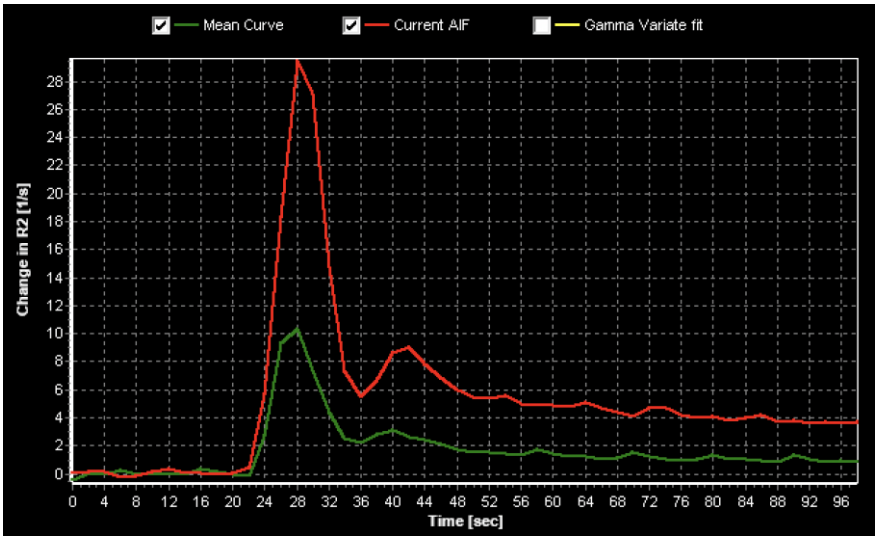


**Figure 16.** Example of slice-averaged effective transverse relaxation rate ($\Delta R_2$) and corresponding arterial input function (AIF) from data acquired at University Hospital Motol. Curve visualization was performed using NordicIce software. The first 22 timepoints represent the pre-bolus baseline, followed by a pronounced increase corresponding to the first pass of the contrast agent and a subsequent, lower-amplitude peak reflecting the second pass (recirculation) of the contrast agent.

The resulting relaxation rate changes are linearly related to the local concentration of the contrast agent, forming the basis for quantitative calculation of the following perfusion-related parameters:

- CBV: Calculated by integrating the area under the tissue concentration-time curve. For absolute CBV quantification, the curve is normalized using the arterial input function (AIF); for relative CBV (rCBV), normalization is typically performed with respect to a reference tissue, such as normal-appearing white matter (Calamante, 2010; Schmainda *et al.*, 2018).
- CBF: Estimated by deconvolution of the tissue concentration-time curve with an AIF, representing the arrival of contrast to the brain. The peak of the resulting tissue residue function corresponds to CBF.
- Mean Transit Time (MTT): Determined as the ratio of CBV to CBF (MTT = CBV/CBF), reflecting the average time blood spends traversing the microvasculature in the region of interest.

For clinical use, rCBV is often reported by comparing tumor values to those in contralateral healthy tissue. rCBV is a promising imaging biomarker in glioma grading, prediction of treatment response, and differentiation of TP from PsP (Boxerman *et al.*, 2017; Liang *et al.*, 2018). The accuracy of these parameters, however, is highly dependent on precise AIF selection, correct baseline determination, and standardized post-processing protocols (Schmainda *et al.*, 2018). One notable technical challenge is contrast agent leakage in the context of a disrupted BBB, common in neurooncological applications, which introduces T1 and T2* effects, distorting the quantification of perfusion parameters. Leakage correction methods, including pre-bolus baseline correction and mathematical modeling of simultaneous T1 and T2* effects or dual-echo sequences, are now routinely recommended to ensure reliable quantification. Despite the demonstrated clinical impact of DSC-derived parameters, their values are highly sensitive to scanner hardware, sequence settings, contrast injection protocols, AIF determination, and post-processing algorithms, which has historically hindered standardization. However, recent multi-center initiatives, such as the adoption of low-flip angle, single-dose DSC protocols, have promoted harmonization across sites, greatly improving reproducibility and enhancing the utility of the technique in clinical trials (Schmainda *et al.*, 2019).

DCE contrast agent kinetics using dynamic T1-weighted imaging to monitor the accumulation and washout of the agent within the extravascular extracellular space (EES) (Li, Huang and Holmes, 2024). During image acquisition, a series of T1-weighted images are rapidly obtained before, during, and after intravenous administration of a gadolinium-

based contrast agent. The resulting SI-time curve for each voxel reflects the dynamic changes in tissue contrast concentration over time (Figure 17).

To enable quantitative analysis in DCE, the measured signal intensity SI-time curve must be accurately converted into a tissue contrast agent concentration-time curve. This conversion is governed by the Bloch equations and is highly sensitive to the tissue's longitudinal relaxation time (T1) both before and after contrast administration. Pre-contrast T1 measurement is essential because the relationship between SI and contrast agent concentration is nonlinear and depends on the baseline (native) T1 value of the tissue. Ideally, a quantitative T1 (qT1) map is acquired prior to the dynamic study, often using a variable flip angle (VFA) approach, which samples several flip angles to robustly estimate T1 on a voxel-wise basis. This step is crucial for accurate quantification, as fixed or assumed T1 values can lead to significant errors in derived concentration curves and pharmacokinetic parameters (Kim, 2018). Baseline calibration scans, such as B1 mapping, are sometimes performed to correct for spatial variations in the transmit radiofrequency (RF) field (B1 inhomogeneity), which can otherwise bias flip angle calibration and therefore T1 estimation. B1 mapping improves the accuracy of both qT1 mapping and the conversion of SI to contrast agent concentration, especially at higher field strengths or with larger fields of view.

The first critical step in quantitative DCE is the conversion of measured SI-time curves into quantitative contrast agent concentration-time curves. In a typical DCE acquisition, signal intensities are acquired at multiple time points using a spoiled gradient echo (SPGR) sequence, which is inherently sensitive to changes in tissue longitudinal relaxation time ($T_1$) as gadolinium-based contrast agent enters and clears from the tissue. However, SI(t) is a nonlinear function of $T_1(t)$ and is also dependent on the acquisition parameters: repetition time (TR), flip angle (α), and local B1 field inhomogeneity. The relationship between SI(t) and $T_1(t)$ in an SPGR sequence can be described by the following equation:

$$SI(t) = M_0 \cdot \frac{1-\exp\left(-\frac{TR}{T_1(t)}\right)}{1-\cos(\alpha)\exp\left(-\frac{TR}{T_1(t)}\right)} \cdot \sin(\alpha),$$

where *SI(t)* is the signal intensity at time *t*, $M_0$ is the equilibrium magnetization, *TR* is the repetition time, $\alpha$ is the flip angle (ideally corrected for B1 inhomogeneity), and $T_1(t)$ is the longitudinal relaxation time at time *t.* Once $T_1(t)$ is determined for each time point, the local tissue gadolinium concentration can be calculated by:

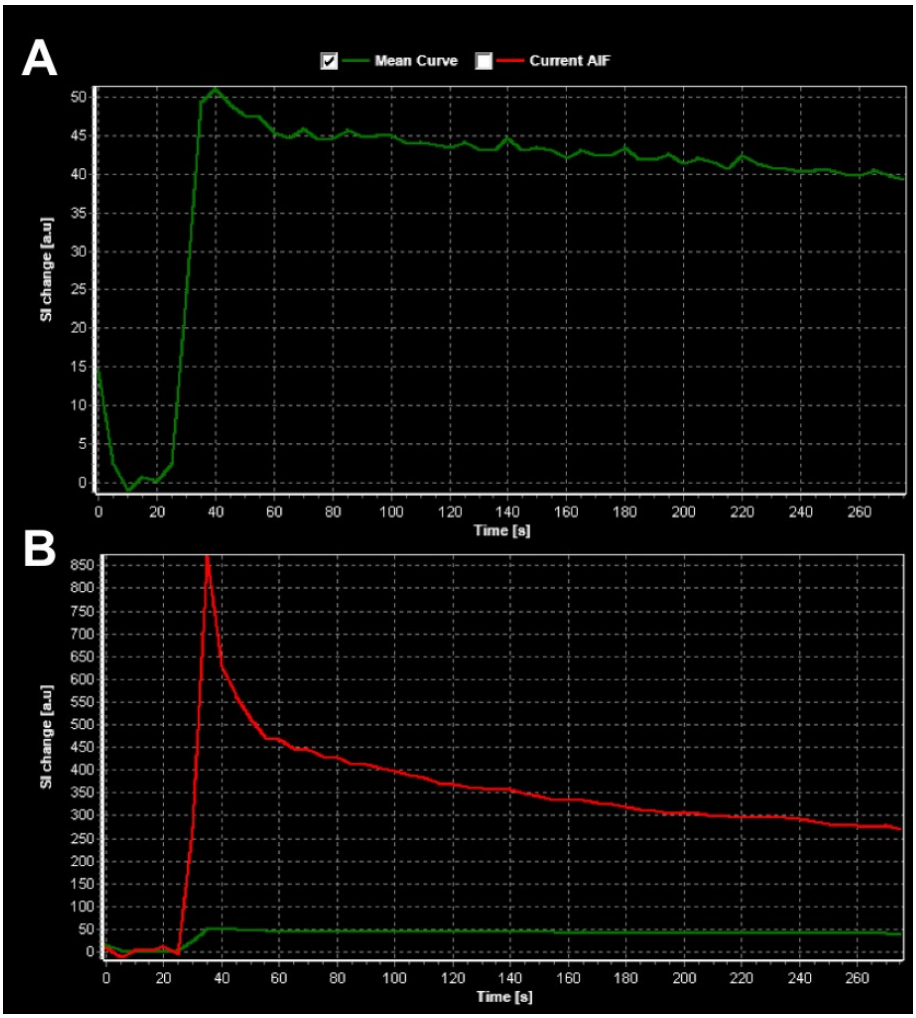


**Figure 17.** SI-time curves for mean slice DCE signal (A) and AIF reference voxels (B). The initial acquisition scans are affected by increased noise due to tissue magnetization not yet reaching steady state. Removal of these early time points is recommended to improve the stability and accuracy of subsequent quantitative measurements (Manning *et al.*, 2021).

$$Gd(t) = \frac{1}{r_1}\left(\frac{1}{T_1(t)} - \frac{1}{T_{1,0}}\right),$$

where *Gd(t)* is the gadolinium concentration at time *t*, $r_1$ is the longitudinal relaxivity of the contrast agent, $T_1(t)$ is the calculated longitudinal relaxation time at time *t*, and $T_{1,0}$ is the pre-contrast $T_1$. This quantitative conversion from *SI(t)* to *Gd(t)* is foundational for pharmacokinetic modeling. The resulting tissue and AIF concentration-time curves are then fitted with compartmental pharmacokinetic models, most commonly the Tofts or extended Tofts models, to extract key physiological parameters (Tofts *et al.*, 1999). The standard Tofts model assumes a two-compartment system (plasma and EES), and describes the tissue concentration as:

$$C_t(t) = K^{trans} \int_0^t C_p(\tau)\, e^{-k_{ep}(t-\tau)} d\tau,$$

Where $C_t(t)$ is the tissue concentration at time *t*, $K^{trans}$ is the volume transfer constant from plasma to EES, $C_p(t)$ is the plasma concentration from the AIF, and $k_{ep}=K^{trans}/v_e$ is the efflux rate constant from EES to plasma. The extended Tofts model incorporates an explicit plasma volume fraction $v_p$, improving accuracy in highly vascularized tissues:

$$C_t(t) = v_p C_t(t) + K^{trans} \int_0^t C_p(\tau)\, e^{-k_{ep}(t-\tau)} d\tau.$$

The choice of model depends on the tissue of interest and the expected physiological properties. These modeling steps yield quantitative parameters such as:

- $K^{trans}$ – volume transfer constant, reflects the rate at which contrast agent moves from the plasma to the EES, integrating both capillary permeability and blood flow. $K^{trans}$ is particularly sensitive to BBB integrity and neovascularization in tumors (O'Connor *et al.*, 2017).
- $v_e$ – EES volume fraction, represents the proportion of tissue volume occupied by the EES and is indicative of the structural characteristics of the tissue.
- $v_p$ – plasma volume fraction, estimates the fractional blood plasma volume in the tissue of interest.
- $k_{ep}$ – efflux rate constant, represents the rate of contrast agent efflux from the EES back to the plasma.

Accurate DCE quantification requires careful estimation of the AIF, high temporal resolution, and robust model fitting (Keil *et al.*, 2017b). Variability in these steps, together with differences in sequence parameters, has contributed to significant inter-study variability (Kim, 2018). Recent guidelines from the Quantitative Imaging Biomarkers Alliance (QIBA) and other collaborative groups have provided consensus recommendations to standardize acquisition and analysis, facilitating the translation of DCE metrics into routine practice (Shukla-Dave *et al.*, 2019).

Both DSC and DCE techniques are most established in the assessment of brain tumors, especially high-grade gliomas. DSC-derived rCBV has proven value for differentiating tumor progression from treatment-related changes such as pseudoprogression and radiation necrosis, correlating with histological markers of angiogenesis and tumor grade (Boxerman

*et al.*, 2017; Liang *et al.*, 2018; R. Fu *et al.*, 2022). DCE-MRI parameters such as $K^{trans}$ and $v_p$ provide complementary information regarding tumor permeability and vascular structure, aiding in tumor grading, delineation, and therapy monitoring. Combined DSC/DCE imaging can further improve diagnostic accuracy in glioblastoma and guide patient-specific management (Artzi *et al.*, 2015).

DSC-MRI is also central in acute stroke imaging, where CBF, CBV, and MTT maps help identify ischemic core and penumbra, informing reperfusion therapy decisions (Wang *et al.*, 2012). DCE-MRI, meanwhile, is increasingly used to assess BBB disruption and to monitor the effects of therapy in both vascular and neuroinflammatory disorders (Villringer *et al.*, 2017).

**Considerations about Contrast Agent Toxicity**

The use of gadolinium-based contrast agents (GBCAs) in MRI has been transformative for clinical neuroimaging, yet mounting evidence has prompted an ongoing re-evaluation of their safety, economic burden, and environmental footprint. While GBCAs provide critical diagnostic value, especially for lesion detection, tumor characterization, and disease monitoring, their use is not without risks, costs, or broader consequences (Scarciglia *et al.*, 2025).

Gadolinium, in its free ionic form, is inherently toxic. In GBCAs, it is chelated to minimize risk, but studies have shown that even in patients with normal renal function, repeated GBCA administration can lead to gadolinium retention and deposition, particularly in neural tissues such as the dentate nucleus and globus pallidus (Vergauwen *et al.*, 2018b; Coimbra *et al.*, 2024). Gadolinium retention is of special concern in populations requiring frequent or high-dose contrast imaging, such as those with MS, hereditary tumor syndromes or high-risk cancer screening protocols. Potential clinical consequences of gadolinium deposition remain a topic of active investigation, with rare reports of adverse neurological symptoms or systemic effects.

Patients with impaired renal function are at particular risk, as reduced excretion may lead to higher levels of circulating and deposited gadolinium, and, in rare cases, nephrogenic systemic fibrosis – a debilitating and potentially fatal condition (Blomqvist *et al.*, 2022). Consequently, the American Society of Neuroradiology and other expert groups recommend heightened caution or alternative imaging strategies in patients with chronic kidney disease,

as well as in pregnancy, children, healthy volunteers, and longitudinal study cohorts, where long-term effects are poorly understood and the risk-benefit ratio may not favor contrast use (Ouyang and Bao, 2025a; Welker *et al.*, 2025).

GBCAs represent a significant economic cost for healthcare systems due to the price of the agents themselves and the need for repeat or enhanced surveillance imaging. Additionally, the environmental impact of gadolinium is increasingly recognized. Anthropogenic gadolinium from medical imaging has been detected in wastewater, rivers, groundwater, and even marine environments, reflecting the incomplete removal of GBCAs during water treatment and the global scale of MRI utilization (Brünjes and Hofmann, 2020; Chaban *et al.*, 2024). Concerns have been raised regarding the persistence and mobility of gadolinium in the environment, with unknown long-term ecological and human health effects.

Despite these challenges, GBCAs continue to deliver substantial clinical value, especially where contrast enhancement provides unique diagnostic, prognostic, or therapeutic information not otherwise attainable (Scarciglia *et al.*, 2025). In neuro-oncology, for example, contrast enhancement is critical for tumor delineation, treatment response evaluation, and surgical or radiation planning. The decision to use GBCAs should thus be carefully individualized, weighing the added diagnostic value against patient risk factors, study objectives, and the cumulative exposure over time. Current consensus statements emphasize a more judicious approach to GBCA use, with particular caution in vulnerable populations and settings where alternatives (such as non-contrast protocols or advanced imaging techniques) are available. Technological innovations, such as artificial intelligence-based imaging and improved MRI sequences, are being actively developed to reduce or eliminate the need for GBCAs in clinical practice (Mallio *et al.*, 2023). As evidence and regulatory guidance evolve, the benefit-risk balance of GBCA use will continue to be closely monitored by the neuroradiological and environmental health communities.

In light of the growing concerns regarding GBCA toxicity, economic burden, and environmental impact, non-invasive perfusion imaging techniques have gained increasing clinical relevance. ASL MRI stands out as a particularly attractive alternative, as it enables voxel-wise, quantitative measurement of CBF without the need for exogenous contrast agents. ASL uses magnetically labeled arterial blood water as an endogenous tracer, allowing for repeated assessments and safer application in sensitive populations such as children, patients with renal insufficiency, pregnant individuals, and healthy volunteers.

While DSC and DCE MRI remain important tools in perfusion imaging, ASL's non-invasive nature and capacity for absolute quantification have led to its growing adoption in both clinical and research neuroimaging. The following section will explore the principles, acquisition strategies, and clinical applications of ASL in greater detail.

## 1.8 ASL MRI

### 1.8.1 Principle

ASL is an MRI technique that enables noninvasive, quantitative measurement of tissue perfusion, most commonly applied to the brain. Unlike conventional perfusion imaging that requires injection of exogenous contrast agents, ASL exploits magnetically labeled endogenous water in arterial blood as a diffusible tracer, allowing for the absolute quantification of CBF in physiological units (ml/100g/min).

The fundamental principle of ASL is to generate a "control" or "label" by inverting the longitudinal magnetization of inflowing arterial blood water protons proximal to the imaging region, using radiofrequency (RF) pulses, typically applied over a defined period known as the labeling duration (LD) (Clement *et al.*, 2022) (Figure 18). The labeled arterial blood flows into the imaging volume, exchanges with tissue water, and thus decreases the MRI signal in voxel in proportion to local perfusion. After a time period called post-labeling delay (PLD), an image of the region of interest is acquired. A pair of images with (label) and without (control) is acquired and the difference reflects the amount of labeled blood delivered to tissue, thus providing a direct and quantifiable measure of tissue perfusion.

### 1.8.2 Technical Development and Historical Perspective

The development of ASL arose from the drive to achieve noninvasive, quantitative measurement of CBF using MRI (Bammer, 2016). Early functional imaging methods had relied primarily on indirect measures of neural activity, such as changes in BOLD, which are only indirectly coupled to perfusion. The idea of labeling endogenous water protons in arterial blood as a diffusible tracer, analogous to radioactive tracers in PET, represented a transformative step toward direct CBF quantification.

The concept of using magnetically labeled arterial water as a tracer for perfusion MRI originated from studies of tissue perfusion kinetics, particularly those employing $^{15}$O-water PET. The adaptation of this tracer-based paradigm to MRI required the development

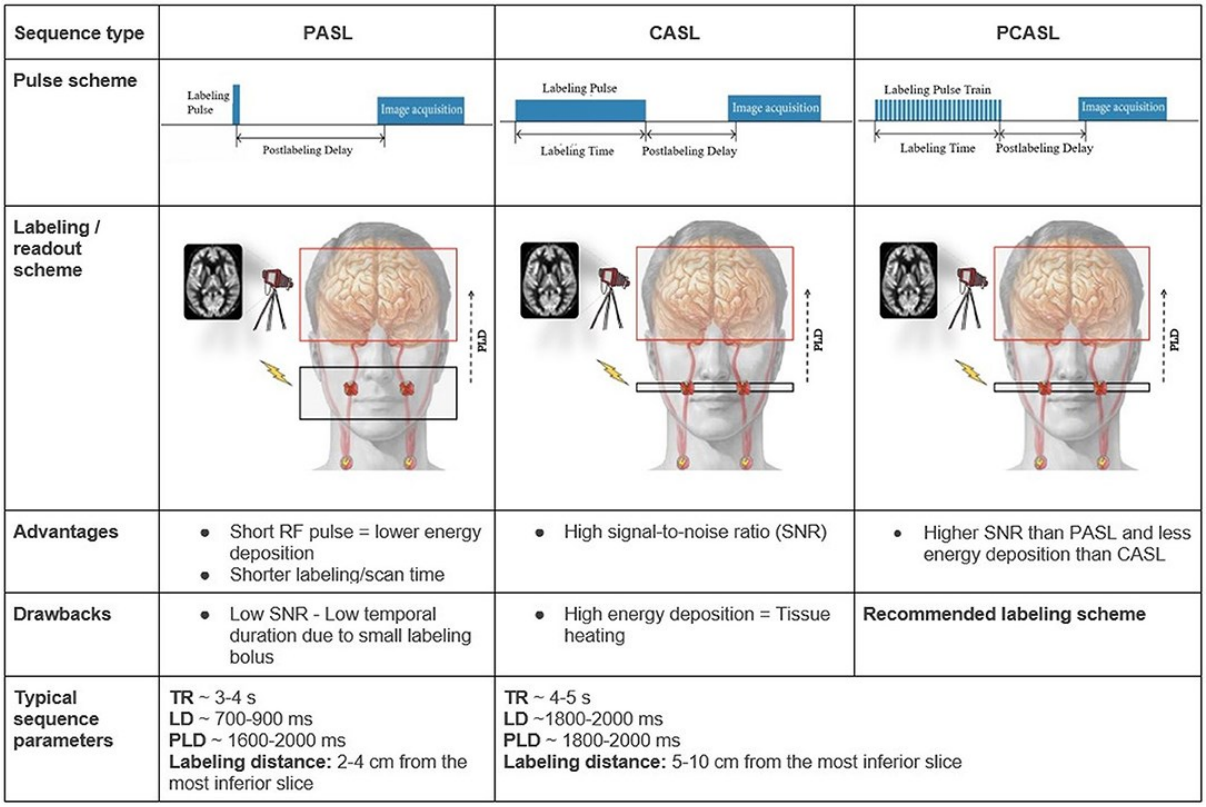


**Figure 18**. Basic overview of ASL implementations. Red circles marked with "H" represent water protons within arterial blood. When a radiofrequency pulse is applied at the labeling plane, these protons passing through the internal carotid arteries are magnetically labeled, as indicated by the red X symbols. *Adapted from* (Clement *et al.*, 2022)*, licensed under CC-BY-4.0.*

of methods to invert or "label" arterial spins and then measure their effect on tissue signal downstream (Buxton *et al.*, 1998). Early work in the 1980s and 1990s explored the use of nuclear magnetic resonance (NMR) techniques to measure cerebral metabolism and blood flow in animal models (Detre, Williams and Koretsky, 1990). The foundational demonstration of ASL perfusion MRI was achieved in rat brain at 4.7T, using a pulsed strategy to magnetically label a slab of arterial water and measure its wash-in to tissue (Williams *et al.*, 1992). These experiments provided proof of principle that endogenous water could serve as an effective tracer for CBF measurement by MRI.

The technical realization of ASL for human applications required several key advances:

- Labeling Strategies. Initial ASL methods used continuous or pulsed labeling of arterial spins upstream from the imaging plane. The approach was soon adapted to pulsed arterial spin labeling (PASL), in which a thick bolus of arterial blood is

inverted by a short radiofrequency pulse, allowing for improved practical implementation. Further refinements addressed issues such as magnetization transfer effects and transit artifacts, which could confound quantification (Wong, Buxton and Frank, 1998).

- Readout and Quantification. Early ASL experiments used single-slice readout, but technical progress enabled multi-slice and, later, volumetric imaging (Detre *et al.*, 1998). Quantitative models for CBF estimation were developed based on the kinetic behavior of labeled water, and methods were introduced to suppress static tissue signal (background suppression), improving sensitivity (Buxton *et al.*, 2004; Golay, Petersen and Hui, 2005).
- Translation to human MRI. The first successful implementation of ASL in humans occurred in the mid-1990s, initially at 1.5T using pulsed labeling strategies (Roberts *et al.*, 1994).

Over time, methodological improvements addressed key limitations and enabled broader adoption of ASL MRI. The availability of higher field strength MRI systems provided enhanced signal-to-noise ratio (SNR) and increased $T_1$ relaxation times, extending the lifetime of the label. The use of head coil transmission and array receivers allowed for larger labeling volumes and improved detection sensitivity. More recently, the development of pseudo-continuous ASL (PCASL) has emerged as the recommended standard, offering robust labeling efficiency and compatibility with clinical workflows (Wu *et al.*, 2007; Alsop *et al.*, 2015a). ASL MRI is now available on most modern MRI platforms and is recognized as one of the few MRI methods capable of absolute quantification of CBF. The historical evolution of ASL, from its early animal experiments to its clinical translation and ongoing technical innovations, highlights the technique's unique ability to bridge basic neuroscience and clinical diagnostics.

### 1.8.3 Labeling and Readout Approaches

The success of ASL MRI relies heavily on the technical details of both how arterial blood water is magnetically labeled and how the resulting perfusion-weighted signal is captured and quantified. Over the past three decades, substantial innovations in labeling and readout strategies have enabled ASL to become a robust and widely applicable technique for quantitative CBF measurement in both research and clinical settings.

### Labeling Approaches

**Pulsed ASL (PASL)** methods label arterial blood by applying a short, spatially selective RF pulse to invert or saturate a slab of blood upstream from the imaging region. After a defined PLD, the labeled blood flows into the tissue and is imaged. PASL sequences such as EPISTAR, FAIR, and PICORE are straightforward to implement and have historically been favored for their flexibility and low RF power deposition. However, PASL produces a less well-defined bolus compared to continuous labeling methods (Petersen *et al.*, 2006).

**Continuous ASL (CASL)** applies a long, low-power RF pulse with a concurrent gradient, continuously inverting inflowing arterial spins at a labeling plane. This creates a steady, well-defined bolus of labeled blood, enabling high labeling efficiency. Despite its theoretical advantages, traditional CASL can cause significant magnetization transfer (MT) effects and high specific absorption rate (SAR), particularly at higher field strengths (Grade *et al.*, 2015).

**Pseudo-Continuous ASL (PCASL)** was introduced to harness the efficiency of CASL while minimizing SAR and MT effects. It uses a rapid train of discrete, low flip angle RF pulses combined with gradients to approximate continuous labeling (Dai *et al.*, 2008). PCASL offers high labeling efficiency, robust reproducibility, and lower RF power, making it the recommended standard for clinical and research applications in contemporary consensus statements (Alsop *et al.*, 2015a).

### Readout Approaches

Single-shot gradient-echo or spin-echo EPI (echo-planar imaging) is a common 2D readout for ASL due to its speed and simplicity. EPI enables rapid multi-slice or whole-brain acquisition, but is susceptible to geometric distortion and variations in PLD across slices, which may necessitate additional post-processing corrections. 3D acquisition techniques such as 3D GRASE (gradient and spin echo), 3D turbo spin echo (TSE), and 3D stack-of-spirals imaging have become increasingly preferred, particularly for PCASL. These approaches improve SNR, minimize slice profile imperfections, facilitate robust background suppression, and ensure a uniform PLD across all slices.

**Hadamard-encoded ASL** and **Look-Locker readout schemes** have emerged as powerful innovations for efficient multi-timepoint acquisition, allowing the simultaneous estimation of CBF and ATT.

- Hadamard-encoded (time-encoded) ASL divides the labeling duration into multiple sub-boli, each encoded using Hadamard matrices, enabling the efficient separation of signal contributions from different time points within a single scan (Wells *et al.*, 2010). This approach greatly increases temporal resolution and SNR efficiency compared to sequentially acquiring each PLD separately.
- Look-Locker readout methods use a rapid series of images following a single labeling pulse, capturing the passage of labeled blood at multiple effective PLDs within the same repetition, which is particularly helpful for mapping ATT and improving quantification accuracy (Petr *et al.*, 2013).

These advanced approaches are increasingly incorporated into research and consensus protocols to enable accurate multi-parametric perfusion mapping, especially in populations with heterogeneous vascular dynamics.

Subtracting the label from the control image isolates the small perfusion-weighted signal – typically only 1-2% of the much larger static tissue signal. Due to the inherently low SNR of the perfusion signal, increasing the number of control-label repetitions is essential to improve SNR and reduce the impact of noise. In addition, acquisition of a separate proton-density ($M_0$) image is necessary for absolute quantification of CBF, as it provides a reference for normalizing the ASL signal. This step accounts for differences in coil sensitivity, scanner gain, and tissue water content, enabling accurate and reproducible CBF estimation. The resulting signal difference, together with the $M_0$ image, is then converted to quantitative CBF maps using mathematical models that account for labeling efficiency, BBB exchange, $T_1$ relaxation, and sequence timing parameters.

Recent expert guidelines strongly recommend the use of PCASL labeling in combination with background-suppressed 3D readout (such as 3D GRASE or 3D TSE) for both clinical and research imaging, citing superior SNR, reproducibility, and quantification accuracy (Alsop *et al.*, 2015a; Hernandez-Garcia *et al.*, 2022b; Lindner *et al.*, 2023). Multi-delay approaches are increasingly advocated to improve robustness across patient populations and vascular conditions (Woods *et al.*, 2024).

### 1.8.4 Quantification and Modeling

One of the key strengths of ASL MRI is its ability to provide quantitative maps of CBF, expressed in ml/100g/min, through the use of well-established kinetic models (Buxton *et al.*,

1998; Alsop *et al.*, 2015a). Quantification in ASL involves both careful signal acquisition and mathematical modeling to interpret the small difference in signal arising from the passage of labeled blood water from arteries into tissue.

The most widely used framework for CBF quantification in ASL is the single-compartment kinetic model (Alsop *et al.*, 2015a). In this model, the perfusion-weighted signal, obtained by subtracting the label and control images, is related to the amount of labeled blood delivered to brain tissue during a specific time window. Key parameters influencing the ASL-CBF signal include:

- Labeling efficiency (α): the fraction of arterial spins successfully labeled by the RF pulse, which varies by technique (e.g., ~0.85 for PCASL).
- Longitudinal relaxation times ($T_1$): both blood and tissue $T_1$ relaxation impact the decay of the ASL signal and thus the quantification.
- LD (τ) and PLD: define the timing of the labeling and the period during which labeled spins travel to the imaging region.
- ATT: The time required for labeled blood to reach the tissue of interest.

The recommended equation for CBF quantification is then:

$$CBF = \frac{6000 \cdot \lambda \cdot \Delta M \cdot e^{\frac{PLD}{T_{1b}}}}{2 \cdot \alpha \cdot M_0 \cdot T_{1b} \cdot (1 - e^{\frac{-\tau}{T_{1b}}})}, \text{ where}$$

- $\Delta M$ is the measured difference between label and control images (PW signal);
- $\lambda$ is the blood–brain partition coefficient for water (typically 0.9 mL/g);
- $M_0$ is the equilibrium magnetization of tissue (obtained from a separate proton-density image);
- $T_{1b}$ is the longitudinal relaxation time of blood;
- $\alpha$ is labeling efficiency;
- $\tau$ is the LD;
- The factor 6000 ensures conversion to conventional CBF units.

While the single-compartment model suffices for most standard applications, more complex models, such as two-compartment or multi-phase models, are available to address specific situations – such as prolonged or variable arterial transit times, or when distinguishing

between intravascular and tissue compartments is needed. Multi-timepoint (multi-PLD) ASL acquisitions, in which data are collected at several post-labeling delays, allow for joint estimation of both CBF and arterial transit time, improving quantification in populations with vascular pathology or advanced age (Woods *et al.*, 2024).

### 1.8.5 Current Limitations

Despite significant advances and expanding clinical adoption, ASL remains subject to several technical limitations and artifacts that impact its routine use and interpretation. Awareness of these challenges is essential for both research and clinical applications.

1. Longer Acquisition Times. ASL typically requires longer acquisition times than DSC or DCE. The inherently low SNR necessitates multiple control-label repetitions to achieve acceptable image quality . As a result, total scan times are frequently 4–6 minutes, compared to the rapid single-bolus acquisitions of DSC/DCE (Lindner *et al.*, 2023).

2. Lower Spatial Resolution. Due to the trade-off between SNR and spatial coverage, ASL acquisitions often have lower spatial resolution (typically 3–5 mm isotropic) than DSC or DCE, which can limit the detection of small lesions or subtle regional perfusion abnormalities (Telischak, Detre and Zaharchuk, 2015). This may particularly affect the assessment of small cortical infarcts or focal pathologies.

3. Susceptibility to Motion and Physiological Noise. Because ASL relies on the subtraction of label and control images, it is inherently sensitive to patient motion and physiological fluctuations between acquisitions (Clement *et al.*, 2018). Even small movements can introduce substantial subtraction artifacts, leading to false positive or negative perfusion signals. Children, older adults, and uncooperative patients are particularly prone to motion-related artifacts (Amukotuwa, Yu and Zaharchuk, 2016).

4. Sequence and Vendor Variability. There remains substantial variability in ASL implementations among MRI vendors, including differences in labeling schemes, background suppression, readout techniques, and default quantification models. Such heterogeneity leads to significant variation in CBF values and image quality across sites and scanners, complicating multi-center studies and longitudinal follow-up.

5. Need for Harmonization and Standardization. Recognizing the impact of sequence heterogeneity, the international ASL community has initiated major harmonization efforts. Consensus guidelines, technical recommendations, and collaborative multi-center initiatives are helping to drive convergence toward standardized protocols and post-processing pipelines (Dijsselhof *et al.*, 2025). Nevertheless, further harmonization is needed to ensure consistency of ASL-derived biomarkers in clinical trials and practice.

Despite these limitations, ongoing technical development, international standardization, and open-source software initiatives are rapidly improving the robustness and reproducibility of ASL (Alsop *et al.*, 2015a; Mutsaerts *et al.*, 2020; Fan *et al.*, 2024). The formation of expert working groups, such as the ISMRM Perfusion Study Group and the Open Science Initiative for Perfusion Imaging (OSIPI), continues to drive protocol harmonization, validation, and education (Bell *et al.*, 2024). As a result, ASL is becoming an increasingly mature and reliable technique, poised for wider adoption in both clinical and research environments.

### 1.8.6 Clinical Validation

The clinical validation of arterial spin labeling (ASL) MRI has been a major focus of research, with numerous studies demonstrating its reliability, reproducibility, and diagnostic value across a wide range of neurological conditions. Early and contemporary studies have shown that ASL-CBF values correlate well with those obtained from gold-standard techniques, particularly $^{15}$O-water PET, which is considered the reference method for quantitative perfusion imaging (Puig *et al.*, 2020; Zhao *et al.*, 2021). Similarly, comparative studies have found good agreement between ASL and DSC-MRI, particularly in major vascular territories and global perfusion deficits, though differences in spatial resolution and sensitivity to transit times can lead to regional discrepancies (Zhang *et al.*, 2015). In cerebrovascular disease and stroke, ASL reliably identifies hypoperfused tissue, perfusion-diffusion mismatch, and collateral flow patterns that are highly concordant with DSC findings (Wang *et al.*, 2013; Zhang *et al.*, 2015).

ASL has been shown effective in a wide variety of clinical contexts. In cerebrovascular disease**,** ASL reliably detects perfusion deficits in both acute and chronic ischemic stroke, moyamoya disease, and other steno-occlusive disorders, providing valuable qualitative and quantitative assessments (Lindner *et al.*, 2023). In the domain of neurodegeneration, large multi-center studies, such as those conducted by the European DEMENTIA consortium,

have demonstrated that ASL can detect regional hypoperfusion patterns characteristic of Alzheimer's disease, frontotemporal dementia, and other neurodegenerative conditions, with diagnostic accuracy comparable to FDG-PET (Chao *et al.*, 2010; Anazodo *et al.*, 2018). ASL also shows sensitivity to both hyperperfusion and hypoperfusion in primary and secondary brain tumors, where it can aid in tumor grading, treatment planning, and distinguishing neoplastic from non-neoplastic lesions, with results similar to those of DSC-MRI (Bayraktar *et al.*, 2024). Furthermore, in epilepsy, ASL is capable of localizing regions of altered perfusion in both ictal and interictal states, supporting its growing role in the noninvasive evaluation of epilepsy and various inflammatory disorders (Storti *et al.*, 2014). Ongoing efforts continue to expand ASL indications, standardize protocols, and educate the broader neuroimaging community.

### 1.8.7 Emerging Applications and Innovations

ASL imaging is a dynamic and rapidly evolving field, with recent technical advances greatly expanding its range of applications and physiological insights (Hernandez-Garcia *et al.*, 2022b). Innovative ASL methods now allow the assessment not only of CBF, but also of BBB permeability, microvascular function, and brain clearance pathways, as well as offering new options for functional brain mapping.

A particularly promising innovation is the use of multi-echo (multi-TE) ASL protocols to noninvasively assess water permeability across the BBB. By acquiring ASL images at multiple echo times, it is possible to disentangle the contributions of intravascular and extravascular compartments, enabling the quantification of BBB water exchange rates (Mahroo *et al.*, 2021b; Ohene *et al.*, 2021). This approach has proven useful in detecting subtle BBB breakdown in aging and neurodegenerative conditions, and in mapping spatial heterogeneity of BBB function in the healthy and diseased brain. Ongoing developments are refining these methods for clinical and research use, showing robust measurement reliability and sensitivity to physiological changes.

Diffusion-prepared ASL further enhances sensitivity to microvascular structure and water exchange by combining ASL labeling with diffusion-weighted preparation modules. This hybrid approach can provide complementary information on BBB integrity, capillary density, and water exchange dynamics, beyond what is possible with standard ASL or diffusion MRI alone (Shao *et al.*, 2022; Morgan *et al.*, 2024). Recent studies have

demonstrated that diffusion-prepared ASL, especially when combined with multi-TE protocols, offers reliable and age-dependent quantification of BBB permeability and microvascular properties.

Another area of rapid progress is velocity-selective ASL (VS-ASL), which labels arterial spins based on their velocity rather than spatial location (Qin *et al.*, 2022b). This technique is particularly advantageous in patients with delayed or variable arterial transit times, as it directly targets the inflowing blood regardless of anatomical variability. VS-ASL has shown promise for robust CBF quantification in cerebrovascular disease, improved sensitivity in watershed regions, and reduced sensitivity to transit delays (Xu *et al.*, 2025). Multi-timepoint and hybrid VS-ASL methods, such as the recently described MULTIVERSE approach, further increase robustness in clinical and research settings.

ASL is also finding new roles in fMRI, where its quantitative CBF measurements complement traditional BOLD-based approaches. Multi-echo and multiband simultaneous ASL/BOLD acquisitions allow the joint mapping of perfusion, blood oxygenation, and molecular-enriched connectivity, providing richer insights into NVC, neurotransmitter systems, and brain network dynamics (Dipasquale *et al.*, 2023). This capability supports more comprehensive studies of cognition, psychiatric disorders, and pharmacological interventions.

Emerging work has demonstrated that ASL can be harnessed to study the glymphatic system. Recent pilot studies using 3D ASL have identified delayed clearance of labeled water protons following head trauma, supporting the use of ASL as a noninvasive biomarker of glymphatic dysfunction (Joseph *et al.*, 2024; Kamagata *et al.*, 2024). Ongoing developments are adapting ASL protocols to monitor glymphatic activity in aging, neurodegeneration, and other neurological conditions.

While these emerging innovations underscore the remarkable versatility and future promise of ASL, they also highlight the increasing complexity of available protocols, analytical approaches, and clinical applications. In light of ongoing technical developments and expanding indications, the challenge of standardizing ASL for routine clinical use has become more urgent than ever. The following section will therefore focus on the central hypothesis and aims of this thesis, with a primary emphasis on establishing robust, harmonized ASL protocols suitable for diverse clinical contexts.

## 1.9 Hypotheses and Aims of the Thesis

The overarching aim of this thesis is to systematically evaluate the clinical feasibility and added value of ASL across a range of clinical scenarios, with a particular emphasis on the standardization of ASL protocols for routine clinical practice. By investigating both adult and pediatric populations, this work aims to address ASL image quality, perfusion-related parameters, and the comparative utility of ASL versus DSC imaging, ultimately underscoring the translational benefits for patient care.

The first research direction focuses on adult gliomas, a well-established application for perfusion imaging. The study is guided by the following specific hypotheses:

- **H1:** Perfusion markers derived from both ASL and DSC MRI are correlated with molecular tumor markers.
- **H2:** ASL and DSC demonstrate comparable predictive performance for glioma characterization.
- **H3:** Perfusion characteristics in the peritumoral region provide additional diagnostic information regarding tumor infiltration and perilesional hemodynamic changes.

The overarching aim of this study is to evaluate the diagnostic potential of ASL in adult gliomas. This is addressed through the following specific objectives:

1. **Comparing** perfusion parameters derived from ASL and DSC MRI using histogram-based analysis of the intratumoral region, to determine the concordance and diagnostic value of each method.
2. **Assessing** perfusion characteristics in peritumoral tissue, with the goal of capturing tumor infiltration and perilesional hemodynamic alterations that may have diagnostic or prognostic significance.
3. **Exploring** correlations between imaging biomarkers and molecular tumor markers, in accordance with the updated 2021 WHO glioma classification, to evaluate the ability of non-invasive perfusion imaging to reflect underlying tumor biology.

This approach aims to clarify the diagnostic value of non-contrast ASL relative to standard DSC, while also providing new insights into the molecular underpinnings of brain tumor pathophysiology.

The subsequent focus shifts to the analysis of normative cerebral hemodynamics in children and neonates. The pediatric ASL study is a retrospective analysis conducted in MR-negative children spanning a broad age range (0–18 years) and is guided by the following specific hypotheses:

- **H4:** Within-session single-delay and multi-delay ASL acquisitions yield distinct GM and WM CBF values.
- **H5:** Significant variations in ATT and CBF are observed across age groups in both WM and GM, reflecting the ongoing maturation of the brain and cerebral vasculature.
- **H6:** Changes in CBF within WM and GM are correlated with brain volumetric changes during pediatric development.

The aims of this study are to:

- **Characterize** normative cerebral perfusion patterns in normal-appearing children by quantifying CBF and ATT using both single-delay and multi-delay ASL acquisitions.
- **Identify** age-related factors that may confound variations in CBF and ATT in children.
- **Contribute** to the ongoing efforts to advance the standardization of ASL protocols for clinical use in pediatric neuroimaging.

The neonatal ASL study focuses on a particularly vulnerable cohort of preterm neonates, for whom cerebral perfusion is a critical parameter for clinical monitoring. This population poses additional challenges due to potentially limited scan quality, as MRI is typically performed without sedation, increasing the risk of significant motion artifacts. The study is guided by the following specific hypotheses:

- **H7:** The quality of ASL scans in preterm neonates is sufficient for reliable clinical interpretation.
- **H8:** ASL-derived CBF values differ between single-delay and multi-delay acquisitions within the same imaging session.
- **H9:** CBF and ATT change throughout gestational and postnatal development in preterm neonates.

The aims of this study are to:

1. **Advance** the understanding of the potential clinical value of ASL for assessing cerebral perfusion in preterm neonates.
2. **Analyze** potential confounding factors affecting cerebral hemodynamics in this vulnerable population.
3. **Support** the standardization of ASL protocols for neonatal imaging and contribute to the establishment of normative reference values.

Building on insights gained from these retrospective analyses, we have initiated prospective research studies at University Hospital Motol. Among these, the PediTuMRI study investigates the utility of ASL in the pre-surgical and follow-up evaluation of pediatric brain tumors. This prospective design allows for the systematic assessment of ASL's clinical applicability in real-world pediatric neuro-oncology.

The pilot study is guided by the following hypotheses:

- **H10:** ASL provides clinically valuable, non-invasive perfusion markers that aid in differentiating pediatric brain tumor entities.
- **H11:** Quantification of ASL-based permeability measurements in the peritumoral region yields additional diagnostic markers that are comparable in value to DCE MRI parameters.

The aims of this study are to:

1. **Evaluate** the diagnostic performance of ASL for the differentiation of pediatric brain tumor subtypes in both pre-surgical and post-treatment settings.
2. **Assess** the efficacy of non-contrast MRI techniques in the diagnostic evaluation and clinical management of pediatric neuro-oncological patients.
3. **Investigate** methodological and quantification challenges related to ASL perfusion and permeability measurements, with the goal of optimizing protocols for pediatric neuro-oncology.

Together, these research directions are designed to address key hypotheses related to the diagnostic and prognostic utility of ASL across diverse clinical populations, and to provide robust evidence supporting the standardization of ASL protocols for routine clinical implementation. The following Methods section details the study designs, imaging protocols, and analytic approaches employed to rigorously test these hypotheses.

# 2. Methods

## 2.1 Adult Glioma ASL Study

### 2.1.1 Population

One hundred and six patients with diffuse glioma (54.2 ± 15.2 years, 66 male/40 female), admitted to Oslo University Hospital, 2011–2021, were retrospectively included in the study. All participants provided written informed consent and the local ethics committee approved the study in accordance with the Declaration of Helsinki. The criteria for inclusion were as follows: age ≥ 18 years, confirmed diagnosis of diffuse glioma based on histological examination, no prior cancer treatment, and available imaging data from a presurgical MRI protocol with DSC and ASL acquired within a single session.

All tumors were tested immunohistochemically for the presence or absence of *IDH1* p.R132H mutant protein and retention or loss of nuclear *ATRX* expression. In cases with immunohistochemical loss of *ATRX* expression, the tumors were tested further with *IDH*-sequencing. In a subset of gliomas additional information on the *TERT*-promoter mutation status, *IDH1/2*-mutation status, 1p/19q-codeletion status, and *MGMT* status was available. All tumors with confirmed *IDH* mutation at position p.132 or p.172 were tested for 1p/19q-codeletion status. Gliomas with *IDH1* or *IDH2* mutation and combined 1p/19q-codeletion have been diagnosed as oligodendrogliomas according to the current CNS WHO classification (2021), whereas those without the presence of complete 1p/19q-codeletion were diagnosed as astrocytoma, *IDH*-mutant. Glioblastomas have been diagnosed based on the absence of an *IDH* mutation with either the presence of a hotspot *TERT*-promoter mutation and/or histomorphological features such as vascular proliferation or necrosis. When only *IDH1* p.R132H negativity and retention of *ATRX* expression were available, the diagnosis of glioblastoma was given in cases where vascular proliferation or necrosis was present and where the age of the patient at initial diagnosis was above 54 years. All other cases were diagnosed as diffuse astrocytomas not otherwise specified (NOS).

### 2.1.2 Image Acquisition

Imaging data were acquired on 3 different 3 tesla GE (GE Healthcare) MRI platforms: SIGNA™ HDxt in 2011–2016 ($n = 44$), Discovery™ MR750 in 2016–2019 ($n = 52$), SIGNA™ Premier in 2019-2021 ($n = 18$). Details about the MRI system, protocol, and

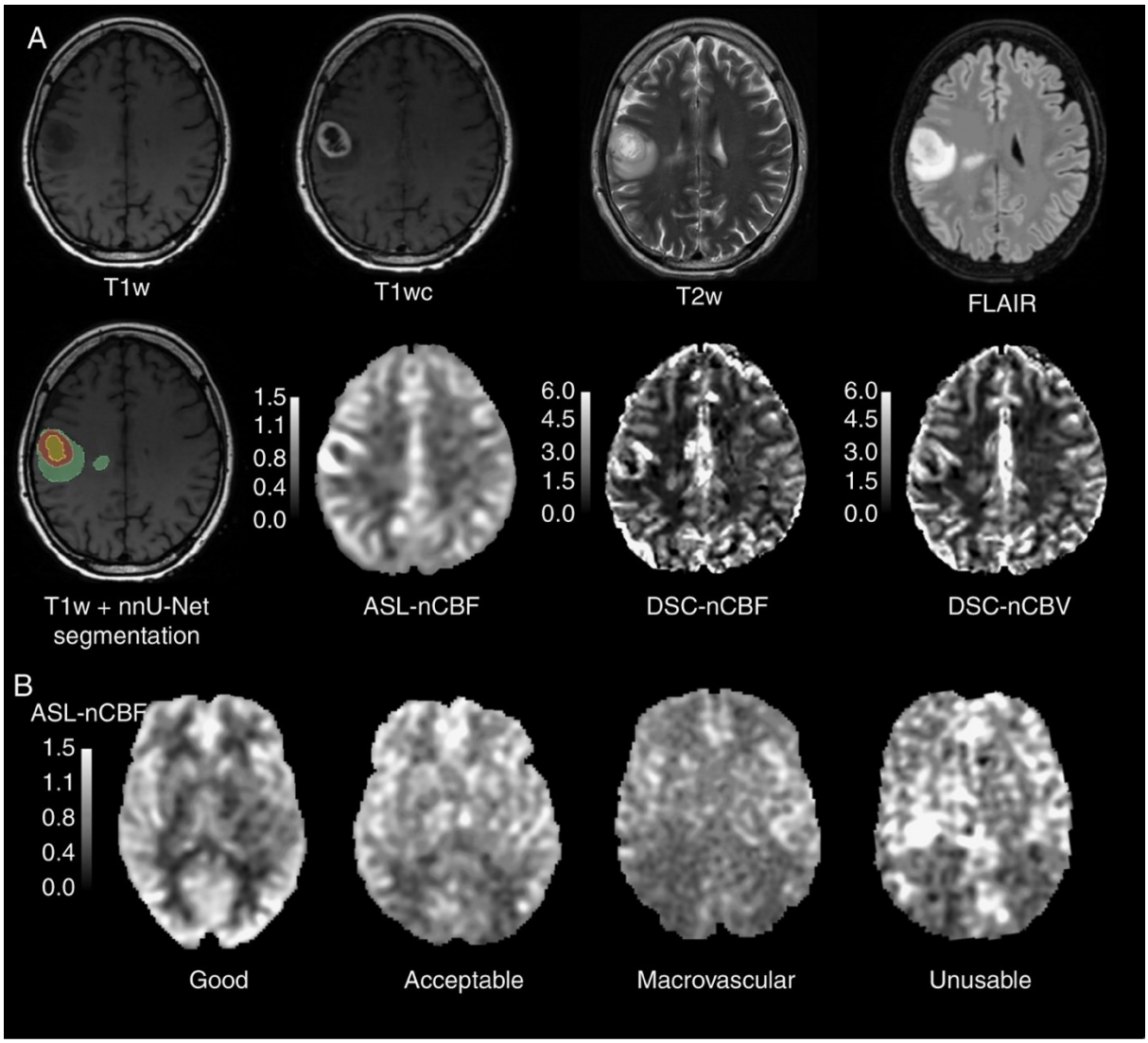


**Figure 19**. (A) 50-year-old female with glioblastoma, grade 4 (*IDH*-wildtype, 1p/19q noncodeleted, *MGMT*-methylated, and p*TERT*-mutant). Structural segmentation resulting from the nnU-Net model shows necrosis (inner rim, yellow), enhancing tumor (middle rim, red), and edema (outer rim, green). (B) Examples of the ASL quality control assessment. Good—the perfusion signal is well-distributed in gray matter, and there are no visible motion or labeling artifacts; acceptable – minor motion or macrovascular artifacts resulting in regional loss of signal, but the acceptable overall quality, especially around the tumors; macrovascular – prominent macrovascular-signal artifact caused by delayed arterial arrival time; unusable –significant signal distortions, motion artifacts, failed labeling, or too high arrival time.

**Table 1**: MRI acquisition parameters across different MRI platforms. HNS - head neck spine, T1w T1-weighted, T2w - T2-weighted, FSPGR - fast spoiled gradient echo, SE - spin echo, IR-FSE - inversion recovery fast spin echo, FLAIR - fluid-attenuated inversion recovery, TR - repetition time, TE - echo time, ETL - echo train length, FA - flip angle, iso - isotropic, recon - reconstructed, res - resolution, BS - Background suppression, gadolinium-based contrast agent - gadoterate meglumine; Dotarem®, Guerbet, Aulnay-sous-Bois, France, and Clariscan®, GE Healthcare, USA.

| | GE Signa HDxt<br>8-channel HNS coil | GE Discovery MR750<br>32-channel HC | GE Signa Premier<br>48-channel AIR™ HC |
|---|---|---|---|
| **Structural sequence parameters** | | | |
| T1w<br>(interpolation,<br>TR/TE/ETL ms, FA°) | 1x1x1.5 $mm^3$ 3D FSPGR<br>(-/6.6/2.3/- ms, 20°) | 1x1x1 $mm^3$ 3D FSPGR (BRAVO)<br>(-/8.2/3.2/- ms, 12°) | 1x1x1 $mm^3$ 3D FSE (CUBE)<br>(zip 2/512 zip, 552/14/22 ms, 12°) |
| T1w post contrast (T1wc)<br>(TR/TE/ETL ms, FA°) | 1x1.071x5 $mm^3$ 2D SE<br>(660/14/- ms, 90°) | 1x1x1 $mm^3$ 3D FSPGR (BRAVO)<br>(-/8.2/3.2/- ms, 12°) | 1x1x1 $mm^3$ 3D FSE (CUBE)<br>(zip 2/512 zip, 552/14/22 ms, 12°) |
| T2w<br>(TR/TE/ETL ms, FA°) | 0.5x0.5x5 (gap 1) $mm^3$ 2D FSE (Propeller)<br>(~6000/~84/28 ms, 90°) | 0.5x0.5x4 (gap 1) $mm^3$ 2D FSE (Propeller)<br>(~6500/~120/26 ms, 142°) | 0.5x0.5 x 3 (gap 0.3) $mm^3$ 2D FSE (Propeller)<br>(9968/118/26 ms, 142°) |
| T2w FLAIR<br>(TR/TI/TE/ETL ms, FA°) | 0.625x0.5x5 (gap 1) $mm^3$ 2D IR-FS<br>(9500/2250/120/0 ms, 90°) | 0.5*0.5*0.5 $mm^3$ 3D IR-FSE (CUBE)<br>(8000/2068/91/160 ms, 90°)<br><br>After Sept. 2018:<br>1x1x1.2 $mm^3$ 3D IR-FSE (T2 prep, CUBE)<br>(7000/1919/90/160 ms, 90°) | 1x1x1.2 $mm^3$ 3D IR-FSE (T2 prep, CUBE, HyperSense)<br>(7000/1942/110/160 ms, 90°) |
| **ASL parameters** | | | |
| Readout | 3D PCASL FSE stack-of-spiral | | |
| Acquired resolution | 512 points/8 arms (recon 128 matrix, FOV 24 cm) | | |
| Reconstructed voxel | 3.79 × 3.79 × 3.0 $mm^3$ | | |
| TR/TE ms, FA° | 4836 / 10.4 ms, 155° | 5025 / 11.1 ms, 111° | 5122 / 55.9 ms, 111° |
| Scan duration (min:s) | 4:37 | 4:48 | 4:48 |
| LD/PLD (ms) | 1450 / 1525 | 1450 / 2025 | 1450 / 2025 |
| Other | NEX 3, M0 scan included, 4 pulses BS, labeling plane positioned at 2 cm distance from the base of cerebellum approximately at the C2/C3 vertebrae | | |
| **DSC parameters (consistent across platforms)** | | | |
| Readout | Gradient-recalled EPI (2D GRE-EPI) | | |
| Acquired resolution | Matrix 128 × 128, FOV 24 cm, slice thickness 5.0 (gap 1) mm, 26 slices | | |
| TR/TE ms, FA° | 1875/45 ms, 60° | | |
| Contrast administration | A dose of 0.1 mmol/kg gadolinium-based contrast agent was given with a power injector at a rate of 5 ml/s with a subsequent 15 ml saline flush | | |
| Dynamic parameters | Temporal resolution 2.0 s, total scan time 84 s, 53 phases, baseline duration 7 s | | |

acquisition parameters of structural pre and postcontrast T1-weighted (T1w and T1wc, respectively), T2-weighted (T2w), and T2-weighted fluid-attenuated inversion recovery (FLAIR), ASL, and DSC are in Table 1, while representative scans from a single subject are displayed in Figure 19 (A).

### 2.1.3 Image Processing

Structural scans (T1w, T1wc, T2w, and FLAIR) were coregistered using normalized mutual information objective function and resliced to the native T1w space. The respective voxel sizes of T1w were 1.0 × 1.0 × 1.5 $mm^3$ (Signa HDxt), 1 mm isotropic (Discovery MR750) and 0.5 mm (interpolated from 1 mm isotropic, on Signa Premier) in Statistical Parametric Mapping 12 (SPM12, version 7765) (Friston *et al.*, 2011).

Tumor and edema were segmented using the nnU-Net segmentation model (Pemberton *et al.*, 2023) on the structural scans (T1w, T1wc, T2w, and FLAIR). The model-generated structural segmentations were validated and adjusted by a board-certified neuroradiologist with 25 years of experience (Andres Server).

ASL images were processed with ExploreASL version 1.10.0 (Mutsaerts *et al.*, 2020) using a simplified single-compartment single-postlabeling delay model. Brain tissue segmentation using CAT12 (v12.7) (Gaser, 2009) involved masking tumor and necrotic areas (already segmented by the nnU-Net) to mitigate their impact on the normal-appearing tissue segmentation. ASL-CBF maps were normalized to mean CBF in the contralateral hemisphere normal-appearing gray matter (GM) (ASL-nCBF). DSC data were processed in nordicICE (v4.1.2; NordicNeuroLab) with the use of whole-volume AIF, motion and leakage correction, and normalization to automatically detected normal-appearing white matter (WM) (Bjørnerud and Emblem, 2010), yielding normalized CBV and CBF (DSC-nCBV and DSC-nCBF, respectively). Finally, DSC-nCBF, DSC-nCBV, and ASL-nCBF maps were coregistered and resliced to the structural scans' space and voxel sizes.

Quality control of ASL-CBF maps was performed by 2 researchers with 10+ and 2 years of experience in ASL (Jan Petr, Yeva Prysiazhniuk). Unclear cases were discussed in a joint session to reach a consensus. ASL scans were classified as "good," "acceptable," "macrovascular," and "unusable" based on the number of macrovascular artifacts and the general image quality (Figure 19 (B)).

### 2.1.4 ROI Analysis

Tumor and edema segmentations were used to create the ROI for quantitative perfusion analysis. For ASL, voxels with a distance less than 5 mm from the tumor mask were excluded from the edema mask to minimize the effect of partial volume effects (PVE) and signal contamination between tissues. Cases with missing edema segmentations or edema volumes smaller than 0.5 $cm^3$ were excluded from the edema analysis. Several statistical descriptors (5th percentile, median, 95th percentile, and interquartile range (IQR)) were extracted for edema and tumor ROIs in the normalized perfusion maps ASL-nCBF, DSC-nCBF, and DSC-nCBV. These 4 descriptors, 3 perfusion parameters, and 2 ROIs yielded together 24 parameters.

### 2.1.5 Data Analysis

Group differences in the above-mentioned statistical descriptors were assessed in groups stratified according to *IDH* mutation, 1p/19q codeletion, p*TERT* mutation, and *MGMT* methylation using a Cohen's *d* with Hedge's correction and a two-tailed Student's *t*-test with Satterthwaite's approximation for unequal variances. Additionally, Cohen's *d* and its confidence interval were estimated with bootstrapping with 1000 iterations. Benjamini-Hochberg procedure was subsequently used to account for multiple comparison bias. The significance level was set to $P \leq 0.05$. To investigate the synergistic effect of molecular markers on tumor and edema perfusion, the best-performing ASL and DSC descriptors in tumor and edema were compared between subgroups of markers that had shown significant perfusion differences and between diffuse glioma entities. Additionally, all values were compared between DSC- and ASL-derived parameters using Spearman correlation. Consequently, derived effect sizes were used for the power analysis (alpha = 0.05 and power = 0.8).

Univariate logistic regression models classifying the molecular status were built separately for each of the 24 statistical descriptors. Their performance was assessed with the area under the receiver operating characteristic curve (AUROCC), sensitivity, and specificity. Bootstrapping with 1000 iterations was used to derive the confidence intervals.

Multivariate classification models, using a multivariate logistic regression model with LASSO regularization and 10-fold cross-validation, were implemented to include both edema and tumor perfusion parameters. Every such model was built separately on ASL-

nCBF, DSC-nCBV, and DSC-nCBF descriptors. The multivariate approach was applied in the subset where both edema and tumor segmentations were present. Due to the insufficient data on 1p/19q codeletion and *MGMT* methylation status, multivariate classification was only analyzed for *IDH* and p*TERT* alterations.

## 2.2 Hemodynamic Trends in MR-negative Children

### 2.2.1 Population

This retrospective study included 32 pediatric subjects (19 males, aged 0.7–17.9 years, mean ± SD: 9.3 ± 5.3 years) who underwent routine MRI examination between July 2021 and March 2022 at Lucile Packard Children's Hospital Stanford. The protocol included ASL as part of the diagnostic setup to assess cerebral perfusion. Additional ASL sequences were included within the same scanning session when increased scanning capacities were available. Inclusion criteria encompassed under 18 years of age, an MR-negative status (no structural or functional abnormalities), and the availability of single- and multi-delay ASL data. MR-negative status was confirmed by an experienced pediatric neuroradiologist (Elizabeth Tong, 7 years of expertise) based on the structural imaging scans and sedation data were retrieved from the database. Participants were instructed to refrain from caffeine consumption for at least six hours prior to imaging. The study received ethics approval from Stanford's IRB the Administrative Panel on Human Subjects in Medical Research (IRB-72827). Written informed consent for secondary data use in the present study was obtained from the parents or guardians of all participants, in accordance with the Declaration of Helsinki.

### 2.2.2 MRI Data Acquisition

MRI data was acquired on a 3T GE Premier (GE Healthcare, Milwaukee, USA) with a 21-channel head and neck coil. All included subjects underwent T1-weighted (3D SPGR, TR/TE 6.8/2.9 ms, flip angle 15°, voxel size isometric 1 $mm^3$) and T2-weighted (2D FSE, TR/TE 4882/103.2 ms, flip angle 111°, voxel size 0.5×0.5×2.5 $mm^3$) scans. Four types of background-suppressed PCASL scans were obtained: single-delay $PCASL_{PLD2025}$ (LD 1450 ms, PLD 2025 ms) and $PCASL_{PLD1525}$ (LD 1450 ms, PLD 1525 ms), as well as multi-delay $PCASL_{7PLD}$ (LD 550 ms, PLDs 700, 1250, 1800, 2350, 2900, 3450, and 4000 ms) and $PCASL_{3PLD}$ (LD 1700 ms, PLDs 300, 2000, and 3700 ms). Further details of the MRI acquisition protocol are provided in Table 2.

For multi-delay sequences, scanner-reconstructed arterial-time (AT)-corrected and uncorrected CBF, as well as ATT maps were extracted (Dai, Shankaranarayanan and Alsop, 2013). For single-delay PCASL, only scanner-reconstructed, uncorrected CBF was retrieved. Image processing, including T1-weighted segmentation, spatial normalization, and population-level analysis, was performed using ExploreASL v1.12 (Mutsaerts *et al.*, 2020). ASL data quality was assessed independently by two researchers with 10+ and 3 years of ASL experience (Jan Petr, Yeva Prysiazhniuk) according to the methodology describe above. Scans were categorized as "good" (well-distributed GM perfusion signal without motion or labeling artifacts), "acceptable" (minor motion or macrovascular artifacts causing regional signal loss), or "vascular" (dominant macrovascular artifact due to delayed arterial arrival). Mean CBF and ATT values in supratentorial GM, deep WM, and total brain (TB) (supratentorial GM and WM) regions were extracted in native space using CAT12. Additionally, absolute volumes and volumes relative to intracranial volume (ICV) were extracted for GM and WM.

### 2.2.3 Statistical analysis

Statistical analyses and visualizations were performed using R statistical software (version 4.3.0; R Foundation for Statistical Computing, Vienna, Austria. https://www.R-project.org/). Paired t-tests and Cohen's d with Hedge's correction were applied to compare mean CBF and ATT values across GM, WM, and TB between ASL variants. Specifically, CBF values from $PCASL_{2025ms}$, $PCASL_{1525ms}$, and $PCASL_{ATC\text{-}7PLD}$ were compared to those from $PCASL_{ATC\text{-}3PLD}$ due to the larger sample sizes of the overlapping datasets. To assess the effect of AT-correction on absolute CBF quantification, both corrected and uncorrected CBF values from $PCASL_{3PLD}$ and $PCASL_{7PLD}$ sequences were analyzed. Student t-tests were used to assess the impact of sex and sedation on GM $CBF_{ATC\text{-}3PLD}$.

A Spearman correlation was employed to investigate the relationship between age and AT-corrected or uncorrected CBF values in GM, WM, and TB for the $PCASL_{3PLD}$ and $PCASL_{7PLD}$ sequences. Differences in correlation strength across GM, WM, and TB were assessed using a combined linear regression model, with the significance of the interaction term indicating differences between the linear models. The differences in the correlation between GM $CBF_{ATC\text{-}3PLD}$ and age across sedated/non-sedated and male/female

**Table 2**. MRI acquisition parameters of structural and perfusion data. T1w - T1-weighted, T2w - T2-weighted, SPGR - spoiled gradient echo, FSE - fast spin echo, FOV - field of view, PCASL - pseudo-continuous ASL, TR - repetition time, TE - echo time, FA - flip angle, LD - labeling duration, PLD - post labeling delay, M0 - equilibrium magnetization, BS - background suppression. Other parameters: M0 scan included, 4 background suppression pulses, labeling plane was fixed to 2 cm below the FOV without manual adjustment.

Perfusion data acquisition parameters

| | $PCASL_{7PLD}$ (n = 18) | $PCASL_{3PLD}$ (n = 32) | $PCASL_{2025ms}$ (n = 19) | $PCASL_{1525ms}$ (n = 10) |
|---|---|---|---|---|
| Labeling and Readout | 3D PCASL FSE stack-of-spiral | 3D PCASL FSE stack-of-spiral | 3D PCASL FSE stack-of-spiral | 3D PCASL FSE stack-of-spiral |
| FOV | 240 mm | 240 mm | 240 mm | 240 mm |
| Acquired resolution | 512 points / 4 arms | 512 points / 8 or 4 arms | 512 points / 8 arms | 512 points / 8 arms |
| Slice thickness / spacing between slices mm | 3 / 3 | 3 / 3 | 4 / 4 | 4 / 4 |
| TR/TE ms, FA° | 7100 / 23.2 ms, 111° | 7100 / 23.2 ms, 111° | 4890 / 52.9 ms, 111° | 4680 / 52.9 ms, 111° |
| Number of excitations (NEX) | 1 | 2 | 3 | 3 |
| (Effective) LD | 550 ms | 1700 ms | 1450 ms | 1450 ms |
| PLD | 700, 1250, 1800, 2350, 2900, 3450, 4000 ms | 300, 2000, 3700 ms | 2025 ms | 1525 ms |

subpopulations were evaluated using ANOVA tests applied to the corresponding linear regression models. A two-parameter linear regression model was estimated using both $PCASL_{3PLD}$ and $PCASL_{7PLD}$ ATT and age in GM, WM, and TB, with acquisition approach included as a separate parameter. The significance of the models was evaluated using ANOVA, and $r^2$ was reported as the correlation coefficient. Voxel-wise Spearman

correlation analyses of $PCASL_{3PLD}$ ATT and CBF with age were performed, incorporating false discovery rate (FDR) correction and cluster correction to visualize the regional effects.

A Spearman correlation was used to compare regional CBF (GM, WM, TB), regional volumes (GM, WM, and combined GM and WM, respectively), and age. Volumetric markers included absolute regional volumes and regional volumes relative to the absolute intracranial volume". Voxel-wise quantification of population mean $PCASL_{ATC\text{-}3PLD}$ CBF and ATT maps was performed alongside the voxel-wise population coefficient of variation (CoV) for $PCASL_{ATC\text{-}3PLD}$ CBF and ATT, defined as the ratio of the voxel-wise standard deviation to the voxel-wise mean. A statistical significance threshold of $p < 0.05$ was applied, with a family-wise error rate (FWER) correction using the Holm method implemented throughout the study.

### 2.3 Hemodynamics in Preterm Neonates

#### 2.3.1 Population

This study included subjects scanned at Lucile Packard Children's Hospital Stanford between August 2022 and December 2023. All participants were scanned using a standardized clinical protocol for preterm neonates that incorporated structural and perfusion MRI sequences. Inclusion criteria were: (1) gestational age at birth <37 weeks, (2) successful completion of the ASL protocol, and (3) absence of major structural abnormalities on diagnostic MRI evaluated by board-certified pediatric neuroradiologists (Elizabeth Tong and Kristen Yeom). Due to scanner upgrades or protocol changes during the study period, some neonates did not undergo the complete ASL protocol. However, these variations did not introduce any systematic bias. A total of 48 neonates met all inclusion criteria and were analyzed. Ethics approval was granted by Stanford's IRB the Administrative Panel on Human Subjects in Medical Research, and informed parental consent for secondary use of the data was obtained in accordance with the Declaration of Helsinki.

#### 2.3.2 Clinical Information

Clinical records were reviewed to determine the cause of preterm labor, which was classified into the following categories: spontaneous labor with intact membranes, preterm premature rupture of membranes (PPROM), labor induction or cesarean delivery due to maternal indications, and labor induction or cesarean delivery due to fetal indications (Goldenberg *et al.*, 2008).

### 2.3.3 MRI Acquisition

MRI data acquisition was conducted on a 3T GE Premier (GE Healthcare, Waukesha, USA) with a 48HAP head coil. The "feed and bundle" method was employed for imaging without the use of sedation in all participants. All included participants underwent T1-weighted (3D FSPGR, TR/TE 6.3/2.5 ms, flip angle 12°, voxel size isotropic 1 $mm^3$) and T2-weighted (2D FSE, TR/TE 2700/110.5 ms, flip angle 111°, voxel size 0.5×0.5×2.5 $mm^3$) scans.

Three types of background-suppressed PCASL with M0 were acquired:

- single-delay - $PCASL_{1PLD}$ (PLD 1525 ms; LD 1450 ms; acquisition duration 4 min 15 s);
- Hadamard-encoded three-delay - $PCASL_{3PLD}$ (PLD 700, 2000, and 3300 ms; LD 1300 ms; acquisition duration 4 min 50 s);
- Hadamard-encoded seven-delay - $PCASL_{7PLD}$ (PLD 700, 1250, 1800, 2350, 2900, 3450, and 4000 ms; LD 550 ms; acquisition duration 4 min 20 s).

Further details of the MRI acquisition protocol are provided in Table 3.

### 2.3.4 Image Analysis

T1w, T2w, raw ASL files, and scanner-reconstructed CBF ($CBF_{1PLD}$, and arterial-time corrected $CBF_{3PLD}$ and $CBF_{7PLD}$) and ATT ($ATT_{3PLD}$ and $ATT_{7PLD}$) were exported from the scanner. Cases with missing raw ASL files were excluded from the analysis (n=2). Brain segmentation in the native space was performed using the BIBSnet (Baby and Infant Brain Segmentation Neural Network) pipeline (Hendrickson *et al.*, 2025). Maps of total GM, WM, and cortical GM (excluding the deep GM regions) were extracted from the resulting segmentations. CBF maps were registered to T1w scans in the native space using affine transformation. Effective resolution of ASL scans was estimated to be able to account for through-slice blurring. A Gaussian point spread function (PSF) was assumed and its full-width at half maximum was estimated by minimizing the root mean square difference between the CBF maps and pseudo CBF image created from PSF-adjusted GM/WM masks, while simultaneously optimizing the GM and WM CBF in the pseudo-CBF image. Finally, weighted mean $CBF_{1PLD}$, $CBF_{3PLD}$, and $CBF_{7PLD}$ values were extracted in left, right, and total cortex ROIs using MATLAB (Mathworks, Natick, MA, USA, version R2023a).

### 2.3.5 Image Quality Assessment

The quality of structural scans (T1w and T2w) and the presence of fetal-type posterior cerebral artery variations were evaluated by a neuroradiologist with 8 years of experience (Rui Duarte Armindo), who was blinded to the rest of the dataset and clinical markers. Scans

**Table 3**. MRI acquisition parameters. FSE – fast spin echo, FOV – field of view, PCASL – pseudo-continuous ASL, TR – repetition time, TE – echo time, FA – flip angle, LD – labeling duration, PLD – post labeling delay. Other parameters: M0 scan included, 4 background suppression pulses, labeling plane was fixed to 2 cm below the FOV without manual adjustment.

ASL MRI data acquisition parameters

| | $PCASL_{7PLD}$ (n = 48) | $PCASL_{3PLD}$ (n = 37) | $PCASL_{1PLD}$ (n = 47) |
|---|---|---|---|
| Labeling and Readout | 3D PCASL FSE stack-of-spiral | 3D PCASL FSE stack-of-spiral | 3D PCASL FSE stack-of-spiral |
| FOV | 240 mm | 200 mm | 240 mm |
| Acquired resolution | 512 points / 4 arms | 512 points / 4 arms | 512 points / 8 arms |
| Slice thickness / spacing between slices mm | 3 / 4 | 3 / 3 | 4 / 4 |
| TR/TE ms, FA° | 6900 / 22.6 ms, 111° | 6900 / 23.2 ms, 111° | 4680 / 52.9 ms, 111° |
| Number of excitations (NEX) | 1 | 2 | 3 |
| (Effective) LD | 550 ms | 1300 ms | 1450 ms |
| PLD | 700, 1250, 1800, 2350, 2900, 3450, 4000 ms | 700, 2000, 3300 ms | 1525 ms |
| Acquisition time (min:s) | 4:20 | 4:50 | 4:15 |

were categorized as “good” for excellent image quality or minor artifacts without significant degradation, “acceptable” for moderate artifacts visibly reducing image quality but not preventing diagnostic interpretation, and “unusable” for severe artifacts compromising diagnostic utility. The quality of ASL scans and the presence of artifacts were assessed by two researchers with 10+ and 4 years of ASL experience (Jan Petr, Yeva Prysiazhniuk) based on the subtracted ASL images. Scans were classified as “good” if the perfusion signal was well-distributed in GM with no visible artifacts, “acceptable” if there were minor motion or macrovascular artifacts causing regional signal decrease but maintaining acceptable overall quality, and “unusable” if there were strong motion or macrovascular artifacts, or failed labeling rendering the scan non-diagnostic.

### 2.3.6 Statistical Analysis

Statistical analyses and visualizations were performed using R (version 4.3.0). A sensitivity analysis of sex, PNA, GA, weight during scanning, birth weight, and causes of preterm birth among subdatasets of three ASL methods was performed using a chi-squared test and ANOVA. To assess the consistency of QC rating of within-session T1w and T2w scans, weighted Cohen’s kappa with squared weights was calculated. To assess differences in scan quality distribution among ASL sequences, the Kruskal-Wallis test was used to account for the ordinality in classes. To assess the difference in the abundance of artifacts, a chi-squared test was used. A $p < 0.05$ was considered statistically significant for all analyses.

ASL data marked as “unusable” were excluded from the consequent analysis of CBF and ATT distribution in preterm neonates. Paired t-tests with Satterthwaite correction for unequal variances and Cohen's d with Hedge’s correction were applied to compare mean cortical CBF and ATT values among ASL variants and between sexes. To assess whether the difference between single- and multi-delay CBF values is associated with ATT variation, Pearson correlation analysis was performed between the differences in $CBF_{3PLD}$ or $CBF_{7PLD}$ and $CBF_{1PLD}$, and the corresponding $ATT_{3PLD}$ or $ATT_{7PLD}$ values, respectively.

Pearson correlation analysis was performed to assess the change of CBF and ATT in GA, PNA, and PMA. Age parameters with a significant correlation to hemodynamic parameters were then used in a linear regression model to predict cortical CBF or ATT.

CBF asymmetry between hemispheres was computed as:

$$Asymmetry = \frac{CBF_{left} - CBF_{right}}{CBF_{left}}$$

Positive values indicate higher CBF in the left cortex.

## 2.4 Pediatric Brain Tumor Perfusion Imaging

### 2.4.1 Population

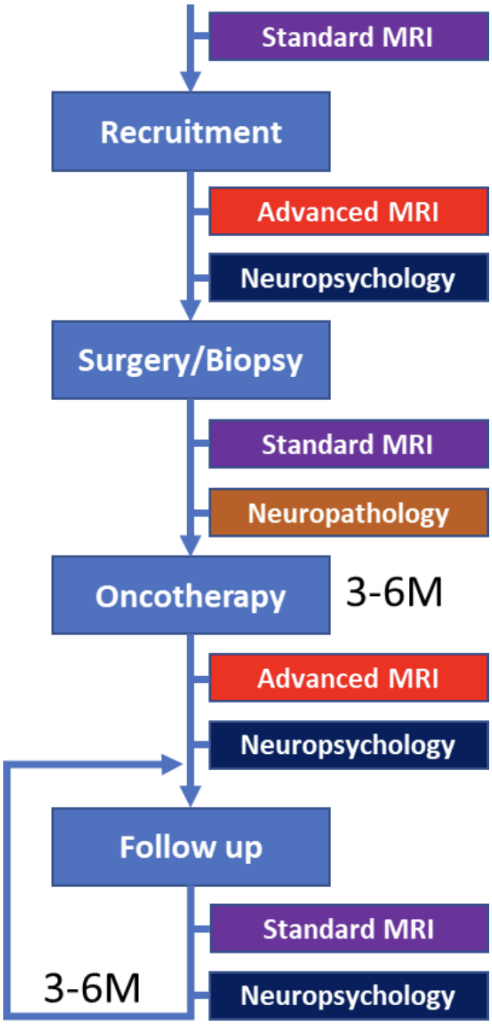


PediTuMRI is an ongoing prospective study conducted at Motol University Hospital since September 2023, focusing on pre-surgical and follow-up imaging of pediatric brain tumors (Figure 20). The imaging protocol comprises either Siemens product sequential multi-delay ASL or Hadamard-encoded multi-echo (multi-TE), multi-inversion time (multi-TI) ASL, in addition to reference DSC and DCE imaging, both acquired within the same session following ASL (Figure 21). The technical details of the acquisition protocol are summarized in Table 4. All participants are scanned according to a standardized clinical protocol; however, some variability in ASL acquisition persists due to scanner system upgrades and ongoing debugging related to the implementation of multi-TE ASL on the scanner system.

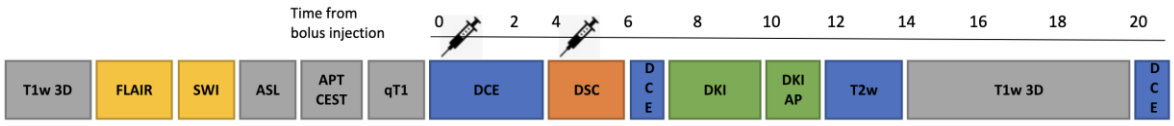


**Figure 21.** Schematic overview of PediTuMRI imaging protocol. The syringe sign indicates GBCA injection (half-dose twice).

Ethics approval was granted by the Institutional review board of the University Hospital Motol, and informed parental consent for obtaining and secondary use of the data was obtained in accordance with the Declaration of Helsinki.

**Table 4.** PediTuMRI acquisition protocol. SPACE – sampling perfection with application optimized contrast using different flip angle evolution, TSE – turbo spin echo, qSWI – quantitative susceptibility-weighted image, APT – amide proton transfer, CEST – chemical exchange saturation transfer, DTI – diffusion tensor imaging, FLAIR – fluid-attenuated inversion recovery, TR – repetition time, TE – echo time, FOV – field of view, FA – flip angle, SBD – subbolus duration, GRASE – gradient and spin echo.

| **Structural sequence parameters** | | | |
|---|---|---|---|
| T1w 3D SPACE | Voxel 1 mm isotropic, TR 600 ms, TE 23 ms, FOV 220 mm, FA evolution | | |
| T2w 2D TSE | Voxel 0.6x0.6x3.5 $mm^3$, TR 5000 ms, TE 90 ms, FOV 240 mm, FA 150° | | |
| T2 qSWI 3D | Voxel 0.3x0.3x1.6 (or 1.8 for children older than 2yo) $mm^3$, TR 27 ms, TE 20 ms, FA 10° | | |
| APT-CEST SPACE | Voxel 1.4x1.4x2.8 $mm^3$, TR 3000 msec, TE 17 msec, turbo factor 140, FA 120°, 7 frequencies with saturation pulses at ±3.0 ppm, ±3.5 ppm, ±4.0 ppm, and 1560 ppm off-resonance, B0 map acquired for correction | | |
| PCASL | Multi-TE ASL (voxel 2.5x2.5x5 $mm^3$, 3D GRASE) | Hadamard-8 | 8x8 matrix, SBD 400 ms, PLD 200 ms, thus TI = SBD + PLD = [600, 1000, 1400, 1800, 2200, 2600, 3000] ms, TR 5000 ms, TE 13.2 ms, FA 15° |
| | | Hadamard-4 | 4x4 matrix, SBD 1000 ms, PLD 600 ms, TI = SBD + PLD = [1600, 2600, 3600] ms, TR 5000 ms, TE [13.8, 41.4, 69, 96.6, 124.2, 151.8, 179.4, 207] ms, FA 15° |
| | | M0 | TR 2300 ms, TE 13.2 ms, phase encoding direction LR and RL |
| | Product multi-PLD PCASL (3D GRASE) | Voxel 1.8x1.8x4 $mm^3$, PLD [700, 1270, 1850, 2420, 2800] ms, LD 1800 ms, TE 22 ms, M0 included | |
| DCE | Voxel 1.4x1.4x4 $mm^3$, 16 slices, TR 4 ms, TE 1.33 ms, 55 measurements, FOV 240, mm, FA 12°, half-dose of 0.1 mmol/kg Gadovist was given with a power injector at a rate and saline flush adapted per weight, multi-FA T1 map and B1 map acquired | | |
| DTI | Voxel 2x2x2 $mm^3$, TR 5300 ms, TE 97 ms, FOV 200 mm, 20 directions, b [0, 1000, 3000] $s/mm^2$ | | |
| DSC | Voxel 1.9x1.9x3.5 $mm^3$, TR 2000 ms, TE 30 ms, FA 60°, FOV 240 mm, 50 measurements, temporal resolution 2 s, half-dose of 0.1 mmol/kg Gadovist was given with a power injector at a rate and saline flush adapted per weight, multi-FA T1 map and B1 map acquired | | |
| Post-contrast T1w 3D SPACE | Voxel 1 mm isotropic, TR 600 ms, TE 23 ms, FOV 220 mm, FA evolution | | |
| Post-contrast T2 FLAIR 2D | Voxel 0.8x0.8x3.5 $mm^3$, TR 8000 ms, TE 105 ms, FOV 240 mm, FA 150° | | |

### 2.4.2 Image Processing

Multi-TE ASL data were processed using the ExploreASL toolbox (version 1.12), incorporating an extended model to account for intra-voxel transit time, as implemented in FSL BASIL (Mutsaerts *et al.*, 2020; Mahroo *et al.*, 2021b; Chappell *et al.*, 2023). APT-

CEST data were processed using custom scripts implementing the quantification methods described in the standardization article (Zhou *et al.*, 2022). Scanner-reconstructed diffusion-weighted imaging (DWI) parameters, including the apparent diffusion coefficient (ADC) and fractional anisotropy (FA), were used for visualization purposes. These were reviewed alongside structural scans – pre- and post-contrast T1-weighted, T2-weighted, and T2-weighted FLAIR images – to ensure radiological completeness.

### 2.4.3 Case examples

Two representative case examples are presented, utilizing multi-modal imaging visualization and tumor segmentations that were manually edited and validated by an experienced (10+ years of experience) pediatric neuroradiologist (Martin Kynčl). MRI scans were co-registered using SPM in accordance with the methodology described above, and image fusion was performed using 3D Slicer. Both cases were selected as in two separate timepoint – before the start of the treatment and after the start of treatment (without surgery to minimize confounders related to surgical resection and associated tissue changes). In both instances, the histopathological diagnosis was confirmed.

### 2.4.4 Quantitative T2 Investigation

To investigate the feasibility of quantifying the potential time of exchange ($T_{exch}$) in pediatric brain tumors, assuming the standard approach of a constant $T2_{blood}$, two different models were employed to assess quantitative T2 values derived from control scans acquired using multi-echo Hadamard-4 PCASL. Model fitting was performed using the MATLAB function *lsqcurvefit*.

The first, uniparametric model does not account for T2 differences among brain tissue, tumor, blood, or CSF, and is used primarily to visualize the distribution of T2 in the brain. In this approach, the optimization estimates the T2 relaxation time for each voxel by minimizing the sum of squared differences between the measured multi-echo signal intensities and a monoexponential decay model, using nonlinear least squares fitting at the given echo times. The model is defined as:

$$S(TE) = e^{\frac{-TE}{T_2}},$$

and the fitting problem can be formulated as:

$$Find\ T_2^* = arg\ min \sum_{i=1}^{8} [SI_i - e^{\frac{-TE_i}{T_2}}]^2,\ T_2 > 0,$$

where $SI_i$ denotes the measured signal intensity at the i-th echo time ($TE_i$), and T2 represents the intra-voxel effective T2. The specific echo times are listed in Table 4.

To further investigate the influence of CSF and blood, both of which exhibit long T2 values, a multiparametric model was implemented. This model assumes separate signal contributions from tissue, blood, and CSF, with the T2 values of blood and CSF fixed according to published values (Spijkerman *et al.*, 2018): $T_{2,blood}$ = 165 ms and $T_{2,CSF}$ = 1600 ms. The signal model is given by:

$$S(TE) = S_{0,tissue} \cdot e^{\frac{-TE}{T_{2,tissue}}} + S_{0,blood} \cdot e^{\frac{-TE}{T_{2,blood}}} + S_{0,CSF} \cdot e^{\frac{-TE}{T_{2,CSF}}}.$$

where the estimated parameters are:

- $T_{2,tissue}$: within-voxel tissue T2, constrained to (0,150] ms, to ensure sufficient differentiation from the blood component;
- $S_{0,tissue}$: relative signal amplitude of tissue (normalized to maximum measured SI), bounded between 0 and 1;
- $S_{0,blood}$: relative amplitude of blood, bounded between 0 and 1;
- $S_{0,CSF}$: relative amplitude of CSF, bounded between 0 and 1.

The optimization is performed using the same nonlinear least squares framework as above, with updated parameter boundaries and the extended signal model. As a subsequent step, the distribution of tissue T2 values is evaluated in WM voxels exhibiting a partial volume > 0.9. Linear correction for partial volume effects from GM and CSF is applied, based on partial volume maps generated by ExploreASL.

# 3. Results

## 3.1 Adult Gliomas

The final dataset included 89 patients (53 male, 53.4 ± 15.3 years, grades 2-4) (Figure 22). Overall, *IDH* mutation status was available for 66 subjects, p*TERT* mutation status for 38 subjects, 1p/19q-codeletion status for 32 subjects, and *MGMT* methylation status for 31 subjects. Histopathological status was confirmed for 33 subjects with glioblastoma, 24 subjects with astrocytoma, and 14 subjects with oligodendroglioma. The majority of ASL images were rated as "good" (73.3%), but "acceptable" (13.3%) and "macrovascular" scores (13.3%) were consistently present across platforms (Table 5). Eight subjects were excluded because ASL data were rated as "unusable." Edema segmentation of substantial volume met the inclusion criteria in 54 subjects.

### 3.1.1 Perfusion Signal Distribution and Molecular Markers

The analysis of signal distributions revealed significant variations across multiple DSC and ASL perfusion parameters depending on the molecular marker status (Table 6). Specifically, in *IDH*-wt gliomas, significantly higher perfusion values were evident in tumors for multiple ASL-nCBF, DSC-nCBV, and DSC-nCBF descriptors.

In tumor, only 5th percentile ASL-nCBF shows a large effect size (Cohen's $d = 0.81$), while in edema, multiple DSC-nCBV (median, 95th percentile, IQR) descriptors show a large effect size (Cohen's $d > 0.8$). Within 1p/19q-codeletion and *MGMT* methylation subgroups, although no statistical significance is observed, Cohen's *d* values indicate substantial mean differences in ASL-nCBF values within edema (Table 7). DSC-nCBF descriptors have large effect sizes in *IDH* and p*TERT* status differentiation, however, when compared to DSC-nCBV, they show a lower discriminative power (Table 8). The retrospective power analysis results of the feasible sample sizes for a reliable comparison of ASL and DSC's most prominent perfusion parameters in the classification of p*TERT* mutation, 1p/19-codeletion, and MGMT alteration status are presented in Table 9.

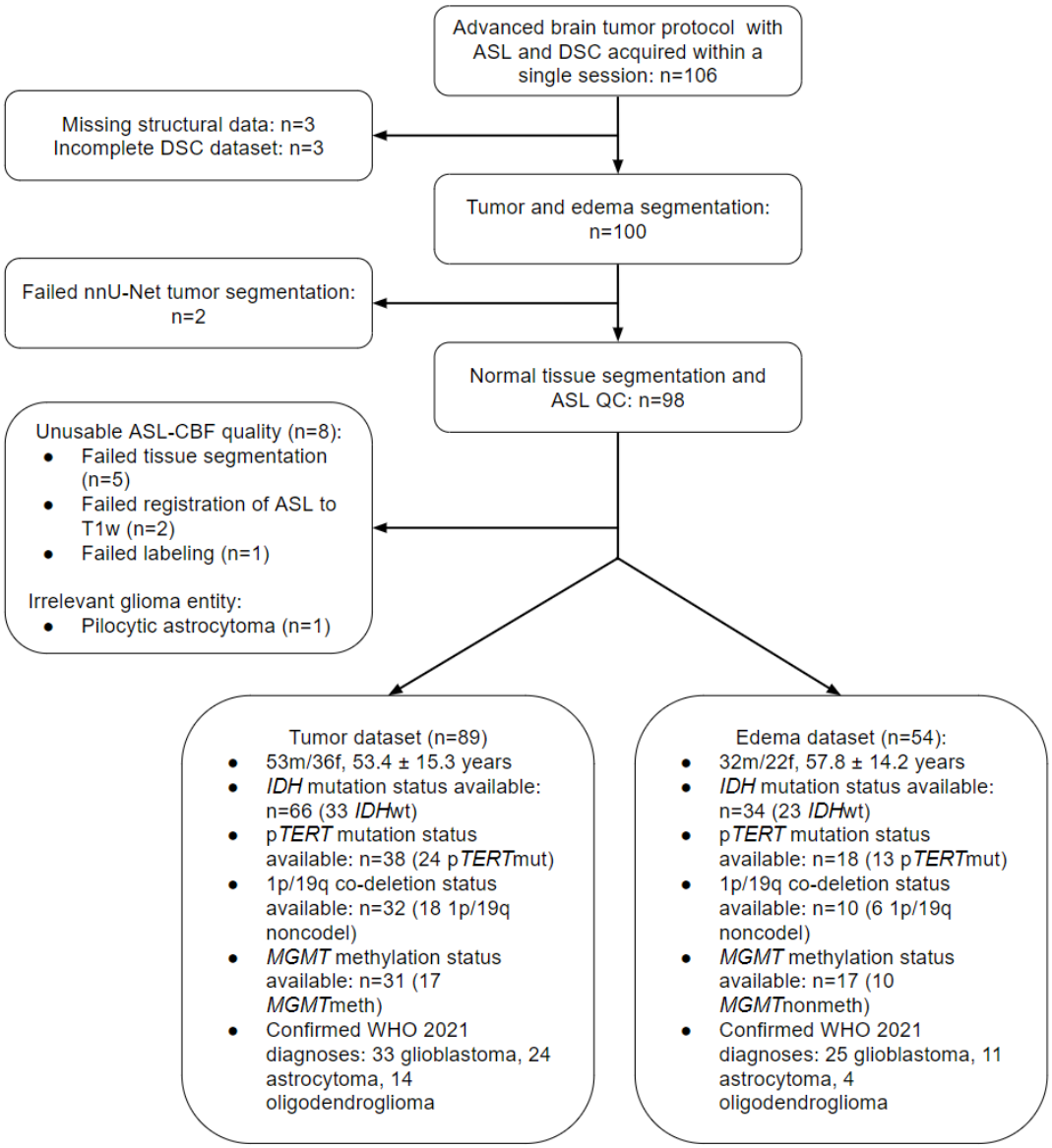


**Figure 22**. Flowchart of the study

**Table 5.** Quality-control results of ASL from the different platforms

| | MRI platform | | |
|---|---|---|---|
| ASL quality | Signa HDxt | Discovery MR750 | Signa Premier |
| Good | 20 | 36 | 9 |
| Acceptable | 5 | 3 | 4 |
| Macrovascular | 3 | 5 | 4 |
| Unusable | 1 | 6 | 1 |

**Table 6.** Perfusion signal distributions in tumor and edema of *IDH*-mutant/wildtype and p*TERT*-mutant/wildtype gliomas. * indicates significant p-values ($p<0.05$) after the Benjamini-Hochberg procedure. n indicates the sample sizes.

| ***IDH*** | | | | | | | | |
|---|---|---|---|---|---|---|---|---|
| | **Tumor** | | | | **Edema** | | | |
| Perfusion parameter | *IDH*mut (mean ± SD) | *IDH*wt (mean ± SD) | Cohen's d (95% CI) | p-value | *IDH*mut (mean ± SD) | *IDH*wt (mean ± SD) | Cohen's d (95% CI) | p-value |
| | n = 33 | n = 33 | | | n = 11 | n = 23 | | |
| ASL-nCBF 5th percentile | 0.45 ± 0.14 | 0.65 ± 0.18 | **1.19** (0.6-1.71) | **8.3e-6*** | 0.41 ± 0.11 | 0.42 ± 0.16 | 0.04 (0-0.6) | 0.89 |
| ASL-nCBF median | 0.81 ± 0.28 | 1.23 ± 0.42 | **1.18** (0.69-1.68) | **1.1e-5*** | 0.88 ± 0.68 | 0.68 ± 0.23 | 0.45 (0-1.52) | 0.37 |
| ASL-nCBF 95th percentile | 1.33 ± 0.75 | 2.09 ± 0.79 | **0.97** (0.32-1.58) | **1.7e-4*** | 1.35 ± 1.02 | 1.29 ± 0.75 | 0.06 (0-1.18) | 0.87 |
| ASL-nCBF IQR | 0.40 ± 0.39 | 0.61 ± 0.31 | 0.58 (0.02-1.24) | **0.0208** | 0.41 ± 0.49 | 0.34 ± 0.31 | 0.18 (0-1.45) | 0.68 |
| DSC-nCBV 5th percentile | 0.36 ± 0.47 | 0.53 ± 0.86 | 0.24 (0-0.69) | 0.32 | 0.13 ± 0.39 | 0.16 ± 0.28 | 0.08 (0-0.95) | 0.84 |
| DSC-nCBV median | 1.50 ± 0.62 | 3.06 ± 1.69 | **1.21** (0.75-1.63) | **1.2e-5*** | 1.27 ± 0.44 | 1.38 ± 0.56 | 0.21 (0-0.9) | 0.54 |
| DSC-nCBV 95th percentile | 4.40 ± 1.49 | 7.60 ± 3.59 | **1.15** (0.75-1.56) | **2.5e-5*** | 4.34 ± 1.07 | 4.75 ± 1.30 | 0.33 (0-0.97) | 0.34 |
| DSC-nCBV IQR | 1.52 ± 0.73 | 2.85 ± 1.45 | **1.15** (0.72-1.55) | **2.2e-5*** | 1.29 ± 0.40 | 1.58 ± 0.70 | 0.46 (0-1.05) | 0.13 |
| **p*TERT*** | | | | | | | | |
| | **Tumor** | | | | **Edema** | | | |
| Perfusion parameter | p*TERT*mut (mean ± SD) | p*TERT*wt (mean ± SD) | Cohen's d (95% CI) | p-value | p*TERT*mut (mean ± SD) | p*TERT*wt (mean ± SD) | Cohen's d (95% CI) | p-value |
| | n = 24 | n = 14 | | | n = 13 | n = 5 | | |
| ASL-nCBF 5th percentile | 0.61 ± 0.19 | 0.47 ± 0.10 | **0.81** (0.21-1.45) | **0.0067** | 0.45 ± 0.11 | 0.44 ± 0.11 | 0.09 (0-1.06) | 0.85 |
| ASL-nCBF median | 1.11 ± 0.38 | 0.84 ± 0.27 | 0.76 (0.04-1.38) | **0.0156** | 0.88 ± 0.63 | 0.62 ± 0.13 | 0.45 (0-0.9) | 0.18 |
| ASL-nCBF 95th percentile | 1.88 ± 0.83 | 1.40 ± 0.73 | 0.58 (0-1.12) | 0.0783 | 1.72 ± 1.24 | 0.93 ± 0.18 | 0.70 (0.25-1.11) | **0.0433** |
| ASL-nCBF IQR | 0.57 ± 0.43 | 0.42 ± 0.37 | 0.34 (0-0.85) | 0.28 | 0.25 ± 0.57 | 0.19 ± 0.04 | 0.64 (0.33-1.07) | 0.0597 |
| DSC-nCBV 5th percentile | 0.42 ± 0.66 | 0.38 ± 0.50 | 0.07 (0-0.69) | 0.82 | 0.14 ± 0.22 | 0.07 ± 0.48 | 0.22 (0-3.2) | 0.76 |
| DSC-nCBV median | 2.47 ± 1.51 | 1.61 ± 0.68 | 0.66 (0.17-1.17) | **0.0217** | 1.45 ± 0.52 | 0.85 ± 0.47 | **1.13** (0.31-2.14) | **0.0457** |
| DSC-nCBV 95th percentile | 6.76 ± 3.70 | 4.76 ± 1.32 | 0.64 (0.16-1.06) | **0.0223** | 5.10 ± 1.30 | 3.40 ± 1.40 | **1.22** (0-2.33) | 0.0517 |
| DSC-nCBV IQR | 2.57 ± 1.58 | 1.58 ± 0.61 | 0.74 (0.14-1.14) | **0.0099** | 1.76 ± 0.74 | 0.99 ± 0.33 | **1.13** (0.39-1.85) | **0.0075** |

**Table 7**. Perfusion signal distributions in tumor and edema of 1p/19q non/co-deleted and *MGMT*-non/methylated gliomas.

| **1p/19q** | | | | | | | | |
|---|---|---|---|---|---|---|---|---|
| | **Tumor** | | | | **Edema** | | | |
| Perfusion parameter | 1p/19q co-del (mean ± SD) | 1p/19q nonco-del (mean ± SD) | Cohen's d (95% CI) | p-value | 1p/19q co-del (mean ± SD) | 1p/19q nonco-del (mean ± SD) | Cohen's d (95% CI) | p-value |
| | n = 14 | n = 18 | | | n = 4 | n = 6 | | |
| ASL-nCBF 5$^{th}$ percentile | 0.47 ± 0.19 | 0.55 ± 0.19 | 0.42 (0-1.10) | 0.25 | 0.44 ± 0.14 | 0.43 ± 0.11 | 0.07 (0-1.67) | 0.91 |
| ASL-nCBF median | 0.84 ± 0.31 | 0.92 ± 0.34 | 0.23 (0-0.9) | 0.51 | 1.32 ± 1.05 | 0.66 ± 0.12 | **0.91** (0-2.5) | 0.30 |
| ASL-nCBF 95$^{th}$ percentile | 1.41 ± 0.85 | 1.46 ± 0.63 | 0.07 (0-0.8) | 0.86 | 2.01 ± 1.57 | 1.09 ± 0.21 | **0.85** (0-2.41) | 0.32 |
| ASL-nCBF IQR | 0.43 ± 0.48 | 0.39 ± 0.22 | 0.12 (0-1.1) | 0.76 | 0.73 ± 0.76 | 0.26 ± 0.08 | **0.91** (0-2.23) | 0.30 |
| DSC-nCBV 5$^{th}$ percentile | 0.37 ± 0.44 | 0.29 ± 0.57 | 0.17 (0-0.91) | 0.62 | 0.25 ± 0.37 | 0.05 ± 0.40 | 0.45 (0-1.73) | 0.46 |
| DSC-nCBV median | 1.57 ± 0.58 | 1.68 ± 1.08 | 0.1 (0-0.79) | 0.75 | 1.52 ± 0.11 | 1.23 ± 0.61 | 0.53 (0-2.19) | 0.31 |
| DSC-nCBV 95$^{th}$ percentile | 4.28 ± 1.46 | 5.04 ± 1.71 | 0.46 (0-1.14) | 0.18 | 4.58 ± 0.32 | 4.71 ± 1.39 | 0.1 (0-2.16) | 0.84 |
| DSC-nCBV IQR | 1.46 ± 0.55 | 1.86 ± 0.83 | 0.53 (0-1.15) | 0.12 | 1.51 ± 0.28 | 1.49 ± 0.54 | 0.03 (0-1.57) | 0.95 |
| ***MGMT*** | | | | | | | | |
| | **Tumor** | | | | **Edema** | | | |
| Perfusion parameter | *MGMT*meth (mean ± SD) | *MGMT* nonmeth (mean ± SD) | Cohen's d (95% CI) | p-value | *MGMT*meth (mean ± SD) | *MGMT* nonmeth (mean ± SD) | Cohen's d (95% CI) | p-value |
| | n = 17 | n = 14 | | | n = 7 | n = 10 | | |
| ASL-nCBF 5$^{th}$ percentile | 0.55 ± 0.22 | 0.56 ± 0.13 | 0.04 (0-0.8) | 0.92 | 0.42 ± 0.11 | 0.46 ± 0.11 | 0.31 (0-1.48) | 0.52 |
| ASL-nCBF median | 0.97 ± 0.38 | 1.01 ± 0.42 | 0.1 (0-0.83) | 0.78 | 1.00 ± 0.85 | 0.69 ± 0.18 | 0.54 (0-2.32) | 0.37 |
| ASL-nCBF 95$^{th}$ percentile | 1.62 ± 0.80 | 1.70 ± 0.85 | 0.09 (0-0.74) | 0.80 | 1.97 ± 1.66 | 1.18 ± 0.44 | 0.67 (0-2.32) | 0.26 |
| ASL-nCBF IQR | 0.48 ± 0.43 | 0.53 ± 0.38 | 0.12 (0-0.88) | 0.73 | 0.70 ± 0.76 | 0.26 ± 0.10 | **0.86** (0-2.44) | 0.18 |
| DSC-nCBV 5$^{th}$ percentile | 0.26 ± 0.52 | 0.51 ± 0.74 | 0.38 (0-1.15) | 0.31 | 0.22 ± 0.26 | 0.03 ± 0.31 | 0.62 (0-1.53) | 0.19 |
| DSC-nCBV median | 2.0 ± 0.93 | 2.29 ± 1.92 | 0.19 (0-0.95) | 0.62 | 1.35 ± 0.55 | 1.18 ± 0.58 | 0.29 (0-1.31) | 0.54 |
| DSC-nCBV 95$^{th}$ percentile | 5.64 ± 1.85 | 6.74 ± 4.80 | 0.31 (0-1.01) | 0.43 | 4.64 ± 1.70 | 4.51 ± 1.48 | 0.08 (0-1.22) | 0.87 |
| DSC-nCBV IQR | 2.16 ± 1.13 | 2.43 ± 1.87 | 0.18 (0-0.94) | 0.64 | 1.53 ± 0.79 | 1.49 ± 0.73 | 0.05 (0-1.14) | 0.92 |

**Table 8**. DSC-nCBF distributions in tumor and edema of *IDH*-mutant/wildtype, p*TERT*-mutant/wildtype, 1p19q-non/codeleted, and *MGMT*-non/methylated gliomas. * indicates significant p-values (p<0.05) after the Benjamini-Hochberg procedure.

| | | | | | | | | |
|---|---|---|---|---|---|---|---|---|
| | | | | ***IDH*** | | | | |
| | Tumor | | | | Edema | | | |
| Perfusion parameter | *IDH*mut (mean ± SD) | *IDH*wt (mean ± SD) | Cohen's d (95% CI) | p-value | *IDH*mut (mean ± SD) | *IDH*wt (mean ± SD) | Cohen's d (95% CI) | p-value |
| | n = 33 | n = 33 | | | n = 11 | n = 23 | | |
| DSC-nCBF 5th percentile | 0.24 ± 0.39 | 0.41 ± 0.73 | 0.29 (0-0.76) | 0.24 | 0.07 ± 0.3 | 0.10 ± 0.25 | 0.13 (0-0.94) | 0.75 |
| DSC-nCBF median | 1.42 ± 0.70 | 2.74 ± 1.52 | **1.1** (0.68-1.52) | **4.3e-5*** | 1.25 ± 0.48 | 1.34 ± 0.62 | 0.14 (0-0.81) | 0.67 |
| DSC-nCBF 95th percentile | 4.60 ± 2.04 | 7.39 ± 3.87 | **0.89** (0.48-1.23) | **6.1e-4*** | 4.35 ± 1.49 | 5.15 ± 2.22 | 0.38 (0-0.9) | 0.23 |
| DSC-nCBF IQR | 1.59 ± 0.83 | 2.83 ± 1.50 | **1.0 (0.5-1.4)** | **1.4e-4*** | 1.38 ± 0.541 | 1.74 ± 0.92 | 0.43 (0-0.91) | 0.16 |
| | | | | **p*TERT*** | | | | |
| | Tumor | | | | Edema | | | |
| | p*TERT*mut (mean ± SD) | p*TERT*wt (mean ± SD) | Cohen's d (95% CI) | p-value | p*TERT*mut (mean ± SD) | p*TERT*wt (mean ± SD) | Cohen's d (95% CI) | p-value |
| | n = 24 | n = 14 | | | n = 13 | n = 5 | | |
| DSC-nCBF 5th percentile | 0.30 ± 0.57 | 0.23 ± 0.36 | 0.13 (0-0.76) | 0.66 | 0.09 ± 0.17 | -0.01 ± 0.37 | 0.37 (0-2.44) | 0.61 |
| DSC-nCBF median | 2.28 ± 1.43 | 1.55 ± 0.86 | 0.57 (0.03-1.07) | 0.057 | 1.39 ± 0.57 | 0.79 ± 0.46 | **1.06** (0.29-2.08) | **0.0443** |
| DSC-nCBF 95th percentile | 6.80 ± 4.13 | 5.24 ± 2.34 | 0.42 (0-0.84) | 0.148 | 5.56 ± 2.69 | 3.24 ± 1.19 | **0.92** (0-1.46) | **0.0228** |
| DSC-nCBF IQR | 2.60 ± 1.69 | 1.77 ± 0.93 | 0.55 (0-0.99) | 0.056 | 1.88 ± 1.07 | 1.01 ± 0.36 | **0.88** (0.28-1.4) | **0.0202** |
| | | | | **1p/19q** | | | | |
| | Tumor | | | | Edema | | | |
| | 1p/19q codel (mean ± SD) | 1p/19q noncodel (mean ± SD) | Cohen's d (95% CI) | p-value | 1p/19q codel (mean ± SD) | 1p/19q noncodel (mean ± SD) | Cohen's d (95% CI) | p-value |
| | n = 14 | n = 14 | | | n = 4 | n = 6 | | |
| DSC-nCBF 5th percentile | 0.28 ± 0.42 | 0.19 ± 0.51 | 0.18 (0-0.92) | 0.60 | 0.16 ± 0.29 | -0.01 ± 0.3 | 0.52 (0-1.83) | 0.40 |
| DSC-nCBF median | 1.49 ± 0.68 | 1.59 ± 1.05 | 0.1 (0-0.74) | 0.76 | 1.5 ± 0.16 | 1.22 ± 0.59 | 0.54 (0-1.6) | 0.30 |
| DSC-nCBF 95th percentile | 4.32 ± 1.66 | 5.21 ± 2.07 | 0.45 (0-1.1) | 0.19 | 4.72 ± 0.49 | 4.59 ± 2.03 | 0.07 (0-1.23) | 0.89 |
| DSC-nCBF IQR | 1.49 ± 0.59 | 1.83 ± 0.77 | 0.47 (0-1.14) | 0.17 | 1.61 ± 0.36 | 1.51 ± 0.68 | 0.15 (0-1.64) | 0.77 |
| | | | | ***MGMT*** | | | | |
| | Tumor | | | | Edema | | | |
| | *MGMT*meth (mean ± SD) | *MGMT* nonmeth (mean ± SD) | Cohen's d (95% CI) | p-value | *MGMT*meth (mean ± SD) | *MGMT* nonmeth (mean ± SD) | Cohen's d (95% CI) | p-value |
| | n = 17 | n = 14 | | | n = 7 | n = 10 | | |
| DSC-nCBF 5th percentile | 0.19 ± 0.46 | 0.33 ± 0.6 | 0.25 (0-0.97) | 0.50 | 0.14 ± 0.20 | -0.02 ± 0.24 | 0.7 (0-1.61) | 0.15 |
| DSC-nCBF median | 1.82 ± 0.8 | 2.15 ± 1.89 | 0.23 (0-0.99) | 0.55 | 1.28 ± 0.56 | 1.13 ± 0.65 | 0.23 (0-1.32) | 0.62 |
| DSC-nCBF 95th percentile | 5.65 ± 1.37 | 6.99 ± 5.59 | 0.34 (0-1.27) | 0.40 | 4.63 ± 1.43 | 5.07 ± 3.31 | 0.15 (0-0.96) | 0.72 |
| DSC-nCBF IQR | 2.06 ± 0.73 | 2.61 ± 2.24 | 0.33 (0-1.1) | 0.40 | 1.52 ± 0.63 | 1.69 ± 1.26 | 0.16 (0-0.94) | 0.71 |

**Table 9**. Post-hoc power analysis results for the promising perfusion parameters in p*TERT* mutation, 1p/19q-codeletion, and *MGMT* alteration status classification.

| Molecular marker | Perfusion parameter of interest | Feasible sample size of subgroup ASL-nCBF / DSC-nCBV |
|---|---|---|
| p*TERT* | Median tumor | 28 / 37 |
| p*TERT* | 95$^{th}$ percentile edema | 33 / 11 |
| 1p/19q | Median edema | 19 / 55 |
| *MGMT* | Median tumor | 1570 / 435 |

### 3.1.2 Subgroup Analysis

*IDH* and p*TERT* markers were chosen for the subgroup analysis with tumor mean and edema 95th percentile of ASL-nCBF and DSC-nCBV as best-performing features (Table 10). Despite limited sample sizes, significant differences were observed in tumor and edema between p*TERT*-mut and p*TERT*-wt gliomas within the *IDH*-wt subgroup ($p = 0.0081$ for tumor median ASL-nCBF and $p = 0.0143$ for 95th percentile of edema DSC-nCBV). Median tumor perfusion significantly differentiated astrocytomas and glioblastomas, as well as oligodendrogliomas and glioblastomas for both ASL-nCBF and DSC-nCBV (corrected $p < 0.05$) (Table 11). Significant perfusion signal differences were observed in both ASL-nCBF and DSC-nCBV median tumor parameters in LGG and HGG subgroups (corrected $p < 0.05$) (Table 12).

**Table 10**. Perfusion signal distributions within *IDH* and p*TERT* subgroups for the best-performing statistical descriptors in tumor and edema.

| **p*TERT* differentiation within *IDH*wt subgroup** | | | | |
|---|---|---|---|---|
| Perfusion parameter | *IDH*wt p*TERT*wt (mean ± SD) | *IDH*wt p*TERT*mut (mean ± SD) | Cohen's d (95% CI) | p-value |
| | n = 4 | n = 17 | | |
| Tumor median ASL-nCBF | 0.86 ± 0.13 | 1.19 ± 0.35 | **0.95** (0.35-1.56) | **0.0081** |
| Tumor median DSC-nCBV | 1.76 ± 0.69 | 2.82 ± 1.65 | 0.66 (0-1.22) | 0.067 |
| | n = 2 | n = 11 | | |
| Edema 95$^{th}$ percentile ASL-nCBF | 0.86 ± 0.1 | 1.49 ± 1.05 | 0.6 (0-0.89) | 0.075 |
| Edema 95$^{th}$ percentile DSC-nCBV | 2.86 ± 0.55 | 5.16 ± 1.4 | **1.59** (0.82-2.64) | **0.0143** |
| **p*TERT* differentiation within *IDH*mut subgroup** | | | | |
| Perfusion parameter | *IDH*mut p*TERT*wt (mean ± SD) | *IDH*mut p*TERT*mut (mean ± SD) | Cohen's d (95% CI) | p-value |
| | n = 10 | n = 7 | | |
| Tumor median ASL-nCBF | 0.83 ± 0.31 | 0.91 ± 0.41 | 0.21 (0-1.39) | 0.68 |
| Tumor median DSC-nCBV | 1.55 ± 0.71 | 1.63 ± 0.51 | 0.11 (0-0.95) | 0.81 |
| | n = 3 | n = 2 | | |
| Edema 95$^{th}$ percentile ASL-nCBF | 0.98 ± 0.23 | 2.95 ± 1.96 | **1.24** (0.55-8.2) | 0.39 |
| Edema 95$^{th}$ percentile DSC-nCBV | 3.76 ± 1.81 | 4.74 ± 0.38 | 0.47 (0-1) | 0.45 |
| ***IDH* differentiation within p*TERT*wt subgroup** | | | | |
| Perfusion parameter | p*TERT*wt *IDH*wt (mean ± SD) | p*TERT*wt *IDH*mut (mean ± SD) | Cohen's d (95% CI) | p-value |
| | n = 4 | n = 10 | | |
| Tumor median ASL-nCBF | 0.86 ± 0.13 | 0.83 ± 0.31 | 0.12 (0-1.18) | 0.76 |
| Tumor median DSC-nCBV | 1.76 ± 0.69 | 1.55 ± 0.71 | 0.28 (0-1.65) | 0.63 |
| | n = 2 | n = 3 | | |
| Edema 95$^{th}$ percentile ASL-nCBF | 0.86 ± 0.1 | 0.98 ± 0.23 | 0.45 (0-4.04) | 0.48 |
| Edema 95$^{th}$ percentile DSC-nCBV | 2.86 ± 0.55 | 3.76 ± 1.81 | 0.43 (0-1) | 0.49 |
| ***IDH* differentiation within p*TERT*mut subgroup** | | | | |
| Perfusion parameter | p*TERT*mut *IDH*wt (mean ± SD) | p*TERT*mut *IDH*mut (mean ± SD) | Cohen's d (95% CI) | p-value |
| | n = 17 | n = 7 | | |
| Tumor median ASL-nCBF | 1.19 ± 0.35 | 0.91 ± 0.41 | 0.74 (0-1.64) | 0.14 |
| Tumor median DSC-nCBV | 2.82 ± 1.65 | 1.63 ± 0.51 | **0.81** (0.15-1.35) | **0.0137** |
| | n = 11 | n = 2 | | |
| Edema 95$^{th}$ percentile ASL-nCBF | 1.49 ± 1.05 | 2.95 ± 1.96 | **1.17** (0-6.84) | 0.48 |
| Edema 95$^{th}$ percentile DSC-nCBV | 5.16 ± 1.4 | 4.74 ± 0.38 | 0.3 (0-1.02) | 0.42 |

**Table 11**. Perfusion signal distributions in diffuse glioma entities. ***** indicates significant p-values ($p < 0.05$) after the Benjamini-Hochberg procedure.

**Astrocytoma and oligodendroglioma differentiation**

| Perfusion parameter | Astrocytoma (mean ± SD) | Oligodendroglioma (mean ± SD) | Cohen's d (95% CI) | p-value |
|---|---|---|---|---|
| | n = 24 | n = 14 | | |
| Tumor median ASL-nCBF | 0.93 ± 0.4 | 0.84 ± 0.31 | 0.22 (0-0.81) | 0.48 |
| Tumor median DSC-nCBV | 1.87 ± 1.18 | 1.57 ± 0.58 | 0.29 (0-0.79) | 0.31 |
| | n = 11 | n = 4 | | |
| Edema 95$^{th}$ percentile ASL-nCBF | 1.07 ± 0.28 | 2.01 ± 1.57 | **1.11** (0-3.47) | 0.32 |
| Edema 95$^{th}$ percentile DSC-nCBV | 4.34 ± 1.08 | 4.58 ± 0.32 | 0.24 (0-0.93) | 0.51 |

**Astrocytoma and glioblastoma differentiation**

| Perfusion parameter | Astrocytoma (mean ± SD) | Glioblastoma (mean ± SD) | Cohen's d (95% CI) | p-value |
|---|---|---|---|---|
| | n = 24 | n = 33 | | |
| Tumor median ASL-nCBF | 0.93 ± 0.4 | 1.22 ± 0.41 | 0.71 (0.09-1.23) | **0.0098*** |
| Tumor median DSC-nCBV | 1.87 ± 1.18 | 3.01 ± 1.69 | 0.75 (0.18-1.2) | **0.0041*** |
| | n = 11 | n = 25 | | |
| Edema 95$^{th}$ percentile ASL-nCBF | 1.07 ± 0.28 | 1.21 ± 0.73 | 0.21 (0-0.69) | 0.42 |
| Edema 95$^{th}$ percentile DSC-nCBV | 4.34 ± 1.08 | 4.92 ± 1.4' | 0.43 (0-1.13) | 0.19 |

**Oligodendroglioma and glioblastoma differentiation**

| Perfusion parameter | Oligodendroglioma (mean ± SD) | Glioblastoma (mean ± SD) | Cohen's d (95% CI) | p-value |
|---|---|---|---|---|
| | n = 14 | n = 33 | | |
| Tumor median ASL-nCBF | 0.84 ± 0.31 | 1.22 ± 0.41 | **0.96** (0.3-1.47) | **0.0016*** |
| Tumor median DSC-nCBV | 1.57 ± 0.58 | 3.01 ± 1.69 | **0.97** (0.53-1.33) | **9.07e-5*** |
| | n = 4 | n = 25 | | |
| Edema 95$^{th}$ percentile ASL-nCBF | 2.01 ± 1.57 | 1.21 ± 0.73 | **0.9** (0-4.36) | 0.39 |
| Edema 95$^{th}$ percentile DSC-nCBV | 4.58 ± 0.32 | 4.92 ± 1.4' | 0.25 (0-0.74) | 0.31 |

**Table 12**. Perfusion signal distributions in low-grade (LGG) and high-grade (HGG) gliomas. * indicates significant p-values ($p < 0.05$) after the Benjamini-Hochberg procedure.

| **LGG and HGG differentiation** | | | | |
|---|---|---|---|---|
| | | Tumor | | |
| Perfusion parameter | LGG (mean ± SD) n=19 | HGG (mean ± SD) n=47 | Cohen's d (95% CI) | p-value |
| Tumor median ASL-nCBF | 0.82 ± 0.29 | 1.13 ± 0.43 | 0.77 (0.3-1.16) | **0.0011*** |
| Tumor median DSC-nCBV | 1.56 ± 0.54 | 2.62 ± 1.63 | 0.73 (0.41-1.02) | **1.1e-4*** |
| | | Edema | | |
| | LGG (mean ± SD) n=5 | HGG (mean ± SD) n=31 | Cohen's d (95% CI) | p-value |
| Edema 95$^{th}$ percentile ASL-nCBF | 1.78 ± 1.46 | 1.18 ± 0.63 | 0.77 (0-4.12) | 0.42 |
| Edema 95$^{th}$ percentile DSC-nCBV | 4.66 ± 0.33 | 4.73 ± 1.34 | 0.05 (0-0.47) | 0.78 |

### 3.1.3 Univariate Classification

Good performance (AUROCC around 0.8) was demonstrated in differentiation of the *IDH* mutation status using a single descriptor of ASL-nCBF or DSC-nCBV (Figure 23 (A) and (B)), with the highest AUROCC achieved by the median tumor DSC-nCBV (AUROCC = 0.83). Both tumor and edema perfusion parameters showed potential in classifying p*TERT* status. Here, the IQR and 95th percentile of DSC-nCBV within edema demonstrated superior performance, achieving the highest AUROCC (0.81 and 0.8). In the task of classifying the 1p/19q-codeletion status, only ASL-nCBF parameters (IQR and median) within the edema region showed strong performance (AUROCC 0.85 and 0.81, respectively) (Table 13). Finally, none of the perfusion parameters exhibited potential in the univariate classification of the *MGMT* methylation status.

**A**

***IDH* status prediction**

| | Tumor | | | | Edema | | | |
|---|---|---|---|---|---|---|---|---|
| Perfusion parameter | Threshold | AUROCC (95% CI) | Sensitivity (95% CI) | Specificity (95% CI) | Threshold | AUROCC (95% CI) | Sensitivity (95% CI) | Specificity (95% CI) |
| ASL-nCBF 5th percentile | 0.54 | **0.80 (0.66-0.89)** | 0.76 (0.59-0.89) | 0.82 (0.66-0.94) | 0.23 | 0.49 (0.29-0.72) | 1 (1-1) | 0 (0-0) |
| ASL-nCBF median | 1.03 | **0.82 (0.69-0.89)** | 0.61 (0.42-0.77) | 0.88 (0.73-0.97) | 1.03 | 0.58 (0.35-0.77) | 0.18 (0-0.56) | 0.96 (0.77-1) |
| ASL-nCBF 95th percentile | 1.54 | **0.82 (0.70-0.91)** | 0.70 (0.52-0.84) | 0.82 (0.67-0.93) | 4.34 | 0.45 (0.25-0.66) | 0.09 (0-0.52) | 0.96 (0.78-1) |
| ASL-nCBF IQR | 0.46 | **0.75 (0.61-0.86)** | 0.64 (0.46-0.79) | 0.88 (0.73-0.97) | 1.87 | 0.47 (0.26-0.71) | 0.09 (0-0.53) | 1 (1-1) |
| DSC-nCBV 5th percentile | 0.77 | 0.55 (0.40-0.70) | 0.42 (0.25-0.60) | 0.85 (0.68-0.94) | -0.34 | 0.51 (0.28-0.74) | 1 (1-1) | 0.09 (0-0.44) |
| DSC-nCBV median | 2.25 | **0.83 (0.69-0.92)** | 0.76 (0.58-0.89) | 0.94 (0.78-1.0) | 0.55 | 0.44 (0.25-0.67) | 1 (1-1) | 0.09 (0-0.76) |
| DSC-nCBV 95th percentile | 5.55 | **0.83 (0.69-0.91)** | 0.73 (0.56-0.87) | 0.85 (0.69-0.95) | 3.13 | 0.58 (0.36-0.79) | 0.96 (0.8-1) | 0.18 (0-0.55) |
| DSC-nCBV IQR | 2.20 | **0.82 (0.69-0.91)** | 0.64 (0.48-0.81) | 0.91 (0.76-0.97) | 0.87 | 0.61 (0.41-0.80) | 0.91 (0.70-1) | 0.27 (0-0.58) |

**B**

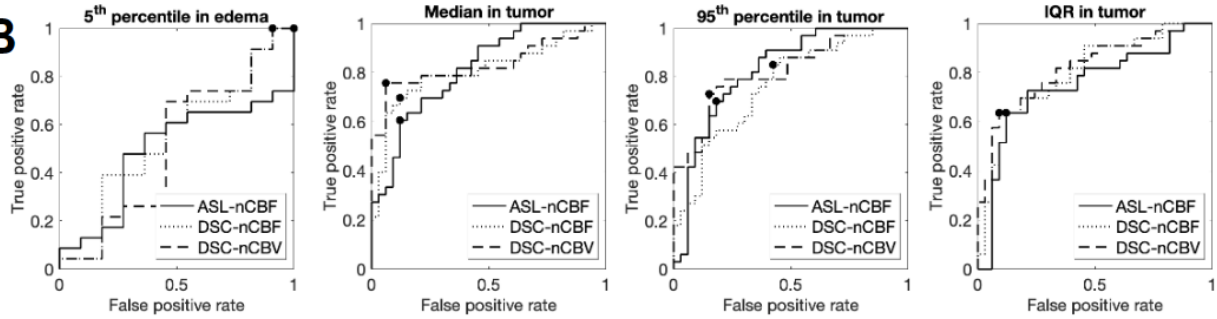


**C**

**p*TERT* status prediction**

| | Tumor | | | | Edema | | | |
|---|---|---|---|---|---|---|---|---|
| Perfusion parameter | Threshold | AUROCC (95% CI) | Sensitivity (95% CI) | Specificity (95% CI) | Threshold | AUROCC (95% CI) | Sensitivity (95% CI) | Specificity (95% CI) |
| ASL-nCBF 5th percentile | 0.54 | 0.67 (0.50-0.82) | 0.67 (0.46-0.84) | 0.69 (0.43-0.88) | 0.28 | 0.53 (0.19-0.83) | 0.92 (0.57-1) | 0.14 (0-0.67) |
| ASL-nCBF median | 1.0 | **0.70 (0.50-0.84)** | 0.63 (0.42-0.80) | 0.88 (0.58-1.0) | 0.70 | 0.60 (0.31-0.84) | 0.69 (0.4-0.92) | 0.71 (0.25-1) |
| ASL-nCBF 95th percentile | 1.63 | 0.68 (0.49-0.83) | 0.54 (0.32-0.73) | 0.88 (0.62-1.0) | 0.99 | 0.69 (0.41-0.89) | 0.77 (0.46-0.93) | 0.57 (0.17-1) |
| ASL-nCBF IQR | 0.33 | 0.62 (0.42-0.77) | 0.71 (0.48-0.87) | 0.50 (0.24-0.77) | 0.23 | **0.70 (0.39-0.91)** | 0.77 (0.46-0.93) | 0.71 (0.2-1) |
| DSC-nCBV 5th percentile | -0.63 | 0.50 (0.32-0.67) | 1.0 (1.0-1.0) | 0 (0-0) | -0.12 | 0.48 (0.19-0.82) | 1.0 (1-1) | 0.29 (0-0.75) |
| DSC-nCBV median | 2.10 | 0.66 (0.48-0.84) | 0.63 (0.42-0.82) | 0.75 (0.47-0.93) | 0.98 | 0.67 (0.33-0.90) | 0.85 (0.54-1) | 0.57 (0.17-1) |
| DSC-nCBV 95th percentile | 4.30 | 0.69 (0.49-0.85) | 0.83 (0.63-0.96) | 0.38 (0.15-0.62) | 4.47 | **0.80 (0.48-0.98)** | 0.77 (0.46-0.93) | 0.86 (0.34-1) |
| DSC-nCBV IQR | 1.71 | **0.74 (0.57-0.88)** | 0.71 (0.50-0.87) | 0.69 (0.43-0.88) | 0.87 | **0.81 (0.54-0.96)** | 1.0 (1-1) | 0.43 (0-0.88) |

**D**

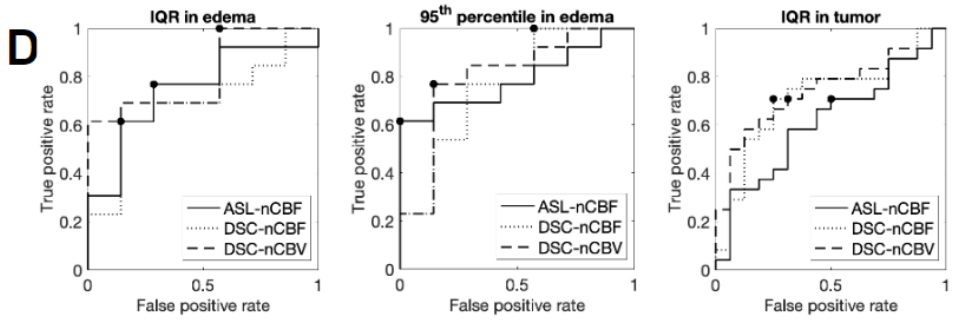


**Figure 23**. *IDH* and p*TERT* status prediction performance of ASL-nCBF and DSC-nCBV univariate models. (A) *IDH* prediction performance metrics. (B) Receiver operating characteristic curves of *IDH*-classifying perfusion descriptors with the highest AUROCC. (C) p*TERT* prediction performance metrics. (D) Receiver operating characteristic curves of p*TERT* classifying perfusion descriptors with the highest AUROCCю

**1p/19q**

| | Tumor | | | | Edema | | | |
|---|---|---|---|---|---|---|---|---|
| Perfusion parameter | Threshold | AUROCC (95% CI) | Sensitivity (95% CI) | Specificity (95% CI) | Threshold | AUROCC (95% CI) | Sensitivity (95% CI) | Specificity (95% CI) |
| ASL-nCBF 5th percentile | 0.87 | 0.58 (0.38-0.75) | 0.11 (0-0.35) | 1.0 (1.0-1.0) | 0.61 | 0.46 (0.06-0.88) | 0 (0-0) | 1.0 (1.0-1.0) |
| ASL-nCBF median | 1.82 | 0.49 (0.31-0.69) | 0.06 (0-0.28) | 1.0 (1.0-1.0) | 1.03 | **0.81 (0.18-1)** | 0.50 (0-1.0) | 1.0 (1.0-1.0) |
| ASL-nCBF 95th percentile | 1.18 | 0.49 (0.31-0.67) | 0.72 (0.47-0.91) | 0.43 (0.22-0.65) | 4.34 | 0.73 (0.24-0.97) | 0.25 (0-1.0) | 1.0 (1.0-1.0) |
| ASL-nCBF IQR | 2.03 | 0.39 (0.21-0.60) | 0.07 (0-0.44) | 1.0 (1.0-1.0) | 0.44 | **0.85 (0.44-1)** | 0.50 (0-1.0) | 1.0 (1.0-1.0) |
| DSC-nCBV 5th percentile | 2.01 | 0.54 (0.34-0.72) | 0 (0-0) | 1.0 (1.0-1.0) | 0.73 | 0.69 (0.24-0.98) | 0.25 (0-1.0) | 1.0 (1.0-1.0) |
| DSC-nCBV median | 2.95 | 0.35 (0.19-0.54) | 0.17 (0.05-0.40) | 0.95 (0.76-1.0) | 1.41 | **0.77 (0.46-0.93)** | 1.0 (1.0-1.0) | 0.77 (0.43-0.93) |
| DSC-nCBV 95th percentile | 5.23 | 0.47 (0.29-0.67) | 0.50 (0.26-0.71) | 0.67 (0.44-0.84) | 5.58 | 0.61 (0.23-0.88) | 0.50 (0-1.0) | 0.82 (0.50-1.0) |
| DSC-nCBV IQR | 2.16 | 0.48 (0.30-0.68) | 0.39 (0.18-0.63) | 0.81 (0.58-0.94) | 2.92 | 0.58 (0.28-0.82) | 0 (0-0) | 1.0 (1.0-1.0) |

***MGMT***

| | Tumor | | | | Edema | | | |
|---|---|---|---|---|---|---|---|---|
| | Threshold | AUROCC (95% CI) | Sensitivity (95% CI) | Specificity (95% CI) | Threshold | AUROCC (95% CI) | Sensitivity (95% CI) | Specificity (95% CI) |
| ASL-nCBF 5th percentile | 0.43 | 0.56 (0.37-0.75) | 0.93 (0.57-1) | 0.40 (0.19-0.62) | 0.44 | 0.63 (0.33-0.85) | 0.7 (0.32-0.92) | 0.63 (0.20-1.0) |
| ASL-nCBF median | 1.54 | 0.49 (0.28-0.70) | 0.21 (0.06-0.53) | 0.95 (0.74-1.0) | 1.03 | 0.52 (0.17-0.86) | 0.29 (0-0.75) | 1.0 (1.0-1.0) |
| ASL-nCBF 95th percentile | 2.78 | 0.46 (0.27-0.68) | 0.29 (0.08-0.56) | 0.90 (0.71-1.0) | 4.34 | 0.55 (0.21-0.83) | 0.29 (0-0.79) | 1.0 (1.0-1.0) |
| ASL-nCBF IQR | 1.06 | 0.47 (0.27-0.70) | 0.29 (0.08-0.55) | 0.9 (0.67-1.0) | 0.44 | 0.61 (0.24-0.88) | 0.43 (0-0.80) | 1.0 (1.0-1.0) |
| DSC-nCBV 5th percentile | 1.38 | 0.58 (0.35-0.77) | 0.14 (0-0.44) | 1.0 (1.0-1.0) | 0.35 | 0.69 (0.31-0.92) | 0.57 (0.20-1.0) | 0.91 (0.56-1.0) |
| DSC-nCBV median | 7.63 | 0.49 (0.29-0.72) | 0.07 (0-0.37) | 1.0 (1.0-1.0) | 2.42 | 0.53 (0.26-0.83) | 0.14 (0-0.67) | 1.0 (1.0-1.0) |
| DSC-nCBV 95th percentile | 8.80 | 0.48 (0.26-0.71) | 0.36 (0.11-0.64) | 0.95 (0.78-1.0) | 7.22 | 0.51 (0.21-0.8) | 0.14 (0-0.63) | 1.0 (1.0-1.0) |
| DSC-nCBV IQR | 7.88 | 0.47 (0.26-0.68) | 0.07 (0-0.36) | 1.0 (1.0-1.0) | 2.99 | 0.48 (0.17-0.78) | 0.14 (0-0.95) | 1.0 (1.0-1.0) |

**Table 13**. 1p19q co-deletion and *MGMT* methylation status prediction performance of univariate ASL-nCBF and DSC-nCBV models.

### 3.1.4 Multivariate Classification

Multivariate models based on ASL- and DSC-derived parameters showed better performance in differentiating *IDH* and p*TERT* mutation status than the respective univariate models (Figure 24). For *IDH* status classification, DSC-nCBF and DSC-nCBV parameters achieved higher AUROCC (0.89 and 0.89, respectively) compared to ASL-nCBF (0.77). For p*TERT* mutation status, ASL-nCBF demonstrated a comparable AUROCC (0.8) to both DSC-nCBF and DSC-nCBV (0.74 and 0.86, respectively).

**A**

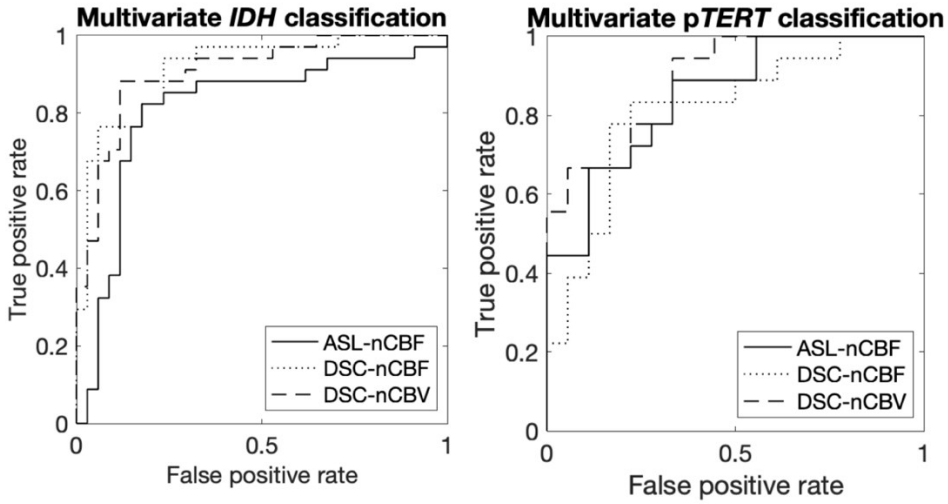


**B**

| | *IDH* | | | p*TERT* | | |
|---|---|---|---|---|---|---|
| Perfusion parameters | AUROCC (95% CI) | Sensitivity (95% CI) | Specificity (95% CI) | AUROCC (95% CI) | Sensitivity (95% CI) | Specificity (95% CI) |
| ASL-nCBF | **0.77 (0.52-0.90)** | 0.55 (0.2-0.86) | 0.96 (0.83-1) | **0.8 (0.53-1)** | 0.85 (0.5-1) | 0.4 (0-1) |
| DSC-nCBV | **0.89 (0.63-0.96)** | 0.82 (0.56-1) | 0.91 (0.73-1) | **0.86 (0.61-0.99)** | 0.85 (0.54-0.94) | 0.6 (0.25-1) |
| DSC-nCBF | **0.89 (0.76-0.98)** | 0.64 (0.36-0.98) | 0.91 (0.75-1) | **0.74 (0.27-1)** | 0.92 (0.75-1) | 0.4 (0-1) |

**Figure 24.** Predictive performance of multivariate logistic regression models built on ASL- and DSC-perfusion parameters. (A) ROC curves of *IDH* and p*TERT* classification models. (B) Performance metrics of *IDH*- and p*TERT*-classification models.

### 3.1.5 Correlation Analysis

Scatterplots of key ASL-nCBF and DSC-nCBV classification features in tumor and edema are displayed in Figure 25. ASL data affected by macrovascular and minor motion artifacts were comparable to the good-quality data in terms of *IDH* and p*TERT* status differentiation. The results of the correlation analysis indicated a stronger correlation between ASL and DSC

perfusion parameters in the tumor region compared to the edema (Table 14). A significant correlation was observed between ASL-nCBF and DSC-nCBF, as well as ASL-nCBF and DSC-nCBV in all statistical descriptors except the 5th percentile in edema. The correlation between ASL-nCBF and DSC-nCBV was stronger than between ASL-nCBF and DSC-nCBF in the 95th percentile and IQR in both tumor and edema.

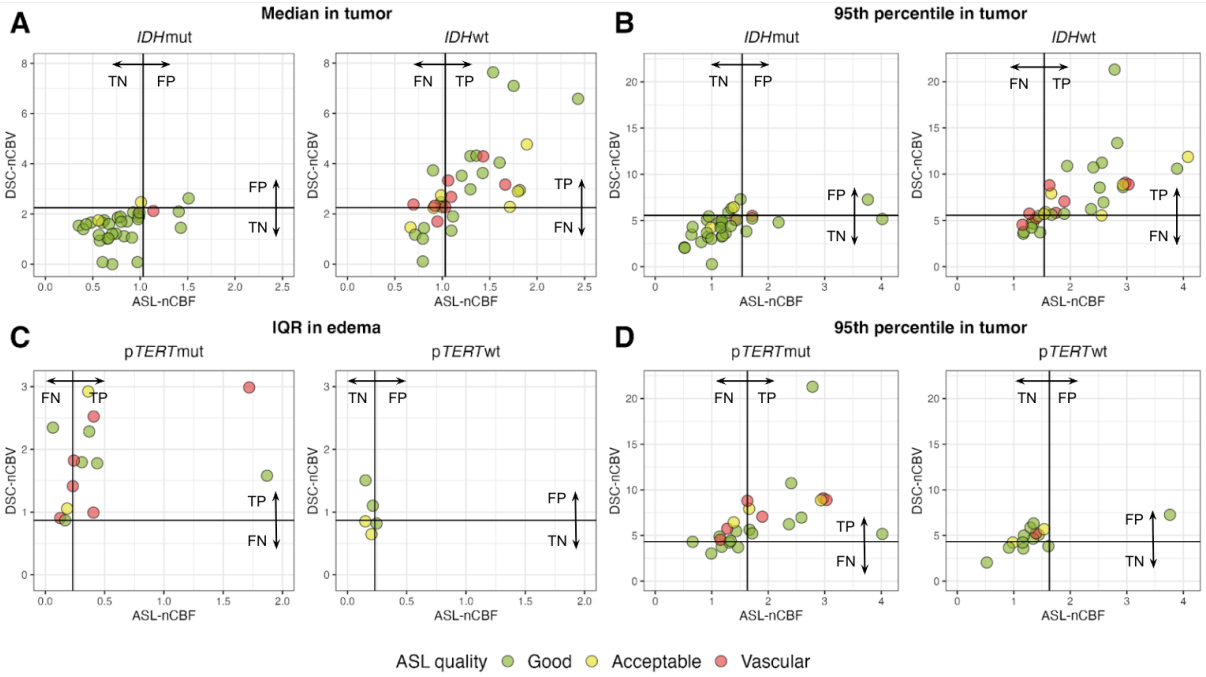


**Figure 26.** Scatterplots of ASL-nCBF and DSC-nCBV parameters in *IDH*-wildtype/mutant and p*TERT*-wildtype/mutant. TP – true positive, TN – true negative, FP – false positive, FN– false negative. Black horizontal lines indicate thresholds of univariate predictive models. Here, *IDH*-wildtype/mutant and p*TERT*-mutant/wildtype represent positive/negative cases respectively, according to the signal distribution analysis.

**Table 14**. Results of the correlation analysis between ASL and DSC perfusion parameters in tumor and edema.

| | | ASL-nCBF vs DSC-nCBF | | ASL-nCBF vs DSC-nCBV | |
|---|---|---|---|---|---|
| ROI | Histogram parameter | $r_s$ | Corrected p-value | $r_s$ | Corrected p-value |
| Tumor | 5$^{th}$ percentile | 0.28 | 0.049 | 0.26 | 0.047 |
| | Median | 0.67 | <0.001 | 0.65 | <0.001 |
| | 95$^{th}$ percentile | 0.68 | <0.001 | 0.78 | <0.001 |
| | IQR | 0.64 | <0.001 | 0.74 | <0.001 |
| Edema | 5$^{th}$ percentile | 0.18 | 0.41 | 0.12 | 0.410 |
| | Median | 0.61 | <0.001 | 0.63 | <0.001 |
| | 95$^{th}$ percentile | 0.34 | 0.045 | 0.37 | 0.045 |
| | IQR | 0.36 | 0.049 | 0.45 | 0.005 |

### 3.2 Pediatric Perfusion

All subjects had $PCASL_{3PLD}$ acquired. 81 scans were obtained, of which 86.4% were classified as good, 12.3% as acceptable, and 1.2% exhibited vascular features; no scans were excluded due to poor quality. Figure 27 provides an overview of the experimental data, and Figure 28 and Table 15 describe the CBF and ATT distributions across ROIs and PCASL variants.

#### 3.2.1 Hemodynamic parameters in multi-delay ASL

No significant difference was observed in ATT between $PCASL_{3PLD}$ and $PCASL_{7PLD}$ ($p > 0.51$) (Table 16). In $PCASL_{3PLD}$, ATT was significantly higher in WM compared to GM ($p = 0.004$, $d = 0.29$) and higher in WM compared to TB ($p = 0.005$, $d = 0.28$). In $PCASL_{7PLD}$, ATT was also significantly higher in WM than in GM and TB ($p < 0.001$, $d = 0.63$ and $p < 0.001$, $d = 0.56$, respectively).

In GM, AT-correction significantly increased $PCASL_{3PLD}$ GM-CBF by 11.6% while having no significant effect on $PCASL_{7PLD}$ GM-CBF. In WM, AT-correction did not impact $PCASL_{3PLD}$ WM-CBF but significantly increased it in $PCASL_{7PLD}$ by 10.2%. For TB, AT-correction significantly raised $PCASL_{3PLD}$ TB-CBF by 10.1% on average, with

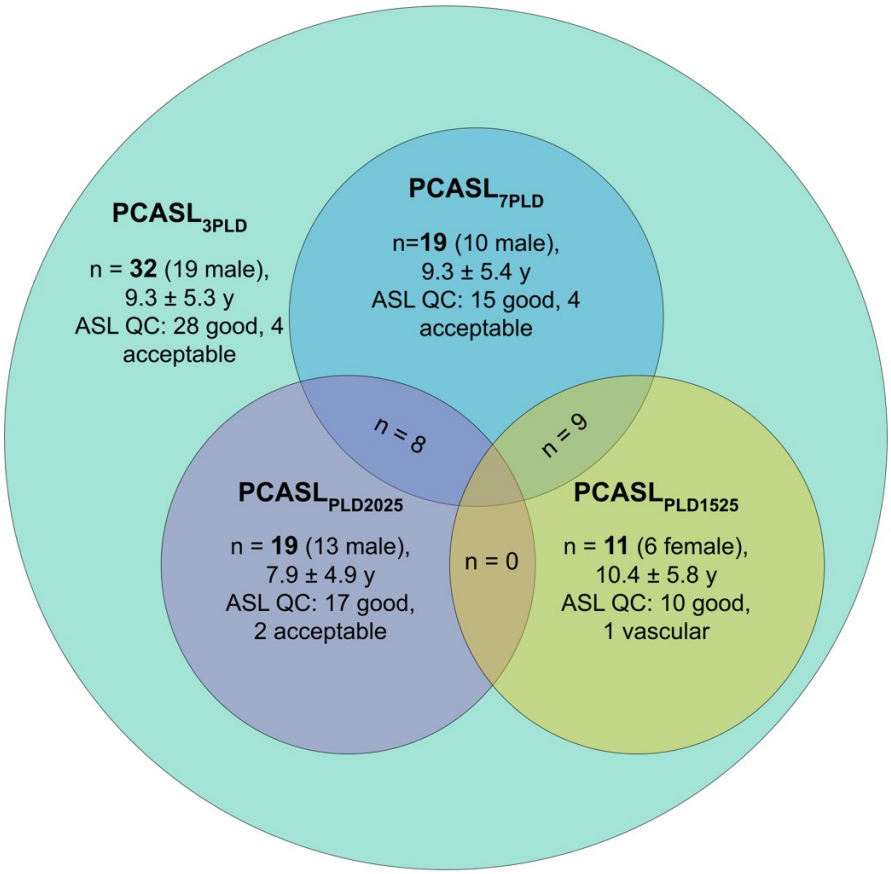


**Figure 27.** Venn diagram of analyzed datasets. "n" indicates the sample sizes, and age is presented as mean ± standard deviation.

no notable effect on TB-CBF in $PCASL_{7PLD}$. After AT-correction, there was no significant difference between $PCASL_{ATC\text{-}3PLD}$ and $PCASL_{ATC\text{-}7PLD}$ TB-CBF. Therefore, we will use $PCASL_{ATC\text{-}3PLD}$ as a reference for multi-delay parameters in further analysis. No significant differences in GM $CBF_{ATC\text{-}3PLD}$ were observed between male and female or between sedated and non-sedated participants ($p = 0.78$, $d = 0.11$; $p = 0.47$, $d = 0.25$, respectively).

Overall, $PCASL_{ATC\text{-}3PLD}$ CBF in GM was significantly higher than in TB ($p < 0.001$, $d = 4.7$), and CBF in TB was significantly higher than in WM ($p < 0.001$, $d = 5.7$).

### 3.2.2 Comparison of regional multi- and single-delay ASL CBF

$PCASL_{PLD2025}$ GM-CBF and $PCASL_{PLD1525}$ GM-CBF were significantly higher than $PCASL_{ATC\text{-}3PLD}$ GM-CBF (Table 16). On average, $PCASL_{PLD2025}$ and $PCASL_{PLD1525}$ GM-CBF were 23.6% and 25.4% higher than $PCASL_{ATC\text{-}3PLD}$ GM-CBF. Similar trends in WM

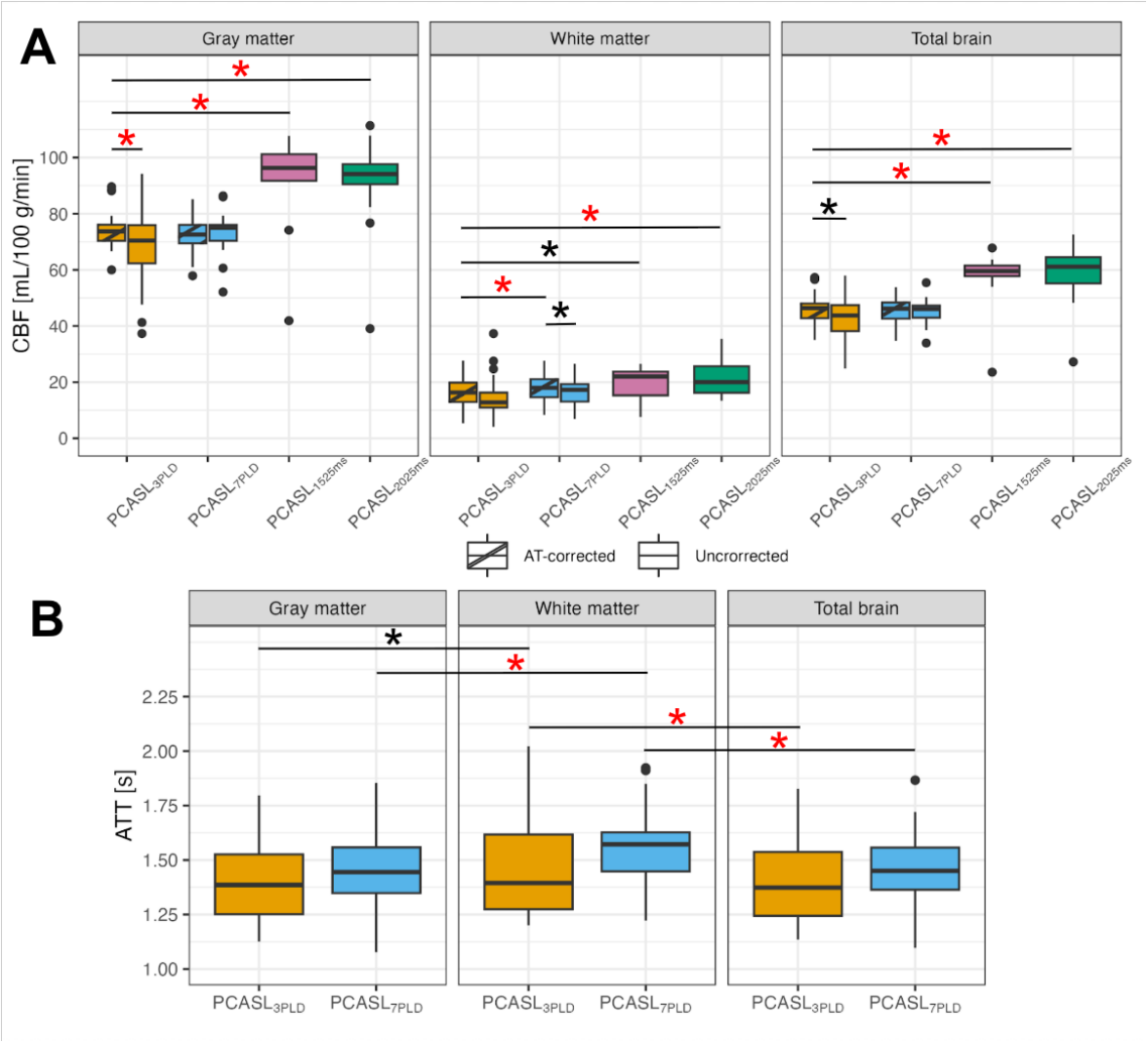


**Figure 28.** A. Boxplots of CBF distributions in the TB, GM, and WM regions. B. Boxplots of ATT distributions in the TB, GM, and WM regions. Red stars indicate significant differences with p-values <0.05 after FWER correction. Black stars indicate significant differences with p-values <0.05 before FWER correction.

were observed; $PCASL_{PLD2025}$ WM-CBF and $PCASL_{PLD1525}$ WM-CBF were significantly higher than $PCASL_{ATC\text{-}3PLD}$ WM-CBF. On average, $PCASL_{PLD2025ms}$ and $PCASL_{PLD1525ms}$ WM-CBF were 24% and 31.7% higher than $PCASL_{ATC\text{-}3PLD}$ WM-CBF. Finally, in TB, there was again a significant difference between $PCASL_{PLD2025}$ TB-CBF and $PCASL_{PLD1525}$ TB-CBF compared to $PCASL_{ATC\text{-}3PLD}$ TB-CBF. On average, $PCASL_{PLD2025}$ and $PCASL_{PLD1525}$ TB-CBF were 24.6% and 30.2% higher than $PCASL_{ATC\text{-}3PLD}$ TB-CBF.

**Table 15.** Mean ± standard deviation of CBF and ATT in pediatric population.

| | $PCASL_{3PLD}$ | $PCASL_{7PLD}$ | $PCASL_{PLD2025}$ | $PCASL_{PLD1525}$ |
|---|---|---|---|---|
| Sample size | n=32 | n=19 | n=19 | n=10 |
| Uncorrected CBF [ml/100 g/min] | | | | |
| GM CBF | 68.3 ± 12.7 | 73.2 ± 8.0 | 91.9 ± 15.0 | 91.0 ± 19.8 |
| WM CBF | 13.5 ± 4.9 | 16.6 ± 5.0 | 21.8 ± 6.3 | 19.4 ± 5.9 |
| TB CBF | 42.7 ± 7.8 | 45.2 ± 4.7 | 58.8 ± 10.0 | 56.7 ± 12.2 |
| AT-corrected CBF [ml/100 g/min] | | | | |
| GM CBF | 73.9 ± 6.2 | 72.3 ± 6.9 | - | - |
| WM CBF | 15.6 ± 4.5 | 17.8 ± 5.0 | - | - |
| TB CBF | 45.8 ± 5.2 | 45.2 ± 4.7 | - | - |
| ATT [s] | | | | |
| GM ATT | 1.39 ± 0.18 | 1.44 ± 0.20 | - | - |
| WM ATT | 1.46 ± 0.22 | 1.57 ± 0.21 | - | - |
| TB ATT | 1.40 ± 0.19 | 1.45 ± 0.21 | - | - |

**Table 16.** Comparative analysis of CBF and ATT parameters between PCASL types, reported as Cohen's d and p-values. "*" indicates p-values < 0.05 after FWER correction.

| ROI | $PCASL_{ATC\text{-}3PLD}$ vs $PCASL_{PLD2025}$ CBF | $PCASL_{ATC\text{-}3PLD}$ vs $PCASL_{PLD1525}$ CBF | $PCASL_{ATC\text{-}3PLD}$ vs $PCASL_{ATC\text{-}7PLD}$ CBF |
|---|---|---|---|
| GM | **d = 1.31, p < 0.001*** | **d = 0.56, p = 0.004*** | d = 0.15, p = 0.27 |
| WM | **d = 0.61, p < 0.001*** | **d = 0.67, p = 0.02** | **d = 0.52, p = 0.003** |
| TB | **d = 1.26, p < 0.001*** | **d = 0.95, p = 0.002*** | d < 0.1, p = 0.44 |
| | $PCASL_{ATC\text{-}3PLD}$ vs $PCASL_{Uncorrected\_3PLD}$ CBF | $PCASL_{ATC\text{-}7PLD}$ vs $PCASL_{Uncorrected\_7PLD}$ CBF | $PCASL_{ATC\text{-}3PLD}$ vs $PCASL_{ATC\text{-}7PLD}$ ATT |
| GM | **d = 0.49, p = 0.004*,** | d = 0.11, p = 0.21 | d < 0.1, p = 0.51 |
| WM | d = 0.16, p = 0.29 | **d = 0.32, p = 0.03** | d < 0.1, p = 0.62 |
| TB | **d = 0.43, p = 0.01** | d < 0.1, p = 0.86 | d < 0.1, p = 0.82 |

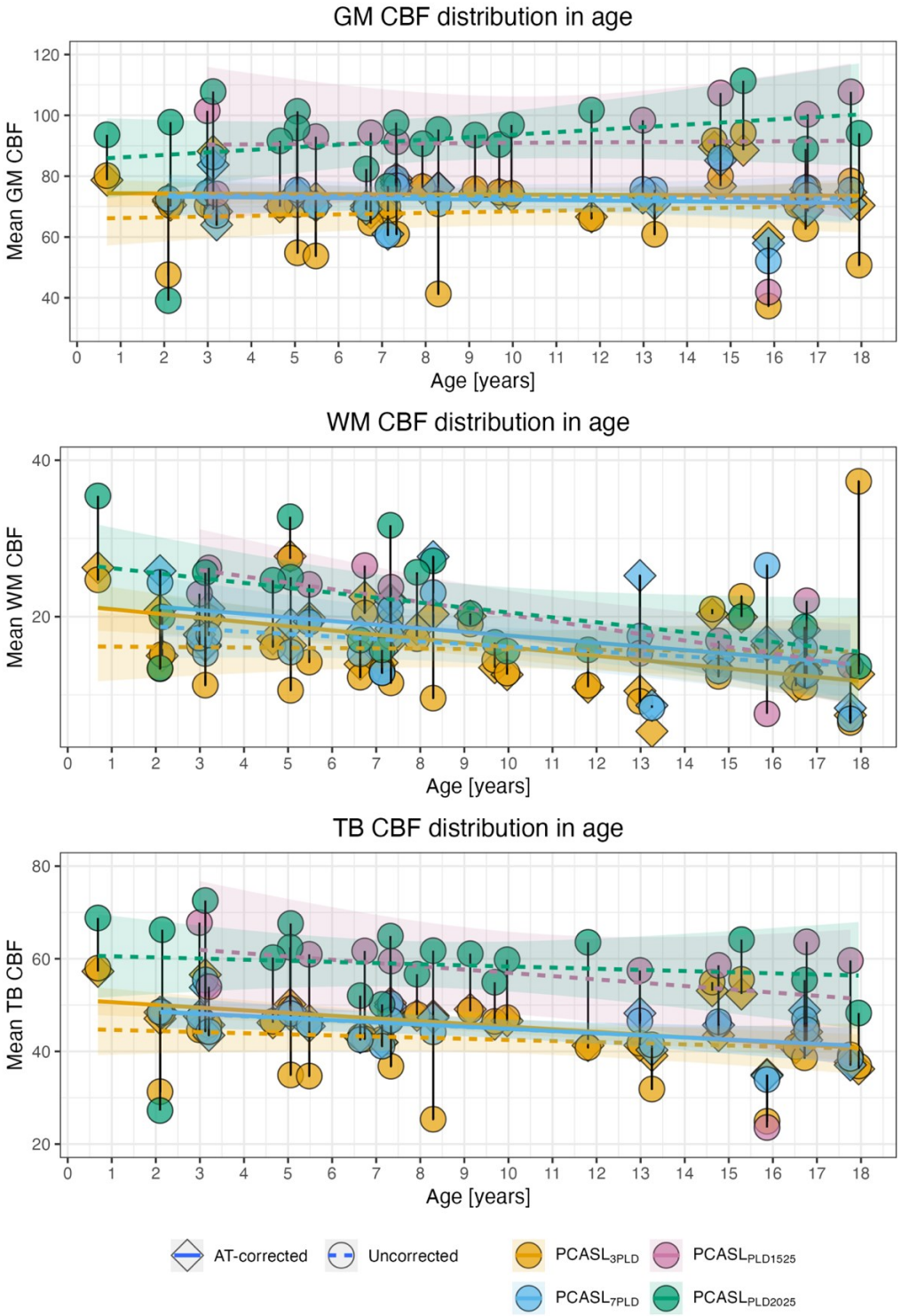


**Figure 29.** Changes of cerebral perfusion with age. A. GM CBF distribution in age. B. WM CBF distribution with age. C. TB CBF distribution with age.

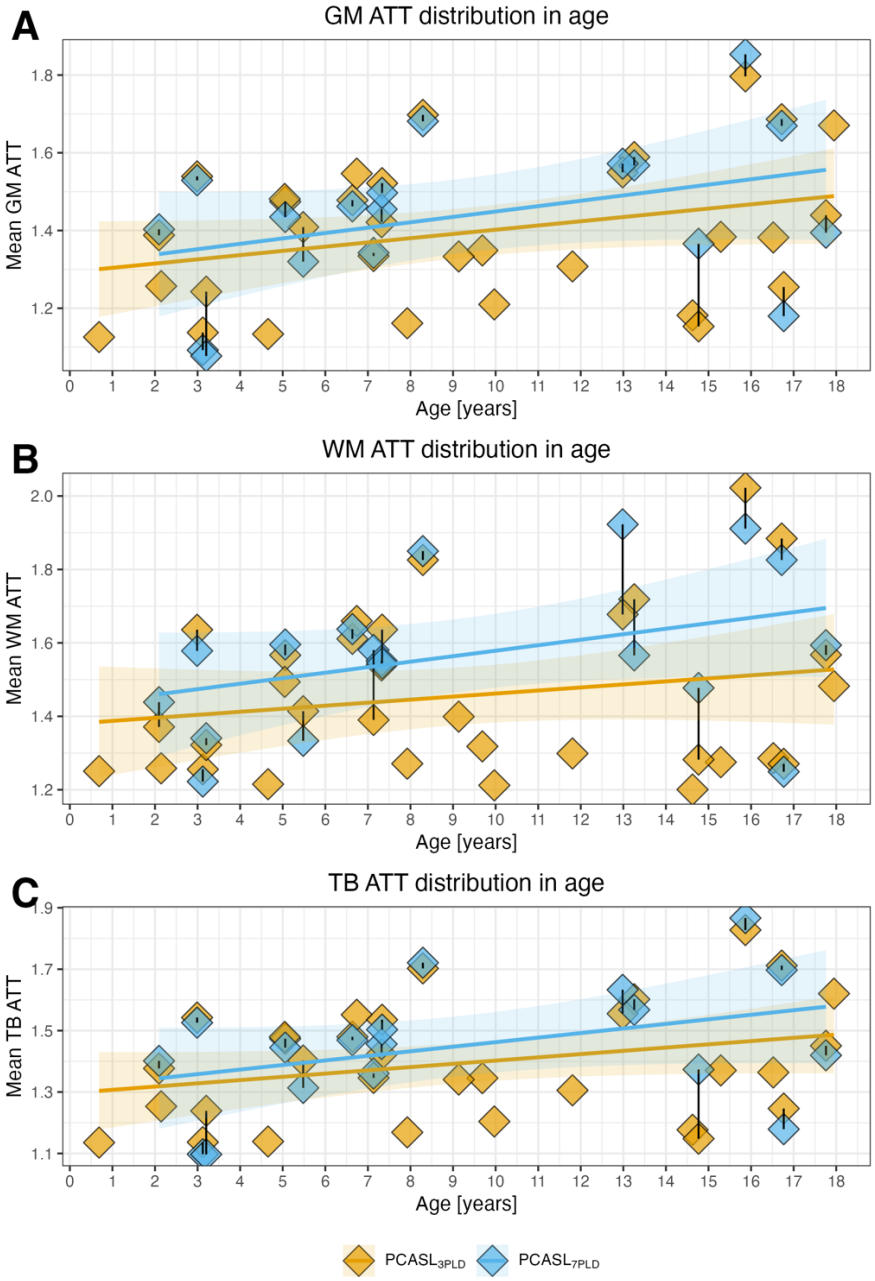


**Figure 30.** Changes of hemodynamic parameters with age. A. GM ATT distribution in age. B. WM ATT distribution in age. C. TB ATT distribution in age.

### 3.2.3 Hemodynamic trends in age

Figure 29 depicts the distribution of CBF across age, and Figure 30 shows the distribution of ATT across age. The correlation analysis revealed a negative association between $PCASL_{ATC\text{-}3PLD}$ CBF and age in both WM and TB (rho = -0.56, $p < 0.001$ and rho = -0.56, $p < 0.001$, respectively), but no significant linear correlation in GM (rho = -0.03, $p = 0.87$). The combined model analysis demonstrated significant differences in the linear regression slopes between GM and TB ($p = 0.01$) and between GM and WM ($p = 0.01$). In the

uncorrected $PCASL_{3PLD}$ and both AT-corrected and uncorrected $PCASL_{7PLD}$ sequences, no significant correlation with age was found across all ROIs, except for uncorrected $PCASL_{7PLD}$ CBF in TB (rho = -0.52, p = 0.03). Furthermore, significant differences were identified in the linear regression models between AT-corrected and uncorrected sequences for both WM (p = 0.02) and TB (p = 0.02). No significant differences were observed when comparing the linear regression models between $PCASL_{ATC\text{-}7PLD}$ and $PCASL_{ATC\text{-}3PLD}$ across GM, WM, and TB (p = 0.85, p = 0.71, p = 0.95, respectively). There was no significant difference between the linear models of the sedated and non-sedated populations (p = 0.07); however, a significant difference was observed between the linear models of female and male participants (p = 0.002) (Figure 31). GM and TB ATT showed a positive linear correlation with age ($r^2$ = 0.12, p = 0.019 and $r^2$ = 0.11, p = 0.021, respectively), but there was no significant correlation between WM ATT and age ($r^2$ = 0.08, p = 0.075) (Figure 31).

$PCASL_{3PLD}$ ATT showed a positive linear correlation with age in GM (rho = 0.39, p = 0.03) but no significant correlation in WM or TB (rho = 0.11, p = 0.53 and rho = 0.28, p = 0.12, respectively). For $PCASL_{7PLD}$ ATT, no significant correlations were observed across any ROIs. Additionally, there were no significant differences in the $PCASL_{3PLD}$ linear regression models between WM and GM or between WM and TB (p = 0.27 and p = 0.47, respectively). While $PCASL_{7PLD}$ WM-ATT did not exhibit a positive correlation with age, there was no significant difference between the linear regression models of $PCASL_{7PLD}$ WM-ATT and $PCASL_{3PLD}$ WM-ATT (p = 0.30).

The voxel-wise analysis results for the correlation between $PCASL_{ATC\text{-}3PLD}$ CBF and ATT with age are presented in Figure 32. Regions with significant negative correlations between CBF and age were primarily localized in the WM and cerebellum. In contrast, regions with significant positive correlations between ATT and age were located in the cerebellum and GM.

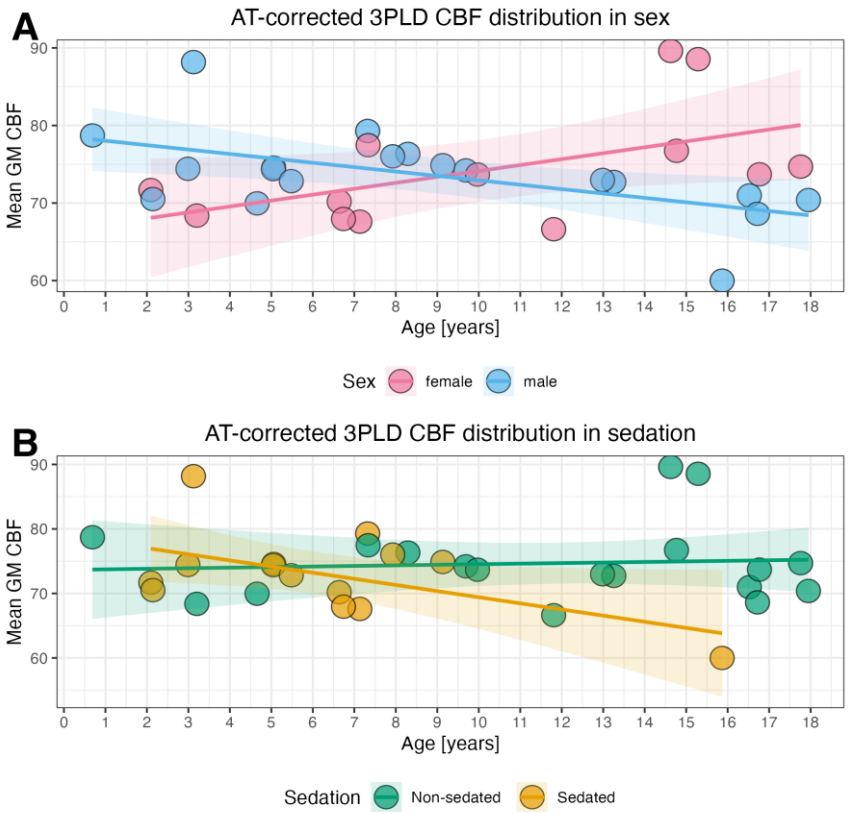


**Figure 31.** Changes in CBF across separate subpopulations. A. Linear regression models for male and female groups. B. Linear regression models for sedated and non-sedated populations.

### 3.2.4 Tissue volume trends across age

Figure 33 shows the correlation of absolute and relative GM and WM volumes with age, while Table 17 presents the correlation analysis results between volumetric parameters, age, and $PCASL_{3PLD}$ CBF. Relative GM volume (to ICV) correlated negatively with age, without a significant correlation with $PCASL_{3PLD}$ GM-CBF. In WM, $PCASL_{3PLD}$ WM-CBF correlated negatively with both absolute and relative WM volumes, while age correlated positively with both. For TB, there was a significant negative correlation between the absolute volume of combined GM and WM with $PCASL_{3PLD}$ TB-CBF and a positive correlation with age.

### 3.2.5 Hemodynamic variations in the pediatric population

Population mean CBF and ATT are visualized in Figures 34 and 35. Population analysis of CoV (Figure 36) points out the increased variance of perfusion in WM and some deep GM structures such as the thalami and putamen.

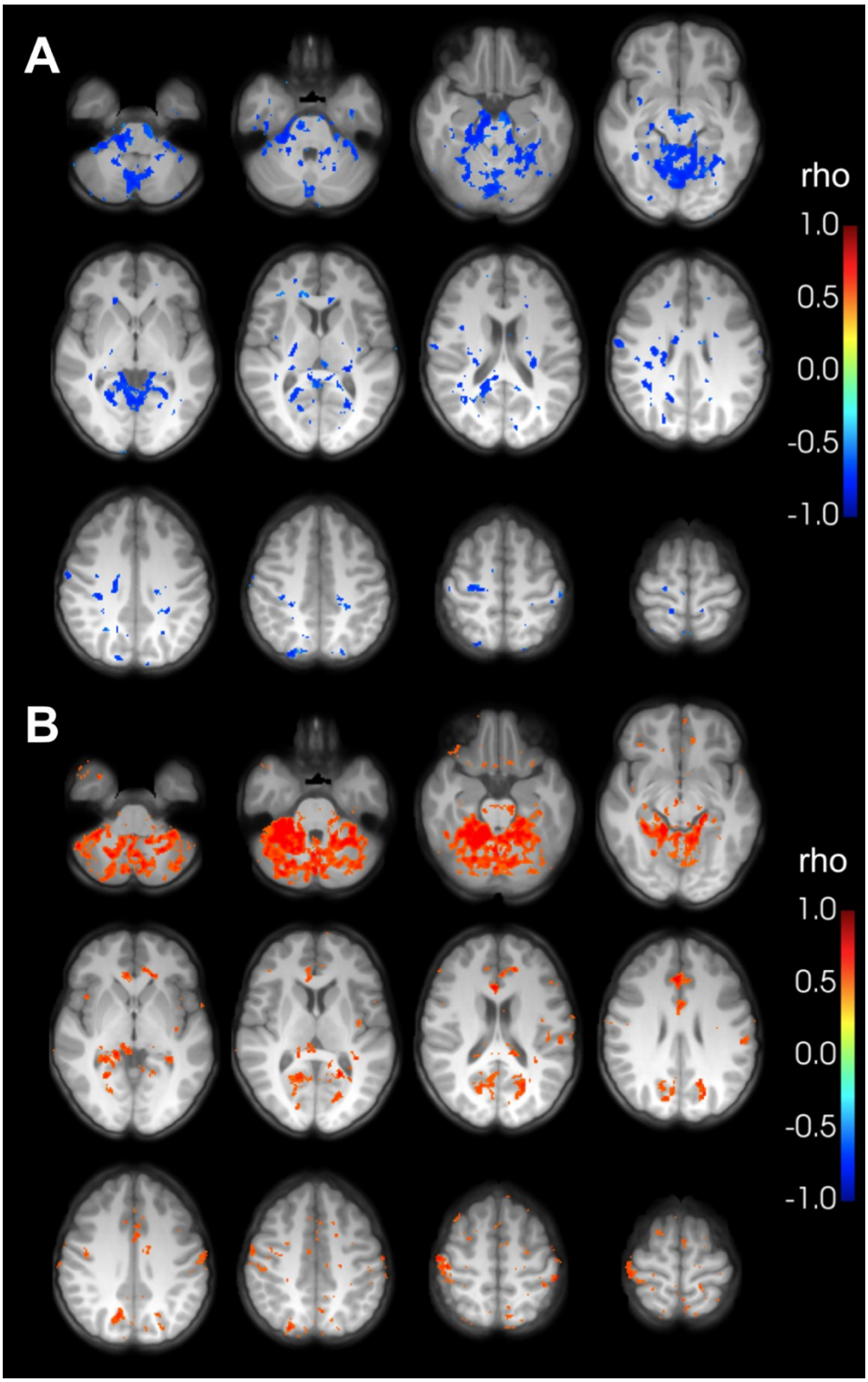


**Figure 32.** Voxel-wise correlation between $PCASL_{3PLD}$ CBF (A) and ATT (B) with age, overlaid on the population T1-weighted image. Only voxels with statistically significant correlations (uncorrected for FWER) are displayed.

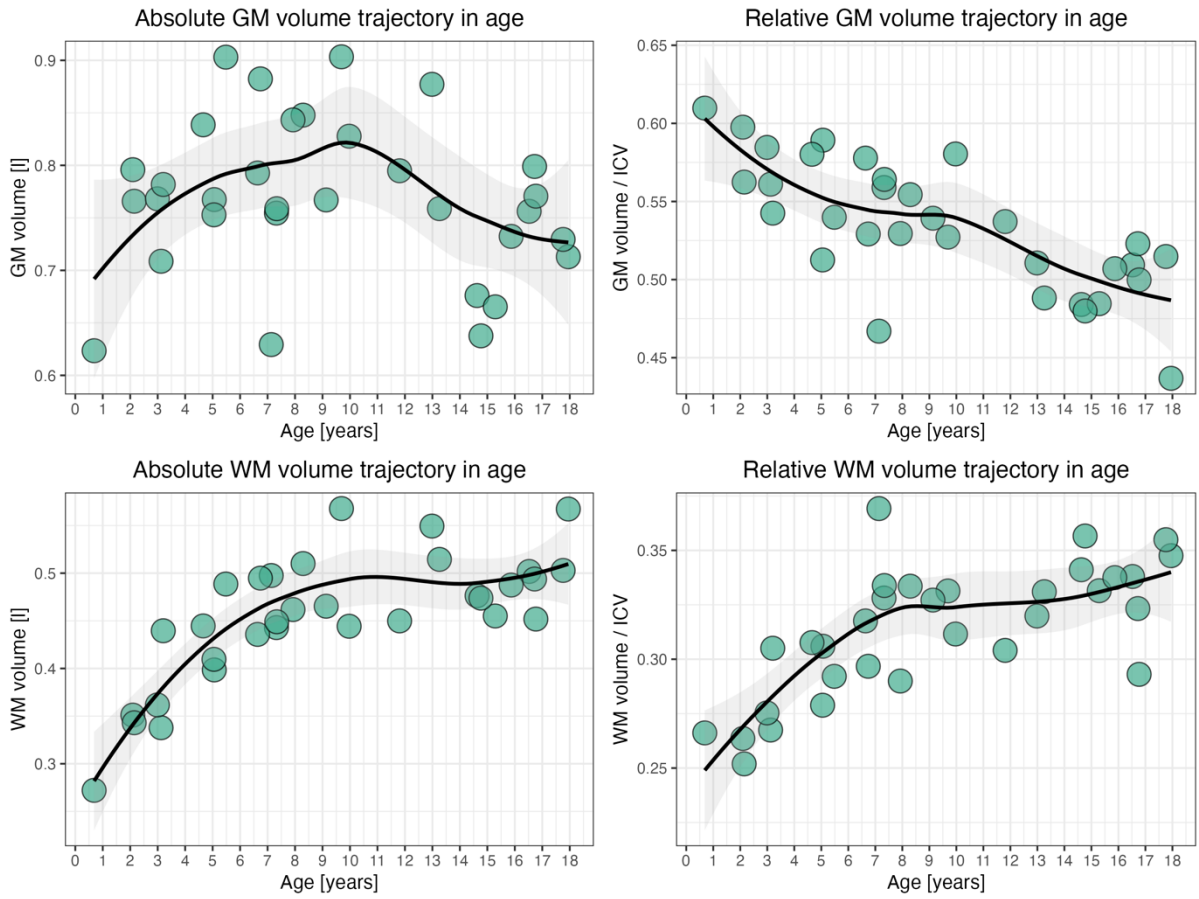


**Figure 33.** Absolute and relative GM and WM volume trends in age.

**Table 17.** Correlation analysis of WM and GM volumes with age and regional CBF. Highlighted in bold are results with $p < 0.05$. "*" indicates p-values < 0.05 after FWER correction. rho – Spearman rank correlation coefficient.

| | Absolute GM volume | GM ICV ratio | Absolute WM volume | WM ICV ratio | Absolute GM + WM volume | GM + WM ICV ratio |
|---|---|---|---|---|---|---|
| Age | rho = -0.13, p = 0.46 | **rho = -0.75, p < 0.001*** | **rho = 0.72, p < 0.001*** | **rho = 0.71, p < 0.001*** | **rho = 0.36, p = 0.046** | rho = 0.26, p = 0.15 |
| $PCASL_{ATC\text{-}3PLD}$ GM CBF | rho = -0.34, p = 0.057 | rho = 0.10, p = 0.59 | | | | |
| $PCASL_{ATC\text{-}3PLD}$ WM CBF | | | **rho = -0.42, p = 0.02** | **rho = -0.36, p = 0.046** | | |
| $PCASL_{ATC\text{-}3PLD}$ TB CBF | | | | | **rho = -0.46, p = 0.008*** | rho = 0.08, p = 0.68 |

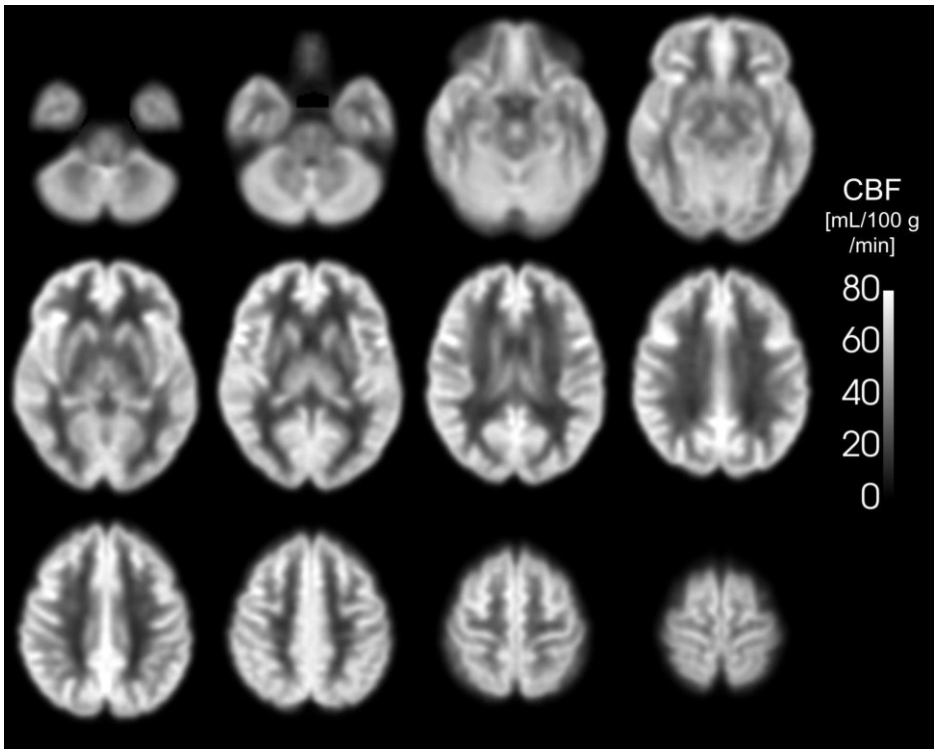


**Figure 34**. Population mean $PCASL_{3PLD}$ CBF.

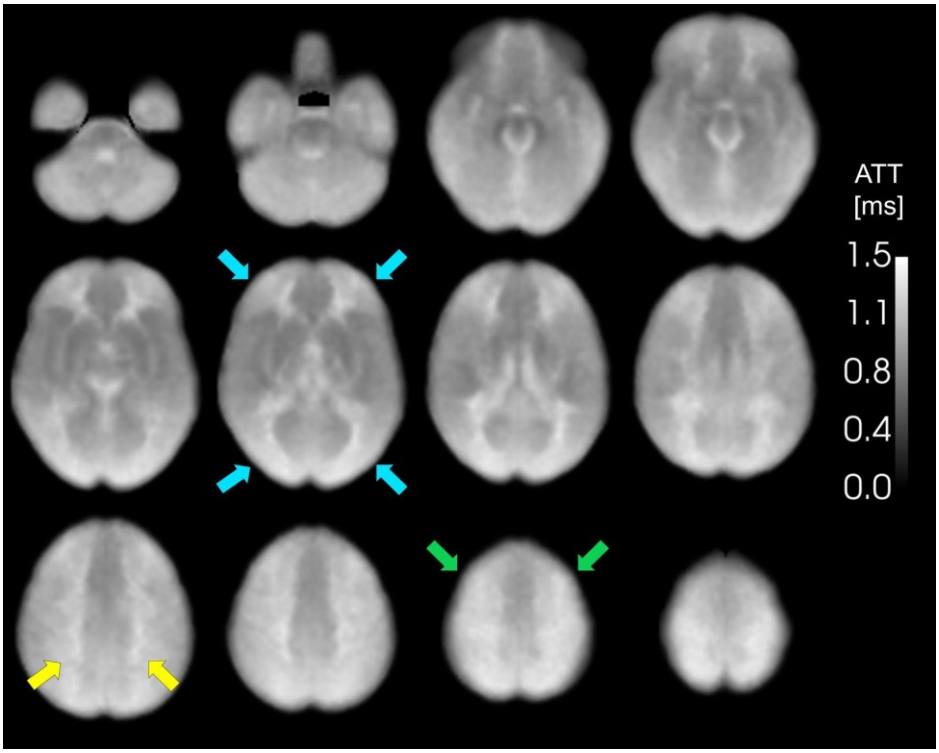


**Figure 35**. Population mean $PCASL_{3PLD}$ ATT. Blue arrows (middle row, second from left) indicate watershed regions with elevated ATT. Yellow arrows (bottom row, first on the left) highlight areas of deep white matter with elevated ATT. Green arrows (bottom row, third from left) point to regions of elevated ATT in superior brain areas.

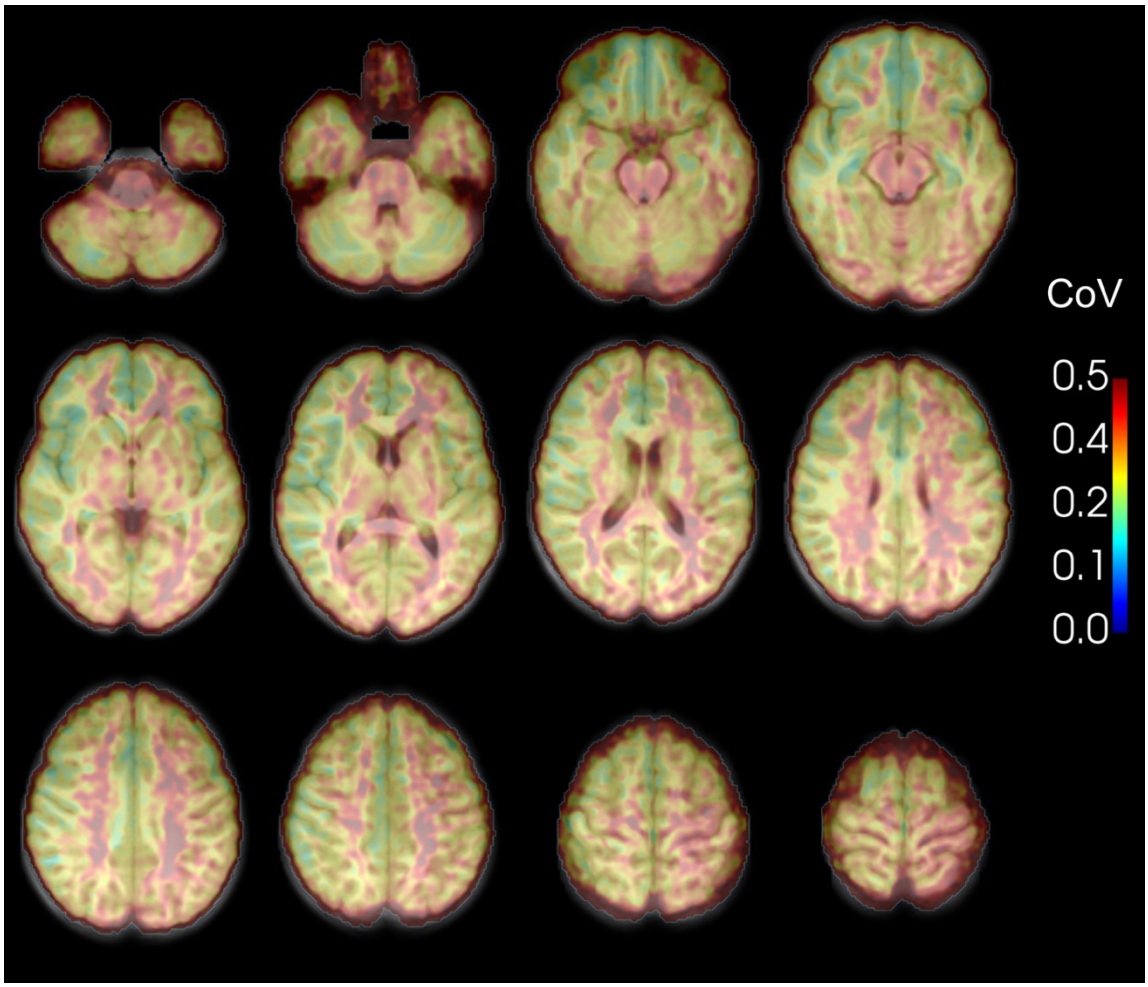


**Figure 36.** Population $PCASL_{3PLD}$ CoV map overlaid on the population T1-weighted image.

### 3.3 Neonatal Perfusion

As shown in Figure 37, forty-eight subjects were included in the analysis (25 males, mean GA 28.7 ± 2.6 weeks, mean PNA 9.7 ± 5.0 weeks, mean PMA 38.5 ± 3.4 weeks, mean weight at scanning 3.25 ± 1.20 kg, mean birth weight 1.13 ± 0.35). There was a significant correlation between GA and PNA age in the analyzed dataset ($r = -0.77$, $p < 0.001$). Overall, 10 (20.8%) participants were born due to spontaneous labor with intact membranes, 12 (25%) due to PPROM, 17 (35.4%) due to maternal indications, and 8 (16.7%) due to fetal indications. One participant (2.1%) had an unknown cause of birth, as the participant was transferred from another medical facility. All participants were scanned with $PCASL_{7PLD}$, 47 with $PCASL_{1PLD}$, and 37 with $PCASL_{3PLD}$; 36 subjects were scanned with all 3 sequences. Sensitivity analysis has not shown any significant differences in sex, PNA, GA, or weight at scanning among the subdatasets, as shown in Table 18.

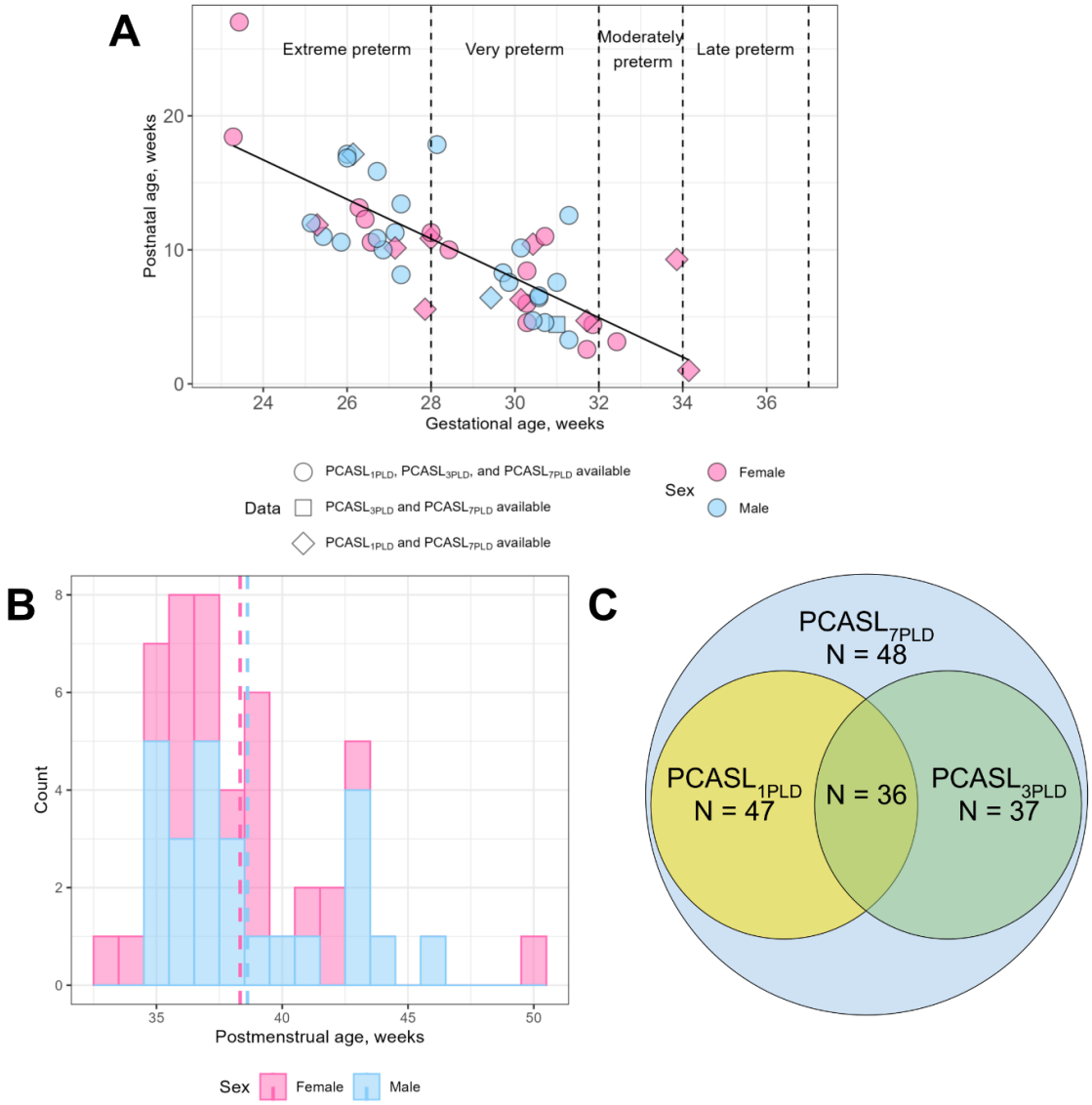


**Figure 37.** Demographic characteristics of the analyzed dataset. **A.** Scatterplot showing the distribution of PNA and GA in the study population, along with data availability. **B.** Histogram illustrating the distribution of PMA in the analyzed population. Dashed lines indicate the mean PMA for female and male populations. **C.** Venn diagram representing the availability of data across sequence types.

### 3.3.1 Image Quality Assessment

As shown in Table 19, quality control analysis of ASL data showed a significant difference both in scan quality and the abundance of artifacts among the sequences. $PCASL_{3PLD}$ sequence was least prone to artifacts and led to the best quality, while $PCASL_{7PLD}$ was the only sequence that suffered from an insufficient signal-to-noise ratio (SNR). $PCASL_{1PLD}$ was most prone to evident motion artifacts. The consistency of ASL scan quality among

**Table 18.** Sensitivity analysis of analyzed subdatasets.

| | $PCASL_{7PLD}$ | $PCASL_{3PLD}$ | $PCASL_{1PLD}$ | p-value |
|---|---|---|---|---|
| Sex | 25 m / 23 f | 23 m / 14 f | 24 m / 23 f | 0.55 |
| PNA | 9.74 ± 4.96 w | 10.11 ± 5.15 w | 9.86 ± 4.97 w | 0.95 |
| GA | 28.74 ± 2.60 w | 28.52 ± 2.49 w | 28.69 ± 2.60 w | 0.92 |
| Weight at scanning | 3.25 ± 1.20 kg | 3.34 ± 1.21 kg | 3.28 ± 1.19 kg | 0.95 |
| Birth weight | 1.13 ± 0.35 kg | 1.13 ± 0.36 kg | 1.13 ± 0.36 kg | 0.99 |
| Cause of preterm labor | 10 spontaneous labor with intact membranes, 12 PPROM, 17 maternal indications, 8 fetal indications, 1 unknown | 10 spontaneous labor with intact membranes, 9 PPROM, 13 maternal indications, 4 fetal indications, 1 unknown | 10 spontaneous labor with intact membranes, 12 PPROM, 16 maternal indications, 8 fetal indications, 1 unknown | 0.99 |

**Table 19.** Results of ASL quality control.

| | | $PCASL_{7PLD}$ | $PCASL_{3PLD}$ | $PCASL_{1PLD}$ | p-value |
|---|---|---|---|---|---|
| QC | Good | 33 (68.8%) | 31 (83.8%) | 26 (55.3%) | 0.0299 |
| | Acceptable | 5 (10.4%) | 3 (8.1%) | 11 (23.4%) | |
| | Unusable | 10 (20.8%) | 3 (8.1%) | 10 (21.3%) | |
| Artifacts | No artifacts | 33 (68.8%) | 31 (83.8%) | 26 (55.3%) | 0.0076 |
| | Lacking signal | 3 (6.25%) | 0 | 0 | |
| | Motion | 12 (25%) | 6 (16.2%) | 21 (44.7%) | |

sequences is visualized in Figure 38. Examples of quality assessment are shown in Figure 39.

Structural quality control showed much better quality for T2w scans (70.8% “good”, 25% “acceptable”, 4.2% “unusable”) than for T1w scans (27% “good”, 47.9% “acceptable”, 25% “unusable”), with a fair agreement of within-session scores (kappa = 0.246, p = 0.0079). In

the patients with “unusable” quality of T1w scans, the quality of ASL scans was below average (only 50% of $PCASL_{1PLD}$, 41.6% of $PCASL_{3PLD}$, and 66.6% of $PCASL_{7PLD}$ scans were of “good” or “acceptable” quality). Patients with “unusable” quality of T2w scans had 50% of $PCASL_{1PLD}$ and $PCASL_{7PLD}$ of “good” and “acceptable” quality.

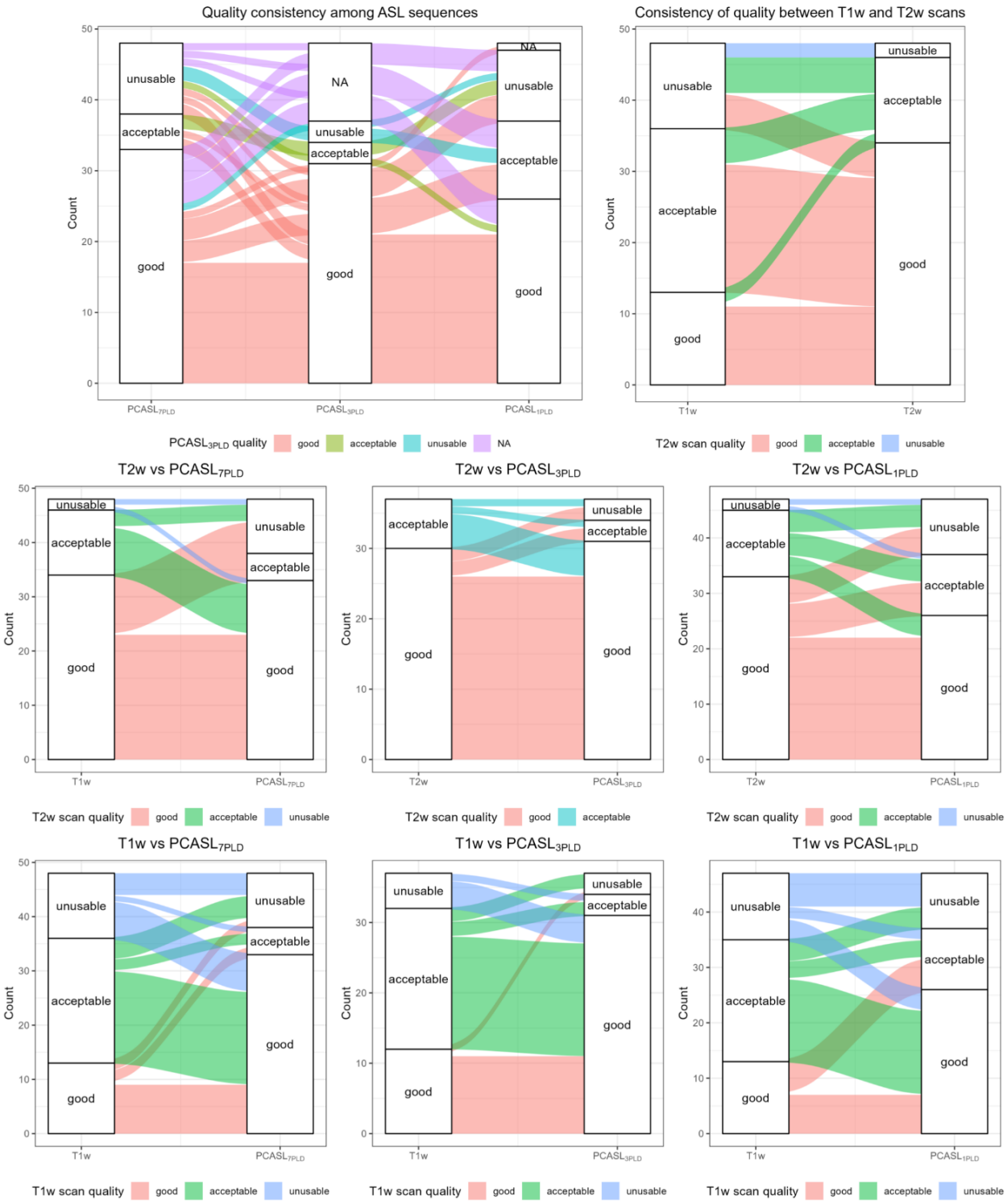


**Figure 38.** Alluvial plot of quality consistency among ASL and structural sequences. ”NA” stands for not available scans.

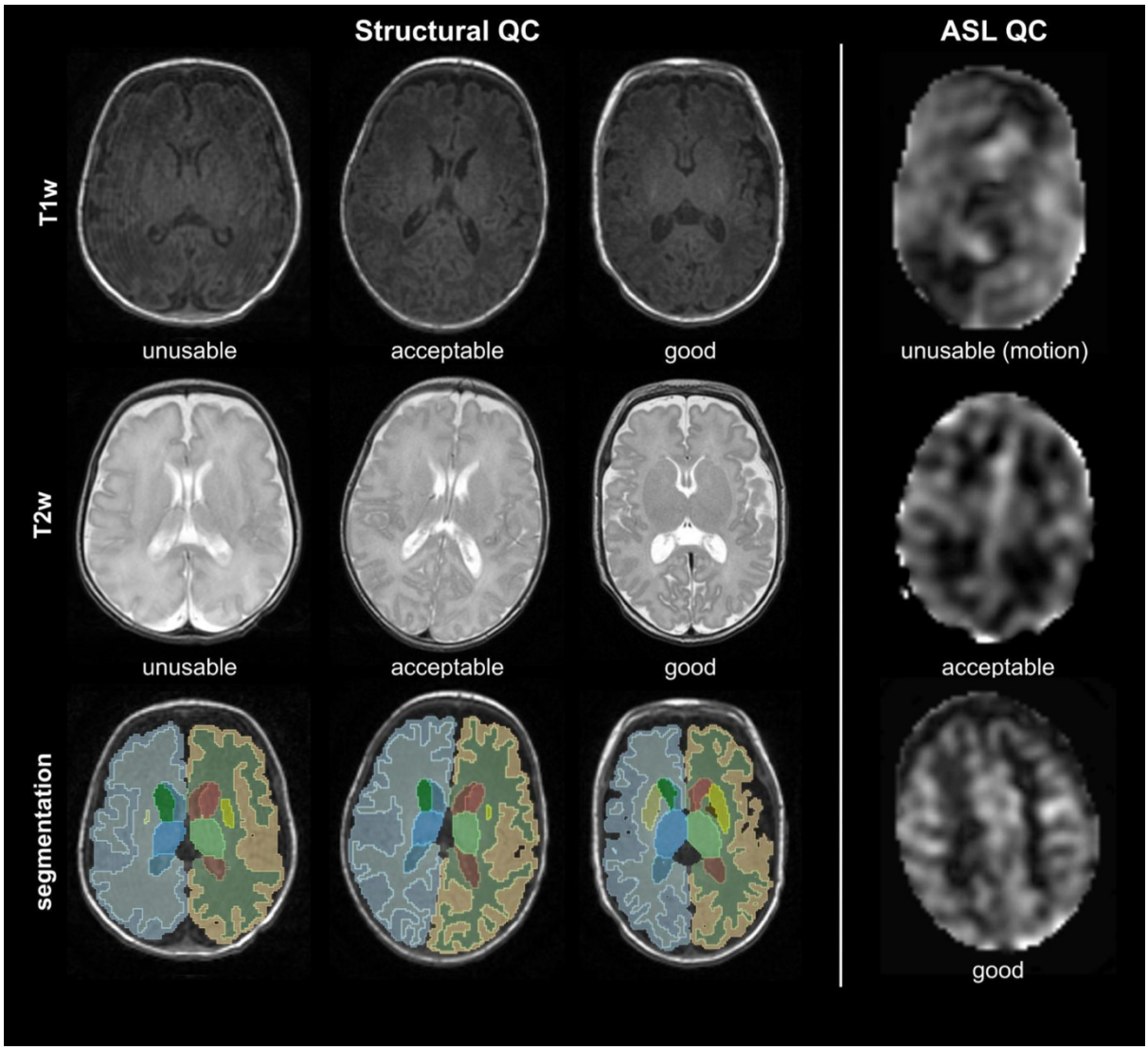


**Figure 39.** Quality control examples for structural and ASL scans.

### 3.3.2 CBF Measurements

Cortical $CBF_{1PLD}$ (mean 13.08 ± 4.28 ml/100 g/min) was significantly lower than cortical $CBF_{3PLD}$ (mean 18.69 ± 5.56 ml/100 g/min, $p < 0.001$, $d = 1.12$), as well as cortical $CBF_{7PLD}$ (mean 20.64 ± 6.06 ml/100 g/min, $p < 0.001$, $d = 1.43$), see Figure 40. Cortical $CBF_{1PLD}$ was significantly different between females (11.39 ± 4.14 ml/100 g/min) and males (14.37 ± 4.01 ml/100 g/min, $p = 0.035$, $d = 0.72$), but there was no significant difference between sexes in cortical $CBF_{3PLD}$ nor in $CBF_{7PLD}$ ($p = 0.16$, $d = 0.43$ and $p = 0.67$, $d = 0.14$, respectively), as shown in Figure 41. There was no significant difference between cortical $CBF_{3PLD}$ and $CBF_{7PLD}$ ($p = 0.16$, $d = 0.33$).

As shown in Figure 42, Bland-Altman plots indicate the biggest difference in cortical CBF was observed between $PCASL_{1PLD}$ and $PCASL_{7PLD}$, also with the largest variance (mean

bias 8.12 ml/100 g/min, 95% CI 5.85 – 10.40 ml/100 g/min, limits of agreement -4.14 – 20.39 ml/100 g/min). There was no significant correlation in the difference between $CBF_{3PLD}$ and $CBF_{1PLD}$ and $ATT_{3PLD}$ (r = -0.13, p = 0.51), and no significant correlation in the difference between $CBF_{7PLD}$ and $CBF_{1PLD}$ and $ATT_{7PLD}$ (r = 0.35, p = 0.07).

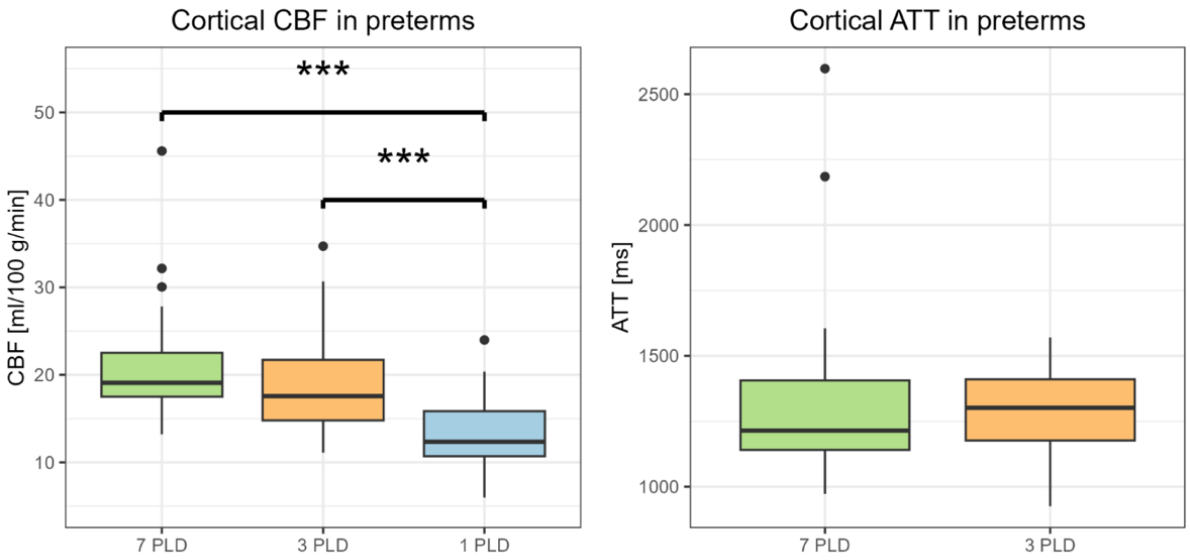


**Figure 40.** Distribution of cortical CBF and ATT among acquisition methods. The central horizontal line represents the median, the box indicates the interquartile range, and the whiskers extend to the data points that lie within 1.5 × the interquartile range from the quartiles. Individual dots represent outliers beyond this range.

### 3.3.3 ATT Distribution

As shown in Supplementary Figure 41, group analysis of ATT showed no significant difference between $ATT_{3PLD}$ (mean 1297.6 ± 160.8 ms) and $ATT_{7PLD}$ (mean 1314.5 ± 308.6 ms, p = 0.77, Cohen's d = 0.06). There was a trend for longer ATT in males than females in both $PCASL_{3PLD}$ (male: 1331.8 ± 168.7 ms; female: 1238.4 ± 113.2 ms; p = 0.0519, d = 0.61) and $PCASL_{7PLD}$ (male: 1441.3 ± 418.3 ms; female: 1244.5 ± 165.1 ms; p = 0.0453, d = 0.60). There was no significant difference in ATT between subjects born prematurely due to fetal indications and subjects born due to other causes ($ATT_{3PLD}$: p = 0.26; d = 0.54; $ATT_{7PLD}$: p = 0.14, d = 0.43).

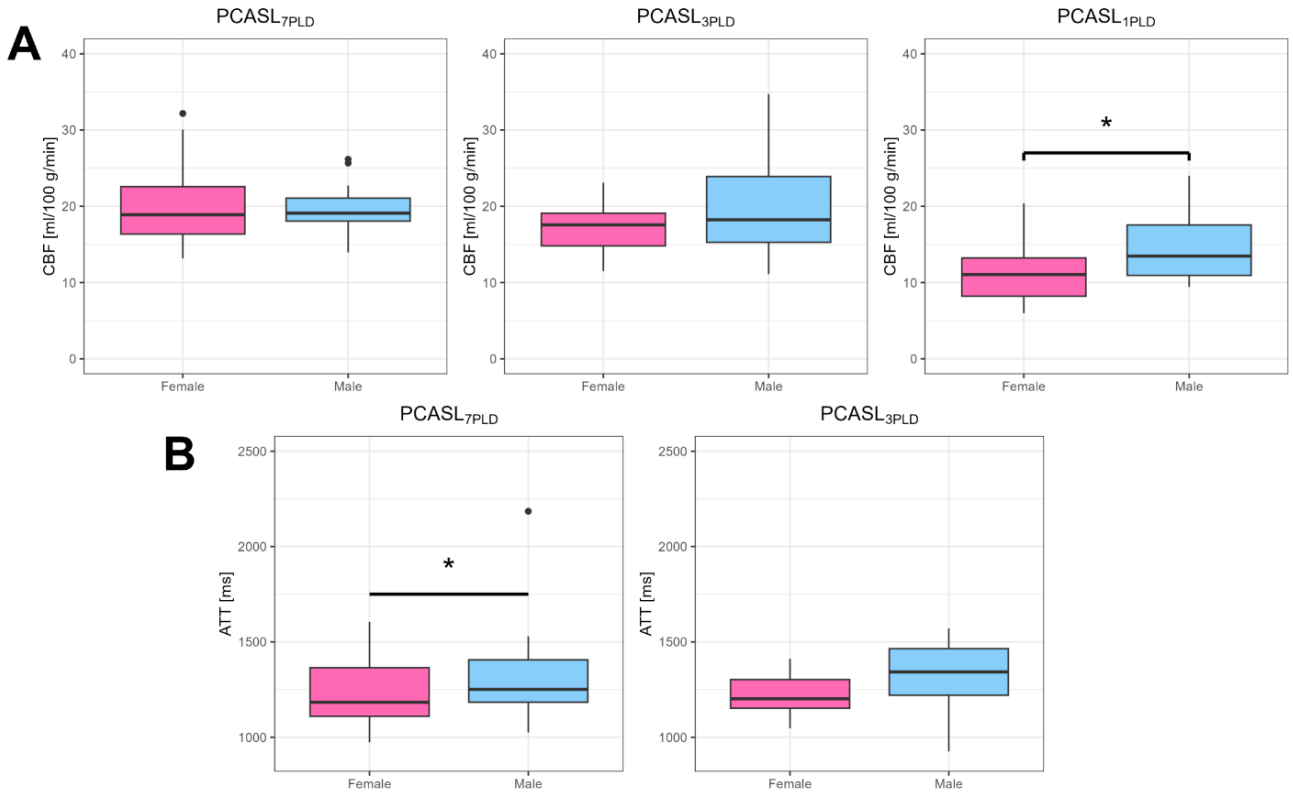


**Figure 41.** Distribution of hemodynamic parameters in sex. A. Distribution of single- and multi-delay cortical CBF in sex. B. Distribution of three- and seven-delay ATT in sex. "*" indicated statistical significance.

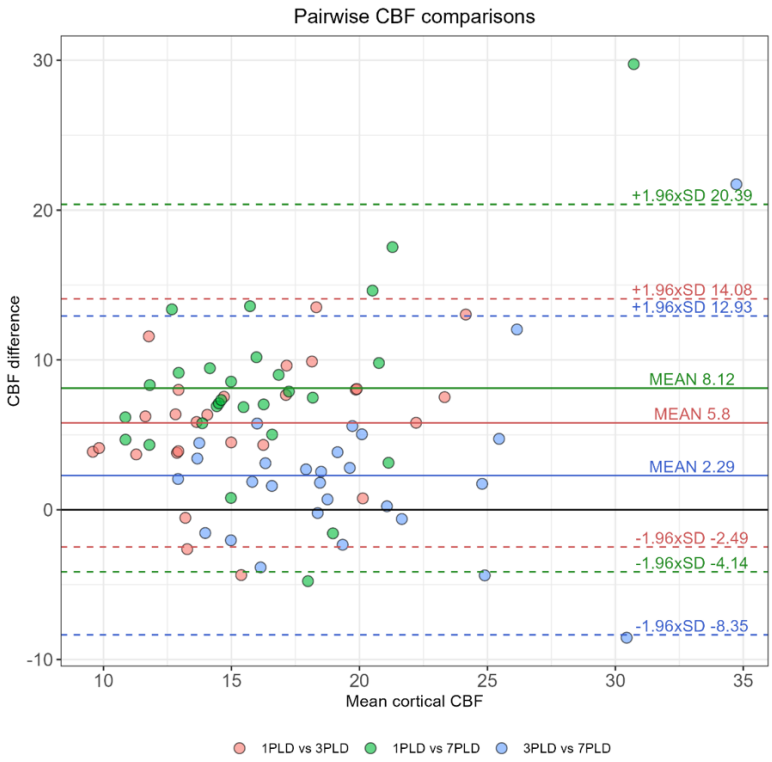


**Figure 42.** Bland-Altman plots of cortical CBF agreement among methods. "Mean" indicates mean bias, and "±1.96xSD" indicate limits of agreement.

### 3.3.4 Relationship between Hemodynamic Values and Age

As shown in Figure 43, cortical $CBF_{3PLD}$ and $CBF_{1PLD}$ showed a significantly positive correlation with PMA, while the relationship between CBF and age was insignificant for $CBF_{7PLD}$. Based on the correlation analysis, PNA and PMA were selected as predictors for linear regression modeling. Neither $ATT_{3PLD}$ nor $ATT_{7PLD}$ showed significant correlation with age Figure 44. Participants prematurely born with fetal variants of the intracranial vasculature did not show a distinct trend in cortical CBF change with PNA Figure 45.

In predicting $CBF_{1PLD}$, the linear regression model incorporating PNA explained a higher proportion of variance compared to the model using PMA (PNA: $R^2 = 17.7\%$, $p = 0.009$; PMA: $R^2 = 13.5\%$, $p = 0.025$). Similarly, the model using PNA was more robust in predicting cortical $CBF_{3PLD}$ than the model using PMA (PNA: $R^2 = 30.9\%$, $p < 0.001$; PMA: $R^2 = 28.4\%$, $p = 0.001$). However, neither PNA nor PMA emerged as statistically significant predictors for cortical $CBF_{7PLD}$ (PNA: $p = 0.09$; PMA: $p = 0.06$).

### 3.3.5 CBF Asymmetry

The distribution of relative CBF asymmetry is shown in Figure 46. No significant variation from 0 in CBF asymmetry was observed ($PCASL_{1PLD}$ $p = 0.89$, $PCASL_{3PLD}$ $p = 0.40$, $PCASL_{7PLD}$ $p = 0.11$) with respect to PMA or fetal-type posterior cerebral artery variants. The distributions of relative CBF asymmetry remained consistent across all measurements: the mean relative asymmetry was $-0.0018 \pm 0.0755$ for $CBF_{1PLD}$, $0.0107 \pm 0.0742$ for $CBF_{3PLD}$, and $0.0178 \pm 0.0653$ for $CBF_{7PLD}$.

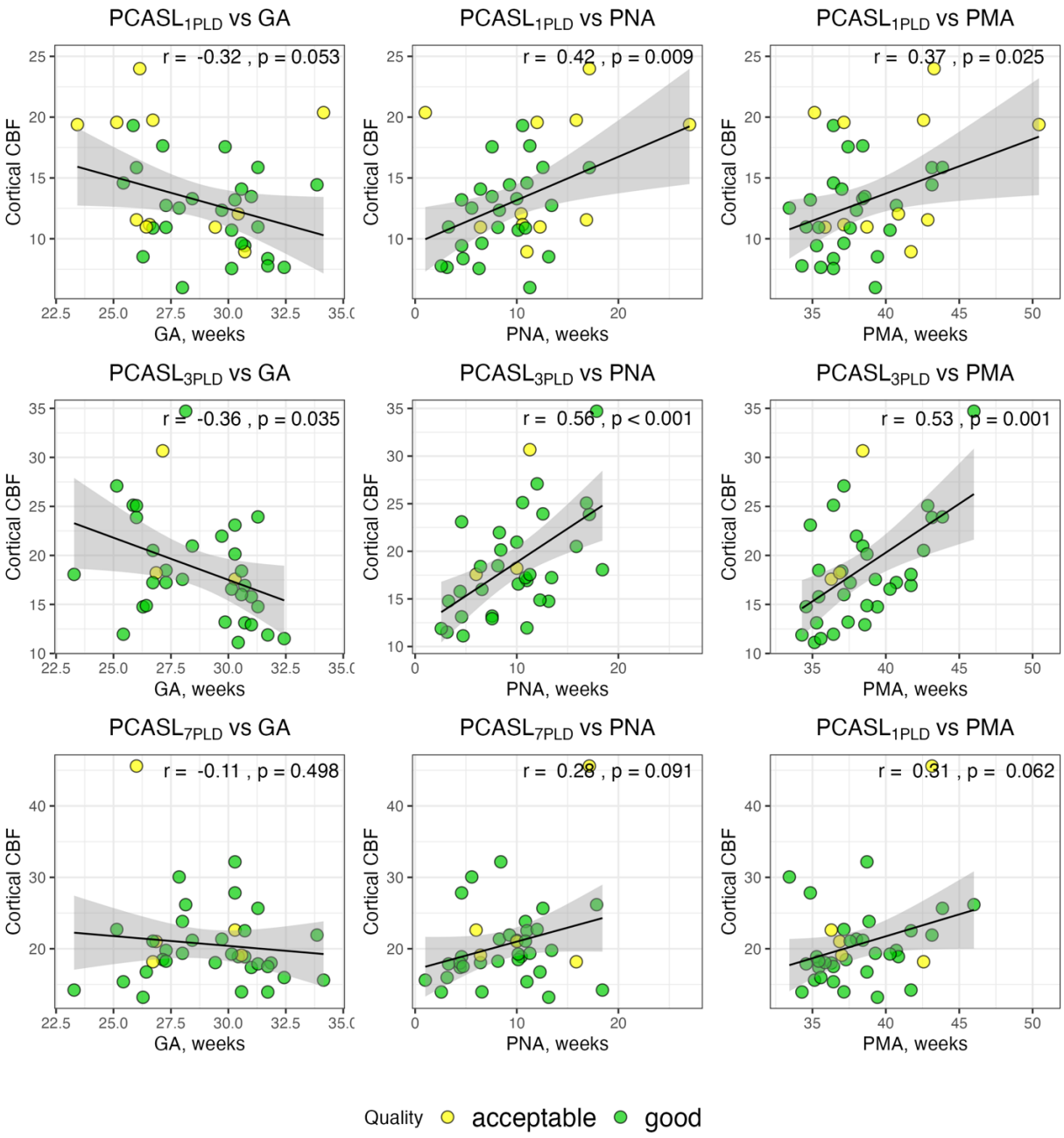


**Figure 43.** Correlation between cortical CBF parameters and GA, PNA, PMA. "r" represents the Pearson correlation coefficient, and "p" indicates the corresponding p-value from the relevant correlation test. The gray shaded area represents the standard error of the estimated correlation.

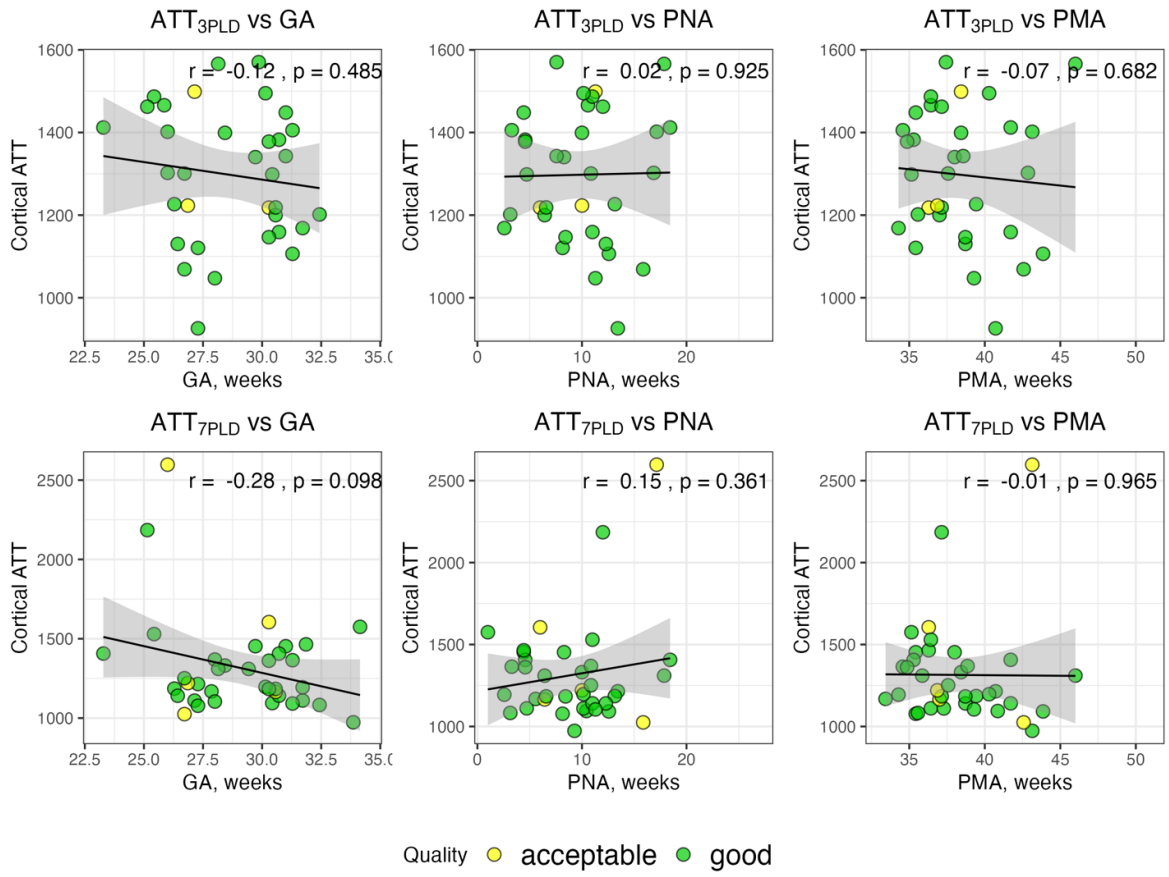


**Figure 44.** Correlation between ATT parameters and age. "r" represents the Pearson correlation coefficient, and "p" indicates the corresponding p-value from the relevant correlation test. The gray shaded area represents the standard error of the estimated correlation distribution.

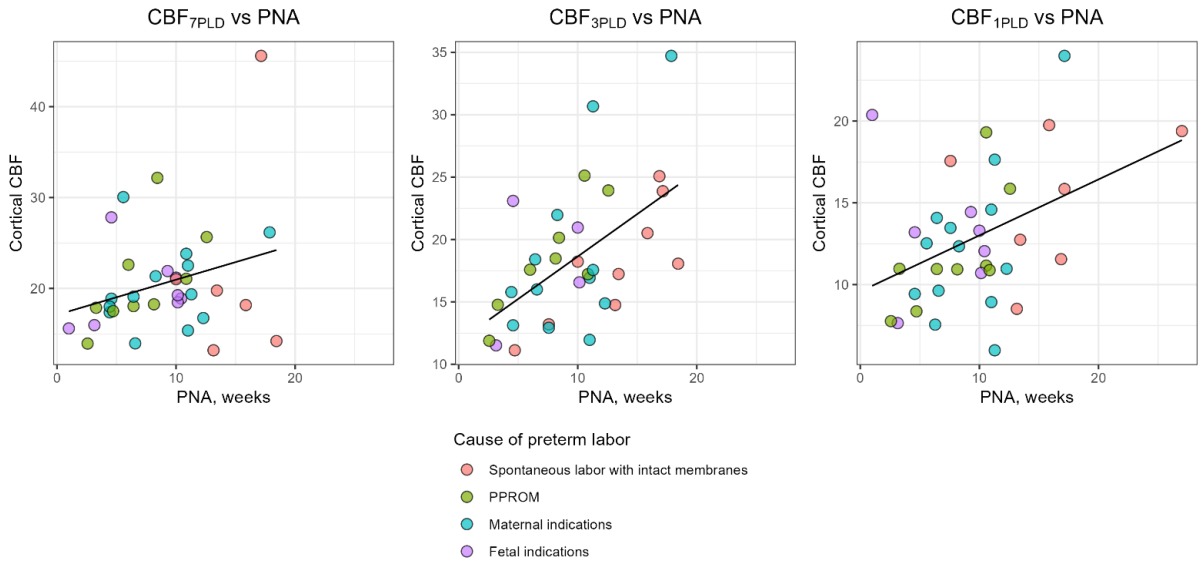


**Figure 45.** Correlation between cortical CBF and PNA in populations with different causes of preterm labor.

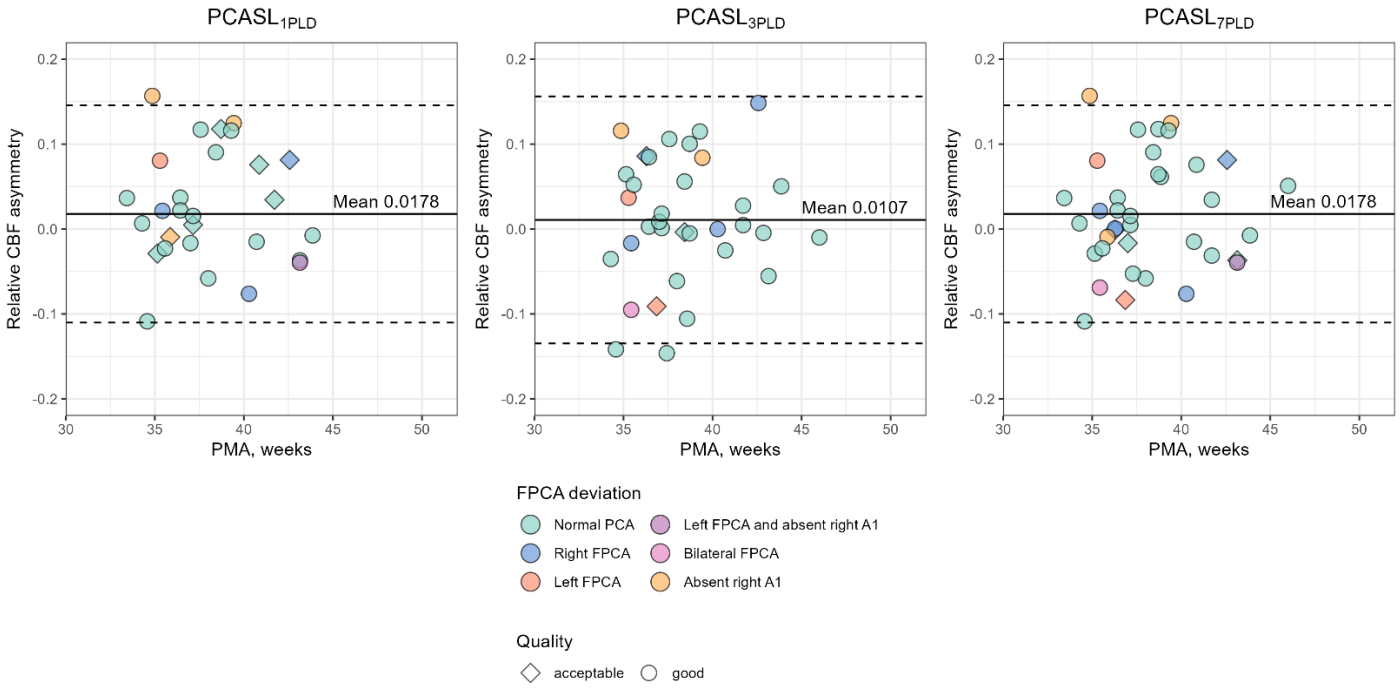


**Figure 46.** Relative hemispheric CBF asymmetry observed in neonates. *FPCA* - fetal-type posterior cerebral artery.

### 3.4 PediTuMRI

#### 3.4.1 Pilocytic astrocytoma

Figure 47 presents multimodal imaging of a 5-year-old female patient diagnosed with a WHO grade 1 pilocytic astrocytoma harboring a *KIAA1549::BRAF* fusion gene. In the pretreatment assessment, the tumor, which contains cystic components, demonstrates a heterogeneous appearance on both diffusion-weighted and contrast-enhanced imaging. Intratumoral perfusion, as evaluated by ASL and DSC imaging, is markedly reduced compared to normal-appearing brain tissue. Furthermore, both ASL ATT and DSC MTT maps reveal prolonged blood arrival times within the tumor region, emphasizing the importance of using longer PLDs for accurate perfusion quantification. It should also be noted that susceptibility artifacts near air-bone interfaces, such as the paranasal sinuses and skull base, may result in signal loss and geometric distortions, necessitating cautious interpretation of DSC-derived parameters.

Figure 48 displays the corresponding follow-up evaluation. Chemotherapy was initiated between the MRI evaluations in accordance with the recommendations of the International Society of Pediatric Oncology (SIOP), consisting of a regimen of carboplatin and vincristine. The tumor volume is decreased relative to the pre-treatment scans; however, the overall contrast-enhancement, diffusion, and perfusion characteristics remain largely unchanged.

Notably, the intratumoral perfusion-weighted signal relative to normal-appearing tissue appears improved compared to the pre-treatment imaging. In addition, APT-CEST imaging demonstrates increased signal within the tumor region, which may reflect either elevated protein concentration or alterations in tissue pH.

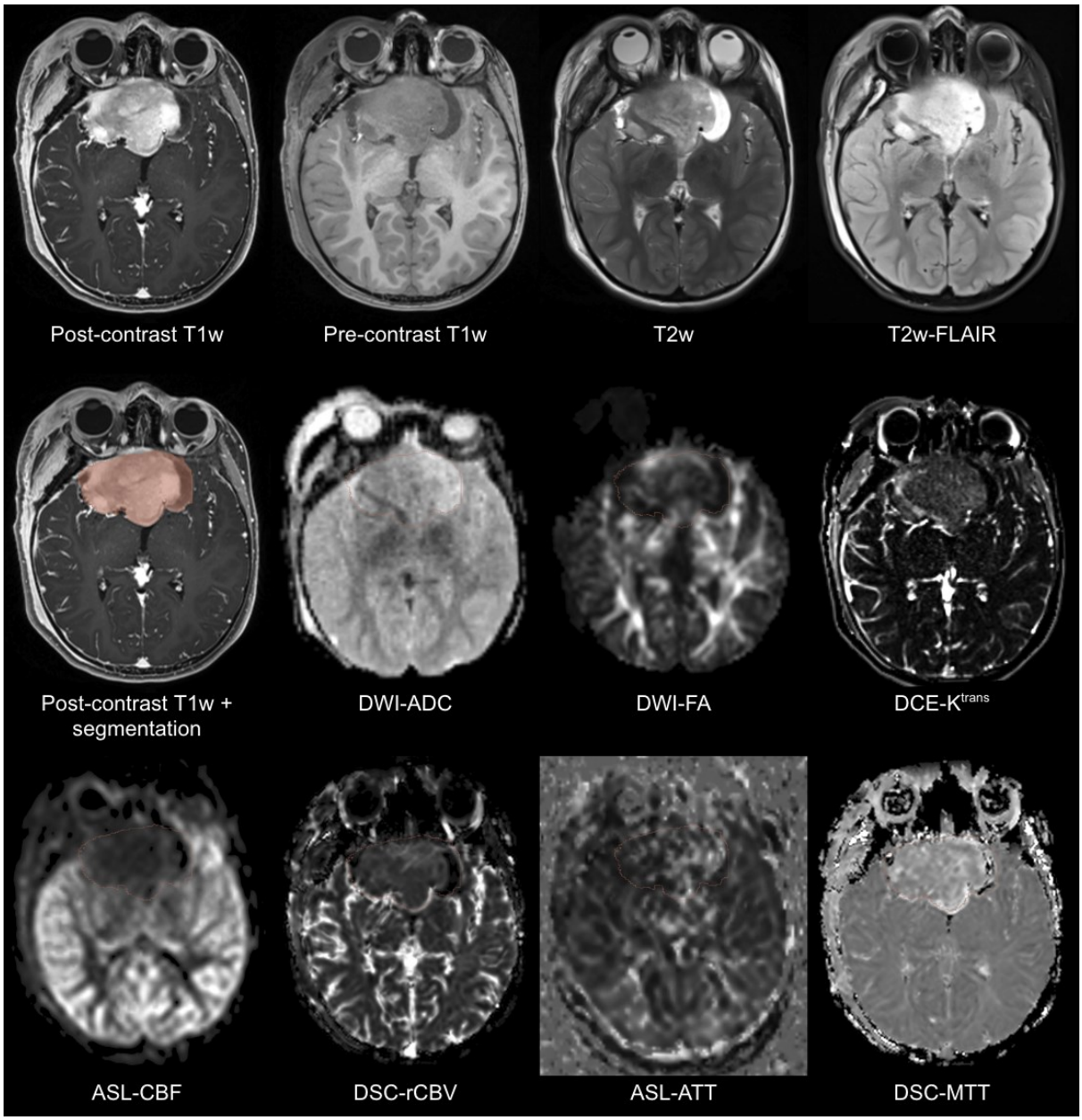


**Figure 47.** Structural (pre- and post-contrast T1w, T2w, T2w FLAIR, and DWI) and perfusion (DCE, ASL, and DSC) pre-treatment scans of a pediatric patient with a WHO grade I pilocytic astrocytoma. ASL was acquired using a sequential multi-delay protocol. APT-CEST imaging was not performed due to the unavailability of the sequence on the scanner at the time of imaging.

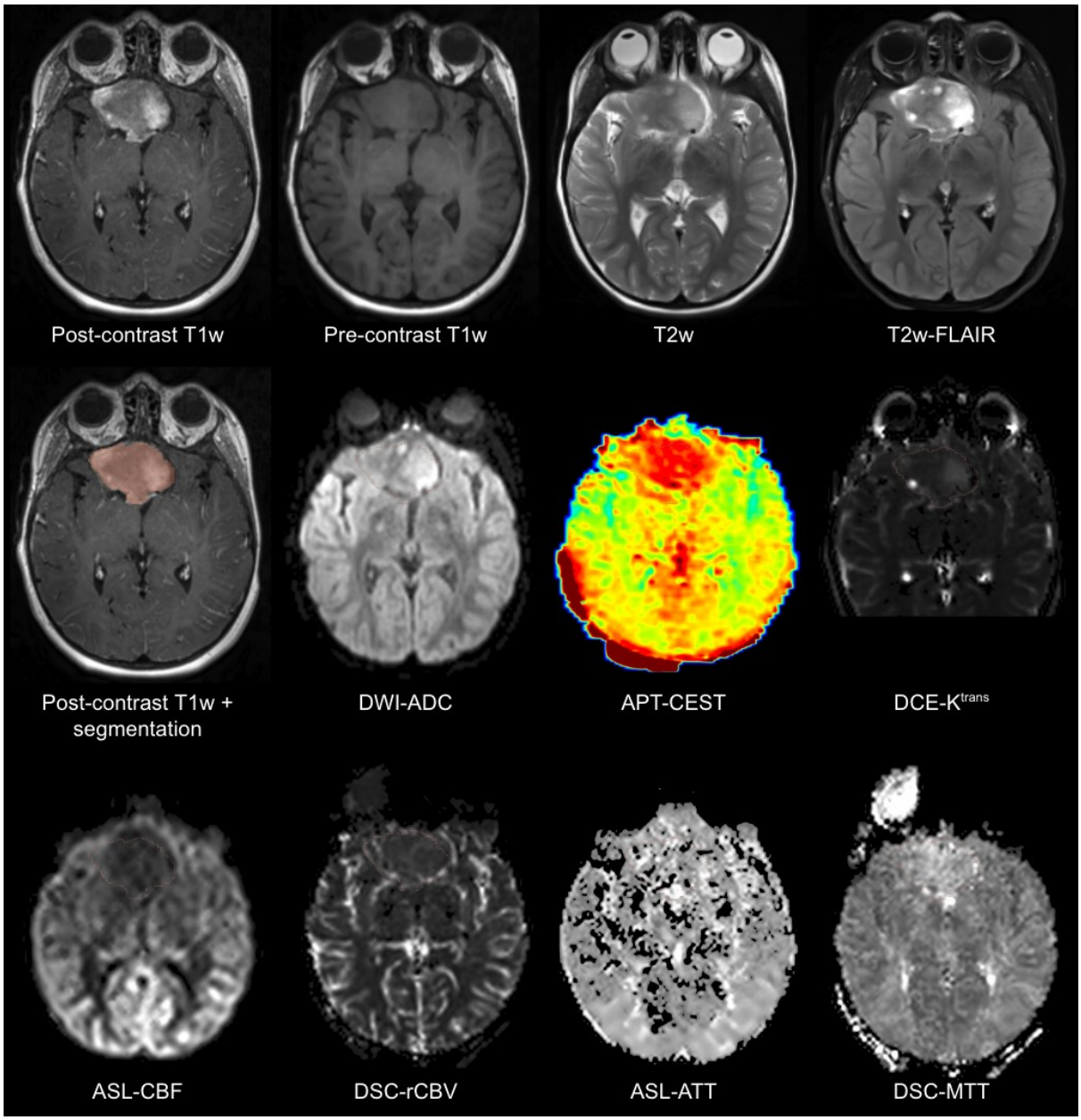


**Figure 48.** Structural (pre- and post-contrast T1w, T2w, T2w FLAIR, and DWI), molecular (APT-CEST) and perfusion (DCE, ASL, and DSC) follow-up scans of a pediatric patient with a WHO grade 1 pilocytic astrocytoma following initiation of chemotherapy. ASL was performed using a sequential multi-delay protocol.

### 3.4.2 Diffuse Low-grade Glioma, *MAPK*-pathway Altered, Pediatric-type

Figures 49 and 50 illustrate a case of a 10-year-old female patient diagnosed with a diffuse low-grade glioma, pediatric-type, harboring a *MAPK* pathway alteration. On the pre-treatment scans, the diffuse growth pattern of the tumor is evidenced by its ill-defined margins. Both perfusion and diffusion imaging profiles reveal moderate heterogeneity, with maximal intratumoral perfusion comparable to that observed in eloquent, normal-appearing

brain tissue. Signal dropout is present in left parietal region due to the placement of a intracranial ventriculoperitoneal (VP) shunt; however, this artifact does not interfere with the assessment of either the intratumoral area or the adjacent eloquent cortex. Outlying ASL CBF signal is observed in the proximity of the shunt.

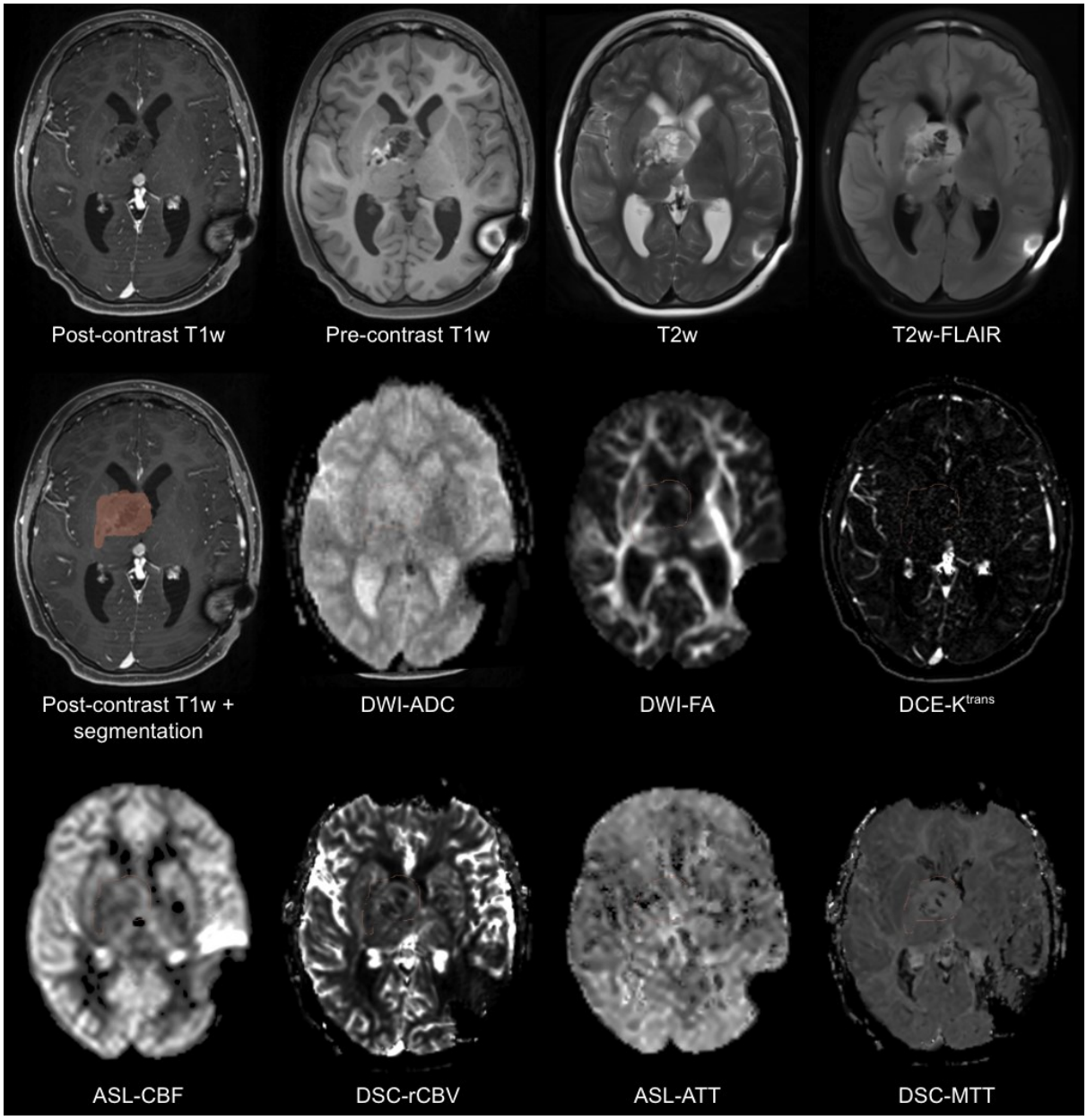


**Figure 49.** Structural (pre- and post-contrast T1w, T2w, T2w FLAIR, and DWI) and perfusion (DCE, ASL, and DSC) pre-treatment scans of a pediatric patient with WHO MAPK-pathway altered diffuse LGG. ASL was acquired using a sequential multi-delay protocol. APT-CEST imaging was not performed due to the unavailability of the sequence on the scanner at the time of imaging.

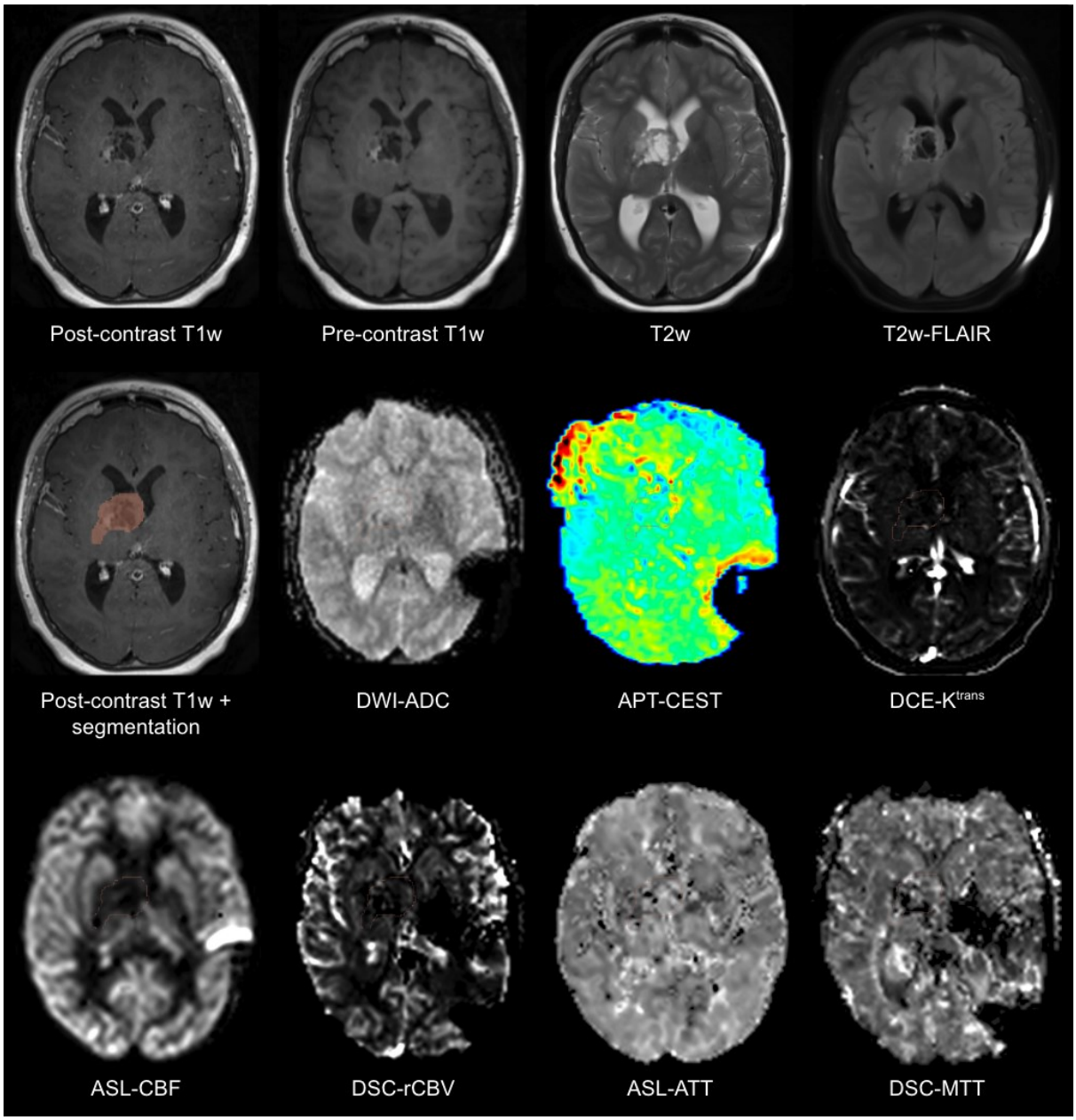


**Figure 50.** Structural (pre- and post-contrast T1w, T2w, T2w FLAIR, and DWI), molecular (APT-CEST) and perfusion (DCE, ASL, and DSC) follow-up scans of a pediatric patient with WHO MAPK-pathway altered diffuse LGG following initiation of biological treatment. ASL was performed using a sequential multi-delay protocol.

Biological therapy with dabrafenib and trametinib was initiated between the pre-treatment and follow-up MRI evaluations. The reduction in tumor volume observed on structural scans is notably accompanied by a decrease in intratumoral perfusion. The presence of a VP shunt resulted in significant disruptions of contralateral perfusion signal on DSC imaging, with some signal disturbances also evident in areas adjacent to the tumor. Markedly elevated ASL CBF signal is again observed, as in the previous assessment, but this does not impede the

evaluation of tumor perfusion or contralateral regions. Additionally, there was no appreciable difference in APT-weighted signal within the tumor, highlighting histopathological differences between this case and the previously described pilocytic astrocytoma, which may underlie the distinct APT-CEST findings.

### 3.4.3 Quantitative T2 experiments

Experiments involving the quantification of absolute T2 have demonstrated that T2 values within tumor and peritumoral regions frequently display outlier values, necessitating additional correction (Figure 51). Univariate T2 models that do not account for the confounding effects of blood or CSF show elevated absolute T2 values in voxels with a high expected partial volume of blood, CSF, cystic components, and tumor tissue. When corrections are applied for blood and CSF components, assuming constant T2 values for these tissues, the issue of elevated T2 within the tumor ROI becomes even more pronounced. This effect is observed not only in tumors with cystic components (Case 2), but also in those with diffuse characteristics (Cases 1 and 3), indicating that such correction is insufficient for accurate estimation of tumor tissue T2. Furthermore, sagittal views of the multivariate tissue T2 maps reveal additional challenges, including signal instability along the inferior-superior axis (indicated by blue arrows in Figure 51). This signal instability is further evidenced by the mean WM qT2 values across slices, which consistently display a U-shaped distribution in all three cases.

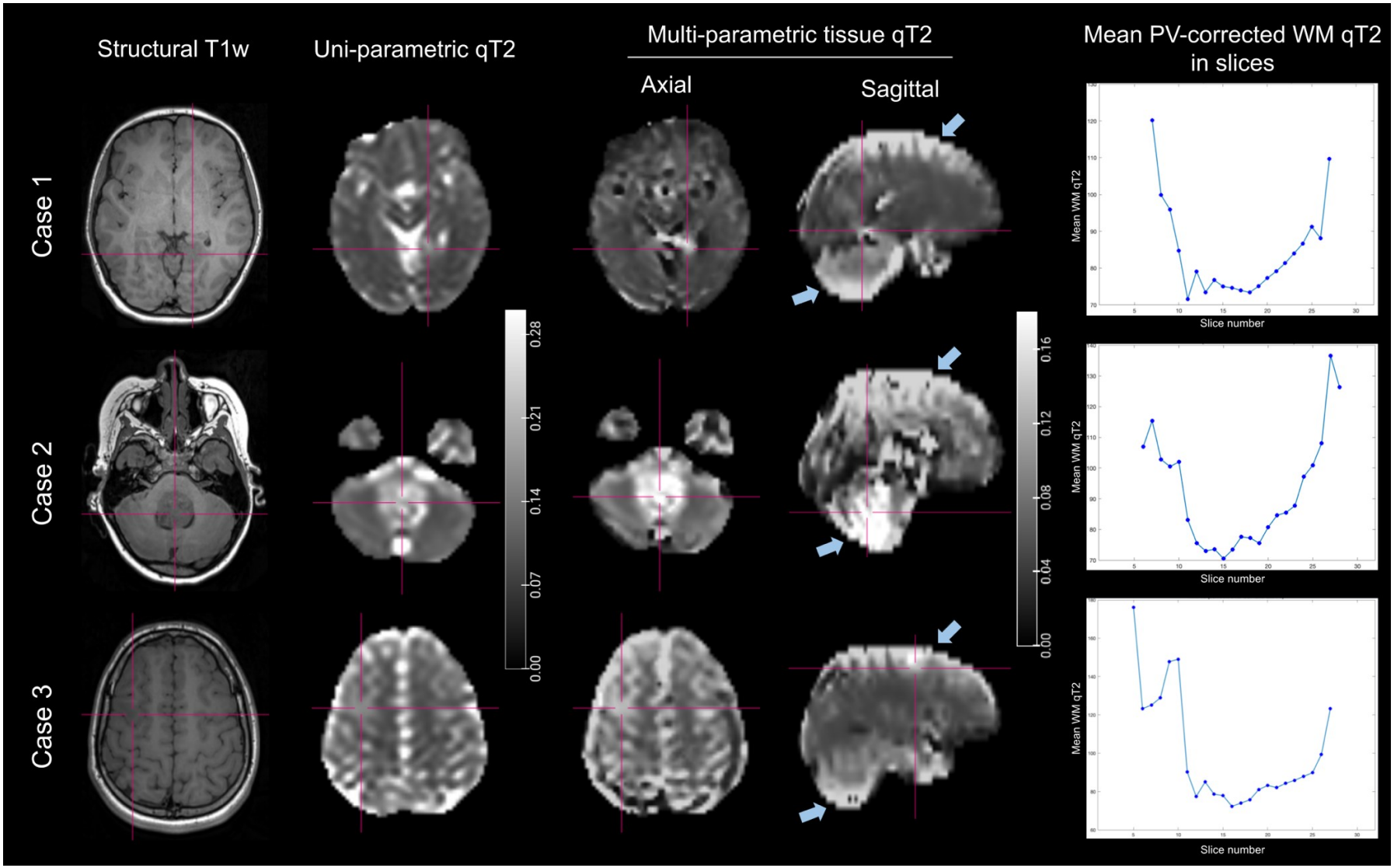


**Figure 51.** Three clinical cases of pediatric brain tumors with corresponding uni-parametric qT2 maps and multi-parametric tissue qT2 maps quanitified from multi-TE control ASL data. Magenta lines point at the intratumoral ROI.

# 4. Discussion

In this work, we explored the utility and feasibility of ASL MRI for clinical evaluation in both adult and pediatric populations. In adults, we analyzed ASL perfusion markers in gliomas and peritumoral regions, demonstrating that the ability of ASL to differentiate molecular subtypes is comparable to that of DSC, with significant correlations observed between perfusion metrics from both modalities. These findings support the clinical applicability of ASL in adult glioma imaging and underscore its potential for non-invasively linking MRI-derived parameters with histopathological markers, which is particularly valuable in cases where biopsy poses significant health risks.

In the pediatric cohort, we assessed developmental trends in hemodynamic parameters among MR-negative children imaged with both single- and multi-delay ASL. We found significant differences in absolute CBF values derived from the two acquisition protocols, with distinct age-dependent patterns observed in WM and GM, as well as significant correlations between perfusion metrics and volumetric brain changes during development. Furthermore, we examined the quality and confounders of ASL scans in preterm neonates – a particularly vulnerable population who may benefit from non-invasive perfusion imaging. Our findings revealed significant differences between single- and multi-delay CBF estimates, with single-delay CBF values being lower, while multi-delay acquisitions produced values more consistent with those obtained from other modalities. Despite concerns regarding motion artifacts in non-sedated neonates, the majority of ASL scans were of good quality and provided complementary information to structural imaging, which itself was also susceptible to quality issues.

Collectively, these results provide a foundation for establishing ASL as a validated clinical tool. Finally, we present two case examples of pre-surgical and follow-up assessments of pediatric brain tumors from an ongoing clinical study investigating the role of ASL in pediatric neuro-oncological diagnostics. This study also aims to identify potential confounders that currently limit the use of ASL for deriving permeability markers in pediatric brain tumors, thereby informing directions for future research.

### 4.1 ASL and DSC in Molecular Markers of Adult Glioma

In line with existing knowledge on high vascularization and perfusion of *IDH*-wt tumors (Álvarez-Torres *et al.*, 2023) our study shows significantly higher tumor perfusion in *IDH*-wt compared with *IDH*-mut gliomas for both ASL and DSC. Group differences are comparable to

previous maximum tumor DSC-nCBV (Cindil *et al.*, 2022) and mean and maximum tumor ASL-CBF (Guo and Jiang, 2023) findings. *IDH* mutation showed no effect on peritumoral edema perfusion. Univariate *IDH* status classification revealed comparable performance for ASL and DSC (AUROCC = 0.82 and AUROCC = 0.83, respectively), surpassing values reported by Hosur et al. (Hosur *et al.*, 2022) (maximum tumor DSC-nCBV AUROCC = 0.66 and maximum tumor ASL-nCBF AUROCC = 0.602). However, they are consistent with the recent meta-analyses on *IDH* status prediction with DSC-nCBV parameters (pooled AUROCC = 0.813 (van Santwijk *et al.*, 2022), AUROCC = 0.745–0.911 (Siakallis *et al.*, 2023)) and previously reported performance metrics for ASL (AUROCC = 0.78) (Peng *et al.*, 2021). The multivariate approach improved the DSC performance up to AUROCC = 0.89 by incorporating multiple histogram parameters into the classification model. For ASL, the multivariate model performance is lower compared to the univariate, potentially owing to the smaller dataset, which reduces the model's robustness. Our investigation complements previous research by directly comparing ASL and DSC in the same population and confirms the comparable performance of both methods in *IDH* status prediction.

In contrast to the *IDH* status, ASL and DSC showed perfusion variations in both the tumor and edema regions with respect to p*TERT* alterations. However, after statistical correction, the signal differences fail to maintain statistical significance. The classification performance of maximum tumor DSC-nCBV (AUROCC = 0.69) and ASL-nCBF (AUROCC = 0.68) is comparable to the mean tumor DSC-nCBV performance previously reported by Zhang et al. (AUROCC = 0.653) (Zhang *et al.*, 2020), with a sample size of 43. Moreover, perfusion heterogeneity in peritumoral edema provided a better performance (IQR of edema DSC-nCBV, AUROCC = 0.81). Multivariate models showed superior results compared to prior findings with DSC-nCBV (maximum AUROCC = 0.86), but ASL-nCBF also showed good efficacy (maximum AUROCC = 0.80).

Contrary to earlier reports of elevated nCBV in 1p/19q-codeleted gliomas (van Santwijk *et al.*, 2022), our study shows nonsignificant differences, aligning with the results of other investigations (N. Wang *et al.*, 2019). While maximum tumor DSC-nCBV previously demonstrated high performance in 1p/19q codeletion detection (AUROCC = 0.73) (Yang *et al.*, 2021), we did not observe the high performance of ASL or DSC tumor perfusion parameters. However, the promising performance of ASL perfusion in peritumoral edema was observed (maximum AUROCC = 0.85). Given the unclear role of 1p/19q-codeletion in tumor

vasculature, our findings prompt further investigation into how it affects peritumoral edema regions. The higher effect sizes and superior performance of ASL compared to DSC perfusion parameters could underscore the significance of microvasculature in 1p/19q-codeleted gliomas.

The impact of *MGMT* promoter methylation on tumor perfusion is debated. Some studies report a significant perfusion signal difference, such as a study by Yoo et al. (maximum tumor ASL-nCBF effect size 0.37) (Yoo *et al.*, 2020) and a study by Zhang et al. (mean tumor DSC-nCBV effect size 0.67) (Zhang *et al.*, 2020), while studies by Song et al. (Song *et al.*, 2022) and Fuster-Garcia et al. (Fuster-Garcia *et al.*, 2021) revealed no distinction. Our study found no significant perfusion signal difference in *MGMT*-non/methylated gliomas.

The subgroup analysis revealed that, despite limited sample sizes, significantly different perfusion patterns can be observed between p*TERT*-mut and p*TERT*-wt subgroups of *IDH*-wt gliomas and between *IDH*-wt and IDH-mut subgroups of p*TERT*-mut gliomas. This finding has the potential to validate the synergetic effect of molecular markers in glioma diagnosis and prompt future diffuse glioma classification development. The analysis of perfusion differentiation between the entities validated that perfusion in tumor and edema were significant markers to discriminate oligodendrogliomas and astrocytomas from glioblastomas.

### 4.2 Correlation between ASL and DSC Parameters in Adult Gliomas

The correlation analysis highlights potential similarities and differences between ASL and DSC parameters in tumor and peritumoral edema. Most parameters exhibit a significant positive correlation between the methods, aligning with prior studies in brain tumors (Järnum *et al.*, 2010; Novak *et al.*, 2019). The significant positive correlation in IQR parameters highlights the potential of ASL as an alternative to DSC in advanced tumor perfusion analysis approaches, such as vascular habitats or fractional tumor burden (Iv *et al.*, 2019; Juan-Albarracín *et al.*, 2019). On the contrary, the correlation between ASL and DSC perfusion parameters is least pronounced in the 5th percentile of edema and tumor perfusion. This observation suggests potential contributions from varying vessel sizes to the perfusion signal. Specifically, the susceptibility-weighted (T2*) DSC perfusion profile predominantly arises from large tortuous vessels, whereas the ASL perfusion profile primarily originates from the microvasculature (Lüdemann *et al.*, 2009). Other potential sources of this disparity are the higher level of noise expected in the 5th percentile and the choice of different reference tissues for ASL and DSC (Ellingson *et al.*, 2012; Alsop *et al.*, 2015a). Furthermore, the correlation

coefficients are lower in the peritumoral edema compared to the tumor region, potentially due to vascular compression (Østergaard *et al.*, 2013) and prolonged arterial transit times, especially impacting the single-delay ASL perfusion with insufficient short PLD. This issue can be addressed through the multi-delay ASL approach; however, currently, there is no consensus on its need for brain tumor imaging (Lindner *et al.*, 2023). Analysis of the impact of ASL data quality on the molecular marker classification shows that the scans affected by macrovascular-signal and minor motion artifacts can be feasibly used for tumor perfusion assessment.

### 4.3 CBF and ATT in MR-negative Children

Despite comparable data quality control outcomes between single- and multi-delay datasets, significant differences in absolute CBF were observed, with multi-delay CBF values aligning more closely with results from other modalities (Chiron *et al.*, 1992). These discrepancies may be attributed to factors such as: i) scanner-specific post-processing algorithms, ii) the consideration of longer PLDs in the multi-delay approach, and iii) lower accuracy in CBF estimation linked with the single-delay approach (van Gelderen, de Zwart and Duyn, 2008; Dai *et al.*, 2012). Notably, AT-correction also significantly affected absolute CBF values, likely due to reduced vascular artifacts, highlighting the crucial role of accounting for arterial transit time in accurately quantifying CBF through ASL methods. Although the recommended post-labeling delay for ASL in children is 1500 ms (Alsop *et al.*, 2015a), our findings indicate that mean ATT in WM is higher than in GM, which is consistent with previous studies (van Osch *et al.*, 2018). Despite the consensus white paper recommendation of a 1500 ms PLD for pediatric populations, our results suggest that this may be insufficient for capturing the CBF signal in WM, given the $PCASL_{7PLD}$ ATT value of 1.57 s. These findings support the need to further refine ASL sequence parameters for pediatric cohorts, with the goal of improving regional perfusion quantification and standardization in future studies. Our study found age-related variations between GM and WM. WM CBF decreased with age and increasing WM volume, while the trend was significantly different for GM, with no significant correlation between age and GM volume.

### 4.4 Age-rated Hemodynamic Changes in Children

Our study found age-related variations between GM and WM. WM-CBF decreased with age and increasing WM volume, while the trend was significantly different for GM, with no significant correlation between age and GM volume. In contrast, GM-ATT increases with age,

while there is no association between WM-ATT and age. Although age-related declines in WM (Leung *et al.*, 2016) and GM (Taki *et al.*, 2011; Wu *et al.*, 2016; Carsin-Vu *et al.*, 2018) CBF after peaking at 7-10 years have been reported in previous studies, our cohort showed no significant negative linear correlation between GM-CBF and age. Instead, we only observed a negative linear correlation in WM, with significantly divergent trends between GM and WM, as seen in all ASL variants. One possible explanation for this discrepancy from previous studies is the use of a linear regression model across all age groups. Another factor could be the confounding effect of age-related increases in GM-ATT, which we addressed by using multi-PLD PCASL, unlike prior studies that used single-delay PCASL or PASL. Additionally, we excluded the cerebellum from the GM analysis due to its considerable confounding effect, as shown in Figure 32.

We identified a significant positive correlation between age and GM-ATT, but not between age and WM-ATT. This trend of GM-ATT change with age may be attributed to the gradual rise in brain volume, thus increasing the distance between the labeling place and ROI. The absence of a similar correlation in WM may be due to the low signal-to-noise ratio typically observed in WM ASL. Interestingly, both CBF and ATT analyses revealed significant age-related trends in the cerebellum, highlighting the need for further investigation of regional hemodynamic changes. Previous studies have shown that cerebellar development in children follows a distinct trajectory compared to the cerebrum, with structural maturation completing later and cerebellar volume peaking after cortical regions (Tiemeier *et al.*, 2010; Gaiser *et al.*, 2024). To specifically isolate the effects of cortical versus cerebellar contributions to hemodynamic trends, we excluded the cerebellum from the primary analysis. Nonetheless, these findings underscore the importance of future research focusing on cerebellar hemodynamics in pediatric populations.

Moreover, volumetric analysis offers key insights into the differential development of WM and GM in children. GM-CBF was independent of absolute GM volume, which exhibited no linear correlation with age, consistent with previous studies reporting an inverted U-shaped relationship (Wilke, Holland and Krägeloh-Mann, 2007; Morel *et al.*, 2021). In contrast, both absolute and relative WM volumes positively correlated with age and were inversely related to WM-CBF changes. Considering the documented decline in total CBF starting at age four (Wu *et al.*, 2016), these findings shed light on distinct developmental patterns in WM and GM perfusion. Additionally, the population CBF CoV map visually highlights a contrast in

hemodynamic variability between WM and GM, with WM exhibiting significantly greater CBF variance in the pediatric cohort compared to GM. These findings underscore the complex interplay between perfusion and brain maturation, with potential implications for pediatric neuroimaging protocols.

### 4.5 Neonatal MR Imaging Quality Evaluation

Achieving high image quality remains a major challenge in many neonatal neuroimaging methods using MRI (Dubois *et al.*, 2021). Our systematic assessment of scan quality demonstrated that $PCASL_{3PLD}$ achieved an optimal compromise between the number of repetitions and a limited range of post-labeling delays, yielding over 90% of scans rated as "good" or "acceptable" in quality. Although Hadamard-encoded ASL is generally expected to be more sensitive to motion artifacts compared to single- or sequential multi-PLD acquisitions (Woods *et al.*, 2024), we observed a lower incidence of motion-affected scans in multi-delay ASL compared to $ASL_{1PLD}$, likely attributable to insufficient time for blood arrival and the inherent instability of CBF in preterm neonates (Vesoulis and Mathur, 2017). Although motion artifacts were less pronounced in $PCASL_{7PLD}$ compared to $PCASL_{1PLD}$, these scans were uniquely affected by signal deficiencies, suggesting a potential need for an increased number of repetitions to enhance signal robustness - an improvement that was observed in the $PCASL_{3PLD}$ protocol, which included more scans with longer PLD. As the overall acquisition quality depends on the exact scanning procedure, we have compared the quality of the structural scans with prior findings. Our findings exhibited increased overall quality (95% of T2w scans and 74% of T1w scans rated as "good" or "acceptable) compared to earlier studies reporting motion artifacts in 56% of MPRAGE and 50% of T2 TSE scans in non-sedated neonates (Hughes *et al.*, 2017). Importantly, ASL scans were often interpretable even when T1w and T2w images were rated as unusable, supporting the complementary role of perfusion imaging when structural quality is limited.

### 4.6 Comparing Neonatal Hemodynamic Values Across ASL Techniques

A key contribution of our study is systematically comparing CBF values obtained from single- and multi-delay ASL within a single scanning session in preterm neonates. Significant differences were observed between $CBF_{1PLD}$ and multi-delay CBF. While $CBF_{1PLD}$ aligns with previously reported GM CBF values in similar populations, multi-delay CBF values are consistent with those obtained from sonographic flowmetry, Xe-133 imaging, NIRS (Proisy *et al.*, 2016; Leon *et al.*, 2022b), and another multi-delay ASL study (Kim *et al.*, 2022).

Discrepancies between single- and multi-delay CBF have also been noted in full-term newborns (Hu *et al.*, no date), though differences in multi-delay values may reflect the impact of advanced large-vessel signal suppression techniques, which may be due to large-vessel signal artifacts. Comparing neonatal ASL techniques with and without vascular artifacts suppression may be pursued in future studies.

The divergence between single- and multi-delay CBF in preterm neonates likely stems from slower blood flow and impaired cerebral autoregulation, leading to regional CBF variability. This variability, most pronounced in the early postnatal period, may persist for months, contributing to long-term neurodevelopmental deficits (Kooi *et al.*, 2017) and is particularly relevant in neonates at elevated risk of brain injury (Pfurtscheller *et al.*, 2023). Variability in CBF can also be linked with ATT variability, reducing SNR in $PCASL_{1PLD}$, which may not be adequately compensated by increased repetitions. This issue is exacerbated by ATT values, which are higher in neonates than in adult populations, consistent with previous studies (Kim *et al.*, 2022; Hu *et al.*, no date). This limitation may reduce the clinical utility of $PCASL_{1PLD}$ in at-risk preterm neonates, suggesting the potential benefit of incorporating longer PLDs in this population.

### 4.7 Impact on Neonatal Hemodynamics due to Sex, Age, and Vascular Anatomical Variations

Prolonged $ATT_{3PLD}$ and $ATT_{7PLD}$ values observed in males suggest sex-related differences in blood arrival times, which may influence CBF quantification. These findings align with previous Doppler ultrasound studies in full-term infants following chorioamnionitis, which reported sex-related differences in blood velocities and vessel resistance (Koch *et al.*, 2014). highlighting complex, sex-specific hemodynamic variations in neonates. In addition to ATT differences, significant sex-related differences in $CBF_{1PLD}$ were also observed in this study. However, prior research on sex-related CBF differences has been inconsistent: while higher CBF in males has been reported using NIRS and Xenon-133 imaging, consistent with our findings (Baenziger *et al.*, 1994; Lin *et al.*, 2013). lower CBF in males has been observed with single-delay pseudo-continuous ASL (J.-N. Wang *et al.*, 2019) and pulsed ASL (Zheng, Freeman and Hwang, 2021). These discrepancies may be attributed to quantification bias related to differences in ATT, with males typically exhibiting prolonged ATT. This difference is particularly relevant in studies using single-delay ASL techniques, which are more sensitive to variations in arrival time. These results underscore the advantages of using multi-delay ASL

to account for such variability and accurately characterize cerebral perfusion. The established male disadvantage in neonatal brain injury and encephalopathy outcomes (Kelly *et al.*, 2023) further emphasizes the importance of investigating sex-related differences in CBF and ATT to better understand underlying mechanisms and guide clinical interventions.

Positive correlations between both cortical $CBF_{1PLD}$ and $CBF_{3PLD}$ and both PNA and PMA were found, consistent with prior studies (Benders *et al.*, 2011; Meng *et al.*, 2021; Zun *et al.*, 2021). Only $CBF_{3PLD}$ showed a significant negative correlation with GA, supporting earlier findings of higher CBF in preterm compared to full-term neonates (Tortora *et al.*, 2017). However, as reported in a seven-delay ASL study, no significant correlation with GA was observed before correction using the Bayley Scales of Infant and Toddler Development (Kim *et al.*, 2022). The lack of correlation between $CBF_{7PLD}$, as well as ATT parameters and age may reflect the complex interplay between perfusion and neurovascular development during the early postnatal adaptation period.

Our results on CBF differences due to cerebral vascular variations showed no significant contralateral asymmetries, despite previous reports of right hemisphere metabolic dominance in smaller newborns (Lin *et al.*, 2013). Fetal-type posterior cerebral artery variants exhibited an ambiguous influence on cerebral perfusion laterality. Future studies investigating perfusion changes across vascular territories are recommended to better understand the impact of fetal-type PCA variants on early-life hemodynamics.

### 4.8 Clinical Implications for Neonatal Imaging

The findings of our study have direct clinical relevance for the evolving role of ASL in neonatal brain imaging. As preterm neonates often undergo MRI for early detection of brain injury and prognostic evaluation, incorporating multi-delay ASL protocols would offer more accurate and interpretable hemodynamic outcomes. Improved sensitivity to ATT and reduced susceptibility to motion artifacts, particularly in $PCASL_{3PLD}$, may allow clinicians to assess cerebral hemodynamics even when structural sequences are degraded. This is crucial for non-sedated, medically fragile neonates where imaging time is constrained. Moreover, as CBF patterns increasingly inform risk stratification, neuroprotective interventions, and follow-up planning, standardizing delay-sensitive ASL protocols across institutions could help translate advanced imaging techniques into actionable clinical insights. Future studies may focus on validating standardized multi-delay ASL protocols across centers.

### 4.9 Advanced ASL for Pediatric Tumors

Advanced ASL techniques hold considerable promise for enhancing clinical MRI through the introduction of novel perfusion and permeability markers, increasing the precision and accuracy of perfusion imaging, and addressing new clinical applications (Hernandez-Garcia *et al.*, 2022b). Pediatric neuro-oncology is a particularly relevant area for these developments, given concerns about GBCA deposition in the developing brain, the need for repeated longitudinal imaging for treatment monitoring or disease progression, and the increased discomfort and risk of motion artifacts associated with GBCA administration in children. Additionally, there is a growing interest in non-contrast or low-contrast MRI protocols for neuro-oncological applications, motivated by both economic and ecological considerations (Azizova *et al.*, 2025b).

Emerging approaches such as multi-TE ASL offer the potential to extend non-invasive MRI protocols by providing not only perfusion but also permeability parameters. However, reliable quantification of exchange-related parameters that reflect BBB permeability depends critically on the accurate determination of absolute T2 values for blood and tissue within the voxel of interest. Our analyses indicate that this quantification is not straightforward in brain tumors, as the T2 values of tumorous tissue frequently differ from those of healthy WM or GM. This challenge is particularly pronounced in pediatric brain tumors, which often exhibit micro- or macrocystic components (e.g., pilocytic astrocytoma) and greater histopathological variability, making the establishment of normative T2 values difficult. Furthermore, from a clinical perspective, it is not feasible to assume tumor subtype-specific T2 values at the time of imaging, especially when permeability metrics may be needed to aid differential diagnosis. Simply applying constant T2 values for blood and CSF has also proven inadequate.

We hypothesize that the observed disturbances in signal distribution along the inferior-superior axis in our quantitative T2 maps are attributable to biases introduced by T1 spoiling effects in the presence of B0 inhomogeneities during multi-echo acquisition. Blood's relatively long T2 (~165 ms) and short T1 (~1600 ms) make it particularly susceptible to significant T1 signal spoiling when non-ideal refocusing pulses are used. To address these biases and improve estimation of true tissue T2 for accurate permeability quantification, further research should focus on applying Extended Phase Graph (EPG) modeling to correct for these effects (Weigel, 2015), including phantom experiments, protocol optimization with B0 mapping, and validation against DCE-MRI. Work in these areas is ongoing. The development and validation of such a

model would be broadly applicable, not only to pediatric and adult brain tumors but also to other conditions characterized by abnormal T2 values, such as epilepsy and edematous tissue. Moreover, this approach may facilitate the standardization of quantitative data across multiple centers with variable B0 inhomogeneity profiles.

Despite the current limitations in permeability quantification with ASL, our data demonstrate that perfusion-related parameters remain highly promising in pediatric gliomas. Preliminary results (Figures 47–50) show that intra- and peritumoral ASL-CBF correlates with DSC-rCBV and provides more robust assessments in the presence of susceptibility artifacts. Building on our findings in adult gliomas and pediatric cohorts, systematic validation of ASL in pediatric brain tumors is warranted, particularly given the clinical demand for safe and reliable perfusion imaging in children requiring repeated MRI studies (Ouyang and Bao, 2025b). Changes in perfusion-weighted signal during follow-up may support the use of ASL-CBF as a biomarker for non-invasive tumor monitoring and molecular profiling. Finally, emerging techniques such as APT-CEST may provide complementary molecular information, further enhancing the ability of multi-modal MRI to differentiate tumor subtypes and inform treatment strategies.

### 4.10 Future Directions: ASL in the Diagnosis and Characterization of Epilepsy

The diagnostic potential of ASL MRI in epilepsy remains to be fully defined, particularly in the context of clinical protocol standardization. Recognizing that pediatric patients constitute the majority of new non-lesional epilepsy cases (Benini *et al.*, 2022), we undertook a systematic review of ASL applications in this population to inform the optimal integration of ASL into future diagnostic workflows. Our work in neuro-oncology further confirmed that ASL-derived CBF is a sensitive marker of regional perfusion changes associated with pathological processes. Building on these insights and the optimization of ASL for relevant cohorts, we are now initiating a prospective clinical study, MrEpiVaR, that employs ASL for CVR assessment in epilepsy. This protocol incorporates a controlled $CO_2$-breathing challenge and dual multi-delay ASL acquisitions tailored to the age variability of the recruited cohort, conducted before and after the challenge. We hypothesize that regional deviations in CVR parameters will pinpoint epileptogenic loci and functionally eloquent areas, providing clinically actionable information to complement standard diagnostic modalities. This work represents a critical step toward establishing ASL-based CVR mapping as a valuable adjunct in the comprehensive evaluation and management of epilepsy.

## 4.11 Limitations

### 4.11.1 Adult Glioma Study

This study has several limitations. The data analyzed in this study were collected over a long period and were affected by the WHO CNS classification changes and 2 system upgrades, which prevented consistent data collection. However, the molecular marker assessment was consistently carried out often prior to the classification revision, which did not bias the dataset. To avoid inconsistencies regarding the classification changes in glioma grading, we rely on the molecular markers analysis. Moreover, the changes in the structural MRI protocols have a negligible impact on the ROI segmentation and analysis. Platform upgrades have impacted the ASL data acquisition since the oldest sub dataset was acquired with shorter PLD, though the number of scans with arterial transit time artifacts was comparable across all platforms. The issue with shorter LD than recommended in the ASL sequence remains present in the standard GE ASL sequence. The use of longer LD can potentially improve the prediction performance of ASL-based models due to the increased signal-to-noise ratio. Additionally, it is important to note that this study has implications only for pretreatment glioma diagnostics and cannot be generalized to posttreatment monitoring.

The choice of a multivariate logistic model is justified for its straightforward interpretability and robustness; however, more advanced predictive models can enhance classification efficiency. With our chosen approach, we also support the future use of perfusion parameters in multiparametric predictive models for glioma diagnostics and contribute to the interpretability of perfusion MRI in the field of Neuro-oncology. An important study limitation is the insufficient sample size for conclusive multi-marker analysis. Despite insignificant perfusion parameter differences, high effect sizes and good classification performances suggest the need for larger populations for conclusive outcomes.

### 4.11.2 Pediatric ASL Study

Our study has limitations. Sedation and sex are known to influence pediatric hemodynamics (Liu *et al.*, 2012; Makki *et al.*, 2019) (27, 28), and our analysis revealed significantly different age-related trends between male and female populations. However, no significant differences were observed between sedated and non-sedated groups, as the effects of sedation remain inconclusive (Zhao *et al.*, no date). Larger cohort studies could explore the effects of different sedation types and levels on pediatric perfusion metrics. Hemodynamic parameters were

analyzed across the entire cohort to account for the non-linear relationship between age and cerebral perfusion (Carsin-Vu *et al.*, 2018). Despite not performing age-specific analyses, we observed significant correlations between age and WM-CBF or GM-ATT, providing valuable insights for ASL standardization in pediatric populations and warranting further investigation. Alternative ASL post-processing methods, such as FSL BASIL (Chappell *et al.*, 2023), which employs a Bayesian model, could be considered for future studies. However, its reliance on parameter initialization is challenging, particularly in pediatric cohorts where such values have yet to be well established. Hence, we used the scanner reconstruction, which applies a nonlinear least-square curve fitting to a perfusion kinetic model (Dai *et al.*, 2012). This approach provided a robust and clinically applicable framework for the initial investigation of ATT and CBF. Although we accounted for common pitfalls of analyzing ASL data, the measurement of CBF in this study was performed without using the gold-standard modality of $[^{15}O]H_2O$ PET and other contrast agent-dependent methods, due to the potential risks of subjecting a pediatric population to these types of study. However, it has been demonstrated that multi-PLD PCASL achieved a high and strong correlation in CBF measurements with PET in normal and affected brain regions, at least in adults (Zhao *et al.*, 2022). Additionally, this study's single-center, single-vendor design may limit its generalizability. Future multi-center, multi-vendor studies are needed to better inform ASL standardization for pediatric cohorts.

### 4.11.3 Neonatal ASL

This study has several limitations. First, the single-delay ASL protocol employed a short PLD of 1525 ms; using a longer PLD could improve the signal-to-noise ratio and reduce discrepancies between single- and multi-delay CBF measurements (Alsop *et al.*, 2015b). Although T2w images had better scan quality, ASL scans were registered to T1w scans despite their susceptibility to artifacts. However, the 2D acquisition and thicker slices of T2w scans can introduce partial volume effects, potentially reducing registration precision. While large-vessel signal can inflate regional CBF values (Hu *et al.*, no date), we excluded deep GM regions to minimize this artifact, focusing instead on cortical perfusion. In neonates, ASL is particularly susceptible to macrovascular contamination due to slower flow velocities and prolonged ATT, which can cause labeled spins to dwell in large vessels and generate spurious hyperintensities, even at long post-labeling delays. The aim of this study was to evaluate the quality of neonatal neuroimaging rather than the performance of the raters; therefore, inter-rater agreement was not assessed. However, further studies evaluating inter-rater variability are recommended to

better understand the stability of clinical ASL image evaluation in neonates. Finally, the limited sample size may have constrained the statistical power of certain analyses, such as age correlations for $ASL_{7PLD}$ and sex-related differences, where positive correlation coefficients and large effect sizes suggest potential trends warranting further investigation. Larger cohort studies are recommended to comprehensively analyze the impact of causes of preterm birth on hemodynamic changes and the influence of structural variants of posterior cerebral artery on perfusion asymmetries in a neonatal brain.

# 5. Conclusions

This thesis demonstrates the significant potential of ASL MRI as a non-invasive tool for quantitative perfusion imaging in both adult and pediatric neuroimaging. In adult gliomas, ASL-based perfusion markers differentiated molecular tumor subtypes, showing diagnostic performance comparable to DSC imaging, and strong correlations were observed between the two modalities. These results underscore the feasibility of using ASL as an alternative or adjunct to contrast-enhanced techniques, especially in patients where gadolinium-based agents are contraindicated or biopsy carries substantial risk. Multivariate and histogram-based analyses further highlighted the added diagnostic value of advanced perfusion features for molecular classification.

In pediatric and neonatal populations, this work provides comprehensive assessments of developmental trends and technical considerations in ASL imaging. The research identified age-related differences in CBF and ATT, demonstrated the significant differences in hemodynamic parameters derived from single- and multi-delay protocols, and established the robustness of ASL even in challenging neonatal and pediatric cohorts. The findings emphasize the promise of advanced ASL for safe, repeatable, and longitudinal monitoring in pediatric brain tumors. At the same time, the results highlight ongoing challenges, particularly in accurate permeability quantification, related to tissue heterogeneity and variable T2 values. These technical issues point to the need for continued methodological innovation, including improved modeling of relaxation effects and harmonization of ASL protocols across sites.

A central contribution of this thesis has been to advance the clinical validation of ASL MRI, providing a strong foundation for its broader adoption in both clinical practice and research. Through rigorous methodological comparisons, in-depth analysis of technical confounders, and demonstration of ASL's diagnostic value across diverse patient populations, this work establishes ASL as a reliable, non-invasive imaging technique for quantitative cerebral perfusion assessment. By identifying current limitations and proposing strategies for protocol optimization, including advanced acquisition schemes and robust quantification approaches, this research charts a path toward further refinement and integration of ASL in precision neuroimaging. Collectively, these efforts not only support the immediate clinical use of ASL, particularly in vulnerable pediatric cohorts, but also lay the groundwork for innovative research aimed at improving patient outcomes through advanced MRI technologies.

The research was guided by formulated hypotheses, which are addressed as follows:

**H1:** *Perfusion markers derived from both ASL and DSC MRI are correlated with molecular tumor markers in adult gliomas.*
We demonstrated significant correlations between ASL- and DSC-derived intratumoral and peritumoral perfusion parameters and key molecular markers such as IDH and pTERT mutation status.

**H2:** *ASL and DSC demonstrate comparable predictive performance for glioma characterization.*
Our findings showed that ASL achieved diagnostic performance similar to DSC for glioma grading and molecular stratification. Univariate and multivariate models based on ASL perfusion features yielded AUROCC values on par with DSC, supporting the clinical interchangeability of these modalities in appropriate contexts.

**H3:** *Perfusion characteristics in the peritumoral region provide additional diagnostic information regarding tumor infiltration and perilesional hemodynamic changes.*
Analysis of peritumoral perfusion patterns revealed that ASL and DSC provide complementary information on tumor infiltration, with signal heterogeneity in perilesional areas correlating with molecular features. This underscores the importance of regional perfusion analysis for comprehensive glioma evaluation.

**H4:** *Within-session single-delay and multi-delay ASL acquisitions yield distinct gray and white matter CBF values in children.*
In the pediatric cohort, we observed significant differences between CBF values obtained from single- versus multi-delay ASL, confirming the importance of protocol choice for accurate quantification in developmental imaging.

**H5:** *Significant variations in ATT and CBF are observed across age groups in both white and gray matter, reflecting ongoing brain maturation.*
Our data demonstrated significant age-dependent changes in WM CBF and GM ATT, highlighting the critical need for age-specific reference values in pediatric ASL.

**H6:** *Changes in CBF within white and gray matter are correlated with brain volumetric changes during pediatric development.*

We observed a significant negative correlation between CBF and absolute volume in both WM and TB, whereas no significant association was found between perfusion and regional volume changes in GM.

**H7:** *The quality of ASL scans in preterm neonates is sufficient for reliable clinical interpretation.*
The quality control assessment indicated that the majority of ASL scans in preterm neonates were of good diagnostic quality, despite the absence of sedation and challenges posed by patient motion. This finding supports the feasibility of ASL for neonatal clinical use.

**H8:** *ASL-derived CBF values differ between single-delay and multi-delay acquisitions within the same imaging session in neonates.*
Comparative analysis revealed systematic differences in CBF estimates depending on the ASL protocol, with multi-delay methods offering improved accuracy in the context of variable arterial transit times – a critical consideration in this vulnerable population.

**H9:** *CBF and ATT change throughout gestational and postnatal development in preterm neonates.*
Our analysis demonstrated a significant increase in CBF with advancing postnatal age, while only three-delay ASL CBF was negatively correlated with gestational age. No significant correlation was observed between ATT and age in preterm neonates.

**H10:** *ASL provides clinically valuable, non-invasive perfusion markers that aid in differentiating pediatric brain tumor entities.*
Preliminary results from the prospective PediTuMRI study indicate that ASL perfusion imaging may help differentiate pediatric brain tumor grades and support radiological decision-making. However, further investigation is ongoing to fully establish the clinical utility of non-contrast MRI in this context.

**H11:** *Quantification of ASL-based permeability measurements in the peritumoral region yields additional diagnostic markers comparable in value to DCE MRI parameters.*
Early analyses indicate that reliable quantification of BBB permeability using ASL-derived metrics remains challenging, primarily due to tissue heterogeneity and unmodeled T2 effects in tumoral and peritumoral regions. Further methodological development is needed to address these limitations, and this remains an active area of ongoing research.

# 6. References


1. Abbott, N.J., Rönnbäck, L. and Hansson, E. (2006) 'Astrocyte–endothelial interactions at the blood–brain barrier', *Nature Reviews Neuroscience*, 7(1), pp. 41–53. Available at: https://doi.org/10.1038/nrn1824.

2. Abedalthagafi, M. *et al.* (2021) 'Epigenomics and immunotherapeutic advances in pediatric brain tumors', *npj Precision Oncology*, 5(1), pp. 1–13. Available at: https://doi.org/10.1038/s41698-021-00173-4.

3. Abuhamed, J. *et al.* (2022) 'Incidence trends of childhood central nervous system tumors in Finland 1990–2017', *BMC Cancer*, 22(1), p. 784. Available at: https://doi.org/10.1186/s12885-022-09862-0.

4. Ahir, B.K., Engelhard, H.H. and Lakka, S.S. (2020) 'Tumor Development and Angiogenesis in Adult Brain Tumor: Glioblastoma', *Molecular Neurobiology*, 57(5), pp. 2461–2478. Available at: https://doi.org/10.1007/s12035-020-01892-8.

5. Ahmadi, K. *et al.* (2023) 'Gray matter hypoperfusion is a late pathological event in the course of Alzheimer's disease', *Journal of Cerebral Blood Flow & Metabolism*, 43(4), pp. 565–580. Available at: https://doi.org/10.1177/0271678X221141139.

6. Ainslie, P.N. *et al.* (2008) 'Elevation in cerebral blood flow velocity with aerobic fitness throughout healthy human ageing', *The Journal of Physiology*, 586(Pt 16), pp. 4005–4010. Available at: https://doi.org/10.1113/jphysiol.2008.158279.

7. Aird, W.C. (2007) 'Phenotypic Heterogeneity of the Endothelium', *Circulation Research*, 100(2), pp. 158–173. Available at: https://doi.org/10.1161/01.RES.0000255691.76142.4a.

8. Alavi, A. *et al.* (2021) 'Unparalleled and revolutionary impact of PET imaging on research and day to day practice of medicine', *Bio-Algorithms and Med-Systems*, 17(4), pp. 203–212. Available at: https://doi.org/10.1515/bams-2021-0186.

9. Alnahhas, I. (2024) 'Molecular Testing in Gliomas: What is Necessary in Routine Clinical Practice?', *Current Oncology Reports*, 26(11), pp. 1277–1282. Available at: https://doi.org/10.1007/s11912-024-01602-w.

10. AlRayahi, J. *et al.* (2023) 'Pediatric Brain Tumors in the Molecular Era: Updates for the Radiologist', *Seminars in Roentgenology*, 58(1), pp. 47–66. Available at: https://doi.org/10.1053/j.ro.2022.09.004.

11. Alsaedi, A. *et al.* (2019) 'The value of arterial spin labelling in adults glioma grading: systematic review and meta-analysis', *Oncotarget*, 10(16), pp. 1589–1601. Available at: https://doi.org/10.18632/oncotarget.26674.

12. Alsop, D.C. *et al.* (2015a) 'Recommended implementation of arterial spin-labeled perfusion MRI for clinical applications: A consensus of the ISMRM perfusion study group and the European consortium for ASL in dementia', *Magnetic Resonance in Medicine*, 73(1), pp. 102–116. Available at: https://doi.org/10.1002/mrm.25197.

13. Alsop, D.C. *et al.* (2015b) 'Recommended implementation of arterial spin-labeled perfusion MRI for clinical applications: A consensus of the ISMRM perfusion study group and the European consortium for ASL in dementia', *Magnetic Resonance in Medicine*, 73(1), pp. 102–116. Available at: https://doi.org/10.1002/mrm.25197.

14. Álvarez-Torres, M.D.M. *et al.* (2023) 'Vascular differences between IDH-wildtype glioblastoma and astrocytoma IDH-mutant grade 4 at imaging and transcriptomic levels', *NMR in biomedicine*, 36(11), p. e5004. Available at: https://doi.org/10.1002/nbm.5004.

15. d'Amati, A. *et al.* (2024) 'Pediatric CNS tumors and 2021 WHO classification: what do oncologists need from pathologists?', *Frontiers in Molecular Neuroscience*, 17. Available at: https://doi.org/10.3389/fnmol.2024.1268038.

16. Amukotuwa, S.A., Yu, C. and Zaharchuk, G. (2016) '3D Pseudocontinuous arterial spin labeling in routine clinical practice: A review of clinically significant artifacts', *Journal of magnetic resonance imaging: JMRI*, 43(1), pp. 11–27. Available at: https://doi.org/10.1002/jmri.24873.

17. Anazodo, U.C. *et al.* (2018) 'Using simultaneous PET/MRI to compare the accuracy of diagnosing frontotemporal dementia by arterial spin labelling MRI and FDG-PET', *NeuroImage: Clinical*, 17, pp. 405–414. Available at: https://doi.org/10.1016/j.nicl.2017.10.033.

18. Anderson, K.E. *et al.* (2007) 'Impairment of nonverbal recognition in Alzheimer disease', *Neurology*, 69(1), pp. 32–41. Available at: https://doi.org/10.1212/01.wnl.0000266561.47619.23.

19. André, C. (2010) 'CADASIL: pathogenesis, clinical and radiological findings and treatment', *Arquivos de Neuro-Psiquiatria*, 68, pp. 287–299. Available at: https://doi.org/10.1590/S0004-282X2010000200026.

20. Andreucci, M. *et al.* (2015) 'The Toxicity of Iodinated Radiographic Contrast Agents in the Clinical Practice', *Journal of Nephrology Advances*, 1(1), p. 6. Available at: https://doi.org/10.14302/issn.2574-4488.jna-14-601.

21. Andrews, A.M. *et al.* (2016) 'Mechanical Injury Induces Brain Endothelial-Derived Microvesicle Release: Implications for Cerebral Vascular Injury during Traumatic Brain Injury', *Frontiers in Cellular Neuroscience*, 10. Available at: https://doi.org/10.3389/fncel.2016.00043.

22. Artzi, M. *et al.* (2015) 'Classification of tumor area using combined DCE and DSC MRI in patients with glioblastoma', *Journal of Neuro-Oncology*, 121(2), pp. 349–357. Available at: https://doi.org/10.1007/s11060-014-1639-3.

23. Attwell, D. *et al.* (2010) 'Glial and neuronal control of brain blood flow', *Nature*, 468(7321), pp. 232–243. Available at: https://doi.org/10.1038/nature09613.

24. Azizova, A. *et al.* (2025a) 'Preoperative prediction of diffuse glioma type and grade in adults: a gadolinium-free MRI-based decision tree', *European Radiology*, 35(3), pp. 1242–1254. Available at: https://doi.org/10.1007/s00330-024-11140-5.

25. Azizova, A. *et al.* (2025b) ‘Preoperative prediction of diffuse glioma type and grade in adults: a gadolinium-free MRI-based decision tree’, *European Radiology*, 35(3), pp. 1242–1254. Available at: https://doi.org/10.1007/s00330-024-11140-5.

26. Baenziger, O. *et al.* (1994) ‘Cerebral blood flow in preterm infants affected by sex, mechanical ventilation, and intrauterine growth’, *Pediatric Neurology*, 11(4), pp. 319–324. Available at: https://doi.org/10.1016/0887-8994(94)90009-4.

27. Bammer, R. (2016) *MR and CT Perfusion and Pharmacokinetic Imaging*. 1st ed. Philadelphia: Wolters Kluwer Health.

28. Bansal, V. *et al.* (2017) ‘Usefulness of Pulsed Arterial Spin Labeling Magnetic Resonance Imaging in New-onset Seizure Patients and Its Comparison with Dynamic Susceptibility Contrast Magnetic Resonance Imaging’, *Journal of Neurosciences in Rural Practice*, 8(4), pp. 569–574. Available at: https://doi.org/10.4103/jnrp.jnrp_141_17.

29. Baranger, J. *et al.* (2021) ‘Brain perfusion imaging in neonates’, *NeuroImage. Clinical*, 31, p. 102756. Available at: https://doi.org/10.1016/j.nicl.2021.102756.

30. Bayraktar, E.S. *et al.* (2024) ‘Comparison of ASL and DSC perfusion methods in the evaluation of response to treatment in patients with a history of treatment for malignant brain tumor’, *BMC Medical Imaging*, 24(1), p. 70. Available at: https://doi.org/10.1186/s12880-024-01249-w.

31. Becker, A.J. (2018) ‘Review: Animal models of acquired epilepsy: insights into mechanisms of human epileptogenesis’, *Neuropathology and Applied Neurobiology*, 44(1), pp. 112–129. Available at: https://doi.org/10.1111/nan.12451.

32. Becks, M.J. *et al.* (2019) ‘Brain CT perfusion improves intracranial vessel occlusion detection on CT angiography’, *Journal of Neuroradiology = Journal De Neuroradiologie*, 46(2), pp. 124–129. Available at: https://doi.org/10.1016/j.neurad.2018.03.003.

33. Bell, A.H. *et al.* (2020) ‘The Neurovascular Unit: Effects of Brain Insults During the Perinatal Period’, *Frontiers in Neuroscience*, 13, p. 1452. Available at: https://doi.org/10.3389/fnins.2019.01452.

34. Bell, L.C. *et al.* (2024) ‘The road to the ISMRM OSIPI: A community-led initiative for reproducible perfusion MRI’, *Magnetic Resonance in Medicine*, 91(5), pp. 1740–1742. Available at: https://doi.org/10.1002/mrm.29736.

35. Bellomo, J. *et al.* (2025) ‘Blood Oxygenation Level–Dependent Cerebrovascular Reactivity–Derived Steal Phenomenon May Indicate Tissue Reperfusion Failure After Successful Endovascular Thrombectomy’, *Translational Stroke Research*, 16(2), pp. 207–216. Available at: https://doi.org/10.1007/s12975-023-01203-y.

36. Benavides, A. *et al.* (2019) ‘Sex Specific Alterations in Preterm Brain’, *Pediatric research*, 85(1), pp. 55–62. Available at: https://doi.org/10.1038/s41390-018-0187-5.

37. Benders, M.J.N.L. *et al.* (2011) ‘Phase-Contrast Magnetic Resonance Angiography Measurements of Global Cerebral Blood Flow in the Neonate’, *Pediatric Research*, 69(6), pp. 544–547. Available at: https://doi.org/10.1203/PDR.0b013e3182176aab.

38. Benini, R. *et al.* (2022) 'Landscape of childhood epilepsies – A multi-ethnic population-based study', *Epilepsy Research*, 183, p. 106936. Available at: https://doi.org/10.1016/j.eplepsyres.2022.106936.

39. Benson, J.C. *et al.* (2023) 'The Monro-Kellie Doctrine: A Review and Call for Revision', *American Journal of Neuroradiology*, 44(1), pp. 2–6. Available at: https://doi.org/10.3174/ajnr.A7721.

40. van den Bent, M.J. *et al.* (2023) 'Primary brain tumours in adults', *Lancet (London, England)*, 402(10412), pp. 1564–1579. Available at: https://doi.org/10.1016/S0140-6736(23)01054-1.

41. Bernetti, C. *et al.* (2025) 'Arterial Spin Labeling MRI in Alzheimer's Disease: A Systematic Review of Cerebral Perfusion Biomarkers', *Journal of Neuroimaging: Official Journal of the American Society of Neuroimaging*, 35(2), p. e70035. Available at: https://doi.org/10.1111/jon.70035.

42. Bernier, M., Cunnane, S.C. and Whittingstall, K. (2018) 'The morphology of the human cerebrovascular system', *Human Brain Mapping*, 39(12), pp. 4962–4975. Available at: https://doi.org/10.1002/hbm.24337.

43. Bhakta, N. *et al.* (2019) 'Childhood cancer burden: a review of global estimates', *The Lancet Oncology*, 20(1), pp. e42–e53. Available at: https://doi.org/10.1016/S1470-2045(18)30761-7.

44. Binnewijzend, M.A.A. *et al.* (2016) 'Cerebral perfusion in the predementia stages of Alzheimer's disease', *European Radiology*, 26(2), pp. 506–514. Available at: https://doi.org/10.1007/s00330-015-3834-9.

45. Bjørnerud, A. and Emblem, K.E. (2010) 'A Fully Automated Method for Quantitative Cerebral Hemodynamic Analysis Using DSC–MRI', *Journal of Cerebral Blood Flow & Metabolism*, 30(5), pp. 1066–1078. Available at: https://doi.org/10.1038/jcbfm.2010.4.

46. Blomqvist, L. *et al.* (2022) 'Gadolinium in Medical Imaging-Usefulness, Toxic Reactions and Possible Countermeasures-A Review', *Biomolecules*, 12(6), p. 742. Available at: https://doi.org/10.3390/biom12060742.

47. Bouyssi-Kobar, M. *et al.* (2018) 'Altered Cerebral Perfusion in Infants Born Preterm Compared with Infants Born Full Term', *The Journal of Pediatrics*, 193, pp. 54-61.e2. Available at: https://doi.org/10.1016/j.jpeds.2017.09.083.

48. Boxerman, J.L. *et al.* (2017) 'Longitudinal DSC-MRI for Distinguishing Tumor Recurrence From Pseudoprogression in Patients With a High-grade Glioma', *American Journal of Clinical Oncology*, 40(3), pp. 228–234. Available at: https://doi.org/10.1097/COC.0000000000000156.

49. Bradley, S. *et al.* (2007) 'I could lose everything: understanding the cost of a brain tumor', *Journal of Neuro-Oncology*, 85(3), pp. 329–338. Available at: https://doi.org/10.1007/s11060-007-9425-0.

50. Brassard, P. *et al.* (2021) 'Losing the dogmatic view of cerebral autoregulation', *Physiological Reports*, 9(15), p. e14982. Available at: https://doi.org/10.14814/phy2.14982.

51. Brassard, P. *et al.* (2023) 'Quantification of dynamic cerebral autoregulation: welcome to the jungle!', *Clinical Autonomic Research*, 33(6), pp. 791–810. Available at: https://doi.org/10.1007/s10286-023-00986-2.

52. Brian, J.E. (1998) 'Carbon Dioxide and the Cerebral Circulation', *Anesthesiology*, 88(5), p. 1365. Available at: https://doi.org/10.1097/00000542-199805000-00029.

53. Brown, C.E. *et al.* (2007) 'Extensive turnover of dendritic spines and vascular remodeling in cortical tissues recovering from stroke', *The Journal of Neuroscience: The Official Journal of the Society for Neuroscience*, 27(15), pp. 4101–4109. Available at: https://doi.org/10.1523/JNEUROSCI.4295-06.2007.

54. Brünjes, R. and Hofmann, T. (2020) 'Anthropogenic gadolinium in freshwater and drinking water systems', *Water Research*, 182, p. 115966. Available at: https://doi.org/10.1016/j.watres.2020.115966.

55. Buxton, R.B. *et al.* (1998) 'A general kinetic model for quantitative perfusion imaging with arterial spin labeling', *Magnetic Resonance in Medicine*, 40(3), pp. 383–396. Available at: https://doi.org/10.1002/mrm.1910400308.

56. Buxton, R.B. *et al.* (2004) 'Modeling the hemodynamic response to brain activation', *NeuroImage*, 23 Suppl 1, pp. S220-233. Available at: https://doi.org/10.1016/j.neuroimage.2004.07.013.

57. Calamante, F. (2010) 'Perfusion MRI using dynamic-susceptibility contrast MRI: quantification issues in patient studies', *Topics in magnetic resonance imaging: TMRI*, 21(2), pp. 75–85. Available at: https://doi.org/10.1097/RMR.0b013e31821e53f5.

58. Campbell, B.C.V. *et al.* (2011) 'Cerebral blood flow is the optimal CT perfusion parameter for assessing infarct core', *Stroke*, 42(12), pp. 3435–3440. Available at: https://doi.org/10.1161/STROKEAHA.111.618355.

59. Campbell, B.C.V. *et al.* (2015a) 'Endovascular Therapy for Ischemic Stroke with Perfusion-Imaging Selection', *New England Journal of Medicine*, 372(11), pp. 1009–1018. Available at: https://doi.org/10.1056/NEJMoa1414792.

60. Campbell, B.C.V. *et al.* (2015b) 'Endovascular Therapy for Ischemic Stroke with Perfusion-Imaging Selection', *New England Journal of Medicine*, 372(11), pp. 1009–1018. Available at: https://doi.org/10.1056/NEJMoa1414792.

61. Candelario-Jalil, E. *et al.* (2007) 'Cyclooxygenase inhibition limits blood-brain barrier disruption following intracerebral injection of tumor necrosis factor-alpha in the rat', *The Journal of Pharmacology and Experimental Therapeutics*, 323(2), pp. 488–498. Available at: https://doi.org/10.1124/jpet.107.127035.

62. Carrera-González, M.D.P., Cantón-Habas, V. and Rich-Ruiz, M. (2022) 'Aging, depression and dementia: The inflammatory process', *Advances in Clinical and*

*Experimental Medicine: Official Organ Wroclaw Medical University*, 31(5), pp. 469–473. Available at: https://doi.org/10.17219/acem/149897.

63. Carsin-Vu, A. *et al.* (2018) 'Measurement of pediatric regional cerebral blood flow from 6 months to 15 years of age in a clinical population', *European Journal of Radiology*, 101, pp. 38–44. Available at: https://doi.org/10.1016/j.ejrad.2018.02.003.

64. Carvalho, C. and Moreira, P.I. (2018) 'Oxidative Stress: A Major Player in Cerebrovascular Alterations Associated to Neurodegenerative Events', *Frontiers in Physiology*, 9, p. 806. Available at: https://doi.org/10.3389/fphys.2018.00806.

65. Cash, A. and Theus, M.H. (2020) 'Mechanisms of Blood-Brain Barrier Dysfunction in Traumatic Brain Injury', *International Journal of Molecular Sciences*, 21(9), p. 3344. Available at: https://doi.org/10.3390/ijms21093344.

66. Cauli, B. and Hamel, E. (2010) 'Revisiting the Role of Neurons in Neurovascular Coupling', *Frontiers in Neuroenergetics*, 2, p. 9. Available at: https://doi.org/10.3389/fnene.2010.00009.

67. Chaban, Y.V. *et al.* (2024) 'Environmental Sustainability and MRI: Challenges, Opportunities, and a Call for Action', *Journal of magnetic resonance imaging: JMRI*, 59(4), pp. 1149–1167. Available at: https://doi.org/10.1002/jmri.28994.

68. Chaigneau, E. *et al.* (2003) 'Two-photon imaging of capillary blood flow in olfactory bulb glomeruli', *Proceedings of the National Academy of Sciences of the United States of America*, 100(22), pp. 13081–13086. Available at: https://doi.org/10.1073/pnas.2133652100.

69. Chandra, A. *et al.* (2017) 'The cerebral circulation and cerebrovascular disease I: Anatomy', *Brain Circulation*, 3(2), pp. 45–56. Available at: https://doi.org/10.4103/bc.bc_10_17.

70. Chao, L.L. *et al.* (2010) 'ASL Perfusion MRI Predicts Cognitive Decline and Conversion From MCI to Dementia', *Alzheimer Disease & Associated Disorders*, 24(1), p. 19. Available at: https://doi.org/10.1097/WAD.0b013e3181b4f736.

71. Chappell, M.A. *et al.* (2023) 'BASIL: A toolbox for perfusion quantification using arterial spin labelling', *Imaging Neuroscience*, 1, pp. 1–16. Available at: https://doi.org/10.1162/imag_a_00041.

72. Chen, D.Y., Di, X. and Biswal, B. (2024) 'Cerebrovascular reactivity increases across development in multiple networks as revealed by a breath-holding task: A longitudinal fMRI study', *Human Brain Mapping*, 45(1). Available at: https://doi.org/10.1002/hbm.26515.

73. Chen, Y. *et al.* (2023) 'Blood-brain barrier dysfunction and Alzheimer's disease: associations, pathogenic mechanisms, and therapeutic potential', *Frontiers in Aging Neuroscience*, 15. Available at: https://doi.org/10.3389/fnagi.2023.1258640.

74. Cheong, E.-N. *et al.* (2024) 'Achieving imaging and computational reproducibility on multiparametric MRI radiomics features in brain tumor diagnosis: phantom and clinical

validation', *European Radiology*, 34(3), pp. 2008–2023. Available at: https://doi.org/10.1007/s00330-023-10164-7.

75. Chien, S. (2007) 'Mechanotransduction and endothelial cell homeostasis: the wisdom of the cell', *American Journal of Physiology-Heart and Circulatory Physiology*, 292(3), pp. H1209–H1224. Available at: https://doi.org/10.1152/ajpheart.01047.2006.

76. Chiron, C. *et al.* (1992) 'Changes in Regional Cerebral Blood Flow During Brain Maturation in Children and Adolescents', *Journal of Nuclear Medicine*, 33(5), pp. 696–703.

77. Chiu, F.-Y. and Yen, Y. (2023) 'Imaging biomarkers for clinical applications in neuro-oncology: current status and future perspectives', *Biomarker Research*, 11(1), p. 35. Available at: https://doi.org/10.1186/s40364-023-00476-7.

78. Christen, T. *et al.* (2014) 'MR vascular fingerprinting: A new approach to compute cerebral blood volume, mean vessel radius, and oxygenation maps in the human brain', *NeuroImage*, 89, pp. 262–270. Available at: https://doi.org/10.1016/j.neuroimage.2013.11.052.

79. Christians, J.K. *et al.* (2023) 'Sex differences in the effects of prematurity and/or low birthweight on neurodevelopmental outcomes: systematic review and meta-analyses', *Biology of Sex Differences*, 14(1), p. 47. Available at: https://doi.org/10.1186/s13293-023-00532-9.

80. Cindil, E. *et al.* (2022) 'Prediction of IDH Mutation Status in High-grade Gliomas Using DWI and High T1-weight DSC-MRI', *Academic Radiology*, 29 Suppl 3, pp. S52–S62. Available at: https://doi.org/10.1016/j.acra.2021.02.002.

81. Claassen, J.A.H.R. *et al.* (2021) 'Regulation of cerebral blood flow in humans: physiology and clinical implications of autoregulation', *Physiological Reviews*, 101(4), pp. 1487–1559. Available at: https://doi.org/10.1152/physrev.00022.2020.

82. Clement, P. *et al.* (2018) 'Variability of physiological brain perfusion in healthy subjects – A systematic review of modifiers. Considerations for multi-center ASL studies', *Journal of Cerebral Blood Flow & Metabolism*, 38(9), pp. 1418–1437. Available at: https://doi.org/10.1177/0271678X17702156.

83. Clement, P. *et al.* (2022) 'A Beginner's Guide to Arterial Spin Labeling (ASL) Image Processing', *Frontiers in Radiology*, 2. Available at: https://doi.org/10.3389/fradi.2022.929533.

84. Cohen, A.D., Nencka, A.S. and Wang, Y. (2018) 'Multiband multi-echo simultaneous ASL/BOLD for task-induced functional MRI', *PLoS ONE*, 13(2), p. e0190427. Available at: https://doi.org/10.1371/journal.pone.0190427.

85. Coimbra, S. *et al.* (2024) 'Toxicity Mechanisms of Gadolinium and Gadolinium-Based Contrast Agents—A Review', *International Journal of Molecular Sciences*, 25(7), p. 4071. Available at: https://doi.org/10.3390/ijms25074071.

86. Comper, W.D. (1996) *Extracellular Matrix*. CRC Press.

87. Cosgrove, D. and Lassau, N. (2010) 'Imaging of perfusion using ultrasound', *European Journal of Nuclear Medicine and Molecular Imaging*, 37 Suppl 1, pp. S65-85. Available at: https://doi.org/10.1007/s00259-010-1537-7.

88. Crompton, M.R. (1962) 'THE PATHOLOGY OF RUPTURED MIDDLE-CEREBRAL ANEURYSMS WITH SPECIAL REFERENCE TO THE DIFFERENCES BETWEEN THE SEXES', *The Lancet*, 280(7253), pp. 421–425. Available at: https://doi.org/10.1016/S0140-6736(62)90281-7.

89. Dai, W. *et al.* (2008) 'Continuous flow-driven inversion for arterial spin labeling using pulsed radio frequency and gradient fields', *Magnetic Resonance in Medicine*, 60(6), pp. 1488–1497. Available at: https://doi.org/10.1002/mrm.21790.

90. Dai, W. *et al.* (2012) 'Reduced resolution transit delay prescan for quantitative continuous arterial spin labeling perfusion imaging', *Magnetic Resonance in Medicine*, 67(5), pp. 1252–1265. Available at: https://doi.org/10.1002/mrm.23103.

91. Dai, W., Shankaranarayanan, A. and Alsop, D.C. (2013) 'Volumetric measurement of perfusion and arterial transit delay using hadamard encoded continuous arterial spin labeling', *Magnetic Resonance in Medicine*, 69(4), pp. 1014–1022. Available at: https://doi.org/10.1002/mrm.24335.

92. Daneman, R. and Prat, A. (2015) 'The blood-brain barrier', *Cold Spring Harbor Perspectives in Biology*, 7(1), p. a020412. Available at: https://doi.org/10.1101/cshperspect.a020412.

93. Dangouloff-Ros, V. *et al.* (2016) 'Arterial Spin Labeling to Predict Brain Tumor Grading in Children: Correlations between Histopathologic Vascular Density and Perfusion MR Imaging', *Radiology*, 281(2), pp. 553–566. Available at: https://doi.org/10.1148/radiol.2016152228.

94. Davis, A.S. *et al.* (2014) 'Outcomes of extremely preterm infants following severe intracranial hemorrhage', *Journal of Perinatology: Official Journal of the California Perinatal Association*, 34(3), pp. 203–208. Available at: https://doi.org/10.1038/jp.2013.162.

95. Davis, M.J. and Hill, M.A. (1999) 'Signaling Mechanisms Underlying the Vascular Myogenic Response', *Physiological Reviews*, 79(2), pp. 387–423. Available at: https://doi.org/10.1152/physrev.1999.79.2.387.

96. Deguchi, S. *et al.* (2020) 'Clinicopathological analysis of T2-FLAIR mismatch sign in lower-grade gliomas', *Scientific Reports*, 10(1), p. 10113. Available at: https://doi.org/10.1038/s41598-020-67244-7.

97. Demeestere, J. *et al.* (2020) 'Review of Perfusion Imaging in Acute Ischemic Stroke', *Stroke*, 51(3), pp. 1017–1024. Available at: https://doi.org/10.1161/STROKEAHA.119.028337.

98. Detre, J.A. *et al.* (1998) 'Noninvasive MRI evaluation of cerebral blood flow in cerebrovascular disease', *Neurology*, 50(3), pp. 633–641. Available at: https://doi.org/10.1212/wnl.50.3.633.

99. Detre, J.A., Williams, D.S. and Koretsky, A.P. (1990) 'Nuclear magnetic resonance determination of flow, lactate, and phosphate metabolites during amphetamine stimulation of the rat brain', *NMR in Biomedicine*, 3(6), pp. 272–278. Available at: https://doi.org/10.1002/nbm.1940030606.

100. Dijsselhof, M.B.J. *et al.* (2025) 'Multi-cohort, multi-sequence harmonisation for cerebrovascular brain age'. bioRxiv, p. 2025.04.22.649344. Available at: https://doi.org/10.1101/2025.04.22.649344.

101. van Dinther, M. *et al.* (2024) 'Lower cerebral blood flow predicts cognitive decline in patients with vascular cognitive impairment', *Alzheimer's & Dementia*, 20(1), pp. 136–144. Available at: https://doi.org/10.1002/alz.13408.

102. Dipasquale, O. *et al.* (2023) 'Molecular-enriched functional connectivity in the human brain using multiband multi-echo simultaneous ASL/BOLD fMRI', *Scientific Reports*, 13(1), p. 11751. Available at: https://doi.org/10.1038/s41598-023-38573-0.

103. Dogariu, O.A. *et al.* (2023) 'Diagnosis and treatment of Watershed strokes: a narrative review', *Journal of Medicine and Life*, 16(6), pp. 842–850. Available at: https://doi.org/10.25122/jml-2023-0127.

104. van Dorth, D. *et al.* (2025) 'Perfusion MRI-based differentiation between early tumor progression and pseudoprogression in glioblastoma and its use in clinical practice', *Neuro-Oncology Practice*, 12(2), pp. 281–290. Available at: https://doi.org/10.1093/nop/npae099.

105. Drew, P.J. (2022) 'Neurovascular coupling: motive unknown', *Trends in Neurosciences*, 45(11), pp. 809–819. Available at: https://doi.org/10.1016/j.tins.2022.08.004.

106. Dubois, J. *et al.* (2021) 'MRI of the Neonatal Brain: A Review of Methodological Challenges and Neuroscientific Advances', *Journal of Magnetic Resonance Imaging*, 53(5), pp. 1318–1343. Available at: https://doi.org/10.1002/jmri.27192.

107. Dunn, J.F. and Isaacs, A.M. (2021) 'The impact of hypoxia on blood-brain, blood-CSF, and CSF-brain barriers', *Journal of Applied Physiology (Bethesda, Md.: 1985)*, 131(3), pp. 977–985. Available at: https://doi.org/10.1152/japplphysiol.00108.2020.

108. Dupont, P. *et al.* (2009) 'Dynamic perfusion patterns in temporal lobe epilepsy', *European Journal of Nuclear Medicine and Molecular Imaging*, 36(5), pp. 823–830. Available at: https://doi.org/10.1007/s00259-008-1040-6.

109. Ellingson, B.M. *et al.* (2012) 'Comparison between intensity normalization techniques for dynamic susceptibility contrast (DSC)-MRI estimates of cerebral blood volume (CBV) in human gliomas', *Journal of Magnetic Resonance Imaging*, 35(6), pp. 1472–1477. Available at: https://doi.org/10.1002/jmri.23600.

110. Engelhardt, S., Patkar, S. and Ogunshola, O.O. (2014) 'Cell-specific blood-brain barrier regulation in health and disease: a focus on hypoxia', *British Journal of Pharmacology*, 171(5), pp. 1210–1230. Available at: https://doi.org/10.1111/bph.12489.

111. Eyding, J. *et al.* (2020) 'Twenty Years of Cerebral Ultrasound Perfusion Imaging—Is the Best yet to Come?', *Journal of Clinical Medicine*, 9(3), p. 816. Available at: https://doi.org/10.3390/jcm9030816.

112. Falcon, C. *et al.* (2024) 'Time-encoded ASL reveals lower cerebral blood flow in the early AD continuum', *Alzheimer's & Dementia*, 20(8), pp. 5183–5197. Available at: https://doi.org/10.1002/alz.14059.

113. Fan, H. *et al.* (2024) 'ISMRM Open Science Initiative for Perfusion Imaging (OSIPI): ASL pipeline inventory', *Magnetic Resonance in Medicine*, 91(5), pp. 1787–1802. Available at: https://doi.org/10.1002/mrm.29869.

114. Fang, J., Wang, Z. and Miao, C. (2023) 'Angiogenesis after ischemic stroke', *Acta Pharmacologica Sinica*, 44(7), pp. 1305–1321. Available at: https://doi.org/10.1038/s41401-023-01061-2.

115. Faraci, F.M. and Heistad, D.D. (1998) 'Regulation of the cerebral circulation: role of endothelium and potassium channels', *Physiological Reviews*, 78(1), pp. 53–97. Available at: https://doi.org/10.1152/physrev.1998.78.1.53.

116. Faraco, G. and Iadecola, C. (2013) 'Hypertension: a harbinger of stroke and dementia', *Hypertension*, 62(5), p. 10.1161/HYPERTENSIONAHA.113.01063. Available at: https://doi.org/10.1161/HYPERTENSIONAHA.113.01063.

117. Farnsworth, R.H. *et al.* (2014) 'Vascular remodeling in cancer', *Oncogene*, 33(27), pp. 3496–3505. Available at: https://doi.org/10.1038/onc.2013.304.

118. Favre, M.E. and Serrador, J.M. (2019) 'Sex differences in cerebral autoregulation are unaffected by menstrual cycle phase in young, healthy women', *American Journal of Physiology. Heart and Circulatory Physiology*, 316(4), pp. H920–H933. Available at: https://doi.org/10.1152/ajpheart.00474.2018.

119. Ferlay, J. *et al.* (2024) *Global Cancer Observatory: Cancer Today*. Lyon, France: International Agency for Research on Cancer. Available at: https://gco.iarc.who.int/today (Accessed: 2 June 2025).

120. Fischer, S. *et al.* (2002) 'Hypoxia-induced hyperpermeability in brain microvessel endothelial cells involves VEGF-mediated changes in the expression of zonula occludens-1', *Microvascular Research*, 63(1), pp. 70–80. Available at: https://doi.org/10.1006/mvre.2001.2367.

121. Fletcher, E.L. *et al.* (2023) 'Anomalies in neurovascular coupling during early diabetes: A review', *Clinical & Experimental Ophthalmology*, 51(1), pp. 81–91. Available at: https://doi.org/10.1111/ceo.14190.

122. Foltyn-Dumitru, M. *et al.* (2025) 'Histopathological and molecular characteristics of IDH-wildtype glioblastoma without contrast enhancement: Implications for clinical outcomes', *Neuro-Oncology*, p. noaf070. Available at: https://doi.org/10.1093/neuonc/noaf070.

123. Forte, A. *et al.* (2010) 'Role of myofibroblasts in vascular remodelling: focus on restenosis and aneurysm', *Cardiovascular Research*, 88(3), pp. 395–405. Available at: https://doi.org/10.1093/cvr/cvq224.

124. Fox, B.M. *et al.* (2021) 'Pathophysiology of Vascular Stenosis and Remodeling in Moyamoya Disease', *Frontiers in Neurology*, 12, p. 661578. Available at: https://doi.org/10.3389/fneur.2021.661578.

125. Friston, K. *et al.* (eds) (2011) 'Statistical Parametric Mapping: the analysis of functional brain images', in *Statistical Parametric Mapping: the analysis of functional brain images.* London: Academic Press. Available at: https://doi.org/10.1016/B978-0-12-372560-8.50052-8.

126. Fu, R. *et al.* (2022) 'Diagnostic performance of DSC perfusion MRI to distinguish tumor progression and treatment-related changes: a systematic review and meta-analysis', *Neuro-oncology Advances*, 4(1), p. vdac027. Available at: https://doi.org/10.1093/noajnl/vdac027.

127. Fu, T. *et al.* (2022) 'Cerebral blood flow alterations in migraine patients with and without aura: An arterial spin labeling study', *The Journal of Headache and Pain*, 23(1), p. 131. Available at: https://doi.org/10.1186/s10194-022-01501-0.

128. Fukuda, S. *et al.* (2008) 'Late circulatory dysfunction and decreased cerebral blood flow volume in infants with periventricular leukomalacia', *Brain and Development*, 30(9), pp. 589–594. Available at: https://doi.org/10.1016/j.braindev.2008.02.001.

129. Fuster-Garcia, E. *et al.* (2021) 'MGMT methylation may benefit overall survival in patients with moderately vascularized glioblastomas', *European Radiology*, 31(3), pp. 1738–1747. Available at: https://doi.org/10.1007/s00330-020-07297-4.

130. Gaiser, C. *et al.* (2024) 'Population-wide cerebellar growth models of children and adolescents', *Nature Communications*, 15(1), p. 2351. Available at: https://doi.org/10.1038/s41467-024-46398-2.

131. Gao, H. *et al.* (2023) 'Damage mechanism and therapy progress of the blood-brain barrier after ischemic stroke', *Cell & Bioscience*, 13(1), p. 196. Available at: https://doi.org/10.1186/s13578-023-01126-z.

132. García-Figueiras, R. *et al.* (2013) 'CT perfusion in oncologic imaging: a useful tool?', *AJR. American journal of roentgenology*, 200(1), pp. 8–19. Available at: https://doi.org/10.2214/AJR.11.8476.

133. Gaser, C. (2009) 'Partial Volume Segmentation with Adaptive Maximum A Posteriori (MAP) Approach', *NeuroImage*, 47, p. S121. Available at: https://doi.org/10.1016/S1053-8119(09)71151-6.

134. van Gelderen, P., de Zwart, J. a. and Duyn, J. h. (2008) 'Pittfalls of MRI measurement of white matter perfusion based on arterial spin labeling', *Magnetic Resonance in Medicine*, 59(4), pp. 788–795. Available at: https://doi.org/10.1002/mrm.21515.

135. Ghosh, H.S. *et al.* (2025) 'Contemporary prognostic signatures and refined risk stratification of gliomas: An analysis of 4400 tumors', *Neuro-Oncology*, 27(1), pp. 195–208. Available at: https://doi.org/10.1093/neuonc/noae164.

136. Golay, X., Petersen, E.T. and Hui, F. (2005) 'Pulsed star labeling of arterial regions (PULSAR): a robust regional perfusion technique for high field imaging', *Magnetic Resonance in Medicine*, 53(1), pp. 15–21. Available at: https://doi.org/10.1002/mrm.20338.

137. Goldenberg, R.L. *et al.* (2008) 'Epidemiology and causes of preterm birth', *The Lancet*, 371(9606), pp. 75–84. Available at: https://doi.org/10.1016/S0140-6736(08)60074-4.

138. Grade, M. *et al.* (2015) 'A neuroradiologist's guide to arterial spin labeling MRI in clinical practice', *Neuroradiology*, 57(12), pp. 1181–1202. Available at: https://doi.org/10.1007/s00234-015-1571-z.

139. Gray, H., Standring, S. and Anhand, N. (eds) (2021) *Gray's Anatomy: the anatomical basis of clinical practice*. 42nd edition. Amsterdam: Elsevier.

140. Greene, C. *et al.* (2024) 'Blood-brain barrier disruption and sustained systemic inflammation in individuals with long COVID-associated cognitive impairment', *Nature Neuroscience*, 27(3), pp. 421–432. Available at: https://doi.org/10.1038/s41593-024-01576-9.

141. Grist, J.T. *et al.* (2021) 'Combining multi-site magnetic resonance imaging with machine learning predicts survival in pediatric brain tumors', *Scientific Reports*, 11(1), p. 18897. Available at: https://doi.org/10.1038/s41598-021-96189-8.

142. Gropper, M.A., Miller, R.D. and Cohen, N.H. (eds) (2020) *Miller's anesthesia*. Ninth edition. Philadelphia, PA: Elsevier.

143. GRUBB, R.L. *et al.* (1974) 'The Effects of Changes in PaCO2 Cerebral Blood Volume, Blood Flow, and Vascular Mean Transit Time', *Stroke*, 5(5), pp. 630–639. Available at: https://doi.org/10.1161/01.STR.5.5.630.

144. Guo, D. and Jiang, B. (2023) 'Noninvasively evaluating the grade and IDH mutation status of gliomas by using mono-exponential, bi-exponential diffusion-weighted imaging and three-dimensional pseudo-continuous arterial spin labeling', *European Journal of Radiology*, 160, p. 110721. Available at: https://doi.org/10.1016/j.ejrad.2023.110721.

145. Gur, R.E. and Gur, R.C. (2016) 'Sex differences in brain and behavior in adolescence: Findings from the Philadelphia Neurodevelopmental Cohort', *Neuroscience and Biobehavioral Reviews*, 70, pp. 159–170. Available at: https://doi.org/10.1016/j.neubiorev.2016.07.035.

146. Hak, J.F. *et al.* (2022) 'Arterial Spin Labeling for the Etiological Workup of Intracerebral Hemorrhage in Children', *Stroke*, 53(1), pp. 185–193. Available at: https://doi.org/10.1161/STROKEAHA.120.032690.

147. Halder, S.K. and Milner, R. (2020) 'Mild hypoxia triggers transient blood–brain barrier disruption: a fundamental protective role for microglia', *Acta Neuropathologica Communications*, 8(1), p. 175. Available at: https://doi.org/10.1186/s40478-020-01051-z.

148. Hall, C.N. *et al.* (2014) 'Capillary pericytes regulate cerebral blood flow in health and disease', *Nature*, 508(7494), pp. 55–60. Available at: https://doi.org/10.1038/nature13165.

149. van Hameren, G. *et al.* (2024) 'From spreading depolarization to blood–brain barrier dysfunction: navigating traumatic brain injury for novel diagnosis and therapy', *Nature Reviews Neurology*, 20(7), pp. 408–425. Available at: https://doi.org/10.1038/s41582-024-00973-9.

150. Hamner, J.W. and Tan, C.O. (2014) 'Relative Contributions of Sympathetic, Cholinergic, and Myogenic Mechanisms to Cerebral Autoregulation', *Stroke*, 45(6), pp. 1771–1777. Available at: https://doi.org/10.1161/STROKEAHA.114.005293.

151. Harris, J.J., Jolivet, R. and Attwell, D. (2012) 'Synaptic Energy Use and Supply', *Neuron*, 75(5), pp. 762–777. Available at: https://doi.org/10.1016/j.neuron.2012.08.019.

152. Hasan, T.F. *et al.* (2018) 'Diagnosis and Management of Acute Ischemic Stroke', *Mayo Clinic Proceedings*, 93(4), pp. 523–538. Available at: https://doi.org/10.1016/j.mayocp.2018.02.013.

153. He, Y. *et al.* (2023) 'What type of cell death occurs in chronic cerebral hypoperfusion? A review focusing on pyroptosis and its potential therapeutic implications', *Frontiers in Cellular Neuroscience*, 17. Available at: https://doi.org/10.3389/fncel.2023.1073511.

154. van der Heide, F.C.T. *et al.* (2022) 'Neurovascular coupling unit dysfunction and dementia: Retinal measurements as tools to move towards population-based evidence', *Frontiers in Endocrinology*, 13, p. 1014287. Available at: https://doi.org/10.3389/fendo.2022.1014287.

155. Hendrickson, T.J. *et al.* (2025) 'BIBSNet: A Deep Learning Baby Image Brain Segmentation Network for MRI Scans', *bioRxiv*, p. 2023.03.22.533696. Available at: https://doi.org/10.1101/2023.03.22.533696.

156. Hendrikx, D. *et al.* (2019) 'Measurement of Neurovascular Coupling in Neonates', *Frontiers in Physiology*, 10, p. 65. Available at: https://doi.org/10.3389/fphys.2019.00065.

157. Henriksen, O.M., del Mar Álvarez-Torres, M., *et al.* (2022) 'High-Grade Glioma Treatment Response Monitoring Biomarkers: A Position Statement on the Evidence Supporting the Use of Advanced MRI Techniques in the Clinic, and the Latest Bench-to-Bedside Developments. Part 1: Perfusion and Diffusion Techniques', *Frontiers in Oncology*, 12. Available at: https://doi.org/10.3389/fonc.2022.810263.

158. Henriksen, O.M., Del Mar Álvarez-Torres, M., *et al.* (2022) 'High-Grade Glioma Treatment Response Monitoring Biomarkers: A Position Statement on the Evidence Supporting the Use of Advanced MRI Techniques in the Clinic, and the Latest Bench-to-Bedside Developments. Part 1: Perfusion and Diffusion Techniques', *Frontiers in Oncology*, 12, p. 810263. Available at: https://doi.org/10.3389/fonc.2022.810263.

159. Hernandez-Garcia, L. *et al.* (2022a) 'Recent Technical Developments in ASL: A Review of the State of the Art', *Magnetic Resonance in Medicine*, 88(5), pp. 2021–2042. Available at: https://doi.org/10.1002/mrm.29381.

160. Hernandez-Garcia, L. *et al.* (2022b) 'Recent Technical Developments in ASL: A Review of the State of the Art', *Magnetic Resonance in Medicine*, 88(5), pp. 2021–2042. Available at: https://doi.org/10.1002/mrm.29381.

161. Higashi, Y. (2022) 'Roles of Oxidative Stress and Inflammation in Vascular Endothelial Dysfunction-Related Disease', *Antioxidants (Basel, Switzerland)*, 11(10), p. 1958. Available at: https://doi.org/10.3390/antiox11101958.

162. Hinzman, J.M. *et al.* (2014) 'Inverse neurovascular coupling to cortical spreading depolarizations in severe brain trauma', *Brain: A Journal of Neurology*, 137(Pt 11), pp. 2960–2972. Available at: https://doi.org/10.1093/brain/awu241.

163. Holstein-Rønsbo, S. *et al.* (2023) 'Glymphatic influx and clearance are accelerated by neurovascular coupling', *Nature Neuroscience*, 26(6), pp. 1042–1053. Available at: https://doi.org/10.1038/s41593-023-01327-2.

164. Hosur, B. *et al.* (2022) 'Advanced multiparametric MRI-based scoring for isocitrate dehydrogenase mutation prediction of gliomas', *Polish Journal of Radiology*, 87, pp. e626–e634. Available at: https://doi.org/10.5114/pjr.2022.121549.

165. van Hout, L.R. *et al.* (2025) 'The effect of aerobic exercise on cerebral perfusion in patients with vascular cognitive impairment, the Excersion-VCI randomised controlled clinical trial', *Cerebral Circulation - Cognition and Behavior*, 8, p. 100386. Available at: https://doi.org/10.1016/j.cccb.2025.100386.

166. Howlett, J.A. *et al.* (2013) 'Cerebrovascular autoregulation and neurologic injury in neonatal hypoxic–ischemic encephalopathy', *Pediatric Research*, 74(5), pp. 525–535. Available at: https://doi.org/10.1038/pr.2013.132.

167. Hu, L.S. *et al.* (2023) 'Integrated molecular and multiparametric MRI mapping of high-grade glioma identifies regional biologic signatures', *Nature Communications*, 14(1), p. 6066. Available at: https://doi.org/10.1038/s41467-023-41559-1.

168. Hu, L.S. *et al.* (2025) 'Advanced Imaging in the Diagnosis and Response Assessment of High-Grade Glioma: AJR Expert Panel Narrative Review', *American Journal of Roentgenology*, 224(1), p. e2330612. Available at: https://doi.org/10.2214/AJR.23.30612.

169. Hu, Z. *et al.* (no date) 'High-Fidelity MRI Assessment of Cerebral Perfusion in Healthy Neonates Less Than 1 Week of Age', *Journal of Magnetic Resonance Imaging*, n/a(n/a). Available at: https://doi.org/10.1002/jmri.29740.

170. Hua, J. *et al.* (2019) 'MRI techniques to measure arterial and venous cerebral blood volume', *NeuroImage*, 187, pp. 17–31. Available at: https://doi.org/10.1016/j.neuroimage.2018.02.027.

171. Hughes, E.J. *et al.* (2017) 'A dedicated neonatal brain imaging system', *Magnetic Resonance in Medicine*, 78(2), pp. 794–804. Available at: https://doi.org/10.1002/mrm.26462.

172. Huneau, C., Benali, H. and Chabriat, H. (2015) 'Investigating Human Neurovascular Coupling Using Functional Neuroimaging: A Critical Review of Dynamic Models',

*Frontiers in Neuroscience*, 9, p. 467. Available at: https://doi.org/10.3389/fnins.2015.00467.

173. Iacoban, C.G. *et al.* (2024) 'Advanced imaging techniques and non-invasive biomarkers in pediatric brain tumors: state of the art', *Neuroradiology*, 66(12), pp. 2093–2116. Available at: https://doi.org/10.1007/s00234-024-03476-y.

174. Iadecola, C. (2017) 'The Neurovascular Unit Coming of Age: A Journey through Neurovascular Coupling in Health and Disease', *Neuron*, 96(1), pp. 17–42. Available at: https://doi.org/10.1016/j.neuron.2017.07.030.

175. Ibaraki, M. *et al.* (2008) 'Quantification of cerebral blood flow and oxygen metabolism with 3-dimensional PET and 15O: validation by comparison with 2-dimensional PET', *Journal of Nuclear Medicine: Official Publication, Society of Nuclear Medicine*, 49(1), pp. 50–59. Available at: https://doi.org/10.2967/jnumed.107.044008.

176. Iliff, J.J. *et al.* (2012) 'A paravascular pathway facilitates CSF flow through the brain parenchyma and the clearance of interstitial solutes, including amyloid β', *Science Translational Medicine*, 4(147), p. 147ra111. Available at: https://doi.org/10.1126/scitranslmed.3003748.

177. Immink, R.V. *et al.* (2019) 'Cerebral autoregulation: with age comes wisdom', *British Journal of Anaesthesia*, 123(3), pp. e466–e468. Available at: https://doi.org/10.1016/j.bja.2019.06.006.

178. Isaacs, D. *et al.* (2024) 'KATP channel–dependent electrical signaling links capillary pericytes to arterioles during neurovascular coupling', *Proceedings of the National Academy of Sciences*, 121(50), p. e2405965121. Available at: https://doi.org/10.1073/pnas.2405965121.

179. Ito, H. *et al.* (2023) 'Oxygen extraction fraction is not uniform in human brain: a positron emission tomography study', *The Journal of Physiological Sciences*, 73(1), p. 25. Available at: https://doi.org/10.1186/s12576-023-00880-6.

180. Iturria-Medina, Y. *et al.* (2016) 'Early role of vascular dysregulation on late-onset Alzheimer's disease based on multifactorial data-driven analysis', *Nature Communications*, 7(1), p. 11934. Available at: https://doi.org/10.1038/ncomms11934.

181. Iv, M. *et al.* (2019) 'Perfusion MRI-Based Fractional Tumor Burden Differentiates between Tumor and Treatment Effect in Recurrent Glioblastomas and Informs Clinical Decision-Making', *American Journal of Neuroradiology*, 40(10), pp. 1649–1657. Available at: https://doi.org/10.3174/ajnr.A6211.

182. Jang, H. *et al.* (2017) 'Alterations in neurovascular coupling following acute traumatic brain injury', *Neurophotonics*, 4(4), p. 045007. Available at: https://doi.org/10.1117/1.NPh.4.4.045007.

183. Järnum, H. *et al.* (2010) 'Perfusion MRI of brain tumours: a comparative study of pseudo-continuous arterial spin labelling and dynamic susceptibility contrast imaging', *Neuroradiology*, 52(4), pp. 307–317. Available at: https://doi.org/10.1007/s00234-009-0616-6.

184. Jarutyte, L. *et al.* (2025) 'Advantages and challenges of using arterial spin labelling MRI to monitor cerebral blood flow in multi-centre clinical trials of neurodegenerative disease: Experience from the RADAR study', *Cerebral Circulation - Cognition and Behavior*, 8, p. 100376. Available at: https://doi.org/10.1016/j.cccb.2024.100376.

185. Jin, R. *et al.* (2013) 'Role of inflammation and its mediators in acute ischemic stroke', *Journal of Cardiovascular Translational Research*, 6(5), pp. 834–851. Available at: https://doi.org/10.1007/s12265-013-9508-6.

186. Johnson, G.B. *et al.* (2020) 'PET Imaging of Tumor Perfusion: A Potential Cancer Biomarker?', *Seminars in Nuclear Medicine*, 50(6), pp. 549–561. Available at: https://doi.org/10.1053/j.semnuclmed.2020.07.001.

187. Johnson, V.E. *et al.* (2018) 'Mechanical disruption of the blood–brain barrier following experimental concussion', *Acta neuropathologica*, 135(5), pp. 711–726. Available at: https://doi.org/10.1007/s00401-018-1824-0.

188. Joseph, C.R. *et al.* (2024) 'Identifying delay in glymphatic clearance of labeled protons post-acute head trauma utilizing 3D ASL MRI (arterial spin labeling): a pilot study', *Scientific Reports*, 14(1), p. 6188. Available at: https://doi.org/10.1038/s41598-024-56236-6.

189. Jt, R. *et al.* (2024) 'Evidence for interictal blood-brain barrier dysfunction in people with epilepsy', *Epilepsia*, 65(5). Available at: https://doi.org/10.1111/epi.17929.

190. Juan-Albarracín, J. *et al.* (2019) 'ONCOhabitats: A system for glioblastoma heterogeneity assessment through MRI', *International Journal of Medical Informatics*, 128, pp. 53–61. Available at: https://doi.org/10.1016/j.ijmedinf.2019.05.002.

191. Kadali, K.R. *et al.* (2025) 'An effective MRI perfusion threshold based workflow to triage additional 18F-FET PET in posttreatment high grade glioma', *Scientific Reports*, 15(1), p. 7749. Available at: https://doi.org/10.1038/s41598-025-90472-8.

192. Kalisvaart, A.C.J. *et al.* (2020) 'An update to the Monro–Kellie doctrine to reflect tissue compliance after severe ischemic and hemorrhagic stroke', *Scientific Reports*, 10(1), pp. 1–15. Available at: https://doi.org/10.1038/s41598-020-78880-4.

193. Kamagata, K. *et al.* (2024) 'Noninvasive Magnetic Resonance Imaging Measures of Glymphatic System Activity', *Journal of magnetic resonance imaging: JMRI*, 59(5), pp. 1476–1493. Available at: https://doi.org/10.1002/jmri.28977.

194. Kaur, C. and Ling, E.A. (2008) 'Blood brain barrier in hypoxic-ischemic conditions', *Current Neurovascular Research*, 5(1), pp. 71–81. Available at: https://doi.org/10.2174/156720208783565645.

195. Keil, V.C. *et al.* (2017a) 'Effects of arterial input function selection on kinetic parameters in brain dynamic contrast-enhanced MRI', *Magnetic Resonance Imaging*, 40, pp. 83–90. Available at: https://doi.org/10.1016/j.mri.2017.04.006.

196. Keil, V.C. *et al.* (2017b) 'Effects of arterial input function selection on kinetic parameters in brain dynamic contrast-enhanced MRI', *Magnetic Resonance Imaging*, 40, pp. 83–90. Available at: https://doi.org/10.1016/j.mri.2017.04.006.

197. Kelly, L.A. *et al.* (2023) 'Sex differences in neonatal brain injury and inflammation', *Frontiers in Immunology*, 14, p. 1243364. Available at: https://doi.org/10.3389/fimmu.2023.1243364.

198. Kermode, A.G. *et al.* (1990) 'Breakdown of the blood-brain barrier precedes symptoms and other MRI signs of new lesions in multiple sclerosis. Pathogenetic and clinical implications', *Brain: A Journal of Neurology*, 113 ( Pt 5), pp. 1477–1489. Available at: https://doi.org/10.1093/brain/113.5.1477.

199. Kety, S.S. and Schmidt, C.F. (1948) 'THE NITROUS OXIDE METHOD FOR THE QUANTITATIVE DETERMINATION OF CEREBRAL BLOOD FLOW IN MAN: THEORY, PROCEDURE AND NORMAL VALUES 1', *Journal of Clinical Investigation*, 27(4), pp. 476–483. Available at: https://doi.org/10.1172/JCI101994.

200. Kibe, Y. *et al.* (2023) 'Imaging features of localized IDH wild-type histologically diffuse astrocytomas: a single-institution case series', *Scientific Reports*, 13(1), p. 23. Available at: https://doi.org/10.1038/s41598-022-25928-2.

201. Kim, H. (2018) 'Variability in Quantitative DCE-MRI: Sources and Solutions', *Journal of nature and science*, 4(1), p. e484.

202. Kim, H.G. *et al.* (2022) 'Association of Cerebral Blood Flow and Brain Tissue Relaxation Time With Neurodevelopmental Outcomes of Preterm Neonates: Multidelay Arterial Spin Labeling and Synthetic MRI Study', *Investigative Radiology*, 57(4), p. 254. Available at: https://doi.org/10.1097/RLI.0000000000000833.

203. Kim, H.W., Hong, J. and Jeon, J.C. (2020) 'Cerebral Small Vessel Disease and Alzheimer's Disease: A Review', *Frontiers in Neurology*, 11, p. 927. Available at: https://doi.org/10.3389/fneur.2020.00927.

204. Kim, S., Jung, U.J. and Kim, S.R. (2024) 'Role of Oxidative Stress in Blood–Brain Barrier Disruption and Neurodegenerative Diseases', *Antioxidants*, 13(12), p. 1462. Available at: https://doi.org/10.3390/antiox13121462.

205. Kim, T.-J. *et al.* (2021) 'Usefulness of arterial spin labeling perfusion as an initial evaluation of status epilepticus', *Scientific Reports*, 11(1), p. 24218. Available at: https://doi.org/10.1038/s41598-021-03698-7.

206. Kirchoff-Torres, K.F. and Bakradze, E. (2018) 'Cerebral Hyperperfusion Syndrome After Carotid Revascularization and Acute Ischemic Stroke', *Current Pain and Headache Reports*, 22(4), p. 24. Available at: https://doi.org/10.1007/s11916-018-0678-4.

207. Kisler, K. *et al.* (2017) 'Cerebral blood flow regulation and neurovascular dysfunction in Alzheimer disease', *Nature Reviews Neuroscience*, 18(7), pp. 419–434. Available at: https://doi.org/10.1038/nrn.2017.48.

208. van der Kleij, L.A. *et al.* (2018) 'The effect of physical exercise on cerebral blood flow in Alzheimer's disease', *NeuroImage : Clinical*, 20, pp. 650–654. Available at: https://doi.org/10.1016/j.nicl.2018.09.003.

209. Knox, E.G. *et al.* (2022) 'The blood-brain barrier in aging and neurodegeneration', *Molecular Psychiatry*, 27(6), pp. 2659–2673. Available at: https://doi.org/10.1038/s41380-022-01511-z.

210. Koch, F.R. *et al.* (2014) 'Sex differences in cerebral blood flow following chorioamnionitis in healthy term infants', *Journal of Perinatology*, 34(3), pp. 197–202. Available at: https://doi.org/10.1038/jp.2013.179.

211. Konstas, A.A., Wintermark, M. and Lev, M.H. (2011) 'CT perfusion imaging in acute stroke', *Neuroimaging Clinics of North America*, 21(2), pp. 215–238, ix. Available at: https://doi.org/10.1016/j.nic.2011.01.008.

212. Kooi, E.M.W. *et al.* (2017) 'Measuring cerebrovascular autoregulation in preterm infants using near-infrared spectroscopy: an overview of the literature', *Expert Review of Neurotherapeutics*, 17(8), pp. 801–818. Available at: https://doi.org/10.1080/14737175.2017.1346472.

213. Kozberg, M. and Hillman, E. (2016) 'Neurovascular coupling and energy metabolism in the developing brain', *Progress in Brain Research*, 225, pp. 213–242. Available at: https://doi.org/10.1016/bs.pbr.2016.02.002.

214. Krabbe-Hartkamp, M.J. *et al.* (1998) 'Circle of Willis: morphologic variation on three-dimensional time-of-flight MR angiograms.', *Radiology*, 207(1), pp. 103–111. Available at: https://doi.org/10.1148/radiology.207.1.9530305.

215. Kranawetter, B. *et al.* (2024) 'Optimal cerebral perfusion pressure during induced hypertension and its impact on delayed cerebral infarction and functional outcome after subarachnoid hemorrhage', *Scientific Reports*, 14(1), p. 30509. Available at: https://doi.org/10.1038/s41598-024-82507-3.

216. Krishnan, B. *et al.* (2021) 'Neurovascular networks in epilepsy: Correlating ictal blood perfusion with intracranial electrophysiology', *NeuroImage*, 231, p. 117838. Available at: https://doi.org/10.1016/j.neuroimage.2021.117838.

217. Krueger, M. *et al.* (2013) 'Blood-Brain Barrier Breakdown after Embolic Stroke in Rats Occurs without Ultrastructural Evidence for Disrupting Tight Junctions', *PLOS ONE*, 8(2), p. e56419. Available at: https://doi.org/10.1371/journal.pone.0056419.

218. KURODA, S. *et al.* (2015) 'Specific Shrinkage of Carotid Forks in Moyamoya Disease: A Novel Key Finding for Diagnosis', *Neurologia medico-chirurgica*, 55(10), pp. 796–804. Available at: https://doi.org/10.2176/nmc.oa.2015-0044.

219. Kuroda, S. *et al.* (2015) 'Specific Shrinkage of Carotid Forks in Moyamoya Disease: A Novel Key Finding for Diagnosis', *Neurologia Medico-Chirurgica*, 55(10), pp. 796–804. Available at: https://doi.org/10.2176/nmc.oa.2015-0044.

220. Kynčl, M. *et al.* (2023) 'Doporučení pro strukturální zobrazení MR mozku v diagnostice epilepsie.', *Česká a Slovenská Neurologie a Neurochirurgie*, 86(1), pp. 18–24.

221. Lacerda, S. and Law, M. (2009) 'Magnetic resonance perfusion and permeability imaging in brain tumors', *Neuroimaging Clinics of North America*, 19(4), pp. 527–557. Available at: https://doi.org/10.1016/j.nic.2009.08.007.

222. Lam, J. *et al.* (2020) 'The utility of arterial spin labeling in the presurgical evaluation of poorly defined focal epilepsy in children'. Available at: https://doi.org/10.3171/2020.7.PEDS20397.

223. Langley, E.A., Blake, S.M. and Coe, K.L. (2022) 'Recent Review of Germinal Matrix Hemorrhage-Intraventricular Hemorrhage in Preterm Infants', *Neonatal network: NN*, 41(2), pp. 100–106. Available at: https://doi.org/10.1891/11-T-722.

224. Lasocki, A. *et al.* (2018) 'MRI Features Can Predict 1p/19q Status in Intracranial Gliomas', *AJNR: American Journal of Neuroradiology*, 39(4), pp. 687–692. Available at: https://doi.org/10.3174/ajnr.A5572.

225. Lasocki, A. *et al.* (2023) 'Correlating MRI features with additional genetic markers and patient survival in histological grade 2-3 IDH-mutant astrocytomas', *Neuroradiology*, 65(8), pp. 1215–1223. Available at: https://doi.org/10.1007/s00234-023-03175-0.

226. Lassen, N.A. (1959) 'Cerebral Blood Flow and Oxygen Consumption in Man', *Physiological Reviews*, 39(2), pp. 183–238. Available at: https://doi.org/10.1152/physrev.1959.39.2.183.

227. Lavrova, A. *et al.* (2022) 'Diagnostic Accuracy of Arterial Spin Labeling in Comparison With Dynamic Susceptibility Contrast-Enhanced Perfusion for Brain Tumor Surveillance at 3T MRI', *Frontiers in Oncology*, 12, p. 849657. Available at: https://doi.org/10.3389/fonc.2022.849657.

228. Le Fèvre, C. *et al.* (2021) 'Pseudoprogression versus true progression in glioblastoma patients: A multiapproach literature review: Part 1 – Molecular, morphological and clinical features', *Critical Reviews in Oncology/Hematology*, 157, p. 103188. Available at: https://doi.org/10.1016/j.critrevonc.2020.103188.

229. Le, L.N.N. *et al.* (2023) 'Cortical oxygen extraction fraction using quantitative BOLD MRI and cerebral blood flow during vasodilation', *Frontiers in Physiology*, 14. Available at: https://doi.org/10.3389/fphys.2023.1231793.

230. Leal-Campanario, R. *et al.* (2017) 'Abnormal Capillary Vasodynamics Contribute to Ictal Neurodegeneration in Epilepsy', *Scientific Reports*, 7(1), p. 43276. Available at: https://doi.org/10.1038/srep43276.

231. Lecrux, C. *et al.* (2011) 'Pyramidal Neurons Are "Neurogenic Hubs" in the Neurovascular Coupling Response to Whisker Stimulation', *Journal of Neuroscience*, 31(27), pp. 9836–9847. Available at: https://doi.org/10.1523/JNEUROSCI.4943-10.2011.

232. Lecrux, C. and Hamel, E. (2011) 'The neurovascular unit in brain function and disease', *Acta Physiologica (Oxford, England)*, 203(1), pp. 47–59. Available at: https://doi.org/10.1111/j.1748-1716.2011.02256.x.

233. Lee, S.-K. *et al.* (2003) 'Postoperative Evaluation of Moyamoya Disease with Perfusion-Weighted MR Imaging: Initial Experience', *AJNR: American Journal of Neuroradiology*, 24(4), pp. 741–747.

234. Lee, S.-P. *et al.* (2001) 'Relative changes of cerebral arterial and venous blood volumes during increased cerebral blood flow: Implications for BOLD fMRI', *Magnetic Resonance in Medicine*, 45(5), pp. 791–800. Available at: https://doi.org/10.1002/mrm.1107.

235. LEENDERS, K.L. *et al.* (1990) 'CEREBRAL BLOOD FLOW, BLOOD VOLUME AND OXYGEN UTILIZATION: NORMAL VALUES AND EFFECT OF AGE', *Brain*, 113(1), pp. 27–47. Available at: https://doi.org/10.1093/brain/113.1.27.

236. Leidhin, C.N. *et al.* (2021) 'Age-related normative changes in cerebral perfusion: Data from The Irish Longitudinal Study on Ageing (TILDA)', *NeuroImage*, 229, p. 117741. Available at: https://doi.org/10.1016/j.neuroimage.2021.117741.

237. Leon, R.L. *et al.* (2022a) 'Cerebral Blood Flow Monitoring in High-Risk Fetal and Neonatal Populations', *Frontiers in Pediatrics*, 9, p. 748345. Available at: https://doi.org/10.3389/fped.2021.748345.

238. Leon, R.L. *et al.* (2022b) 'Cerebral Blood Flow Monitoring in High-Risk Fetal and Neonatal Populations', *Frontiers in Pediatrics*, 9, p. 748345. Available at: https://doi.org/10.3389/fped.2021.748345.

239. Leung, J. *et al.* (2016) 'Developmental trajectories of cerebrovascular reactivity in healthy children and young adults assessed with magnetic resonance imaging', *The Journal of Physiology*, 594(10), pp. 2681–2689. Available at: https://doi.org/10.1113/JP271056.

240. Li, X., Huang, W. and Holmes, J.H. (2024) 'Dynamic Contrast-Enhanced (DCE) MRI', *Magnetic Resonance Imaging Clinics of North America*, 32(1), pp. 47–61. Available at: https://doi.org/10.1016/j.mric.2023.09.001.

241. Li, Z. *et al.* (2025) 'Functional MRI study of neurovascular coupling in patients with non-lesional epilepsy', *Frontiers in Human Neuroscience*, 18, p. 1517565. Available at: https://doi.org/10.3389/fnhum.2024.1517565.

242. Liang, J. *et al.* (2018) 'Diagnostic Values of DCE-MRI and DSC-MRI for Differentiation Between High-grade and Low-grade Gliomas: A Comprehensive Meta-analysis', *Academic Radiology*, 25(3), pp. 338–348. Available at: https://doi.org/10.1016/j.acra.2017.10.001.

243. Lim, H.-K. *et al.* (2023) 'Seizure-induced neutrophil adhesion in brain capillaries leads to a decrease in postictal cerebral blood flow', *iScience*, 26(5), p. 106655. Available at: https://doi.org/10.1016/j.isci.2023.106655.

244. Limaye, W. and Ahmad, T. (2024) 'Advanced MRI imaging techniques in pediatric brain tumors', *Pediatric Radiology*, 54(8), pp. 1235–1246. Available at: https://doi.org/10.1007/s00247-024-05966-w.

245. Lin, A.-L. *et al.* (2010) 'Nonlinear coupling between cerebral blood flow, oxygen consumption, and ATP production in human visual cortex', *Proceedings of the National Academy of Sciences of the United States of America*, 107(18), pp. 8446–8451. Available at: https://doi.org/10.1073/pnas.0909711107.

246. Lin, P.-Y. *et al.* (2013) 'Regional and hemispheric asymmetries of cerebral hemodynamic and oxygen metabolism in newborns', *Cerebral Cortex (New York, N.Y.: 1991)*, 23(2), pp. 339–348. Available at: https://doi.org/10.1093/cercor/bhs023.

247. Lindner, T. *et al.* (2023) 'Current state and guidance on arterial spin labeling perfusion MRI in clinical neuroimaging', *Magnetic Resonance in Medicine*, 89(5), pp. 2024–2047. Available at: https://doi.org/10.1002/mrm.29572.

248. Liu, J. *et al.* (2014) 'Vascular remodeling after ischemic stroke: mechanisms and therapeutic potentials', *Progress in Neurobiology*, 115, pp. 138–156. Available at: https://doi.org/10.1016/j.pneurobio.2013.11.004.

249. Liu, P. *et al.* (2019) 'Assessment of cerebral blood flow in neonates and infants: A phase-contrast MRI study', *NeuroImage*, 185, pp. 926–933. Available at: https://doi.org/10.1016/j.neuroimage.2018.03.020.

250. Liu, Y. *et al.* (2012) 'Arterial spin labeling MRI study of age and gender effects on brain perfusion hemodynamics', *Magnetic Resonance in Medicine*, 68(3), pp. 912–922. Available at: https://doi.org/10.1002/mrm.23286.

251. Liu, Z. and Li, Y. (2016) 'Cortical Cerebral Blood Flow, Oxygen Extraction Fraction, and Metabolic Rate in Patients with Middle Cerebral Artery Stenosis or Acute Stroke', *AJNR: American Journal of Neuroradiology*, 37(4), pp. 607–614. Available at: https://doi.org/10.3174/ajnr.A4624.

252. Lochhead, J.J., Ronaldson, P.T. and Davis, T.P. (2024) 'The role of oxidative stress in blood-brain barrier disruption during ischemic stroke: Antioxidants in clinical trials', *Biochemical Pharmacology*, 228, p. 116186. Available at: https://doi.org/10.1016/j.bcp.2024.116186.

253. Louis, D.N. *et al.* (2021) 'The 2021 WHO Classification of Tumors of the Central Nervous System: a summary', *Neuro-Oncology*, 23(8), pp. 1231–1251. Available at: https://doi.org/10.1093/neuonc/noab106.

254. Louveau, A. *et al.* (2017) 'Understanding the functions and relationships of the glymphatic system and meningeal lymphatics', *The Journal of Clinical Investigation*, 127(9), pp. 3210–3219. Available at: https://doi.org/10.1172/JCI90603.

255. Lüdemann, L. *et al.* (2009) 'Brain tumor perfusion: Comparison of dynamic contrast enhanced magnetic resonance imaging using T1, T2, and T2* contrast, pulsed arterial spin labeling, and H215O positron emission tomography', *European Journal of Radiology*, 70(3), pp. 465–474. Available at: https://doi.org/10.1016/j.ejrad.2008.02.012.

256. Luglietto, D. *et al.* (2025) 'Pediatric Gliomas in the Modern Era', in D. Armocida, D. Garbossa, and M. Salvati (eds) *Neurosurgery's Frontline Role in Gliomas Treatment: Trends, Technologies and Treatments*. Cham: Springer Nature Switzerland, pp. 111–125. Available at: https://doi.org/10.1007/978-3-031-81850-9_8.

257. MacGregor Sharp, M. *et al.* (2020) 'Demonstrating a reduced capacity for removal of fluid from cerebral white matter and hypoxia in areas of white matter hyperintensity associated with age and dementia', *Acta Neuropathologica Communications*, 8, p. 131. Available at: https://doi.org/10.1186/s40478-020-01009-1.

258. Magyar-Sumegi, Z.D. *et al.* (2025) 'Chronic impairment of neurovascular coupling and cognitive decline in young survivors of severe traumatic brain injury', *GeroScience* [Preprint]. Available at: https://doi.org/10.1007/s11357-025-01683-w.

259. Mahroo, A. *et al.* (2021a) 'Robust Multi-TE ASL-Based Blood–Brain Barrier Integrity Measurements', *Frontiers in Neuroscience*, 15. Available at: https://doi.org/10.3389/fnins.2021.719676.

260. Mahroo, A. *et al.* (2021b) 'Robust Multi-TE ASL-Based Blood–Brain Barrier Integrity Measurements', *Frontiers in Neuroscience*, 15. Available at: https://doi.org/10.3389/fnins.2021.719676.

261. Makki, M.I. *et al.* (2019) 'Total cerebrovascular blood flow and whole brain perfusion in children sedated using propofol with or without ketamine at induction: An investigation with 2D-Cine PC and ASL', *Journal of Magnetic Resonance Imaging*, 50(5), pp. 1433–1440. Available at: https://doi.org/10.1002/jmri.26725.

262. Mallio, C.A. *et al.* (2023) 'Artificial Intelligence to Reduce or Eliminate the Need for Gadolinium-Based Contrast Agents in Brain and Cardiac MRI: A Literature Review', *Investigative Radiology*, 58(10), pp. 746–753. Available at: https://doi.org/10.1097/RLI.0000000000000983.

263. Mangia, S. *et al.* (2025) 'Reduced removal of waste products from energy metabolism takes center stage in human brain aging', *Scientific Reports*, 15(1), p. 8127. Available at: https://doi.org/10.1038/s41598-025-90342-3.

264. Manning, C. *et al.* (2021) 'Sources of systematic error in DCE-MRI estimation of low-level blood-brain barrier leakage', *Magnetic Resonance in Medicine*, 86(4), pp. 1888–1903. Available at: https://doi.org/10.1002/mrm.28833.

265. Manquat, E. *et al.* (2023) 'Cerebral autoregulation and cerebral blood flow response to mean arterial pressure challenge following induction of general anaesthesia for neuroradiology procedure', *Frontiers in Anesthesiology*, 2. Available at: https://doi.org/10.3389/fanes.2023.1169961.

266. Marchi, N. *et al.* (2012) 'Blood–brain barrier dysfunction and epilepsy: Pathophysiologic role and therapeutic approaches', *Epilepsia*, 53(11), pp. 1877–1886. Available at: https://doi.org/10.1111/j.1528-1167.2012.03637.x.

267. Martinez-Lemus, L.A. (2012) 'The Dynamic Structure of Arterioles', *Basic & Clinical Pharmacology & Toxicology*, 110(1), pp. 5–11. Available at: https://doi.org/10.1111/j.1742-7843.2011.00813.x.

268. Martinez-Lemus, L.A., Hill, M.A. and Meininger, G.A. (2009) 'The Plastic Nature of the Vascular Wall: A Continuum of Remodeling Events Contributing to Control of Arteriolar Diameter and Structure', *Physiology*, 24(1), pp. 45–57. Available at: https://doi.org/10.1152/physiol.00029.2008.

269. Mathias, K. *et al.* (2024) 'Blood-brain barrier permeability in the ischemic stroke: An update', *Microvascular Research*, 151, p. 104621. Available at: https://doi.org/10.1016/j.mvr.2023.104621.

270. Mayer, T.E. *et al.* (2000) 'Dynamic CT Perfusion Imaging of Acute Stroke', *AJNR: American Journal of Neuroradiology*, 21(8), pp. 1441–1449.

271. Meng, L. *et al.* (2021) 'Diagnostic performance of arterial spin-labeled perfusion imaging and diffusion-weighted imaging in full-term neonatal hypoxic-ischemic encephalopathy', *Journal of Integrative Neuroscience*, 20(4), pp. 985–991. Available at: https://doi.org/10.31083/j.jin2004099.

272. Meng, L. *et al.* (2022) 'ATRX status in patients with gliomas: Radiomics analysis', *Medicine*, 101(37), p. e30189. Available at: https://doi.org/10.1097/MD.0000000000030189.

273. Menshawi, K., Mohr, J.P. and Gutierrez, J. (2015) 'A Functional Perspective on the Embryology and Anatomy of the Cerebral Blood Supply', *Journal of Stroke*, 17(2), pp. 144–158. Available at: https://doi.org/10.5853/jos.2015.17.2.144.

274. Meyer-Baese, L., Jaeger, D. and Keilholz, S. (2025) 'Neurovascular coupling: a review of spontaneous neocortical dynamics linking neuronal activity to hemodynamics and what we have learned from the rodent brain', *Journal of Neurophysiology*, 133(2), pp. 644–660. Available at: https://doi.org/10.1152/jn.00418.2024.

275. Mikami, T. *et al.* (2015) 'Vascular remodeling of the circle of Willis in moyamoya disease', *Neurological Research*, 37(10), pp. 880–885. Available at: https://doi.org/10.1179/1743132815Y.0000000069.

276. Mishra, A. *et al.* (2016) 'Astrocytes mediate neurovascular signaling to capillary pericytes but not to arterioles', *Nature Neuroscience*, 19(12), pp. 1619–1627. Available at: https://doi.org/10.1038/nn.4428.

277. Moltoni, G. *et al.* (2024) 'ASL, DSC, DCE perfusion MRI and 18F-DOPA PET/CT in differentiating glioma recurrence from post-treatment changes', *La radiologia medica*, 129(9), pp. 1382–1393. Available at: https://doi.org/10.1007/s11547-024-01862-3.

278. Moore, K.L., Dalley, A.F. and Agur, A.M.R. (2014) *Clinically oriented anatomy*. 7th ed. Philadelphia: Wolters Kluwer/Lippincott Williams & Wilkins Health.

279. Morel, B. *et al.* (2021) 'Normal volumetric and T1 relaxation time values at 1.5 T in segmented pediatric brain MRI using a MP2RAGE acquisition', *European Radiology*, 31(3), pp. 1505–1516. Available at: https://doi.org/10.1007/s00330-020-07194-w.

280. Morgan, C.A. *et al.* (2024) 'Measurement of blood-brain barrier water exchange rate using diffusion-prepared and multi-echo arterial spin labelling: Comparison of quantitative values and age dependence', *NMR in biomedicine*, 37(12), p. e5256. Available at: https://doi.org/10.1002/nbm.5256.

281. Moyaert, P. *et al.* (2023) 'Imaging blood-brain barrier dysfunction: A state-of-the-art review from a clinical perspective', *Frontiers in Aging Neuroscience*, 15. Available at: https://doi.org/10.3389/fnagi.2023.1132077.

282. Munoz, P.A. *et al.* (2023) *Childhood cancers – Every child and adolescent deserves an equal chance*, *JRC Publications Repository*. Available at:

https://publications.jrc.ec.europa.eu/repository/handle/JRC136059 (Accessed: 2 June 2025).

283. Mutsaerts, H.J.M.M. *et al.* (2020) 'ExploreASL: An image processing pipeline for multi-center ASL perfusion MRI studies', *NeuroImage*, 219, p. 117031. Available at: https://doi.org/10.1016/j.neuroimage.2020.117031.

284. Nakagawa, K. *et al.* (2009) 'Autoregulation in the Posterior Circulation Is Altered by the Metabolic State of the Visual Cortex', *Stroke*, 40(6), pp. 2062–2067. Available at: https://doi.org/10.1161/STROKEAHA.108.545285.

285. Nasel, C. *et al.* (2019) 'A Quantitative Comparison of Clinically Employed Parameters in the Assessment of Acute Cerebral Ischemia Using Dynamic Susceptibility Contrast Magnetic Resonance Imaging', *Frontiers in Physiology*, 9, p. 1945. Available at: https://doi.org/10.3389/fphys.2018.01945.

286. Newton, J.C. *et al.* (2025) 'Out-of-pocket costs for patients diagnosed with high-grade glioma and their carers', *Neuro-Oncology Practice*, 12(2), pp. 231–245. Available at: https://doi.org/10.1093/nop/npae107.

287. Nogueira, R.C. *et al.* (2021) 'Cerebral Autoregulation in Ischemic Stroke: From Pathophysiology to Clinical Concepts', *Brain Sciences*, 11(4), p. 511. Available at: https://doi.org/10.3390/brainsci11040511.

288. Norling, A.M. and Lipsitz, L.A. (2024) 'Exercise to Mitigate Cerebrovascular Aging: A Geroscience Perspective', *The Journals of Gerontology Series A: Biological Sciences and Medical Sciences*, 79(7), p. glae083. Available at: https://doi.org/10.1093/gerona/glae083.

289. Nourhashemi, M. *et al.* (2019) 'Neurovascular coupling in the developing neonatal brain at rest', *Human Brain Mapping*, 41(2), pp. 503–519. Available at: https://doi.org/10.1002/hbm.24818.

290. Novak, J. *et al.* (2019) 'A comparison of pseudo-continuous arterial spin labelling and dynamic susceptibility contrast MRI with and without contrast agent leakage correction in paediatric brain tumours', *The British Journal of Radiology*, 92(1094), p. 20170872. Available at: https://doi.org/10.1259/bjr.20170872.

291. O'Connor, J.P.B. *et al.* (2017) 'Imaging biomarker roadmap for cancer studies', *Nature Reviews Clinical Oncology*, 14(3), pp. 169–186. Available at: https://doi.org/10.1038/nrclinonc.2016.162.

292. von Oertzen, T.J. *et al.* (2023) 'SPECT and PET in nonlesional epilepsy', *Clinical Epileptology*, 36(2), pp. 104–110. Available at: https://doi.org/10.1007/s10309-023-00577-1.

293. Ohene, Y. *et al.* (2021) 'Increased blood-brain barrier permeability to water in the aging brain detected using noninvasive multi-TE ASL MRI', *Magnetic Resonance in Medicine*, 85(1), pp. 326–333. Available at: https://doi.org/10.1002/mrm.28496.

294. O'Herron, P. *et al.* (2016) 'Neural correlates of single-vessel haemodynamic responses in vivo', *Nature*, 534(7607), pp. 378–382. Available at: https://doi.org/10.1038/nature17965.

295. Ohuma, E.O. *et al.* (2023) 'National, regional, and global estimates of preterm birth in 2020, with trends from 2010: a systematic analysis', *The Lancet*, 402(10409), pp. 1261–1271. Available at: https://doi.org/10.1016/S0140-6736(23)00878-4.

296. Olesen, J. (2024) 'Cerebral blood flow and arterial responses in migraine: history and future perspectives', *The Journal of Headache and Pain*, 25(1), p. 222. Available at: https://doi.org/10.1186/s10194-024-01903-2.

297. Ortiz, G.G. *et al.* (2014) 'Role of the blood-brain barrier in multiple sclerosis', *Archives of Medical Research*, 45(8), pp. 687–697. Available at: https://doi.org/10.1016/j.arcmed.2014.11.013.

298. van Osch, M.J. *et al.* (2018) 'Advances in arterial spin labelling MRI methods for measuring perfusion and collateral flow', *Journal of Cerebral Blood Flow and Metabolism: Official Journal of the International Society of Cerebral Blood Flow and Metabolism*, 38(9), pp. 1461–1480. Available at: https://doi.org/10.1177/0271678X17713434.

299. Østergaard, L. *et al.* (2013) 'The Relationship between Tumor Blood Flow, Angiogenesis, Tumor Hypoxia, and Aerobic Glycolysis', *Cancer Research*, 73(18), pp. 5618–5624. Available at: https://doi.org/10.1158/0008-5472.CAN-13-0964.

300. Ostrom, Q.T. *et al.* (2022) 'CBTRUS Statistical Report: Pediatric Brain Tumor Foundation Childhood and Adolescent Primary Brain and Other Central Nervous System Tumors Diagnosed in the United States in 2014–2018', *Neuro-Oncology*, 24(Suppl 3), pp. iii1–iii38. Available at: https://doi.org/10.1093/neuonc/noac161.

301. Ouyang, M. *et al.* (2024) 'Spatiotemporal cerebral blood flow dynamics underlies emergence of the limbic-sensorimotor-association cortical gradient in human infancy', *Nature Communications*, 15(1), p. 8944. Available at: https://doi.org/10.1038/s41467-024-53354-7.

302. Ouyang, M. and Bao, L. (2025a) 'Gadolinium Contrast Agent Deposition in Children', *Journal of Magnetic Resonance Imaging*, 61(1), pp. 70–82. Available at: https://doi.org/10.1002/jmri.29389.

303. Ouyang, M. and Bao, L. (2025b) 'Gadolinium Contrast Agent Deposition in Children', *Journal of Magnetic Resonance Imaging*, 61(1), pp. 70–82. Available at: https://doi.org/10.1002/jmri.29389.

304. Owens, T.C., Anton, N. and Attia, M.F. (2023) 'CT and X-ray contrast agents: Current clinical challenges and the future of contrast', *Acta Biomaterialia*, 171, pp. 19–36. Available at: https://doi.org/10.1016/j.actbio.2023.09.027.

305. Ozono, I. *et al.* (2024) 'Super T2-FLAIR mismatch sign: a prognostic imaging biomarker for non-enhancing astrocytoma, IDH-mutant', *Journal of Neuro-Oncology*, 169(3), pp. 571–579. Available at: https://doi.org/10.1007/s11060-024-04758-4.

306. Pancaldi, A. *et al.* (2023) 'Neuropsychological Outcomes of Children Treated for Brain Tumors', *Children (Basel, Switzerland)*, 10(3), p. 472. Available at: https://doi.org/10.3390/children10030472.

307. Paniukov, D. *et al.* (2020) 'Cerebral blood flow increases across early childhood', *NeuroImage*, 204, p. 116224. Available at: https://doi.org/10.1016/j.neuroimage.2019.116224.

308. Pantel, A.R. *et al.* (2024) 'PET Imaging of Metabolism, Perfusion, and Hypoxia: FDG and Beyond', *Cancer Journal (Sudbury, Mass.)*, 30(3), pp. 159–169. Available at: https://doi.org/10.1097/PPO.0000000000000716.

309. Park, S. *et al.* (2022) 'Brain networks in migraine with and without aura: An exploratory arterial spin labeling MRI study', *Acta Neurologica Scandinavica*, 145(2), pp. 208–214. Available at: https://doi.org/10.1111/ane.13536.

310. Payne, S. (2016) *Cerebral Autoregulation*. Cham: Springer International Publishing (SpringerBriefs in Bioengineering). Available at: https://doi.org/10.1007/978-3-319-31784-7.

311. Pemberton, H.G. *et al.* (2023) 'Multi-class glioma segmentation on real-world data with missing MRI sequences: comparison of three deep learning algorithms', *Scientific Reports*, 13(1), p. 18911. Available at: https://doi.org/10.1038/s41598-023-44794-0.

312. Peng, H. *et al.* (2021) 'Predicting Isocitrate Dehydrogenase (IDH) Mutation Status in Gliomas Using Multiparameter MRI Radiomics Features', *Journal of Magnetic Resonance Imaging*, 53(5), pp. 1399–1407. Available at: https://doi.org/10.1002/jmri.27434.

313. Peng, S.-L. *et al.* (2015) 'Optimization of phase-contrast MRI for the quantification of whole-brain cerebral blood flow', *Journal of magnetic resonance imaging : JMRI*, 42(4), pp. 1126–1133. Available at: https://doi.org/10.1002/jmri.24866.

314. Peng, S.-L. *et al.* (2018) 'Age-related changes in cerebrovascular reactivity and their relationship to cognition: A four-year longitudinal study', *NeuroImage*, 174, pp. 257–262. Available at: https://doi.org/10.1016/j.neuroimage.2018.03.033.

315. Petersen, E.T. *et al.* (2006) 'Non-invasive measurement of perfusion: a critical review of arterial spin labelling techniques', *The British Journal of Radiology*, 79(944), pp. 688–701. Available at: https://doi.org/10.1259/bjr/67705974.

316. Petr, J. *et al.* (2013) 'Partial volume correction in arterial spin labeling using a Look-Locker sequence', *Magnetic Resonance in Medicine*, 70(6), pp. 1535–1543. Available at: https://doi.org/10.1002/mrm.24601.

317. Pfurtscheller, D. *et al.* (2023) 'Insights into Neonatal Cerebral Autoregulation by Blood Pressure Monitoring and Cerebral Tissue Oxygenation: A Qualitative Systematic Review', *Children*, 10(8), p. 1304. Available at: https://doi.org/10.3390/children10081304.

318. Piechnik, S.K., Chiarelli, P.A. and Jezzard, P. (2008) 'Modelling vascular reactivity to investigate the basis of the relationship between cerebral blood volume and flow under CO2 manipulation', *NeuroImage*, 39(1), pp. 107–118. Available at: https://doi.org/10.1016/j.neuroimage.2007.08.022.

319. Pottkämper, J.C.M. *et al.* (2020) 'The postictal state — What do we know?', *Epilepsia*, 61(6), p. 1045. Available at: https://doi.org/10.1111/epi.16519.

320. Powers, W.J. *et al.* (1985) 'Cerebral blood flow and cerebral metabolic rate of oxygen requirements for cerebral function and viability in humans', *Journal of Cerebral Blood Flow and Metabolism: Official Journal of the International Society of Cerebral Blood Flow and Metabolism*, 5(4), pp. 600–608. Available at: https://doi.org/10.1038/jcbfm.1985.89.

321. Premilovac, D. and Sutherland, B.A. (2022) 'Acute and long-term changes in blood flow after ischemic stroke: challenges and opportunities', *Neural Regeneration Research*, 18(4), pp. 799–800. Available at: https://doi.org/10.4103/1673-5374.350699.

322. Presa, J.L. *et al.* (2020) 'Vasculo-Neuronal Coupling and Neurovascular Coupling at the Neurovascular Unit: Impact of Hypertension', *Frontiers in Physiology*, 11. Available at: https://doi.org/10.3389/fphys.2020.584135.

323. Prohovnik, I. *et al.* (1988) 'Cerebral perfusion as a diagnostic marker of early Alzheimer's disease', *Neurology*, 38(6), pp. 931–931. Available at: https://doi.org/10.1212/WNL.38.6.931.

324. Proisy, M. *et al.* (2016) 'Brain Perfusion Imaging in Neonates: An Overview', *American Journal of Neuroradiology*, 37(10), pp. 1766–1773. Available at: https://doi.org/10.3174/ajnr.A4778.

325. Promjunyakul, N. *et al.* (2015) 'Characterizing the white matter hyperintensity penumbra with cerebral blood flow measures', *NeuroImage: Clinical*, 8, pp. 224–229. Available at: https://doi.org/10.1016/j.nicl.2015.04.012.

326. Promjunyakul, N. *et al.* (2018) 'Baseline NAWM structural integrity and CBF predict periventricular WMH expansion over time', *Neurology*, 90(24), pp. e2119–e2126. Available at: https://doi.org/10.1212/WNL.0000000000005684.

327. Prysiazhniuk, Y. *et al.* (2024) 'Diffuse glioma molecular profiling with arterial spin labeling and dynamic susceptibility contrast perfusion MRI: A comparative study', *Neuro-Oncology Advances*, 6(1), p. vdae113. Available at: https://doi.org/10.1093/noajnl/vdae113.

328. Puig, O. *et al.* (2020) 'Comparison of simultaneous arterial spin labeling MRI and 15O-H2O PET measurements of regional cerebral blood flow in rest and altered perfusion states', *Journal of Cerebral Blood Flow & Metabolism*, 40(8), pp. 1621–1633. Available at: https://doi.org/10.1177/0271678X19874643.

329. Qin, Q. *et al.* (2022a) 'Velocity-selective arterial spin labeling perfusion MRI: A review of the state of the art and recommendations for clinical implementation', *Magnetic Resonance in Medicine*, 88(4), pp. 1528–1547. Available at: https://doi.org/10.1002/mrm.29371.

330. Qin, Q. *et al.* (2022b) 'Velocity-selective arterial spin labeling perfusion MRI: A review of the state of the art and recommendations for clinical implementation', *Magnetic Resonance in Medicine*, 88(4), pp. 1528–1547. Available at: https://doi.org/10.1002/mrm.29371.

331. R, M. *et al.* (2025) ‘Towards precision MRI biomarkers in epilepsy with normative modelling’, *Brain : a journal of neurology* [Preprint]. Available at: https://doi.org/10.1093/brain/awaf090.

332. Raichle, M.E. and Gusnard, D.A. (2002) ‘Appraising the brain’s energy budget’, *Proceedings of the National Academy of Sciences*, 99(16), pp. 10237–10239. Available at: https://doi.org/10.1073/pnas.172399499.

333. Rempe, R.G., Hartz, A.M.S. and Bauer, B. (2016) ‘Matrix metalloproteinases in the brain and blood-brain barrier: Versatile breakers and makers’, *Journal of Cerebral Blood Flow and Metabolism: Official Journal of the International Society of Cerebral Blood Flow and Metabolism*, 36(9), pp. 1481–1507. Available at: https://doi.org/10.1177/0271678X16655551.

334. Retailleau, K. *et al.* (2015) ‘Piezo1 in Smooth Muscle Cells Is Involved in Hypertension-Dependent Arterial Remodeling’, *Cell Reports*, 13(6), pp. 1161–1171. Available at: https://doi.org/10.1016/j.celrep.2015.09.072.

335. Rhee, C.J. *et al.* (2018) ‘Neonatal cerebrovascular autoregulation’, *Pediatric research*, 84(5), pp. 602–610. Available at: https://doi.org/10.1038/s41390-018-0141-6.

336. Rhodin, J.A.G. (2014) ‘Architecture of the Vessel Wall’, in *Comprehensive Physiology*. John Wiley & Sons, Ltd, pp. 1–31. Available at: https://doi.org/10.1002/cphy.cp020201.

337. Rieger, H. and Welter, M. (2015) ‘Integrative models of vascular remodeling during tumor growth’, *Wiley Interdisciplinary Reviews. Systems Biology and Medicine*, 7(3), pp. 113–129. Available at: https://doi.org/10.1002/wsbm.1295.

338. Roberts, D.A. *et al.* (1994) ‘Quantitative magnetic resonance imaging of human brain perfusion at 1.5 T using steady-state inversion of arterial water’, *Proceedings of the National Academy of Sciences of the United States of America*, 91(1), pp. 33–37. Available at: https://doi.org/10.1073/pnas.91.1.33.

339. Roux, A. *et al.* (2024) ‘Prognostic significance of MRI contrast enhancement in newly diagnosed glioblastoma, IDH-wildtype according to WHO 2021 classification’, *Journal of Neuro-Oncology*, 169(2), pp. 445–455. Available at: https://doi.org/10.1007/s11060-024-04747-7.

340. Sanders, A. *et al.* (2023) ‘Associations between everyday activities and arterial spin labeling-derived cerebral blood flow: A longitudinal study in community-dwelling elderly volunteers’, *Human Brain Mapping*, 44(8), pp. 3377–3393. Available at: https://doi.org/10.1002/hbm.26287.

341. van Santwijk, L. *et al.* (2022) ‘A systematic review and meta-analysis on the differentiation of glioma grade and mutational status by use of perfusion-based magnetic resonance imaging’, *Insights into Imaging*, 13(1), p. 102. Available at: https://doi.org/10.1186/s13244-022-01230-7.

342. Sarda, S.P., Sarri, G. and Siffel, C. (2021) ‘Global prevalence of long-term neurodevelopmental impairment following extremely preterm birth: a systematic literature review’, *Journal of International Medical Research*, 49(7), p. 03000605211028026. Available at: https://doi.org/10.1177/03000605211028026.

343. Sasannia, S. *et al.* (2025) 'Blood-brain barrier breakdown in brain ischemia: Insights from MRI perfusion imaging', *Neurotherapeutics*, 22(1), p. e00516. Available at: https://doi.org/10.1016/j.neurot.2024.e00516.

344. Satterthwaite, T.D. *et al.* (2014a) 'Impact of puberty on the evolution of cerebral perfusion during adolescence', *Proceedings of the National Academy of Sciences*, 111(23), pp. 8643–8648. Available at: https://doi.org/10.1073/pnas.1400178111.

345. Satterthwaite, T.D. *et al.* (2014b) 'Impact of puberty on the evolution of cerebral perfusion during adolescence', *Proceedings of the National Academy of Sciences*, 111(23), pp. 8643–8648. Available at: https://doi.org/10.1073/pnas.1400178111.

346. Scarciglia, A. *et al.* (2025) 'Gadolinium-Based Contrast Agents (GBCAs) for MRI: A Benefit–Risk Balance Analysis from a Chemical, Biomedical, and Environmental Point of View', *Global Challenges*, 9(3), p. 2400269. Available at: https://doi.org/10.1002/gch2.202400269.

347. Schaller, B. and Graf, R. (2004) 'Cerebral Ischemia and Reperfusion: The Pathophysiologic Concept as a Basis for Clinical Therapy', *Journal of Cerebral Blood Flow & Metabolism*, 24(4), pp. 351–371. Available at: https://doi.org/10.1097/00004647-200404000-00001.

348. van der Scheer, J.W. *et al.* (2018) 'A comparison of static and dynamic cerebral autoregulation during mild whole-body cold stress in individuals with and without cervical spinal cord injury: a pilot study', *Spinal Cord*, 56(5), pp. 469–477. Available at: https://doi.org/10.1038/s41393-017-0021-7.

349. Schmainda, K.M. *et al.* (2018) 'Multisite Concordance of DSC-MRI Analysis for Brain Tumors: Results of a National Cancer Institute Quantitative Imaging Network Collaborative Project', *AJNR. American journal of neuroradiology*, 39(6), pp. 1008–1016. Available at: https://doi.org/10.3174/ajnr.A5675.

350. Schmainda, K.M. *et al.* (2019) 'Moving Toward a Consensus DSC-MRI Protocol: Validation of a Low–Flip Angle Single-Dose Option as a Reference Standard for Brain Tumors', *American Journal of Neuroradiology*, 40(4), pp. 626–633. Available at: https://doi.org/10.3174/ajnr.A6015.

351. Schneider, A.M. *et al.* (2023) 'Posterior circulation ischaemic stroke diagnosis and management', *Clinical Medicine*, 23(3), pp. 219–227. Available at: https://doi.org/10.7861/clinmed.2022-0499.

352. Schramm, S. *et al.* (2024) 'Perfusion imaging by arterial spin labeling in migraine: A literature review', *Journal of Cerebral Blood Flow & Metabolism*, 44(8), pp. 1253–1270. Available at: https://doi.org/10.1177/0271678X241237733.

353. Schwartz, T.H. (2007) 'Neurovascular Coupling and Epilepsy: Hemodynamic Markers for Localizing and Predicting Seizure Onset', *Epilepsy Currents*, 7(4), pp. 91–94. Available at: https://doi.org/10.1111/j.1535-7511.2007.00183.x.

354. Sforza, M. *et al.* (2022) 'The impact of cerebral vasomotor reactivity on cerebrovascular diseases and cognitive impairment', *Journal of Neural Transmission*, 129(11), pp. 1321–1330. Available at: https://doi.org/10.1007/s00702-022-02546-w.

355. Shao, X. *et al.* (2022) 'Reliability of BBB water exchange rate assessed by diffusion-prepared pseudo-continuous ASL (DP-pCASL): Preliminary results from the Cognitive Recovery After Elective Surgery (CREATES) Study', *Alzheimer's & Dementia*, 18(S6), p. e066644. Available at: https://doi.org/10.1002/alz.066644.

356. Sharifian, M.J. *et al.* (2024) 'Incidence trends of adult glioma in Norway and its association with occupation and education: A registry-based cohort study', *Cancer Epidemiology*, 89, p. 102524. Available at: https://doi.org/10.1016/j.canep.2024.102524.

357. Shukla-Dave, A. *et al.* (2019) 'Quantitative imaging biomarkers alliance (QIBA) recommendations for improved precision of DWI and DCE-MRI derived biomarkers in multicenter oncology trials', *Journal of magnetic resonance imaging: JMRI*, 49(7), pp. e101–e121. Available at: https://doi.org/10.1002/jmri.26518.

358. Shyam Prabhakaran (2015) 'Imaging markers of stroke risk in asymptomatic carotid artery stenosis', *Brain Circulation*, 1(1), pp. 38–46. Available at: https://doi.org/10.4103/2394-8108.166373.

359. Siakallis, L. *et al.* (2023) 'The role of DSC MR perfusion in predicting IDH mutation and 1p19q codeletion status in gliomas: meta-analysis and technical considerations', *Neuroradiology*, 65(7), pp. 1111–1126. Available at: https://doi.org/10.1007/s00234-023-03154-5.

360. Sierra-Marcos, A. *et al.* (2016) 'Accuracy of arterial spin labeling magnetic resonance imaging (MRI) perfusion in detecting the epileptogenic zone in patients with drug-resistant neocortical epilepsy: comparison with electrophysiological data, structural MRI, SISCOM and FDG-PET', *European Journal of Neurology*, 23(1), pp. 160–167. Available at: https://doi.org/10.1111/ene.12826.

361. Simons, M., Levin, J. and Dichgans, M. (2023) 'Tipping points in neurodegeneration', *Neuron*, 111(19), pp. 2954–2968. Available at: https://doi.org/10.1016/j.neuron.2023.05.031.

362. Slart, R.H.J.A. *et al.* (2024) '[15O]H2O PET: Potential or Essential for Molecular Imaging?', *Seminars in Nuclear Medicine*, 54(5), pp. 761–773. Available at: https://doi.org/10.1053/j.semnuclmed.2023.08.002.

363. Smith, C.A. *et al.* (2023) 'Candidate neuroinflammatory markers of cerebral autoregulation dysfunction in human acute brain injury', *Journal of Cerebral Blood Flow and Metabolism: Official Journal of the International Society of Cerebral Blood Flow and Metabolism*, 43(8), pp. 1237–1253. Available at: https://doi.org/10.1177/0271678X231171991.

364. Song, S. *et al.* (2022) 'MGMT promoter methylation status shows no effect on [18F]FET uptake and CBF in gliomas: a stereotactic image-based histological validation study', *European Radiology*, 32(8), pp. 5577–5587. Available at: https://doi.org/10.1007/s00330-022-08606-9.

365. Song, Y. *et al.* (2016) 'Dysfunction of Neurovascular/Metabolic Coupling in Chronic Focal Epilepsy', *IEEE transactions on bio-medical engineering*, 63(1), pp. 97–110. Available at: https://doi.org/10.1109/TBME.2015.2461496.

366. Spijkerman, J.M. *et al.* (2018) 'T2 mapping of cerebrospinal fluid: 3 T versus 7 T', *Magnetic Resonance Materials in Physics, Biology and Medicine*, 31(3), pp. 415–424. Available at: https://doi.org/10.1007/s10334-017-0659-3.

367. Sriram, K. *et al.* (2012) 'Autoregulation and mechanotransduction control the arteriolar response to small changes in hematocrit', *American Journal of Physiology-Heart and Circulatory Physiology*, 303(9), pp. H1096–H1106. Available at: https://doi.org/10.1152/ajpheart.00438.2012.

368. Stackhouse, T.L. and Mishra, A. (2021) 'Neurovascular Coupling in Development and Disease: Focus on Astrocytes', *Frontiers in Cell and Developmental Biology*, 9. Available at: https://doi.org/10.3389/fcell.2021.702832.

369. Steinmetz, J.D. *et al.* (2024) 'Global, regional, and national burden of disorders affecting the nervous system, 1990–2021: a systematic analysis for the Global Burden of Disease Study 2021', *The Lancet Neurology*, 23(4), pp. 344–381. Available at: https://doi.org/10.1016/S1474-4422(24)00038-3.

370. Stobart, J.L. and Anderson, C.M. (2013) 'Multifunctional role of astrocytes as gatekeepers of neuronal energy supply', *Frontiers in Cellular Neuroscience*, 7, p. 38. Available at: https://doi.org/10.3389/fncel.2013.00038.

371. Storti, S.F. *et al.* (2014) 'Combining ESI, ASL and PET for quantitative assessment of drug-resistant focal epilepsy', *NeuroImage*, 102, pp. 49–59. Available at: https://doi.org/10.1016/j.neuroimage.2013.06.028.

372. Stupp, R. *et al.* (2005) 'Radiotherapy plus concomitant and adjuvant temozolomide for glioblastoma', *The New England Journal of Medicine*, 352(10), pp. 987–996. Available at: https://doi.org/10.1056/NEJMoa043330.

373. Sweeney, M.D. *et al.* (2018) 'The role of brain vasculature in neurodegenerative disorders', *Nature neuroscience*, 21(10), pp. 1318–1331. Available at: https://doi.org/10.1038/s41593-018-0234-x.

374. Sweeney, M.D., Ayyadurai, S. and Zlokovic, B.V. (2016) 'Pericytes of the neurovascular unit: key functions and signaling pathways', *Nature Neuroscience*, 19(6), pp. 771–783. Available at: https://doi.org/10.1038/nn.4288.

375. Sweeney, M.D., Sagare, A.P. and Zlokovic, B.V. (2018) 'Blood–brain barrier breakdown in Alzheimer disease and other neurodegenerative disorders', *Nature Reviews Neurology*, 14(3), pp. 133–150. Available at: https://doi.org/10.1038/nrneurol.2017.188.

376. Swinford, C.G. *et al.* (2023) 'Altered Cerebral Blood Flow in Older Adults with Alzheimer's Disease: A Systematic Review', *Brain imaging and behavior*, 17(2), pp. 223–256. Available at: https://doi.org/10.1007/s11682-022-00750-6.

377. Sydnor, V.J. *et al.* (2021) 'Neurodevelopment of the association cortices: Patterns, mechanisms, and implications for psychopathology', *Neuron*, 109(18), pp. 2820–2846. Available at: https://doi.org/10.1016/j.neuron.2021.06.016.

378. Taki, Y. *et al.* (2011) 'Correlation between gray matter density-adjusted brain perfusion and age using brain MR images of 202 healthy children', *Human Brain Mapping*, 32(11), pp. 1973–1985. Available at: https://doi.org/10.1002/hbm.21163.

379. Tang, C. *et al.* (2024) 'Prediction of TERT mutation status in gliomas using conventional MRI radiogenomic features', *Frontiers in Neurology*, 15. Available at: https://doi.org/10.3389/fneur.2024.1439598.

380. Tang, N. *et al.* (2023) 'Sononeoperfusion: a new therapeutic effect to enhance tumour blood perfusion using diagnostic ultrasound and microbubbles', *Cancer Imaging*, 23(1), p. 29. Available at: https://doi.org/10.1186/s40644-023-00545-y.

381. Tarantini, S. *et al.* (2017) 'Impaired neurovascular coupling in aging and Alzheimer's disease: Contribution of astrocyte dysfunction and endothelial impairment to cognitive decline', *Experimental Gerontology*, 94, pp. 52–58. Available at: https://doi.org/10.1016/j.exger.2016.11.004.

382. Tatu, L. *et al.* (1998) 'Arterial territories of the human brain', *Neurology*, 50(6), pp. 1699–1708. Available at: https://doi.org/10.1212/WNL.50.6.1699.

383. Taylor, C. *et al.* (2022) 'Discriminators of pseudoprogression and true progression in high-grade gliomas: A systematic review and meta-analysis', *Scientific Reports*, 12, p. 13258. Available at: https://doi.org/10.1038/s41598-022-16726-x.

384. Telischak, N.A., Detre, J.A. and Zaharchuk, G. (2015) 'Arterial spin labeling MRI: clinical applications in the brain', *Journal of magnetic resonance imaging: JMRI*, 41(5), pp. 1165–1180. Available at: https://doi.org/10.1002/jmri.24751.

385. Tesler, F., Linne, M.-L. and Destexhe, A. (2023) 'Modeling the relationship between neuronal activity and the BOLD signal: contributions from astrocyte calcium dynamics', *Scientific Reports*, 13(1), p. 6451. Available at: https://doi.org/10.1038/s41598-023-32618-0.

386. Thammasart, S. *et al.* (2025) 'Associations between cerebral blood flow and progression of white matter hyperintensities', *Frontiers in Neuroimaging*, 3. Available at: https://doi.org/10.3389/fnimg.2024.1463311.

387. Thomas, B.P. *et al.* (2020) 'Brain Perfusion Change in Patients with Mild Cognitive Impairment After 12 Months of Aerobic Exercise Training', *Journal of Alzheimer's Disease*, 75(2), pp. 617–631. Available at: https://doi.org/10.3233/JAD-190977.

388. Tiemeier, H. *et al.* (2010) 'Cerebellum development during childhood and adolescence: a longitudinal morphometric MRI study', *NeuroImage*, 49(1), pp. 63–70. Available at: https://doi.org/10.1016/j.neuroimage.2009.08.016.

389. Tofts, P.S. *et al.* (1999) 'Estimating kinetic parameters from dynamic contrast-enhanced t1-weighted MRI of a diffusable tracer: Standardized quantities and symbols', *Journal of Magnetic Resonance Imaging*, 10(3), pp. 223–232. Available at: https://doi.org/10.1002/(SICI)1522-2586(199909)10:3<223::AID-JMRI2>3.0.CO;2-S.

390. Tomoto, T. *et al.* (2023) 'One-year aerobic exercise increases cerebral blood flow in cognitively normal older adults', *Journal of Cerebral Blood Flow and Metabolism: Official*

*Journal of the International Society of Cerebral Blood Flow and Metabolism*, 43(3), pp. 404–418. Available at: https://doi.org/10.1177/0271678X221133861.

391. Tortora, D. *et al.* (2017) 'Prematurity and brain perfusion: Arterial spin labeling MRI', *NeuroImage : Clinical*, 15, pp. 401–407. Available at: https://doi.org/10.1016/j.nicl.2017.05.023.

392. Tortora, D., Severino, M. and Rossi, A. (2020) 'Arterial spin labeling perfusion in neonates', *Seminars in Fetal and Neonatal Medicine*, 25(5), p. 101130. Available at: https://doi.org/10.1016/j.siny.2020.101130.

393. Toubasi, A.A. *et al.* (2024) 'Chronic active lesions preferentially localize in watershed territories in multiple sclerosis', *Annals of Clinical and Translational Neurology*, 11(11), pp. 2912–2922. Available at: https://doi.org/10.1002/acn3.52202.

394. Touyz, R.M. *et al.* (2018) 'Vascular smooth muscle contraction in hypertension', *Cardiovascular Research*, 114(4), pp. 529–539. Available at: https://doi.org/10.1093/cvr/cvy023.

395. Toyoda, K., Minematsu, K. and Yamaguchi, T. (1994) 'Long-term changes in cerebral blood flow according to different types of ischemic stroke', *Journal of the Neurological Sciences*, 121(2), pp. 222–228. Available at: https://doi.org/10.1016/0022-510x(94)90356-5.

396. Tsigaras, Z.A. *et al.* (2023) 'The pressure reactivity index as a measure of cerebral autoregulation and its application in traumatic brain injury management', *Critical Care and Resuscitation: Journal of the Australasian Academy of Critical Care Medicine*, 25(4), pp. 229–236. Available at: https://doi.org/10.1016/j.ccrj.2023.10.009.

397. Tuma, R.F., Durán, W.N. and Ley, K. (2008) *Microcirculation*. 2nd ed. Amsterdam Boston: Elsevier/Academic Press (Handbook of physiology. [Section 2, Cardiovascular system, v. 4]).

398. Tyc, V.L. *et al.* (1995) 'Children's distress during magnetic resonance imaging procedures', *Children's Health Care: Journal of the Association for the Care of Children's Health*, 24(1), pp. 5–19. Available at: https://doi.org/10.1207/s15326888chc2401_2.

399. Tzeng, Y.-C. and Ainslie, P.N. (2014) 'Blood pressure regulation IX: cerebral autoregulation under blood pressure challenges', *European Journal of Applied Physiology*, 114(3), pp. 545–559. Available at: https://doi.org/10.1007/s00421-013-2667-y.

400. Uchino, H. *et al.* (2025) 'Association between intracranial vascular vulnerability and indirect revascularization development in moyamoya disease', *Neurosurgical Review*, 48(1), p. 387. Available at: https://doi.org/10.1007/s10143-025-03544-8.

401. Vagvala, S. *et al.* (2022) 'Imaging diagnosis and treatment selection for brain tumors in the era of molecular therapeutics', *Cancer Imaging*, 22(1), p. 19. Available at: https://doi.org/10.1186/s40644-022-00455-5.

402. Varatharaj, A. and Galea, I. (2017) 'The blood-brain barrier in systemic inflammation', *Brain, Behavior, and Immunity*, 60, pp. 1–12. Available at: https://doi.org/10.1016/j.bbi.2016.03.010.

403. Varela, M. *et al.* (2012) 'Mean cerebral blood flow measurements using phase contrast MRI in the first year of life', *NMR in biomedicine*, 25(9), pp. 1063–1072. Available at: https://doi.org/10.1002/nbm.2771.

404. Vavilala, M.S. *et al.* (2002) 'Dynamic cerebral autoregulation in healthy adolescents', *Acta Anaesthesiologica Scandinavica*, 46(4), pp. 393–397. Available at: https://doi.org/10.1034/j.1399-6576.2002.460411.x.

405. Vergauwen, E. *et al.* (2018a) 'Central nervous system gadolinium accumulation in patients undergoing periodical contrast MRI screening for hereditary tumor syndromes', *Hereditary Cancer in Clinical Practice*, 16(1), p. 2. Available at: https://doi.org/10.1186/s13053-017-0084-7.

406. Vergauwen, E. *et al.* (2018b) 'Central nervous system gadolinium accumulation in patients undergoing periodical contrast MRI screening for hereditary tumor syndromes', *Hereditary Cancer in Clinical Practice*, 16, p. 2. Available at: https://doi.org/10.1186/s13053-017-0084-7.

407. Vernooij, M.W. *et al.* (2008) 'Total cerebral blood flow and total brain perfusion in the general population: the Rotterdam Scan Study', *Journal of Cerebral Blood Flow and Metabolism: Official Journal of the International Society of Cerebral Blood Flow and Metabolism*, 28(2), pp. 412–419. Available at: https://doi.org/10.1038/sj.jcbfm.9600526.

408. Vesoulis, Z.A. and Mathur, A.M. (2017) 'Cerebral Autoregulation, Brain Injury, and the Transitioning Premature Infant', *Frontiers in Pediatrics*, 5. Available at: https://doi.org/10.3389/fped.2017.00064.

409. Vestergaard, M.B. *et al.* (2017) 'Comparison of global cerebral blood flow measured by phase-contrast mapping MRI with 15O-H2O positron emission tomography', *Journal of Magnetic Resonance Imaging*, 45(3), pp. 692–699. Available at: https://doi.org/10.1002/jmri.25442.

410. Viessmann, O. *et al.* (2022) 'Static and dynamic BOLD fMRI components along white matter fibre tracts and their dependence on the orientation of the local diffusion tensor axis relative to the B0-field', *Journal of Cerebral Blood Flow & Metabolism*, 42(10), pp. 1905–1919. Available at: https://doi.org/10.1177/0271678X221106277.

411. Villringer, K. *et al.* (2017) 'DCE-MRI blood-brain barrier assessment in acute ischemic stroke', *Neurology*, 88(5), pp. 433–440. Available at: https://doi.org/10.1212/WNL.0000000000003566.

412. Voges, N. *et al.* (2012) 'Modeling of the neurovascular coupling in epileptic discharges', *Brain Topography*, 25(2), pp. 136–156. Available at: https://doi.org/10.1007/s10548-011-0190-1.

413. Wagner, M. *et al.* (2012) 'Age-Related Changes of Cerebral Autoregulation: New Insights with Quantitative T2′-Mapping and Pulsed Arterial Spin-Labeling MR Imaging', *AJNR: American Journal of Neuroradiology*, 33(11), pp. 2081–2087. Available at: https://doi.org/10.3174/ajnr.A3138.

414. Wamelink, I.J.H.G. *et al.* (2023) 'The patients' experience of neuroimaging of primary brain tumors: a cross-sectional survey study', *Journal of Neuro-Oncology*, 162(2), pp. 307–315. Available at: https://doi.org/10.1007/s11060-023-04290-x.

415. Wan, X. *et al.* (2025) 'Evaluation of Neurovascular Coupling in Early-Onset and Late-Onset Epilepsy of Unknown Etiology', *Journal of magnetic resonance imaging: JMRI*, 61(6), pp. 2489–2500. Available at: https://doi.org/10.1002/jmri.29678.

416. Wang, D.J.J. *et al.* (2012) 'The Value of Arterial Spin-Labeled Perfusion Imaging in Acute Ischemic Stroke', *Stroke*, 43(4), pp. 1018–1024. Available at: https://doi.org/10.1161/STROKEAHA.111.631929.

417. Wang, D.J.J. *et al.* (2013) 'Multi-delay multi-parametric arterial spin-labeled perfusion MRI in acute ischemic stroke — Comparison with dynamic susceptibility contrast enhanced perfusion imaging', *NeuroImage: Clinical*, 3, pp. 1–7. Available at: https://doi.org/10.1016/j.nicl.2013.06.017.

418. Wang, J.-N. *et al.* (2019) 'Application value of three-dimensional arterial spin labeling perfusion imaging in investigating cerebral blood flow dynamics in normal full-term neonates', *BMC Pediatrics*, 19(1), p. 495. Available at: https://doi.org/10.1186/s12887-019-1876-x.

419. Wang, N. *et al.* (2019) 'Arterial Spin Labeling for Glioma Grade Discrimination: Correlations with IDH1 Genotype and 1p/19q Status', *Translational Oncology*, 12(5), pp. 749–756. Available at: https://doi.org/10.1016/j.tranon.2019.02.013.

420. Wang, S. *et al.* (2022) 'Impact of impaired cerebral blood flow autoregulation on cognitive impairment', *Frontiers in Aging*, 3. Available at: https://doi.org/10.3389/fragi.2022.1077302.

421. Wang, Y. *et al.* (2023) 'Mitochondrial oxidative stress in brain microvascular endothelial cells: Triggering blood-brain barrier disruption', *Mitochondrion*, 69, pp. 71–82. Available at: https://doi.org/10.1016/j.mito.2023.01.007.

422. Wardlaw, J.M., Smith, C. and Dichgans, M. (2013) 'Mechanisms of sporadic cerebral small vessel disease: insights from neuroimaging', *The Lancet Neurology*, 12(5), pp. 483–497. Available at: https://doi.org/10.1016/S1474-4422(13)70060-7.

423. Wardlaw, J.M., Smith, C. and Dichgans, M. (2019) 'Small vessel disease: mechanisms and clinical implications', *The Lancet Neurology*, 18(7), pp. 684–696. Available at: https://doi.org/10.1016/S1474-4422(19)30079-1.

424. Weigel, M. (2015) 'Extended phase graphs: Dephasing, RF pulses, and echoes - pure and simple', *Journal of Magnetic Resonance Imaging*, 41(2), pp. 266–295. Available at: https://doi.org/10.1002/jmri.24619.

425. Weijs, R.W. *et al.* (2024) 'Cerebrovascular CO2 reactivity and dynamic cerebral autoregulation through the eighth decade of life and their implications for cognitive decline', *Journal of Cerebral Blood Flow and Metabolism: Official Journal of the International Society of Cerebral Blood Flow and Metabolism*, 44(5), pp. 712–725. Available at: https://doi.org/10.1177/0271678X231219568.

426. Welker, K.M. *et al.* (2025) 'State of Practice: ASNR Statement on Gadolinium-Based Contrast Agent Use in Patients with Chronic Kidney Disease', *AJNR. American journal of neuroradiology*, 46(2), pp. 227–230. Available at: https://doi.org/10.3174/ajnr.A8501.

427. Weller, M. *et al.* (2021) 'EANO guidelines on the diagnosis and treatment of diffuse gliomas of adulthood', *Nature Reviews Clinical Oncology*, 18(3), pp. 170–186. Available at: https://doi.org/10.1038/s41571-020-00447-z.

428. Wells, J. *et al.* (2017) 'MRI of cerebral micro-vascular flow patterns: A multi-direction diffusion-weighted ASL approach', *Journal of Cerebral Blood Flow & Metabolism*, 37(6), pp. 2076–2083. Available at: https://doi.org/10.1177/0271678X16660985.

429. Wells, J.A. *et al.* (2010) 'In vivo hadamard encoded continuous arterial spin labeling (H-CASL)', *Magnetic Resonance in Medicine*, 63(4), pp. 1111–1118. Available at: https://doi.org/10.1002/mrm.22266.

430. Whitaker, A.A. *et al.* (2024) 'Lower middle cerebral artery blood velocity during low-volume high-intensity interval exercise in chronic stroke', *Journal of Cerebral Blood Flow & Metabolism*, 44(5), pp. 627–640. Available at: https://doi.org/10.1177/0271678X231201472.

431. WHO Classification of Tumous Editorial Board (2021) *Central Nervous System Tumours*. 5th ed. Edited by Organisation mondiale de la santé and Centre international de recherche sur le cancer. Lyon: WHO (World health organization classification of tumours, 6).

432. Wiesmann, M. and Seidel, G. (2000) 'Ultrasound Perfusion Imaging of the Human Brain', *Stroke*, 31(10), pp. 2421–2425. Available at: https://doi.org/10.1161/01.STR.31.10.2421.

433. Wilke, M., Holland, S.K. and Krägeloh-Mann, I. (2007) 'Global, Regional, and Local Development of Gray and White Matter Volume in Normal Children', *Experimental brain research. Experimentelle Hirnforschung. Experimentation cerebrale*, 178(3), pp. 296–307. Available at: https://doi.org/10.1007/s00221-006-0732-z.

434. Williams, D.S. *et al.* (1992) 'Magnetic resonance imaging of perfusion using spin inversion of arterial water', *Proceedings of the National Academy of Sciences of the United States of America*, 89(1), pp. 212–216. Available at: https://doi.org/10.1073/pnas.89.1.212.

435. Willie, C.K. *et al.* (2014) 'Integrative regulation of human brain blood flow', *The Journal of Physiology*, 592(5), pp. 841–859. Available at: https://doi.org/10.1113/jphysiol.2013.268953.

436. Wing, B.H. *et al.* (2017) 'Developing the Standard of Care for Post-Concussion Treatment: Neuroimaging-Guided Rehabilitation of Neurovascular Coupling', *The Open Neuroimaging Journal*, 11, pp. 58–71. Available at: https://doi.org/10.2174/1874440001711010058.

437. Wintermark, M. *et al.* (2004) 'Admission Perfusion CT: Prognostic Value in Patients with Severe Head Trauma', *Radiology*, 232(1), pp. 211–220. Available at: https://doi.org/10.1148/radiol.2321030824.

438. Wolters, F.J. *et al.* (2017) 'Cerebral Perfusion and the Risk of Dementia', *Circulation*, 136(8), pp. 719–728. Available at: https://doi.org/10.1161/CIRCULATIONAHA.117.027448.

439. Wong, E.C., Buxton, R.B. and Frank, L.R. (1998) 'Quantitative imaging of perfusion using a single subtraction (QUIPSS and QUIPSS II)', *Magnetic Resonance in Medicine*, 39(5), pp. 702–708. Available at: https://doi.org/10.1002/mrm.1910390506.

440. Woods, J.G. *et al.* (2024) 'Recommendations for quantitative cerebral perfusion MRI using multi-timepoint arterial spin labeling: Acquisition, quantification, and clinical applications', *Magnetic Resonance in Medicine*, 92(2), pp. 469–495. Available at: https://doi.org/10.1002/mrm.30091.

441. Wu, C. *et al.* (2016) 'Age-Related Changes of Normal Cerebral and Cardiac Blood Flow in Children and Adults Aged 7 Months to 61 Years', *Journal of the American Heart Association*, 5(1), p. e002657. Available at: https://doi.org/10.1161/JAHA.115.002657.

442. Wu, C.-H. *et al.* (2024) 'Phasic perfusion dynamics among migraine subtypes: a multimodel arterial spin labeling investigation', *The Journal of Headache and Pain*, 25(1), p. 167. Available at: https://doi.org/10.1186/s10194-024-01880-6.

443. Wu, D. *et al.* (2023) 'The blood–brain barrier: Structure, regulation and drug delivery', *Signal Transduction and Targeted Therapy*, 8(1), pp. 1–27. Available at: https://doi.org/10.1038/s41392-023-01481-w.

444. Wu, W.-C. *et al.* (2007) 'A theoretical and experimental investigation of the tagging efficiency of pseudocontinuous arterial spin labeling', *Magnetic Resonance in Medicine*, 58(5), pp. 1020–1027. Available at: https://doi.org/10.1002/mrm.21403.

445. Wymer, D.T. *et al.* (2020) 'Phase-Contrast MRI: Physics, Techniques, and Clinical Applications', *RadioGraphics*, 40(1), pp. 122–140. Available at: https://doi.org/10.1148/rg.2020190039.

446. Xie, H. *et al.* (2020) 'Environmental enrichment enhances post-ischemic cerebral blood flow and functional hyperemia in the ipsilesional somatosensory cortex', *Brain Research Bulletin*, 160, pp. 91–97. Available at: https://doi.org/10.1016/j.brainresbull.2020.04.007.

447. Xiong, X.-Y., Liu, L. and Yang, Q.-W. (2016) 'Functions and mechanisms of microglia/macrophages in neuroinflammation and neurogenesis after stroke', *Progress in Neurobiology*, 142, pp. 23–44. Available at: https://doi.org/10.1016/j.pneurobio.2016.05.001.

448. Xiong, Z.-G. *et al.* (2008) 'Acid-Sensing Ion Channels (ASICs) as Pharmacological Targets for Neurodegenerative Diseases', *Current opinion in pharmacology*, 8(1), pp. 25–32. Available at: https://doi.org/10.1016/j.coph.2007.09.001.

449. Xu, F. *et al.* (2025) 'MULti-TImepoint VElocity-selective Reconciled with Spatially-sElective (MULTIVERSE) ASL: Improving robustness to both shortened and prolonged arterial transit time', *Magnetic Resonance in Medicine* [Preprint]. Available at: https://doi.org/10.1002/mrm.30540.

450. Xu, H. *et al.* (2023) 'Neurovascular coupling changes in patients with magnetic resonance imaging negative focal epilepsy', *Epilepsy & Behavior*, 138, p. 109035. Available at: https://doi.org/10.1016/j.yebeh.2022.109035.

451. Yamin, G. *et al.* (2024) 'Arterial Spin-Labeling and DSC Perfusion Metrics Improve Agreement in Neuroradiologists' Clinical Interpretations of Posttreatment High-Grade Glioma Surveillance MR Imaging—An Institutional Experience', *American Journal of Neuroradiology*, 45(4), pp. 453–460. Available at: https://doi.org/10.3174/ajnr.A8190.

452. Yang, L. *et al.* (2025) 'From Mechanisms to Medicine: Neurovascular Coupling in the Diagnosis and Treatment of Cerebrovascular Disorders: A Narrative Review', *Cells*, 14(1), p. 16. Available at: https://doi.org/10.3390/cells14010016.

453. Yang, X. *et al.* (2021) 'Predicting 1p/19q codeletion status using diffusion-, susceptibility-, perfusion-weighted, and conventional MRI in IDH-mutant lower-grade gliomas', *Acta Radiologica*, 62(12), pp. 1657–1665. Available at: https://doi.org/10.1177/0284185120973624.

454. Yang, Y. and Torbey, M.T. (2020) 'Angiogenesis and Blood-Brain Barrier Permeability in Vascular Remodeling after Stroke', *Current Neuropharmacology*, 18(12), pp. 1250–1265. Available at: https://doi.org/10.2174/1570159X18666200720173316.

455. Yin, L. *et al.* (2022) 'Long-term development of dynamic changes in neurovascular coupling after acute temporal lobe epilepsy', *Brain Research*, 1784, p. 147858. Available at: https://doi.org/10.1016/j.brainres.2022.147858.

456. Yoo, R.-E. *et al.* (2020) 'Arterial spin labeling perfusion-weighted imaging aids in prediction of molecular biomarkers and survival in glioblastomas', *European Radiology*, 30(2), pp. 1202–1211. Available at: https://doi.org/10.1007/s00330-019-06379-2.

457. Younkin, D. *et al.* (1988) 'Regional variations in human newborn cerebral blood flow', *The Journal of Pediatrics*, 112(1), pp. 104–108. Available at: https://doi.org/10.1016/S0022-3476(88)80131-8.

458. Zenaro, E., Piacentino, G. and Constantin, G. (2017) 'The blood-brain barrier in Alzheimer's disease', *Neurobiology of Disease*, 107, pp. 41–56. Available at: https://doi.org/10.1016/j.nbd.2016.07.007.

459. Zhang, Han-wen *et al.* (2020) 'DSC and DCE Histogram Analyses of Glioma Biomarkers, Including IDH, MGMT, and TERT, on Differentiation and Survival', *Academic Radiology*, 27(12), pp. e263–e271. Available at: https://doi.org/10.1016/j.acra.2019.12.010.

460. Zhang, Shui-xia *et al.* (2015) 'Comparative study of DSC-PWI and 3D-ASL in ischemic stroke patients', *Journal of Huazhong University of Science and Technology [Medical Sciences]*, 35(6), pp. 923–927. Available at: https://doi.org/10.1007/s11596-015-1529-8.

461. Zhao, M.Y. *et al.* (2021) 'Cerebrovascular reactivity measurements using simultaneous 15O-water PET and ASL MRI: Impacts of arterial transit time, labeling efficiency, and hematocrit', *NeuroImage*, 233, p. 117955. Available at: https://doi.org/10.1016/j.neuroimage.2021.117955.

462. Zhao, M.Y. *et al.* (2022) 'Using arterial spin labeling to measure cerebrovascular reactivity in Moyamoya disease: Insights from simultaneous PET/MRI', *Journal of Cerebral Blood Flow and Metabolism: Official Journal of the International Society of Cerebral Blood Flow and Metabolism*, 42(8), pp. 1493–1506. Available at: https://doi.org/10.1177/0271678X221083471.

463. Zhao, M.Y. *et al.* (2023) 'Revascularization improves vascular hemodynamics − a study assessing cerebrovascular reserve and transit time in Moyamoya patients using MRI', *Journal of Cerebral Blood Flow & Metabolism*, 43(2_suppl), pp. 138–151. Available at: https://doi.org/10.1177/0271678X221140343.

464. Zhao, M.Y. *et al.* (2024) 'Measuring Quantitative Cerebral Blood Flow in Healthy Children: A Systematic Review of Neuroimaging Techniques', *Journal of Magnetic Resonance Imaging*, 59(1), pp. 70–81. Available at: https://doi.org/10.1002/jmri.28758.

465. Zhao, M.Y. *et al.* (no date) 'Measuring Quantitative Cerebral Blood Flow in Healthy Children: A Systematic Review of Neuroimaging Techniques', *Journal of Magnetic Resonance Imaging*, n/a(n/a). Available at: https://doi.org/10.1002/jmri.28758.

466. Zhao, Y. *et al.* (2024) 'Knockdown of ATRX enhances radiosensitivity in glioblastoma', *Chinese Neurosurgical Journal*, 10(1), p. 19. Available at: https://doi.org/10.1186/s41016-024-00371-6.

467. Zhao, Z. *et al.* (2015a) 'Establishment and Dysfunction of the Blood-Brain Barrier', *Cell*, 163(5), pp. 1064–1078. Available at: https://doi.org/10.1016/j.cell.2015.10.067.

468. Zhao, Z. *et al.* (2015b) 'Establishment and Dysfunction of the Blood-Brain Barrier', *Cell*, 163(5), pp. 1064–1078. Available at: https://doi.org/10.1016/j.cell.2015.10.067.

469. Zheng, Q., Freeman, C.W. and Hwang, M. (2021) 'Sex-related differences in arterial spin-labelled perfusion of metabolically active brain structures in neonatal hypoxic–ischaemic encephalopathy', *Clinical Radiology*, 76(5), pp. 342–347. Available at: https://doi.org/10.1016/j.crad.2020.12.026.

470. Zhou, J. *et al.* (2022) 'Review and consensus recommendations on clinical APT-weighted imaging approaches at 3T: Application to brain tumors', *Magnetic Resonance in Medicine*, 88(2), pp. 546–574. Available at: https://doi.org/10.1002/mrm.29241.

471. Zhou, J. *et al.* (2025) 'The global, regional, and national brain and CNS cancers burden and trends from 1990 to 2021', *Scientific Reports*, 15(1), p. 19228. Available at: https://doi.org/10.1038/s41598-025-04636-7.

472. Zhu, Q. *et al.* (2024) 'Intratumoral calcification: not only a diagnostic but also a prognostic indicator in oligodendrogliomas', *European Radiology*, 34(6), pp. 3674–3685. Available at: https://doi.org/10.1007/s00330-023-10405-9.

473. Zhu, W.M. *et al.* (2022) 'Neurovascular coupling mechanisms in health and neurovascular uncoupling in Alzheimer's disease', *Brain: A Journal of Neurology*, 145(7), pp. 2276–2292. Available at: https://doi.org/10.1093/brain/awac174.

474. Zierfuss, B., Larochelle, C. and Prat, A. (2024) 'Blood-brain barrier dysfunction in multiple sclerosis: causes, consequences, and potential effects of therapies', *The Lancet.*

*Neurology*, 23(1), pp. 95–109. Available at: https://doi.org/10.1016/S1474-4422(23)00377-0.

475. Zlokovic, B.V. (2005) 'Neurovascular mechanisms of Alzheimer's neurodegeneration', *Trends in Neurosciences*, 28(4), pp. 202–208. Available at: https://doi.org/10.1016/j.tins.2005.02.001.

476. Zlokovic, B.V. (2008) 'The blood-brain barrier in health and chronic neurodegenerative disorders', *Neuron*, 57(2), pp. 178–201. Available at: https://doi.org/10.1016/j.neuron.2008.01.003.

477. Zun, Z. *et al.* (2021) 'Longitudinal Trajectories of Regional Cerebral Blood Flow in Very Preterm Infants during Third Trimester Ex Utero Development Assessed with MRI', *Radiology*, 299(3), pp. 691–702. Available at: https://doi.org/10.1148/radiol.2021202423.